

Electronic Structure and Bonding in Molecular f Element Chemistry

A thesis submitted to The University of Manchester for the degree of Doctor of Philosophy in
the Faculty of Science and Engineering.

2021

Benjamin E. Atkinson

Department of Chemistry, School of Natural Sciences

Contents

List of Figures	5
List of abbreviations	9
Abstract	11
Declaration	13
Justification for journal format	15
Copyright Statement	17
Acknowledgements	19
I Introduction	21
1 Background: Quantum chemistry	25
1.1 Basis sets	26
1.2 Wavefunction theory	27
1.3 Density functional theory	38
1.4 Relativity	44
1.5 Reducing computational cost	45
1.6 Analytical techniques	47
2 Background: Molecular uranium chemistry	55
2.1 Uranyl	55

2.2	Uranium-pnictogen chemistry	57
2.3	Diuranium complexes	65
II	Results	79
3	Post Hartree-Fock calculations of pnictogen-uranium bonding in EUF_3 ($\text{E} = \text{N-Bi}$)	81
	Supplementary information	87
4	High oxidation state electron-poor metal-to-ligand backbonding in a crystalline uranium(V)-dinitrogen complex	95
	Supplementary information	126
5	Synthesis, characterisation and electronic structure of U_2N_2 complexes	149
	Supplementary information	170
6	U_2N_2 rings in diuranium complexes: a comparative computational study	183
	Supplementary information	210
7	Exchange coupling in complexes containing diuranium diamond cores	239
	Supplementary information	255
8	The ditungsten decacarbonyl dianion	263
	Supplementary information	270
III	Conclusion	283

Word Count: 55848

List of Figures

- 1.1 The division of orbitals in CASSCF calculations into three spaces; inactive, active and virtual. Examples of allowed excitations are shown as solid, blue arrows. Excitations included in the CASPT2 perturbation are shown as dashed, red arrows. 33
- 2.1 A qualitative AnO_2^{2+} MO diagram. The HOMO of UO_2^{2+} is the $\text{O}2p \sigma_u$, shown doubly occupied. Reproduced with permission from *Coordination Chemistry Reviews*.⁵⁶ 56
- 2.2 The natural orbitals of the [6,6] active space for NUF_3 (left), PUF_3 (middle) and AsUF_3 (right). Calculations at the CASPT2 level of theory. Occupation numbers shown in brackets. Reproduced with permission from *Angewandte Chemie International Edition* (NUF_3 and PUF_3)⁶⁰ and *Inorganic Chemistry* (AsUF_3)⁶¹. . . 58
- 2.3 The reaction scheme for the synthesis of the first isolable terminal uranium nitride complex (structure 4) as performed by D. M. King *et al.* and first reported in *Science*⁶⁶, and the reaction scheme from structure 4 to the first terminal nitride isolated at ambient conditions (structure 7). 12C4 = 12-crown-4. Reproduced with permission from *Nature*¹ 60

2.4	The structures of early examples of phosphorus-uranium complexes, shown as thermal ellipsoids as derived from X-ray crystallography. Structure 1, $\text{U}[\mu_5\text{-C}_5(\text{CH}_3)_5][(\text{CH}_3)_2\text{PCH}_2\text{CH}_2\text{P}(\text{CH}_3)_2]$ reported by M. R. Duttera <i>et al.</i> in 1984 and reproduced with permission from <i>the Journal of the American Chemical Society</i> . ⁶⁸ . Structure 2, $\text{U}[\mu_5\text{-C}_5(\text{CH}_3)_5][\text{OP}(\text{CH}_3)_3][\text{P}-2,4,6\text{-t-Bu}_3\text{C}_6\text{H}_2]$ reported by D. S. J. Arney <i>et al.</i> in 1996 and reproduced with permission from <i>the Journal of the American Chemical Society</i>	62
2.5	The synthesis of the uranium phosphide (structure 2) and phosphinidine (structure 4) identified by B. M. Gardner <i>et al.</i> . Reproduced with permission from <i>Angewandte Chemie - International Edition</i> . ⁷⁰	63
2.6	The synthesis of the uranium arsenide (structure 2c), uranium arsinidene (structure 3c) and tetrameric complex (structure 4) identified by B. M. Gardener <i>et al.</i> Reproduced with permission from <i>Nature Chemistry</i> . ⁶⁷	64
2.7	The structures of the $\text{U}[\text{Tren}^{\text{DMBS}}]\text{ESiMe}_3$ complexes, from X-ray crystallography, as reported by T. M. Rookes <i>et al.</i> E = P (a), As (b), Sb (c) and Bi (d). Reproduced with permission from <i>Angewandte Chemie - International Edition</i> . ⁷¹	65
2.8	The active orbitals of U_2 . Symmetry labels and occupation numbers are given (for degenerate orbitals, the occupancy is of both orbitals). Reproduced with permission from <i>Nature</i> . ⁹¹	67
2.9	The structures of U_2H_2 (left), and U_2H_4 (centre, P. F. Souter <i>et al.</i> , and right, J. Raab <i>et al.</i>). Bond lengths in ångstrom, angles in degrees. Structural parameters in bold are that calculated by J. Raab <i>et al.</i> ⁹³ at the CASPT2 level of theory, italic are that from P. F. Souter <i>et al.</i> at the DFT/BP86 level of theory.	69

2.10 The structure of previously reported diuranium-N ₂ complexes. Structure images adapted with permission from <i>Organometallics</i> 2013, 32, 15, 4214–4222. ⁹⁷ Copyright 2013 American Chemical Society.	71
2.11 The structure of previously reported diuranium bis-nitride complexes. For F , ethyl groups on the bridging carbon of the calix[4]-tetrapyrrole are omitted for clarity.	72
2.12 Possible UO ₂ ⁺ cation-cation interaction dimers. Reproduced with permission from <i>Inorg. Chem.</i> 2019, 58, 15, 10148–10159. ¹¹⁰ Copyright 2019 American Chemical Society.	74
2.13 The structure of some previously reported diuranium bis-chalcenide complexes. K is adapted from the Journal of the American Chemical Society, ⁸⁵ L from Nature Chemistry, ¹⁰⁹ M from Inorganic Chemistry, ¹¹⁰ , N from Chemical Science, and P from the Journal of the American Chemical Society, ¹¹¹ all with permission. . . .	74
4.1 The structure of the U(V)–N ₂ complex identified in this work (left), and the structure of the core model used in post-Hartree Fock calculations (right). . . .	96
4.2 Relative energy (kJ mol ^{–1}) vs U1-N1 distance (Å). ‘XRD’ and ‘Relaxed’ calculations are on the full molecule 2 ; ‘Core’ is the model shown in Figure 4.1 (2 core). All scans are rigid, i.e. in which all geometric parameters other than the U1-N1 distance are frozen, except the Relaxed / UPBE scan, in which other geometric parameters are optimised at each point.	97
4.3 The natural orbitals of the RASSCF calculation on 2 core at U1-N1 = 2.56 Å, the minimum energy point on the scan. Bottom row: RAS1, middle: RAS2, top: RAS3. The isosurfaces enclose 90% of the orbital electron density. Occupation numbers are shown in Table S1	99

6.1	The structure of U_2N_2 ring-containing complexes previously isolated. For B , ethyl groups on the bridging carbon of the calix[4]-tetrapyrrole are omitted for clarity.	183
6.2	The crystal structure of $\text{U}_2\text{N}_2\text{L}_6\text{THF}$ ($\text{L} = [\text{OSi}(\text{O}^t\text{Bu})_3]^-$). Hydrogens omitted for clarity. L. Barluzzi and M. Mazzanti, personal correspondence.	184

List of abbreviations

BCP	Bond Critical Point
BSDFT	Broken Symmetry Density Functional Theory
CASPT2	CASSCF with second order perturbation theory
CASSCF	Complete Active Space Self Consistent Field
CC	Coupled Cluster
CCP	Cage Critical Point
CI	Configuration Interaction
DFT	Density Functional Theory
DIIS	Direct Inversion of the Iterative Subspace
DKH	Douglas-Kroll-Hess (Hamiltonian)
ECP	Effective Core Potential
GASSCF	General Active Space Self Consistent Field
GGA	Generalised Gradient Approximation
GTO	Gaussian Type Orbital
IAO	Intrinsic Atomic Orbital
IBO	Intrinsic Bonding Orbital
IR	Infrared
KS	Kohn-Sham
LDA	Local Density Approximation
LMO	Localised Molecular Orbital

MCSCF	Multiconfigurational Self Consistent Field
MPn	Møller–Plesset perturbation theory (nth order)
MS-CASPT2	Multi State CASPT2
NAO	Natural Atomic Orbital
NBO	Natural Bonding Orbital
NPA	Natural Population Analysis
QTAIM	Quantum Theory of Bonding in Molecules
RASSCF	Restricted Active Space Self Consistent Field
RASSI	Restricted Active Space-State Interaction
RCP	Ring Critical Point
RECP	Relativistic Effective Core Potential
RI	Resolution of the Identity
ROHF	Restricted Open Shell Hartree Fock
SA-CASSF	State Averaged-Complete Active Space Self Consistent Field
SCF	Self Consistent Field
STO	Slater Type Orbital
UHF	Unrestricted Hartree Fock

Abstract

This thesis focuses on the electronic structure of uranium in molecules, and in particular uranium-nitrogen chemistry. Theoretical techniques, most notably density functional theory (DFT) and multiconfigurational calculations, are used to analyse novel bonding.

Multiconfigurational calculations are performed on the molecules EUNF_3 ($\text{E} = \text{N-Bi}$) in Chapter 3. NUF_3 is identified as having a $\text{U}\equiv\text{N}$ bond, but PUF_3 and AsUF_3 are identified as having single bonds, in contrast to previous studies which used a smaller active space and identified a triple bond for all three molecules.

A $\text{U(V)}\text{-N}_2$ complex is studied in Chapter 4, a rare example of a high oxidation state metal centre binding to a poor π donor ligand. Potential energy surface calculations scans demonstrate that the U-N_2 potential is shallow, and while DFT under-predicts the U-N_2 bond length, post-Hartree Fock calculations on a model system are closer to the crystal structure.

Diuranium complexes which feature a diamond U_2X_2 motif are studied in Chapters 5, 6 and 7. In Chapter 5, the synthesis of a $\text{U(IV)} \text{U}_2\text{N}_2$ complex is reported, alongside a study of its electronic structure where a 12 electron delocalised bonding system is identified. Chapter 6 builds on this work, comparing the U(IV) complex studied in Chapter 5 with the two other previously reported U_2N_2 ring-containing complexes. Complexes U_2X_2 rings with different bridging ligands are studied in Chapter 7. The relationship between bonding in the ring and magnetic properties is explored.

Chapter 8 reports the isolation, characterisation and computational study of $\text{W}_2(\text{CO})_{10}^{2-}$. The crystal structure obtained has the carbonyl complex in the eclipsed conformer. Calculations are performed on the gas phase dianion which predict the staggered geometry is preferred, suggesting that the observed geometry is due to crystal packing forces.

Declaration

No portion of the work referred to in the thesis has been submitted in support of an application for another degree or qualification of this or any other university or other institute of learning.

Justification for journal format

This thesis is in journal format, where the results chapters are articles published in a peer reviewed journal, or in a format suitable for publication. This has encouraged publication throughout my course of study, without rewriting for this thesis.

Copyright Statement

- (i) The author of this thesis (including any appendices and/or schedules to this thesis) owns certain copyright or related rights in it (the “Copyright”) and s/he has given The University of Manchester certain rights to use such Copyright, including for administrative purposes.
- (ii) Copies of this thesis, either in full or in extracts and whether in hard or electronic copy, may be made only in accordance with the Copyright, Designs and Patents Act 1988 (as amended) and regulations issued under it or, where appropriate, in accordance with licensing agreements which the University has from time to time. This page must form part of any such copies made.
- (iii) The ownership of certain Copyright, patents, designs, trademarks and other intellectual property (the “Intellectual Property”) and any reproductions of copyright works in the thesis, for example graphs and tables (“Reproductions”), which may be described in this thesis, may not be owned by the author and may be owned by third parties. Such Intellectual Property and Reproductions cannot and must not be made available for use without the prior written permission of the owner(s) of the relevant Intellectual Property and/or Reproductions.
- (iv) Further information on the conditions under which disclosure, publication and commercialisation of this thesis, the Copyright and any Intellectual Property and/or Reproductions described in it may take place is available in the University IP Policy (see <http://documents.manchester.ac.uk/DocuInfo.aspx?DocID=24420>), in any relevant Thesis restriction declarations deposited in the University Library, The University Library's

regulations (see <http://www.library.manchester.ac.uk/about/regulations/>) and in The University's policy on Presentation of Theses.

Acknowledgements

First, I would like to thank Prof. Nikolas Kaltsoyannis for the opportunity to undertake this PhD, and for his support throughout my PhD. I've greatly enjoyed my PhD, the freedom to drive its direction and to study a variety of actinide containing molecules, with Nik's constant advice. I am also grateful to Prof. Han-Shi Hu for her help and advice in the first few months of my PhD. I have enjoyed the collaborative nature of my thesis, and am thankful to Prof. Steve Liddle, University of Manchester, and Prof. Marinella Mazzanti, École Polytechnique Fédérale de Lausanne.

Thanks to the EPSRC and the University of Manchester for financial support, and the assistance given by Research IT and the use of the Computational Shared Facility at The University of Manchester. I recently joined Research IT while finishing off my thesis, and have been appreciative of how welcoming Pen and the Research IT team have been, especially given that I joined the team remotely.

I'd also like to thank everyone in the Kaltsoyannis group and the Dover Street Building for their friendship, assistance and cake. I've greatly missed the supportive atmosphere of the office, and am looking forward to when we can meet up again. Thanks to Sophie, Tom, Nic, Jon, Naomi, James, Vikki, Jiali, Angelica, Jonny, Adam, Jon and Lin. Because we've been spending a lot of time at home, I have spent a lot more time with my housemates Dom, Jake, Lefteris and Yuxin. I've appreciated their friendship and support throughout my time writing up.

Finally, I'm hugely thankful to my parents, Peter, Neepea and Gill, for their love, support and encouragement.

Part I

Introduction

Bonding between actinides and main group atoms/ligands has long been of interest. The covalency and bonding motifs observed distinguish the actinides from the lanthanides and transition metals. Uranium's central role in nuclear power necessitates a detailed knowledge of its chemistry, including at the most fundamental level.

Uranium-nitrogen chemistry is of particular interest due to the potential of uranium nitride as a superior nuclear fuel, due to its properties such as higher melting point, thermal conductivity and density. Additionally, there is interest in the magnetic properties of uranium containing molecules, uranium's capacity to reduce dinitrogen and possible application of uranium catalysts in uranium fixation.¹⁻⁴

Structure of this thesis

The main focus of my PhD has been theoretical study of uranium-containing molecules. More specifically, I have focused on novel uranium-nitrogen bonding and the electronic and magnetic properties of diuranium complexes. Chapter 1 describes the theoretical background of the methods used in this thesis to study molecular electronic structure.

Next, Chapter 2 includes a brief discussion of key aspects of actinide chemistry as a whole, before moving on to focus on areas particularly relevant to this thesis; uranium-pnictogen chemistry, diuranium complexes, and computational work in these areas.

Chapter 3 reports calculations on the pnictogen-uranium bond in EUF_3 ($\text{E} = \text{N-Bi}$). This was published in 2018 in *Chemical Communications*.⁵

A novel high oxidation state U(V)-dinitrogen complex is reported in Chapter 4. This work was in collaboration with Prof. Steve Liddle, University of Manchester, and was published in 2019 in *Nature Chemistry*.⁶

The synthesis, characterisation and electronic structure of two U(IV) nitrogen-bridged diuranium complexes is reported in Chapter 5. This work is developed in Chapter 6, where

several previously experimentally isolated diuranium bis-nitride complexes are compared computationally. Chapter 7 compares the magnetic properties several diranium complexes, where the bridging ligand is varied.

Finally, Chapter 8 makes a brief diversion to transition metal carbonyls with a report of the isolation, characterisation and theoretical study of $W_2CO_{10}^{2-}$. This work was performed in collaboration with Prof. Steve Liddle, and published in *Dalton Transactions*.⁷

1

Background: Quantum chemistry

The basis of the electronic structure of atoms and molecules is the time-independent Schrödinger equation, which for a molecule with N nuclei and n electrons is:

$$\hat{H}\Psi(\vec{r}_n, \vec{r}_N) = E\Psi(\vec{r}_n, \vec{r}_N) \quad (1.1)$$
$$\text{where } \hat{H} = \sum_n \hat{T}_n + \sum_N \hat{T}_N + \sum_n \sum_{m>n} \hat{V}_{nm} + \sum_N \sum_{M>N} \hat{V}_{NM} + \sum_N \sum_n \hat{V}_{Nn}$$

and where \hat{H} is the Hamiltonian (total energy) operator, $\Psi(\vec{r}_n, \vec{r}_N)$ is the total wavefunction, E is the energy eigenvalue, \hat{T} is the kinetic energy operator, \hat{V} is the Coulombic energy operator, and \vec{r}_N & \vec{r}_n are the position vectors of the nuclei and electrons, respectively. The kinetic and Coulombic energy operators have the form:

$$\hat{T} = -\frac{\hbar^2 \nabla^2}{2m}, \quad \hat{V}_{12} = \frac{q_1 q_2}{4\pi\epsilon_0 r_{12}} \quad (1.2)$$

where m is the mass, q_N is the charge of N , r_{12} is the distance between particles 1 and 2, and ϵ_0 is the vacuum permittivity.⁸

An important assumption in efforts to approximate the wavefunction of a molecule is the Born-Oppenheimer approximation; because the nucleus is many times more massive than electrons, electronic motion can be considered as instantaneous on the nuclear timescale. As such, the total wavefunction can be written $\Psi_{\text{total}} \simeq \Psi_{\text{electronic}} \times \Psi_{\text{nuclear}}$; the Hamiltonian is similarly split into electronic and nuclear parts.

Within the Born-Oppenheimer approximation, other than for very simple hydrogenic systems, the Schrödinger equation is not analytically solvable. Either inexact techniques must be used to obtain an approximate wavefunction, or alternative strategies such as calculating the total electron density $\rho_{\text{el.}} = |\Psi_{\text{el.}}|^2$ using Density Functional Theory (DFT).⁸

1.1 Basis sets

A basis set is a set of functions which are used to generate molecular orbitals (MOs) of a system. For molecular studies, they are typically atom centred and represent the atomic orbitals of a molecule. The two most common types of basis functions which make up the set are Slater-type orbitals (STOs) and Gaussian-type orbitals (GTOs).⁹

STOs have the form:

$$\eta^{\text{STO}} = Nr^{n-1}e^{-\zeta r}Y_{lm_l}(\theta, \phi) \quad (1.3)$$

where N is a normalisation constant, n is the principal quantum number, ζ is the exponent which controls how diffuse the orbital is (*i.e.* small ζ represents a diffuse orbital), l is the angular momentum quantum number and m_l is the angular momentum projection quantum number. $Y_{lm_l}(\theta, \phi)$ are the spherical harmonic functions; describing the angular part of the orbital. STOs have the same form as hydrogenic orbitals, and their behaviour as $r \rightarrow 0$ is physical, tending to infinity (and so a non-zero cusp at the nucleus in their radial distribution functions, for s orbitals). However, three and four centre two-electron integrals must be performed numerically. GTOs have the form:

$$\chi^{\text{GTO}} = NY_{l,m_l}(\theta, \phi)r^{2n-2-1}e^{-\alpha r^2} \quad (1.4)$$

where N is a normalisation constant, and $Y_{l,m_l}(\theta, \phi)$ are the spherical harmonic functions, l is the angular momentum quantum number and m_l is the angular momentum projection quantum number. The constant α is the exponent that represents how diffuse the orbital is. The

advantage of GTOs is that calculating the Coulomb and exchange integrals is very efficient since the product of two GTOs (centred on different atoms) is a finite sum of GTOs. However, as $r \rightarrow 0$, their behaviour is unphysical, tending to a limit; hydrogenic orbitals tend to infinity. For this reason that a linear combination of Gaussian functions is often used to approximate STOs to give a ‘contracted Gaussian function’.⁹

The number of these functions employed is denoted the ‘zeta’; a double zeta uses two orbitals for each valence orbital, a triple zeta uses three, *etc.* Basis sets typically employ a slightly more complex arrangement, termed ‘split-valence’ where only some orbitals are given an increased zeta. Polarisation functions (or correlation functions, due to their importance in capturing correlation energy) are typically added, including higher angular momentum functions than would be required for a neutral atomic valence configuration. A large number of electrons in systems containing heavy atoms can make calculations very computationally demanding. These calculations can be made much more efficient with the use of effective core potentials (ECPs). Since core electrons play little role in chemical interactions, their interaction can be replaced with a function that represents their interaction with the nucleus and can also take into account relativistic effects.⁹ Their role in describing relativistic effects is discussed in more detail in section 1.4.

1.2 Wavefunction theory

Hartree Fock

One of the earliest techniques for approximating the electronic wavefunction was that by D. R. Hartree, who assumed that the total wavefunction could be treated as a product of one-electron wavefunctions, *i.e.* for an n -electron wavefunction $\Psi_{\text{el.}} = \prod_n \phi_n$, where $\phi_n = \phi_n(\vec{r}_n)$.

This assumption importantly neglects exchange energy by neglecting the Pauli principle, that the electronic wavefunction must be antisymmetric with respect to permutation of

electrons (because electrons are fermions). The Hartree-Fock method satisfies the Pauli principle by representing the total wavefunction as a single Slater determinant, representing a single electronic configuration:¹⁰

$$\Psi_{\text{HF}} = \frac{1}{\sqrt{n!}} \begin{vmatrix} \phi_1 & \phi_2 & \cdots & \phi_n \\ \phi_1 & \phi_2 & \cdots & \phi_n \\ \vdots & \vdots & \ddots & \vdots \\ \phi_1 & \phi_2 & \cdots & \phi_n \end{vmatrix} = \frac{1}{\sqrt{n!}} \begin{vmatrix} \phi_1 & \phi_2 & \phi_3 & \cdots & \phi_n \end{vmatrix} \quad (1.5)$$

The assumption that the wavefunction is a single determinant represents the approximation central to Hartree-Fock; that electron-electron interactions can be described as a single electron interacting with a ‘mean-field’ of the others, and that the motion of a single electron is separable from the others.

The energy that this neglects is termed ‘correlation energy’. Since Hartree-Fock obeys the variational principle (that a trial wavefunction’s energy can never be below that of the true ground state), correlation energy is always a negative, stabilising, term. Correlation energy is generally described as being split into two components: dynamic correlation, instantaneous interactions not captured in the mean-field approach of Hartree Fock, and static correlation, large deviations from a single Slater determinant wavefunction.¹⁰

The self-consistent field method is used to generate an approximate solution since only one-electron systems can be solved exactly. The Fock operator gives the energy of a molecular orbital and is defined as:

$$\hat{F}\phi_i = \left[\hat{h} + \sum_j \left(\hat{J}_{ij} - \hat{K}_{ij} \right) \right] \phi_i = \varepsilon_i \phi_i \quad (1.6)$$

where \hat{h} is the one-electron Hamiltonian, \hat{J} and \hat{K} are the Coulomb and exchange integrals, and ε_n is the orbital energy. The one-electron Hamiltonian, Coulomb and exchange integrals have

the form:

$$\hat{h}_i = \hat{T} + \sum_N \hat{V}_{iN} \quad (1.7)$$

$$\hat{J}_{ij} = [ij|ij] \quad (1.8)$$

$$\hat{K}_{ij} = [ij|ji] \quad (1.9)$$

$$\text{where: } [ab|cd] = \left\langle \phi_a(\vec{r}_1) \phi_b(\vec{r}_1) \left| \frac{1}{r_{12}} \right| \phi_c(\vec{r}_2) \phi_d(\vec{r}_2) \right\rangle \quad (1.10)$$

The indices a, b, c and d refer to the orbitals, 1 and 2 to the electrons.

The Hartree-Fock energy is then given by:

$$E_{HF} = \langle \Psi_{HF} | \hat{H} | \Psi_{HF} \rangle = \sum_i \langle \phi_i | \hat{h}_i | \phi_i \rangle + \frac{1}{2} \sum_{ij} (\hat{J}_{ij} - \hat{K}_{ij}) \quad (1.11)$$

$$= \sum_i \varepsilon_i - \frac{1}{2} \sum_{ij} (\hat{J}_{ij} - \hat{K}_{ij}) \quad (1.12)$$

As shown above, the sum of the orbital energies is not equal to the total Hartree-Fock energy due to the double counting of two-electron energies.¹¹

In the most simple optimisation scheme, an initial guess of the molecular orbitals is used to generate the Fock matrix (whose elements are $F_{ij} = \langle \phi_i | \hat{F} | \phi_j \rangle$), and by diagonalising the Fock matrix, a new trial set of MOs is generated. This new set of MOs is used to generate a new Fock matrix, which is again diagonalised. When the MOs are sufficiently similar to that calculated in the previous iteration, the Fock matrix is self-consistent and so the SCF process is complete. Modern programs use schemes to speed up SCF convergence such as ‘direct inversion in the iterative subspace’ (DIIS).¹¹

Spin

Spin, the intrinsic angular momentum fundamental particles possess, was largely neglected in the above discussion of Hartree-Fock. Electrons are fermions, and have spin of $\frac{1}{2}$; the spin magnitude is $\frac{\hbar}{2}$ and projection of $\pm\frac{\hbar}{2}$, notated $|\alpha\rangle$ or $|\beta\rangle$ where:

$$\langle\alpha|\alpha\rangle = \langle\beta|\beta\rangle = 1, \quad \langle\alpha|\beta\rangle = \langle\beta|\alpha\rangle = 0 \quad (1.13)$$

The one electron orbitals are then four-dimensional spinorbitals $|\phi_i\rangle = |\chi(\vec{r})_i\rangle |\sigma_i\rangle$, where $|\chi(\vec{r})_i\rangle$ is the spatial component of the orbital, and $|\sigma_i\rangle$ corresponds to spin. This allows two electrons to occupy each orbital, so for closed-shell molecules, the Hartree-Fock energy becomes:

$$E_{HF} = 2 \sum_i \varepsilon_i - \sum_{ij} (\hat{J}_{ij} - \hat{K}_{ij}) \quad (1.14)$$

Open-shell molecules are either treated using unrestricted Hartree-Fock (UHF), whereby the spatial component of alpha and beta orbitals are allowed to differ or restricted open-shell Hartree-Fock (ROHF), where spatial orbitals are kept equal but some orbitals are only singly occupied. Unrestricted calculations are most common, partly because such methods are easier to implement, but also because they can account for spin polarisation. However, UHF wavefunctions are no longer eigenfunctions of the square of the spin angular momentum operator \hat{S}^2 . This can result in \hat{S}^2 expectation values which substantially differ from that expected, known as spin contamination as the wavefunction is contaminated by contributions from higher spin states. Deviations of around 5% can typically be ignored, however, deviations greater than this are typically a sign that the wavefunction is poorly represented by one Slater determinant.

Post Hartree-Fock methods

Given the central approximation in Hartree-Fock is that the wavefunction can be described by one Slater determinant, a logical approach to improving on Hartree-Fock is including more than one Slater determinant in a trial wavefunction. There are various methodologies which include excited configurations; the simplest in concept, full configuration interaction (full CI) includes all configurations of a given space and spin symmetry and would give an exact solution to the Schrödinger equation (with an infinite basis set, within the constraints of the Born-Oppenheimer approximation and noting that the Schrödinger equation ignores relativistic effects). CI becomes more tractable by limiting the number of excitations from the Hartree-Fock reference configuration, for example, CISD includes only single and double excitations. Excitation operators are used to notate included configurations; for example for a double excitation \hat{C}_{ij}^{ab} denotes excitation from occupied orbitals i and j to virtual orbitals a and b . The CISD wavefunction is then:

$$|\Psi_{\text{CISD}}\rangle = \left(1 + \sum_{ai} c_i^a \hat{C}_i^a + \frac{1}{2} \sum_{abij} c_{ij}^{ab} \hat{C}_{ij}^{ab} \right) |\Psi_{\text{HF}}\rangle \quad (1.15)$$

The coefficients c are solved iteratively as an eigenvalue equation. CI methods have several drawbacks; CISD is not size-extensive (i.e. when A and B are well separated, $E(A + B) \neq E(A) + E(B)$) and computationally expensive, with the amount of correlation energy recovered quite small while higher-order methods (including triple, quadruple *etc.* excitations) become very expensive.¹²

Coupled-cluster (CC) methods employ an exponential operator, which eliminates some of

the disadvantages of CI:

$$|\Psi_{CC}\rangle = e^{\hat{T}} \quad (1.16)$$

$$\hat{T} = \hat{T}_1 + \hat{T}_2 + \hat{T}_3 \dots \quad (1.17)$$

$$\hat{T}_1 = \sum_{ai} t_i^a \hat{C}_i^a, \hat{T}_2 = \sum_{abij} t_{ij}^{ab} \hat{C}_{ij}^{ab} \quad (1.18)$$

The cluster amplitudes, t , are optimised variationally. The exponential operator is expanded as a Taylor series. For coupled-cluster with double excitations (CCD), this has the form:

$$e^{\hat{T}} = 1 + \hat{T}_2 + \frac{1}{2!} \hat{T}_2^2 + \frac{1}{3!} \hat{T}_2^3 + \dots \quad (1.19)$$

The advantage of CC techniques versus CI is the inclusion of ‘connected’ excitations; \hat{T}_2^2 is a quadruple excitation ‘connected’ by the double amplitudes—these connected excitations ensure CC is size extensive. Inclusion of triple excitations with CCSDT is typically too computationally expensive, so triple excitations are often included as a perturbative correction denoted CCSD(T) (perturbation theory is discussed in section 1.2). Triple excitation energy is typically overestimated in CCSD(T), however generally this conveniently results in greater accuracy by being approximately equal to the quadruple excitation contribution.¹¹

Multiconfigurational self-consistent field

In the above post-Hartree-Fock methods, the reference Hartree-Fock orbitals are not themselves optimised. Multiconfigurational self-consistent field (MCSCF) methods do however optimise MOs and are not reliant on such a Hartree-Fock reference. The most commonly employed MCSCF method is the Complete Active Space Self-Consistent Field (CASSCF) method, whereby the MOs are divided into three spaces. As depicted in Figure 1.1, orbitals in the core have occupancies fixed at 2, and inactive orbitals at 0, but all configurations of orbitals

inside the active space are included (of a given spin multiplicity and space symmetry). The

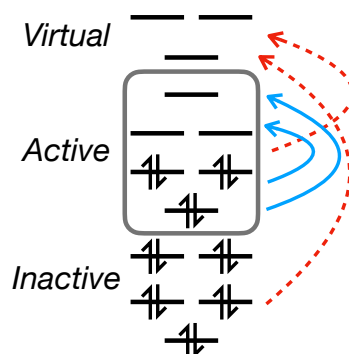


Figure 1.1: The division of orbitals in CASSCF calculations into three spaces; inactive, active and virtual. Examples of allowed excitations are shown as solid, blue arrows. Excitations included in the CASPT2 perturbation are shown as dashed, red arrows.

active space is generally described with the notation $[n,m]$, where n is the number of electrons in the active space, and m is the number of included orbitals.¹³

The number of configurations rapidly increases on increasing the size of the active space, and, ignoring symmetry constraints, is given by the Weyl formula:¹⁴

$$n_c = \frac{2S+1}{M+1} \begin{pmatrix} M+1 \\ \frac{1}{2}N-S \end{pmatrix} \begin{pmatrix} M+1 \\ M-\frac{1}{2}N-S \end{pmatrix} \quad (1.20)$$

where S is the total spin quantum number, N is the number of electrons in the active space and M is the number of orbitals.

An improperly chosen active space can generate false conclusions since any correlation energy captured is only in the active space. Strictly, MCSCF techniques do not obey the variational principle (however largely do with a properly chosen active space); poor active spaces which, for example, do not include all of a set of degenerate orbitals can give non-variational energies.

The general aim is to include orbitals in the active space which will have occupancies significantly different from 0 and 2, since these will contribute greatest to the correlation energy

recovered. The active space should ideally include all valence orbitals, though this is intractable for larger systems, especially in the case of actinides where $5f$, $6d$ and $7s$ (13 orbitals) should in principle be included.¹⁵ A smaller active space can be used to best describe a particular atom, bond or coordination sphere, to recover the most important bonding characteristics. The largest active space possible currently is around [16,16], beyond which point other techniques must be used to reduce computational cost.

Further restrictions on the configurations included in the wavefunction allow for a larger active space. Restricted active space-SCF (RASSCF) typically refers to a scheme where active orbitals are split into three spaces, with limits imposed on excitations between these spaces. The number of excitations out of RAS1, and into RAS3 are defined and all such configurations are included in the RASSCF wavefunction. Typically, and in this thesis, bonding orbitals are placed in RAS1, corresponding antibonding orbitals in RAS3, and any nonbonding metal centred orbitals (*i.e.* $5f$ orbitals for the actinides) are placed in RAS2, and double excitations are allowed out of RAS1 and into RAS3. This is typically notated as (n,m,l; a,b,c), where n is the total number of active electrons, m is the maximum order of excitations out of RAS1 and l the maximum into RAS3, and a, b and c are the number of active orbitals in RAS1, RAS2 and RAS3 respectively.¹⁶ Other partitioning schemes, such as generalised active space-SCF (GASSCF) whereby the active space is partitioned into any number of spaces, are possible but are not used in this thesis. Also possible, but not used in this thesis, are techniques such as density matrix renormalisation group, in which the number of configurations is efficiently truncated to exclude those which only have small contributions to the wavefunction, allowing for much larger active spaces (up to [100,100]).

State-averaged CASSCF (SA-CASSCF) calculations are commonly performed on molecules with low-lying excited states. The same set of orbitals are used, with the states differing by the weights of configurations. The optimised energy is the average energy of the

states considered, with each state being weighted equally (in principle, weightings can be varied but this is rarely advantageous). This has the advantage of generating states orthogonal to each other, however since the set of orbitals is a compromise between all states, energies can become affected and an enlarged active space may be necessary.

A good CASSCF calculation will recover long-range static correlation well, but little dynamic correlation so can offer a good qualitative description of the electronic structure of a molecule. However dynamic correlation is very important in accurately describing relative energies of states, or energy gradients (and so molecular geometries). For this reason, CASSCF with second-order perturbation theory (CASPT2) is commonly used; the perturbation is those excitations not described by the active space, *i.e.* excitations from the core into the active space or the inactive space, and excitations from the active space to the inactive space.¹⁰

Perturbation Theory

Perturbation theory methods are used to find an approximate solution of an insoluble problem, by using a solvable problem as a starting point - the Hamiltonian \hat{H} is split into the 'zeroth-order' \hat{H}_0 and perturbation \hat{V} . This perturbation and consequently the wavefunction and the energy are split into a power series, *i.e.*

$$\hat{V} = \lambda^1 \hat{V}^{(1)} + \lambda^2 \hat{V}^{(2)} + \lambda^3 \hat{V}^{(3)} + \dots \quad (1.21)$$

$$\Psi = \psi^{(0)} + \lambda^1 \psi^{(1)} + \lambda^2 \psi^{(2)} + \lambda^3 \psi^{(3)} + \dots \quad (1.22)$$

$$E = E^{(0)} + \lambda^1 E^{(1)} + \lambda^2 E^{(2)} + \lambda^3 E^{(3)} + \dots \quad (1.23)$$

The first-order correction to the energy is:

$$(\hat{H}^{(0)} - E^{(0)}) |\psi^{(1)}\rangle = (E^{(1)} - \hat{V}^{(1)}) |\psi^{(0)}\rangle, \text{ so } E^{(1)} = \langle \psi^{(0)} | \hat{V}^{(1)} | \psi^{(0)} \rangle \quad (1.24)$$

The first-order correction to the wavefunction is, for $k \neq n$:

$$|\psi_n^{(1)}\rangle = \sum_{k \neq n} |\psi_k^{(0)}\rangle \frac{\langle \psi_k^{(0)} | \hat{H}^{(1)} | \psi_n^{(0)} \rangle}{E_n^{(0)} - E_k^{(0)}} \quad (1.25)$$

And the second-order correction to the energy is given by:

$$E_n^{(2)} = \langle \psi_n^{(0)} | \hat{H}^{(2)} | \psi_n^{(0)} \rangle + \sum_{k \neq n} |\psi_k^{(0)}\rangle \frac{\langle \psi_n^{(0)} | \hat{H}^{(1)} | \psi_k^{(0)} \rangle \langle \psi_k^{(0)} | \hat{H}^{(1)} | \psi_n^{(0)} \rangle}{E_n^{(0)} - E_k^{(0)}} \quad (1.26)$$

While higher-order perturbations are used, second-order is by far the most common due to diminishing returns from the added computational cost. Notably, the zeroth-order wavefunction gives the first-order energy, and the first-order wavefunction gives the second-order energy, *etc.*⁸

In this thesis, perturbation is used at three levels of theory; Møller–Plesset (MP), which improves upon Hartree Fock, CCSD(T), which applies a perturbative triple excitations correction to CCSD, and CASPT2 which applies a perturbative correction to CASSCF. Møller–Plesset will be discussed to demonstrate the mechanics of perturbation theory, followed by a brief discussion of CASPT2 which has been used extensively.

In MP perturbation theory, \hat{H}_0 is generally defined as the Fock operator, *i.e.*:

$$\hat{H}_0 \equiv \hat{F}, \quad \hat{V} \equiv \hat{H} - \hat{F} \quad (1.27)$$

$$= \sum_{p \geq q} \frac{1}{r_{pq}} - \frac{1}{2} \sum_{p,q} (\hat{J}_{pq} - \hat{K}_{pq}) \quad (1.28)$$

$$E(\text{MP0}) = \sum_i \varepsilon_i, \text{ and } E(\text{MP1}) = E^{(0)} + E^{(1)} \quad (1.29)$$

$$= \sum_i \varepsilon_i - \frac{1}{2} \sum_{ij} (\hat{J}_{ij} - \hat{K}_{ij}) = E_{\text{HF}} \quad (1.30)$$

As such, a second-order correction, MP2, is needed to gain any improvement on Hartree-Fock.

The basis of states in MP2 is excited slater determinants, and by equation 1.26 the MP2 energy

is, where x, y are occupied orbitals and r, s are virtual orbitals:

$$E(\text{MP2}) = E^{(0)} + E^{(1)} + E^{(2)} \quad (1.31)$$

$$E(\text{MP2}) = E^{(0)} + E^{(1)} + E^{(2)} \quad (1.32)$$

$$= E_{\text{HF}} + \frac{1}{4} \sum_{x,y} \sum_{r,s} \frac{\langle xy||rs \rangle \langle rs||xy \rangle}{\epsilon_x + \epsilon_y - \epsilon_r - \epsilon_s} \quad (1.33)$$

where $\langle xy||rs \rangle = [xy|rs] - [xy|sr]$, and $[xy|rs]$ has the form given in equation 1.10.

In the case of CASPT2, CASSCF is the starting point and \hat{H}_0 is the CASSCF Hamiltonian, the perturbation is those excitations not described by the active space, *i.e.* double excitations from the core into the active space or the inactive space, excitations from the active space to the inactive space, or mixtures thereof. The approach is similar to that of MP2, however, made substantially more complicated due to the number of different types of excitation.¹⁷ The ‘intruder state’ problem is a notable challenge in performing CASPT2 calculations, whereby configurations (typically Rydberg, with diffuse orbitals) have energies which make the denominator, analogous to equation 1.33, close to zero. This causes the weight of the reference wavefunction to disappear, and the wavefunction to ‘blow up’. This is typically dealt by use of a ‘level shift’, whereby virtual orbitals are artificially shifted up in energy to dampen the impact of these intruder states.¹⁸

Inclusion of dynamic correlation is very important in calculating excited state excitation energies. Multi-state CASPT2 (MS-CASPT2) relies on an SA-CASSCF reference; a CASPT2 calculation is performed on each state, and the states are allowed to mix *via* a diagonalisation of an effective Hamiltonian.¹⁷

Natural orbitals

Natural orbitals are those that diagonalise the 1 particle reduced density matrix. The associated operator of the density matrix is:

$$\gamma(\vec{r}, \vec{r}') = |\Psi\rangle \langle\Psi| = N \int \Psi^*(\vec{r}', \vec{r}_2 \dots \vec{r}_N) \Psi(\vec{r}, \vec{r}_2 \dots \vec{r}_N) d\vec{r}_2 \dots d\vec{r}_N \quad (1.34)$$

where Ψ is the total electronic wavefunction.⁸ The associated eigenvalue of a natural orbital is its occupation number, as opposed to the one-electron energy of ‘canonical’ orbitals which diagonalise the Fock matrix. For a closed shell Hartree-Fock wavefunction, the two sets of orbitals are equivalent. For post Hartree-Fock, particularly MCSCF, methods optimisation of natural orbitals gives faster convergence.¹⁹ Additionally, the occupation number eigenvalue is useful in the analysis of MCSCF wavefunctions.

1.3 Density functional theory

Density functional theory (DFT) is a method of studying electronic structure by using functionals which act on the density $\rho(\vec{r}) = N |\Psi_{\text{tot}}|^2$ (for a N -electron system), rather than the wavefunction as discussed above. The origins of DFT are in the study of the electronic properties of solids, most simply by treatment of electrons as a uniform electron gas experiencing a constant potential in the solid (‘jellium’), for which a total energy functional was developed (including kinetic, potential and exchange energy terms). While this approach enjoyed some success in the early modelling of solids, the constant potential is a very large approximation especially in molecular applications. The success of DFT in computational chemistry lies in its theoretical underpinnings, and also later developments of more advanced and accurate density functionals.

Hohenberg-Kohn theorems

The theoretical underpinnings of DFT are in the Hohenberg-Kohn theorems; firstly that an exact energy functional exists, and secondly that with an exact energy functional, DFT is variational.²⁰

The first theorem states that “ $V(\vec{r})$ is (to within a constant) a unique functional of $\rho(\vec{r})$; since in turn, $V(\vec{r})$ fixes \hat{H} we see that the full many-particle ground state is a unique functional of $\rho(\vec{r})$.”²⁰ This means that since the exact ground-state density defines the potential, which in turn defines the Hamiltonian and consequently the ground-state wavefunction and energy, there exists some functional $E[\rho(\vec{r})]$ of the density which gives the ground state energy. The theorem does not say anything about the form of the functional however.

The second theorem demonstrates that the variational theorem applies to DFT; that the energy of some trial electron density can only be greater than or equal to the true ground-state energy. This only applies to the energy obtained from the exact functional however—approximate functionals do give non-variational energies.¹¹

The Kohn-Sham system

The energy functional can be split into several terms:

$$E[\rho(\vec{r})] = T[\rho(\vec{r})] + V_{ne}[\rho(\vec{r})] + V_{ee}[\rho(\vec{r})] \quad (1.35)$$

T is the kinetic energy functional, V_{ne} and V_{ee} are the nucleus-electron and electron-electron potential functionals, respectively. Only V_{ne} is known exactly, which has the form:

$$V_{ne}[\rho(\vec{r})] = - \sum_k \int \frac{Z_k}{|\vec{r} - \vec{r}_k|} \rho(\vec{r}) d\vec{r} \quad (1.36)$$

where k are the nuclei of the system, and Z_k is their charge. The Kohn-Sham system allows functionals for other parts of the energy to be created. The Kohn-Sham system is a fictitious

system of non-interacting electrons which have the same density as the real, interacting system. The kinetic and electronic parts are then split into their non-interacting and interacting parts:

$$E[\rho(\vec{r})] = T[\rho(\vec{r})] + V_{ne}[\rho(\vec{r})] + V_{ee}[\rho(\vec{r})] + \Delta T[\rho(\vec{r})] + \Delta V_{ee}[\rho(\vec{r})] \quad (1.37)$$

where $\Delta T[\rho(\vec{r})]$ is the correction to the kinetic energy for interacting electrons, and ΔV_{ee} represents non-classical electron-electron interactions. In the Kohn-Sham system, only those final two ‘corrections’ are not known, and together are termed the exchange-correlation functional E_{xc} . The Kohn-Sham DFT (KS-DFT) energy functional is given by:

$$E[\rho(\vec{r})] = \sum_i \left(\langle \phi_i | -\frac{1}{2} \nabla_i^2 | \phi_i \rangle - \langle \phi_i | \sum_k \int \frac{Z_k}{|\vec{r}_i - \vec{r}_k|} | \phi_i \rangle + \langle \phi_i | \int \frac{\rho(\vec{r}')}{2|\vec{r}_i - \vec{r}'|} d\vec{r}' | \phi_i \rangle \right) + E_{xc}[\rho(\vec{r})] \quad (1.38)$$

for an i electron system, with $|\phi_i\rangle$ being an occupied Kohn-Sham orbital.¹¹ The form of E_{xc} has been an active area of research for more than 50 years, with many forms proposed of varying complexity and accuracy.

Jacob's ladder

The construction of exchange-correlation functionals varies greatly; some use a small number of parameters derived *ab initio*, others a large number fitted to reproduce experimental data. Some functionals only describe exchange energy or correlation energy so must be used in combination, while others were derived as a single exchange-correlation function. Functionals can be grouped by the type of terms which contribute. Perdew termed this ‘Jacob’s Ladder’, with the unknown exact functional being the “dream” of DFT at the top of the ladder.^{11,21}

1. **Local density approximation (LDA)** functionals approximate E_{xc} as a function of the value of the density at some position \vec{r} only. Functionals of this form are derived from the uniform electron gas, but have been expanded to account for spin polarised systems

(the local spin density approximation, LSDA). Examples of local density approximation functionals include LDA, derived entirely from the uniform electron gas, and VWN, VWN5 and SVWN—slight parameterisations of LDA, but which in practice give similar results.^{22,23}

2. **Generalised gradient approximation (GGA)** functionals additionally include terms which depend on the gradient of the electron density. GGAs are usually constructed as a correction to an LDA functional. An example of a non-empirical functional is that by Perdew, Burke and Ernzerhof, 'PBE', a gradient correction to LDA, constructed to obey certain principles such as correct properties of the uniform electron gas, and uniform scaling.²⁴ Becke's 1988 exchange functional (B88) is semi-empirical, as it is fitted to the Hartree-Fock exchange energy of noble gas atoms. Lee, Yang and Parr created a correlation functional fitting parameters to the Hartree-Fock orbitals of the helium atom (LYP) and commonly used with the B88 correlation functional (together known as BLYP).²⁵
3. **Meta-GGA** functionals further include higher order terms, either the second derivative of the density, or the Kohn-Sham orbital kinetic energy. An example of a non-empirical meta-GGA exchange-correlation functional, which includes KS kinetic energy terms, is that by Tao, Perdew, Staroverov and Scuseria (TPSS).²⁶ Part of the Minnesota family of functionals, M06-L is an example of a highly parameterised functional, fit against a large database of atomisation energies, ionisation potentials, barrier heights and other properties for atoms, organic molecules and inorganic molecules.²⁷
4. **Hybrid** functionals replace a proportion of the exchange energy with Hartree-Fock exchange. Hybrid functionals are justified by the adiabatic connection, bridging non-interacting (non-hybrid DFT functionals) and fully-interacting methods (Hartree-Fock). B3LYP is a widely used hybrid functional, the counterpart to BLYP with 20% exact exchange.²⁸ PBE0 is the hybrid counterpart to PBE, with 25% exchange.²⁹

5. **Double-hybrid** functionals additionally incorporate an MP2-like correction to the exchange-correlation energy, whereby an MP2 calculation is performed on the KS orbitals. For example, the B2PLYP functional (double-hybrid counterpart to BLYP) includes 53% exact exchange, and 23% perturbative correction.³⁰

Large-scale database studies have found that higher rungs give more accurate molecular properties.^{31,32} However double-hybrid functionals have substantial computational costs, so hybrid functionals remain the most commonly used. In 2017, M. Medvedev *et al.* suggested that by over-relying on empirical fitting of molecular properties, more modern functionals are "straying from the path toward the exact functional".³³ They performed calculations on a range of neutral and cationic atoms with 2, 4 and 10 electrons, and compared densities obtained with a variety of density functionals to that obtained by *ab initio* techniques. They found some more modern, highly parametrised, functionals perform more poorly than those with more physical rigour. In a comment on M. Medvedev *et al.*'s paper, K. Kepp suggests that charged, small atoms have little relevance to molecular properties, however.³⁴

This thesis largely uses the GGA functional PBE, and its hybrid counterpart PBE0 (along with D3 dispersion correction, discussed below). PBE was recently identified as the best performing functional for a variety of uranium-containing molecules in a range of oxidation states by D. Reta *et al.*,³⁵. This thesis additionally uses PBE0 due to its similarly good performance, and also due to the importance of exact exchange in describing exchange interactions in diuranium complexes.

Kohn-Sham SCF

The self-consistent field method is used in KS-DFT to optimise the density analogously to Hartree-Fock. The one electron operator is:

$$h_i^{KS} = -\frac{1}{2}\nabla_i^2 - \sum_k \int \frac{Z_k}{|\vec{r}_i - \vec{r}_k|} + \int \frac{\rho(\vec{r}')}{2|\vec{r}_i - \vec{r}'|} d\vec{r}' + \frac{\delta E_{xc}}{\delta \rho} \quad (1.39)$$

$$h_i^{KS} |\phi_i\rangle = \varepsilon_i |\phi_i\rangle \quad (1.40)$$

There is then a set of eigenvalue equations which are minimised iteratively to obtain the KS-DFT energy. As with Hartree-Fock, the sum of the orbital energy eigenvalues is not equal to the total energy due to double-counting of electron-electron interactions.¹¹

Dispersion correction

A particular failing of DFT is description of long-range interactions, because contributions to the exchange-correlation energy are local, only depending the value of the density or its (second) derivative. This tends to be successful at accurately reproducing short-range interactions, but long range induced-dipole interactions cannot be reproduced. For example, the helium dimer is not bound in KS-DFT but due to induced-dipole interactions there is an attractive potential sufficiently deep for a single vibrational state. To correct for this omission, an empirical correction can be applied to DFT energies and gradients. Grimme's dispersion correction adds an atom pairwise contribution, with an empirical coefficient being calculated for each element with a variety of functionals. This thesis uses the third version of Grimme's dispersion correction (DFT-D3), as it was identified by D. Reta *et al.* as giving the most accurate geometries and properties, in combination with the PBE functional.^{35,36}

1.4 Relativity

Special relativity postulates that the speed of light, c , is a constant in all inertial frames, and that physical laws are invariant in all such frames. Therefore, these laws must be unchanged by a Lorentz transform (a transformation between two inertial frames). The time-dependent Schrödinger equation does not satisfy this requirement since it is a first order differential equation in time, and second order in space:¹⁰

$$\hat{H}\Psi(\vec{r}_n, \vec{r}_N, t) = i\hbar \frac{\partial}{\partial t} \Psi(\vec{r}_n, \vec{r}_N, t) \quad (1.41)$$

Paul Dirac derived the Dirac equation, the relativistic wave equation for spin- $\frac{1}{2}$ particles such as electrons:

$$[c\boldsymbol{\alpha} \cdot \mathbf{p} + \beta mc^2] \Psi = i\hbar \frac{\partial \Psi}{\partial t} \quad (1.42)$$

$$\text{where } \boldsymbol{\alpha} = \begin{pmatrix} 0 & \boldsymbol{\sigma}_x + \boldsymbol{\sigma}_y + \boldsymbol{\sigma}_z \\ \boldsymbol{\sigma}_x + \boldsymbol{\sigma}_y + \boldsymbol{\sigma}_z & 0 \end{pmatrix}, \boldsymbol{\beta} = \begin{pmatrix} \mathbf{I} & 0 \\ 0 & \mathbf{I} \end{pmatrix} \quad (1.43)$$

$$\boldsymbol{\sigma}_x = \begin{pmatrix} 0 & 1 \\ 1 & 0 \end{pmatrix} \boldsymbol{\sigma}_y = \begin{pmatrix} 0 & -i \\ i & 0 \end{pmatrix} \boldsymbol{\sigma}_z = \begin{pmatrix} 1 & 0 \\ 0 & -1 \end{pmatrix} \mathbf{I} = \begin{pmatrix} 1 & 0 \\ 0 & 1 \end{pmatrix} \quad (1.44)$$

The $\boldsymbol{\sigma}_{x,y,z}$ matrices are analogous to representations of the spin operators, without the factor of $\frac{1}{2}$. Solutions to the Dirac equation have four components; two are accounted for by spin, the other two are interpreted as describing electrons and positrons.¹⁰

Chemically, an important result of relativity is the relativistic contraction; that the mass of a particle increases when it moves at a significant fraction of the speed of light:

$$m = m_0 \left(1 - \frac{v^2}{c^2}\right)^{-\frac{1}{2}} \quad (1.45)$$

Since orbital angular momentum is conserved, orbitals become more radially contracted. While this effect can typically be ignored for light elements, for heavy elements such as uranium it cannot be neglected. Since the 1s electrons become heavier, they contract, as do other s-orbitals. Consequently, they screen nuclear charge more effectively and d- and f-orbitals become more radially extended. Due to the countering effects of spin-orbit coupling, p-orbitals are largely unaffected.

Spin-orbit coupling is another important factor entirely derived from relativity. It is a result of the interaction of the magnetic moments of both the spin and orbital angular momentum and means that the total spin is not a true good quantum number.

Full implementation of relativistic effects *via* computing the four-component wavefunction is generally very challenging, so approximate methods are generally employed. An example is the Douglas-Kroll-Hess (DKH) Hamiltonian, which block diagonalises the Dirac Hamiltonian, allowing the positron states to be neglected and reducing the wavefunction to two components (this transformation is performed iteratively, and is typically done to second-order). For multiconfigurational wavefunctions, the effects of spin-orbit coupling can be additionally accounted for by mixing wavefunctions of multiple spin-orbit free states (including those with different spin quantum numbers) with a spin-orbit Hamiltonian.³⁷ However recently methods which account for spin-orbit coupling natively have become more tractable for larger molecules, including two-component methods which include spin-orbit coupling and fully relativistic four-component methods, including with the actinides.^{38,39}

1.5 Reducing computational cost

Computational study of large molecules which contain multiple metal centres makes techniques which reduce the computational cost of calculations very important. The most expensive part of a wavefunction theory or DFT calculation is the two-electron integrals. This

thesis employs two different types of technique to speedup calculations; reducing the number of explicit electrons included in the wavefunction with pseudopotentials, and with Cholesky decomposition or density fitting, related techniques which speed up two-electron integrals

Effective core potentials (ECPs), or pseudopotentials, replace core electrons with a potential which replicates their interaction with valence electrons. In addition to reducing the number of electrons explicitly included in the wavefunction, scalar relativistic effects can be accounted for in the form of the potential–core electrons, which have the largest kinetic energy are most affected by scalar relativistic effects, as discussed above in section 1.4. Relativistic ECPs (RECPs) use a modified Hamiltonian, which for an n valence electron atom is of the form:

$$\hat{H} = \sum_i \hat{T}_i^n + \sum_i \sum_{j>i}^n \hat{V}_{ij} + \hat{V}_{av} \quad (1.46)$$

The potential of the core electrons and nucleus are represented by \hat{V}_{av} , which for an atom with a core charge of Q (*i.e.* nuclear charge - core electrons) is:

$$\hat{V}_{av} = - \sum_i^n \frac{-Q}{r_i} + \sum_i^n \sum_{l,k} A_{lk} e^{-a_{lk} r_i^2} \hat{P}_l \quad (1.47)$$

A_{lk} is the parameter fitted to atomic all-electron fully-relativistic calculations, representing the interaction between a valence orbital of angular momentum l and core electron of angular momentum k . The operator \hat{P}_l projects onto orbitals with angular momentum l .⁴⁰ The ECPs used in this thesis on uranium include 60 electrons in the core, this is all electrons with principal quantum number $n \leq 4$. Explicitly treated electrons are described with a specially designed basis set designed to reproduce the valence region, however the number of radial nodes differs due to inclusion of core electrons in the pseudopotential; orbitals with $n = 5$ have no radial nodes, $n = 6$ have 1 *etc.* for a 60 electron uranium RECP.^{40,41}

Cholesky decomposition and density fitting (sometimes known as resolution of the identity,

RI) are two related techniques which reduce the computational time of two electron integrals. In the density fitting approach, a one-electron density is approximated by a large auxiliary basis set, reducing four index two-electron integrals to two or three index. The basis set is constructed to minimise the error this introduces. This typically necessitates inclusion of orbitals with / two or three larger than the standard basis set for post Hartree-Fock calculations, making construction of an auxiliary basis set challenging.⁴² As such, density fitting techniques are only used in Chapter 8 on $W_2(CO)_{10}^{2-}$ where such auxiliary basis sets are available. Cholesky decomposition is similar in spirit to density fitting, and is mathematically related however not dependent on an auxiliary basis. Cholesky decomposition is supported in OpenMolcas and used in this thesis to substantially speed up MCSCF calculations performed in the program.⁴³

1.6 Analytical techniques

In addition to calculating the electronic structure accurately, it is important to quantitatively analyse the properties of the calculated structure. This thesis has made most use of three broad categories of atomic and molecular properties; atomic charges, bond indices and localised molecular orbitals (LMOs). Atomic charges typically reflect the formal oxidation state of the atom, though usually differ significantly from this formal charge reflecting covalency rather than purely ionic interactions. The bond order between a pair of atoms, how many electron pairs are bonded between the two atoms, has long been an important concept to chemists; bond indices metrics use the calculated wavefunction/density to give a quantitative measure of the bond order. Molecular orbitals are often highly delocalised across a molecule, which makes their interpretation challenging so LMOs, centred on 2 atoms (or more in the case of delocalised bonding) are used to give a description of the nature of the bonding between atoms in the molecule.

There are a great variety of methods which produce such properties, which mainly differ

by how they partition the wavefunction between atoms and bonds. This thesis has used three analytical techniques to explore atomic and bond properties; Intrinsic Bonding Orbitals (IBO)^{44,45} and Natural Bonding Orbitals (NBO),⁴⁶ both based on analysis of orbitals and the quantum theory of atoms in molecules (QTAIM),⁴⁷ based on analysis of the electron density. A brief overview of examples of more primitive population indices is given and their limitations, before discussing IBOs, NBOs and QTAIM.

Mulliken population analysis partitions charge by basis set coefficients. The Mulliken population on atom k , N_k is, for atomic orbital basis functions r and s on atom k and t which are on other atoms:

$$N_k = \sum_j^{\text{electrons}} \left(\sum_{r,s} c_{jr} c_{js} S_{rs} + \sum_{r,t} c_{jr} c_{jt} S_{rt} \right) \quad (1.48)$$

where the overlap matrix element $S_{rs} = \langle \phi_r | \phi_s \rangle$ and c_{jr} is the molecular orbital coefficient of atomic orbital r and electron j . The Mulliken charge q_k is then $q_k = Z_k - N_k$, where Z_k is the nuclear charge. There are two key flaws in Mulliken population analysis. Firstly, population from off-diagonal elements of the overlap matrix (the second term in the above equation) are equally split between the two atoms. Equally dividing the off-diagonal ‘shared’ charge can give some unintuitive results, particularly for polarised bonds. Secondly, because charge is partitioned by basis set coefficients, their values are basis dependent and for large bases can produce unrealistic results, with charge ‘leaking’ to adjacent atoms with diffuse functions. Unphysical occupancies of particular atomic orbitals can occur, either greater than two or negative, because atomic orbitals in the molecule are non-orthogonal.¹¹

Boys and Pipek-Mezey are two examples of localisation schemes to generate LMOs, however they differ in their localisation functionals. Pipek-Mezey minimises the number of atoms over which charge is spread in the orbital by maximising the localisation functional:

$$L = \sum_i \sum_A^{\text{occupied atoms}} q_A(i)^2 \quad (1.49)$$

where $q_A(i)^2$ is the charge of LMO i on atom A .^{45,48} If the Mulliken charge is minimised, Pipek-Mezey LMOs suffer from the same basis set dependency issues of Mulliken population analysis. Boys LMOs minimise the spatial extent of the orbitals, by maximising the functional:

$$L = \prod_{i>j} (\vec{r}_i - \vec{r}_j)^2 \quad (1.50)$$

for MOs ϕ_i and ϕ_j .⁴⁹ Boys LMOs typically mix π and σ systems, which can hinder their interpretability. By contrast, Pipek-Mezey LMOs typically preserve π and σ systems.

The Wiberg bond index BO_W is given by:

$$BO_W(AB) = \sum_a \sum_b P_{ab}^2 S_{ab}^2 \quad (1.51)$$

where a and b are indices of atomic orbitals on atoms A and B respectively, and P and S are the one-particle density matrix and overlap matrix respectively. The Wiberg bond index was originally conceived for semi-empirical orthogonal orbitals, so simple application to a non-orthogonal atomic basis has similar basis dependence issues as Mulliken population analysis.⁵⁰

Intrinsic bonding orbitals

Intrinsic bonding orbitals (IBOs) are constructed *via* projection onto a minimum-quality atomic basis set, which eliminates basis set dependence issues of other analytical techniques. This minimum quality basis is composed of the atomic orbitals of a free atom, for example for carbon 1s, 2s and 2p orbitals. To account for polarisation in the molecular environment, the depolarised MOs in the minimum-quality basis are projected back onto the full basis set. The intrinsic atomic orbital (IAO) basis is then a projection of the minimum quality basis onto the

full basis. The IAO charge on atom A, q_A , of a closed shell molecule is:

$$q_A = Z_A - 2 \left(\sum_a \sum_i \langle \chi_a | \phi_i \rangle \langle \phi_i | \chi_a \rangle \right) \quad (1.52)$$

where Z_A is the nuclear charge, $|\chi_a\rangle$ are the IAOs on atom A, $|\phi_i\rangle$ are the occupied MOs.

G. Knizia showed that IAO charges are not basis-dependent, converging to a limit with increasing basis size where Mulliken charges change sign in a chemically non-intuitive manner. IBOs are constructed in a manner similar to Pipek-Mezey orbitals. The localisation functional which is maximised is:

$$L = \sum_i \sum_A^{\text{occupied atoms}} (n_A(i'))^4 \quad (1.53)$$

where $n_A(i')$ is the number of electrons in IBO $|\psi_{i'}\rangle$ from IAOs on atom A. The 4 exponent has a small effect on the character of IBOs, an exponent of 2 (essentially Pipek-Mezey with the IAO charge) gives similar results in most cases but can slightly change the character of highly delocalised systems such as benzene.

The minimal quality basis used is from the cc-pVTZ basis, as these contracted functions are free-atom Hartree Fock atomic orbitals.^{44,45} In this thesis, this is extended to uranium by constructing a minimal quality basis from the cc-pVTZ-PP basis, including 5f, 6d, 6p and 7s valence orbitals. S. Rudel *et al.* applied IBOs to uranium, on a complex featuring a UN₂ core isoelectronic to uranyl. They constructed a minimal quality basis from Hartree-Fock atomic orbitals in the def-TZVPP basis, but noted that primitives from the cc-pVTZ-PP basis yielded similar results.⁵¹

Natural bond orbital analysis

Natural bond orbital (NBO) analysis creates orbitals with maximum occupation over a minimum number of atoms, recovering a Lewis-like structure. They are constructed in a multiple step

process, from atomic orbitals to Natural Atomic Orbitals (NAOs), Natural Hybrid Orbitals (NHOs, linear combinations of NAOs) then Natural Bond Orbitals (NBOs, linear combinations of atomic orbitals).

Natural Atomic Orbitals are atom-centred orbitals which importantly are orthonormal. As such they are highly suited as a basis for ‘Natural’ Population Analysis (NPA), or calculation of atomic charges. The first step in construction of NAOs is orthogonalisation of the basis set in a manner which variationally maximises the resemblance of the non-orthogonal and orthogonal bases, by minimising with the functional:

$$\sum_k p_k \int ||\chi_k\rangle - |\chi'_k\rangle|^2 d\tau \quad (1.54)$$

where $|\chi_k\rangle$ is the atomic orbital in the non-orthogonal basis, and $|\chi'_k\rangle$ is in the corresponding orbital in the orthogonal basis, and p_k is the population of that orbital. Then, the density matrix is diagonalised in atomic blocks to generate NAOs. The natural atomic charge and populations are then calculated analogously to Mulliken analysis, but in the NAO basis.

Natural bonding orbitals are identified by trialing various Lewis structures which are linear combinations of NHOs; if all trial NBOs have occupancies greater than 1.90 the Lewis structure is accepted. If a suitable Lewis structure cannot be identified, either a lower occupancy threshold or a more delocalised structure is accepted (e.g. three-centre two-electron bonds). NBOs are categorised as core, lone pair, bonding, antibonding or Rydberg. Natural localised molecular orbitals (NLMOs) can additionally be constructed from NBOs which have double occupancy (for a closed shell system) at the expense of being more poorly localised. Many of the molecules studied in this thesis have delocalised bonding, and are less suited to NBO analysis, but natural population analysis (NPA) in the NAO basis is used extensively, as is the Wiberg bond order in the NAO basis.

Quantum theory of atoms in molecules (QTAIM)

By contrast to the above orbital-based analytical techniques, QTAIM analyses the topology of the electron density to calculate atomic and bond properties. Part of the justification for QTAIM is that the density is an observable (and measurable with x-ray diffraction), whereas wavefunctions are essentially mathematical constructs.¹¹

Critical points are points at which the gradient of ρ is zero in all directions. They are classified by the signs of the Hessian eigenvectors (*i.e.* the curvature) at the critical point. Three negative curvatures, notated (3, -3) indicating that the density is a local maximum is a nuclear critical point; the point is on the nucleus, or very close for hydrogen. Two negative and 1 positive curvatures, (3, -1), indicates a bond critical point (BCP) which is linked to the two bonded atoms along both directions of the maximum density trajectory (*i.e.* the direction of the positive curvature). This trajectory is the ‘bond path’, and together the critical points and bond paths give a molecular graph. In QTAIM, atoms which are chemically bonded share a bond critical point and are linked by a bond path. Ring critical points (RCP) have two positive and 1 negative (3, +1), and cage critical points (CCP) have 3 positive curvatures (3, +3).

The electronic density is divided into ‘atomic basins’, the surface of which have zero flux in the electron density gradient vector field (*i.e.* the gradient vector field does not cross the basin surface). This surface satisfies:

$$\nabla\rho(\vec{r})\cdot\vec{n}(\vec{r})=0 \quad (1.55)$$

for all \vec{r} on the surface S_Ω , where $\vec{n}(\vec{r})$ is normal to \vec{r} .⁵²

Atomic and molecular properties in QTAIM can be divided into critical point properties, derived from the topology of the density at a critical point, and integrated properties, derived from integration of density as partitioned into atomic basins.

Critical point properties

The value of the electron density at a bond critical point, ρ_b is reflective of the strength of that bond. For closed-shell main group molecules, typically $\rho_b > 0.20\text{ebohr}^{-3}$ for a covalent bond, and $\rho_b < 0.10\text{ebohr}^{-3}$ for a closed-shell interaction.⁵² However, ρ_b is typically lower for actinide bonds, other than strong multiple bonds.^{53–55}

The Laplacian of the density, $\nabla^2\rho_b$ is the sum of the three curvatures, which for a BCP two are negative and one positive. Large negative curvatures indicate that density is concentrated along the bond path, while a large positive curvature reflects concentration of electron density between the nuclei. For a covalent interaction, $\nabla^2\rho_b < 0$ as the negative curvatures dominate, whereas for closed shell interactions $\nabla^2\rho_b$ is positive. Polarised covalent bonds however can be either positive or negative.

The bond ellipticity, ε , is a measure of the distribution of electron density around the bond path. For negative hessian eigenvalues λ_1 and λ_2 , the ellipticity is:

$$\varepsilon = \frac{\lambda_1}{\lambda_2} - 1 \text{ for } |\lambda_1| < |\lambda_2| \quad (1.56)$$

The ellipticity is essentially a measure of double bond character; an ellipticity of 0 indicates a cylindrical distribution, *i.e.* either a σ^2 single bond or a $\sigma^2\pi^4$ triple bond. Double bond character, $\sigma^2\pi^2$ is generally indicated by $\varepsilon > 0.2$.

The energy densities at critical points can provide further information about bonding. They use information in the density matrix, rather than just the density (*i.e.* the diagonal elements of the density matrix). The local statement of the virial theorem relates the Laplacian, potential energy density $V(\vec{r})$ and gradient kinetic energy density $G(\vec{r})$ by:

$$\frac{\hbar^2}{4m}\nabla^2\rho(\vec{r}) = 2G(\vec{r}) + V(\vec{r}), \text{ where } G(\vec{r}) = \frac{\hbar^2}{2m}N \int \nabla\Psi * \cdot \nabla\Psi d\tau \quad (1.57)$$

Since the potential energy is negative and kinetic energy is positive, positive $\nabla^2\rho_b$ suggests interactions dominated by local excess of kinetic energy, and negative $\nabla^2\rho_b$ suggests an excess of potential energy. The total electronic energy density $H = G + V$ is typically negative for interactions with significant covalency.

Integrated properties

The QTAIM charge is the nuclear charge, minus the integrated electron density in the atomic basin Ω . This can be equivalently written in terms of the overlap matrix:

$$q(\Omega) = Z(\Omega) - \int_{\Omega} \rho(\vec{r}) d\vec{r} = \sum_i S_{ii}(\Omega) \quad (1.58)$$

The delocalisation index, $\delta(A, B)$ is the QTAIM bond order. For atoms A and B, $\delta(A, B)$ is given by:

$$\delta(A, B) = 2 \sum_i \sum_j S_{ij}(A) S_{ij}(B) \quad (1.59)$$

where $S_{ij}(A)$ is the overlap integral over the atomic basin of A. Because $\delta(A, B)$ is an integrated property, it can be calculated for any pair of atoms in the molecule; there does not need to be a bond critical point between the two atoms.

2

Background: Molecular uranium chemistry

2.1 Uranyl

The electronic structure of the uranyl ion, UO_2^{2+} (and its other actinyl analogues) has long been an active area of study due to its prevalence in uranium coordination chemistry, a result of the strength of the $\text{U}\equiv\text{O}$ bond. The dication has a $D_{\infty h}$ linear structure, and the linear motif is rarely broken in its coordination compounds. Uranyl has a well established $\pi_u^4\pi_g^4\sigma_g^2\sigma_u^2$ closed-shell electronic structure and a formal $\text{U}\equiv\text{O}$ triple bond (a qualitative MO diagram is shown in Figure 2.2) but the exact ordering of these valence orbitals has only been more recently firmly confirmed. Valence orbitals are predominantly 2p character on oxygen, and the 5f orbitals (ungerade) and 6d orbitals (gerade) on uranium do not mix with each other, due to the $D_{\infty h}$ symmetry.⁵⁶ The linear structure is a result of the ‘inverse trans effect’ as first proposed by R. G. Denning in 1992, whereby the two trans oxides are stabilised (as opposed to the regular ‘trans effect’ whereby trans ligands are labilised).⁵⁷ This effect was explained by N. Kaltsoyannis in 2000 with quasi-relativistic frozen core DFT calculations (at the BP86/triple- ζ STO level of theory). By varying the size of the frozen core on uranium, Kaltsoyannis demonstrated that the ‘semi-core like’ $6p_U$ orbitals mix with the valence orbitals when outside the frozen core. $5f_{z^3} - 6p_z$ hybridisation lowers the energy of the $6p \sigma_u$ at the expense of a reduction in bonding character of the HOMO σ_u .

Contrasting uranyl with its lanthanide and transition metal analogues, and with the

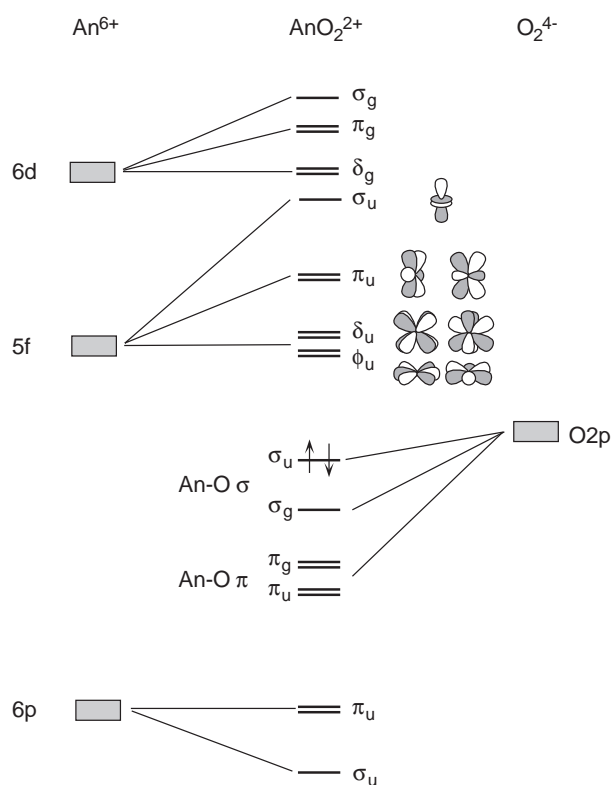


Figure 2.1: A qualitative AnO_2^{2+} MO diagram. The HOMO of UO_2^{2+} is the $\text{O}2p \sigma_u$, shown doubly occupied. Reproduced with permission from *Coordination Chemistry Reviews*.⁵⁶

‘thiouranyl’ analogue, serves to highlight the uniqueness of the covalency found in the actinides and the importance of the binding ligand. Lanthanide complexes generally feature interactions which are almost entirely ionic, and the trans effect generally weakens the linear arrangement in transition metals. For example, P. Pykkö and T. Tamm performed DFT, MP2 and CCSD(T) calculations on MoO_2^{2+} and WO_2^{2+} . Their calculations suggested $\text{M}\equiv\text{O}$ bond orders of three, like uranyl, but with a distinctly non-linear geometry—a $\text{O}\hat{\text{M}}\text{O}$ bond angle of 100.9° for MoO_2^{2+} and 101.4° for WO_2^{2+} (at the CCSD(T) level of theory). Calculations at the CASPT2 level of theory, as performed by A. F. Lucena *et al.* in 2017, suggested that thiouranyl adopts a non-linear structure with the supersulphide μ_2 bound to uranium, due to the poor $2p_S \rightarrow 6d_U \mu_2$ overlap for UO_2^{2+} (disfavouring the superoxide isomer), the stronger S–S σ bond present in the supersulphide and a weakening of the $5f_U \sigma_u$ bonding orbital in the linear US_2^{2+} isomer.

2.2 Uranium-pnictogen chemistry

The simplest terminal uranium nitride, UN was first identified by D. W. Green and G. T. Reedy in 1976. In argon matrix IR spectra, they identified a U^{14}N stretch at 1000.9 cm^{-1} . They also made a tentative assignment of 1050 cm^{-1} to the antisymmetric stretch of U^{14}N_2 .⁵⁸ The uranium nitride molecules which have been studied spectroscopically were summarised by D. M. King and S. T. Liddle in 2013; the molecules UN, UN_2 , NUNH and NUF_3 all having $\text{U}\equiv^{14}\text{N}$ stretching frequencies between between $938\text{--}1051\text{ cm}^{-1}$, and all isolated in argon or neon matrices.⁵⁹

The molecules NUF_3 , PUF_3 and AsUF_3 were isolated in an argon matrix and studied computationally in 2008 and 2009 papers by L. Andrews *et al.*^{60,61} They obtained argon matrix isolated IR spectra of the three molecules, with U-F stretches being observed in the $520\text{--}620\text{ cm}^{-1}$ region for all three molecules. The only pnictogen-uranium stretch observed was for NUF_3 (at 938 cm^{-1}); the P-U stretch and As-U stretch were not observed but calculated to be outside the window of the experimental spectra. The observed U-F stretches are consistent with the formation of the C_{3v} EUF_3 isomer—rather than, for example, FNUF_2 (as is observed with the hydride analogues). However, for AsUF_3 and PUF_3 , there is no direct experimental evidence of the triple bonds; structural assignments can be made only by comparison of the calculated and observed U-F stretches.

L. Andrews *et al.* performed DFT calculations alongside calculations at the CASPT2 level of theory. An all-electron ANO-RCC basis set was used and relativistic effects were accounted for with a second-order Douglas-Kroll-Hess (DKH) Hamiltonian. A [6,6] active space composed of the σ and π bonding and antibonding orbitals was used, to fully describe the E-U bond—the natural orbitals of the active space, alongside occupation numbers, are shown in Figure 2.2. Their calculations found a triple pnictogen-uranium bond for all three molecules, with

increasingly weak π bonding down group 15 due to worsening orbital overlap—the effective bond orders were 2.78, 2.39 and 2.21 for NUF_3 , PUF_3 and AsUF_3 respectively. DFT calculations supported the conclusions of the CASPT2 calculations, however, DFT frequency calculations provided a slightly improved fit to the observed spectra. In the 2008 paper, DFT calculations with the PW91 functional were presented for NUF_3 and PUF_3 . In the 2009 paper, the functionals B3LYP and BPW91 were used in calculations on PUF_3 and AsUF_3 . For both papers, the 6-311+G(3df) basis set was used on nitrogen and fluorine, and the SDD basis set on phosphorus, arsenic and uranium, which includes a 60 electron relativistic ECP on uranium. Differences between the calculated and observed frequencies were attributed to the effects of the argon matrix, and the neglect of anharmonic effects. They additionally suggest that the argon matrix may distort the geometry of the molecule to allow coordination of an argon atom to uranium.

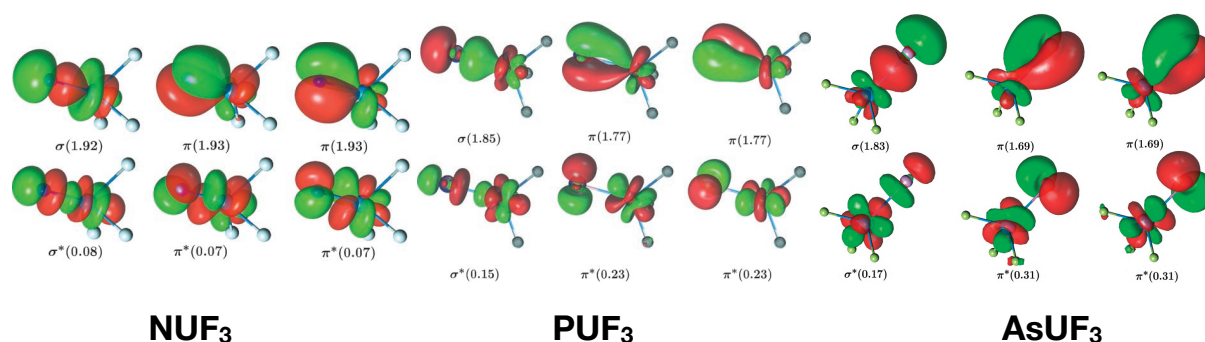


Figure 2.2: The natural orbitals of the [6,6] active space for NUF_3 (left), PUF_3 (middle) and AsUF_3 (right). Calculations at the CASPT2 level of theory. Occupation numbers shown in brackets. Reproduced with permission from Angewandte Chemie International Edition (NUF_3 and PUF_3)⁶⁰ and Inorganic Chemistry (AsUF_3)⁶¹.

The thorium analogues (*i.e.* NThF_3 , PThF_3 and AsThF_3) were studied by X. Wang and L. Andrews in 2009, where they presented argon matrix IR absorption spectra alongside DFT calculations.⁶² The Th-F stretches were observed in a similar region to the U-F stretches in EuF_3 ; the pseudo- a_1 symmetry stretch was between 569 and 576 cm^{-1} , and the pseudo- e symmetry stretch was between 525 and 529 cm^{-1} . However, the N-Th stretch was observed at 430 cm^{-1} , suggestive of a single bond. As in the uranium case, the P-Th and As-Th stretches were not observed and calculated to be outside the range of the experimental

spectra. Calculations were performed using both BP86 and B3LYP. The 6-311+G(3df) basis set was used on nitrogen and fluorine, and SDD was used on phosphorus, arsenic and thorium (including a 60 electron RECP). In all three cases, a $^3A''$ C_s ground state was calculated, with a sigma bond and the unpaired electrons predominantly of pnictogen np character, with weak π bonding overlap.

L. Andrews *et al.* obtained IR spectra of the thorium and uranium pnictogen (N, P and As) hydrides, in three papers; one in 2007 on thorimine ($HN=ThH_2$),⁶³ a 2008 paper on uranium- NH_3 complexes,⁶⁴ and a 2017 paper on uranium and thorium complexes with phosphine and arsine.⁶⁵ Argon matrix IR spectra were supported by DFT calculations and coupled-cluster with single, double and perturbative triple excitations (CCSD(T)) calculations were presented in the 2017 paper for the thorium containing species only. DFT calculations were performed with both PW91 and B3LYP. In their PW91 calculations, the $HE=AnH_2$ isomer was the global minimum in all cases, apart from $HP=UH_2$, for which H_2PUH was found to be $0.1 \text{ kcal mol}^{-1}$ lower in energy. All thorium isomers were in the singlet multiplicity, and for uranium, the $HE=UH_2$ isomers were triplets and H_2E-UH were quintets. For the three thorium systems studied by L. Andrews *et al.*, only the $HE=ThH_2$ species was observed, whereas for the three uranium systems both $HE=UH_2$ and H_2E-NH were observed. Also, in the ammonia-uranium experiment, $U:NH_3$ was observed. The EUH_3 isomer was not observed, demonstrating the need for highly electronegative ligands (such as fluoride) to stabilise the formal U(VI) oxidation state and contract the 5f orbitals (improving π bonding overlap) as well as the relative weakness of the $An-H$ bond versus that of $E-H$.

The first isolable terminal uranium nitride complex, structure 4 as shown in Figure 2.3, was synthesised by D. M. King *et al.* in 2012.⁶⁶ Their structural assignment was confirmed by x-ray crystallography (with an observed $N\equiv U$ bond length of 1.83 \AA), and supported by DFT calculations. The use of a highly sterically hindered polydentate ‘Tren^{TIPS}’ ligand

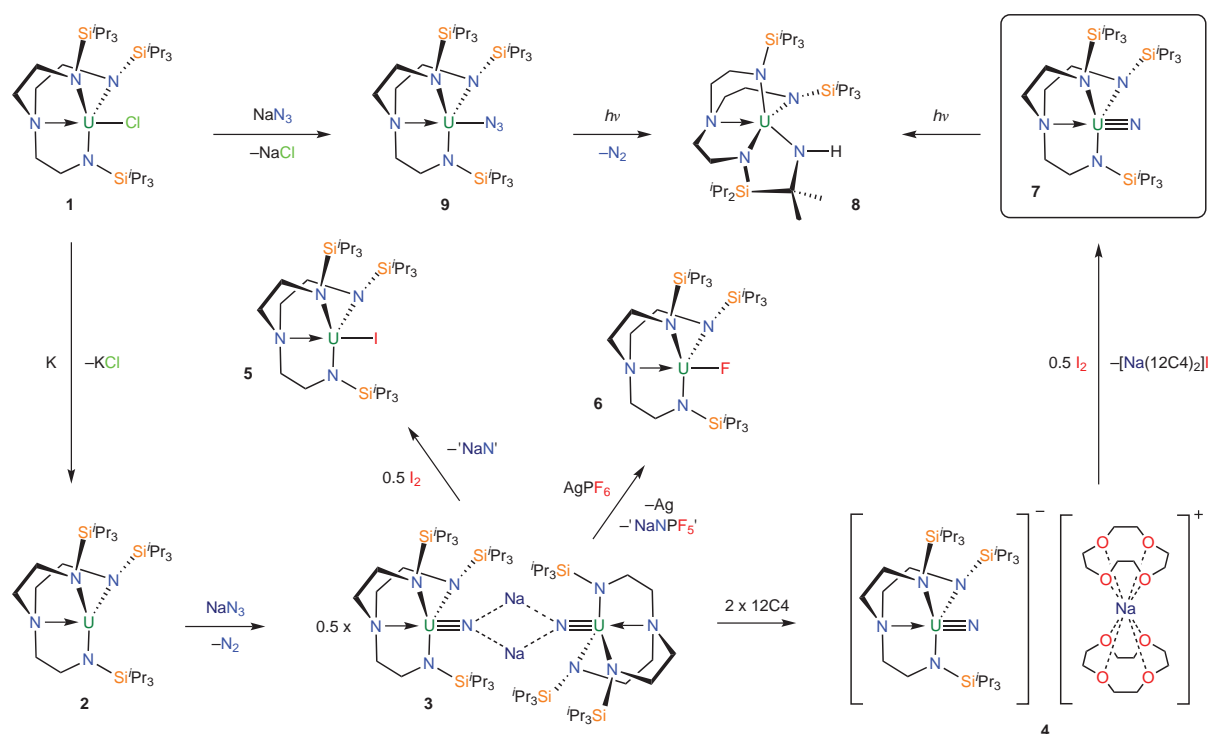


Figure 2.3: The reaction scheme for the synthesis of the first isolable terminal uranium nitride complex (structure 4) as performed by D. M. King *et al.* and first reported in *Science*⁶⁶, and the reaction scheme from structure 4 to the first terminal nitride isolated at ambient conditions (structure 7). 12C4 = 12-crown-4. Reproduced with permission from Nature¹

was necessary to prevent the formation of bridging azides on reduction of structure 2 with sodium azide, instead, structure 3 was formed which features two uranium nitrides bridged by two sodium atoms. On treatment with two equivalents of 12-crown-4, the sodium atoms were encapsulated and an anionic terminal uranium nitride, structure 4, was obtained. DFT calculations were performed at the BP86/triple- ζ STO level of theory, with a scalar ZORA Hamiltonian to account for relativistic effects. They supported the description of a $\text{N}\equiv\text{U}$ triple bond; the geometry optimisation was a good match to the crystallographic parameters (and consistent with other $\text{N}\equiv\text{U}$ triple bonds), the Kohn-Sham orbitals represented a $\pi^4\sigma^25f_U^1$ configuration, and the Mayer bond order was calculated to be 2.91.

The analogous molecular complex (structure 7 in Figure 2.3) was synthesised by D. M. King *et al.* in 2013, by reducing the anionic complex with half an equivalent of I₂.¹ This was the first terminal nitride molecule isolated at ambient conditions; previous identified terminal nitrides

were all isolated in argon matrices. The infrared spectrum obtained gave a $\text{U}\equiv\text{N}$ stretch of 914 cm^{-1} , consistent with other observed triple $\text{U}\equiv\text{N}$ bonds. NMR spectra (^1H , ^{13}C and ^{29}Si) were consistent with a C_{3v} diamagnetic structure, consistent with this bonding description. Single crystal X-ray diffraction gave a $\text{U}\equiv\text{N}$ bond length of 1.799 \AA , little changed from 1.825 \AA for the anionic structure 4; this reflects the removal of an electron from a non-bonding $5f_U$ orbital in structure 4. DFT calculations were performed, with the same methods as used for the anionic complex. Geometry optimisations were a good match to the crystallographic data; all optimised bond distances and angles were reported to be within 0.05 \AA and 2° , respectively. While the Mayer bond order is essentially unchanged, Natural Bond Orbital (NBO) analysis does show a change in uranium orbital character on oxidation from U(V) to U(VI). The σ NBO is 32:68 U:N character for the anionic U(V) complex, versus 41:59 U:N for the molecular U(VI) complex. Additionally, the U s:p:d:f character is 5:4:44:47 for anionic U(V), and 1:1:9:89 for molecular U(VI). This suggests that, in the U(VI) oxidation state, the $5f_U$ valence orbitals provide an improved energetic match and improved size-match for covalent bonding with nitrogen, versus U(V). The π NBOs showed a similar but smaller effect; for one of the near-degenerate π orbitals, there was a U:N character of 27:73 for anionic U(V), versus 30:70 for molecular U(VI). The s and p character of the π NBOs was reported to be negligible, and the d:f characters were 28:72 for anionic U(V) and 19:81 for molecular U(VI).

The established range of bonding environments is much more limited for the heavy pnictogens. The reactivity of the U-E or U-EH moiety requires significant kinetic stabilisation, challenging for uranium and other large metals, necessitating a large R group in a U-ER linkage.⁶⁷ Two early examples of uranium-phosphorus complexes are shown in Figure 2.4, both featuring bulky $\mu_5\text{-C}_5(\text{CH}_3)_5$ ligands on uranium and phosphorus ligands with large R groups; structure 1 featuring a bidentate phosphine ligand and structure 2 a phosphinidene.

Q. Wu *et al.* performed DFT calculations on $\text{NU}[\text{Tren}^{\text{TIPS}}]$ (structure 7 of figure 2.3) and the

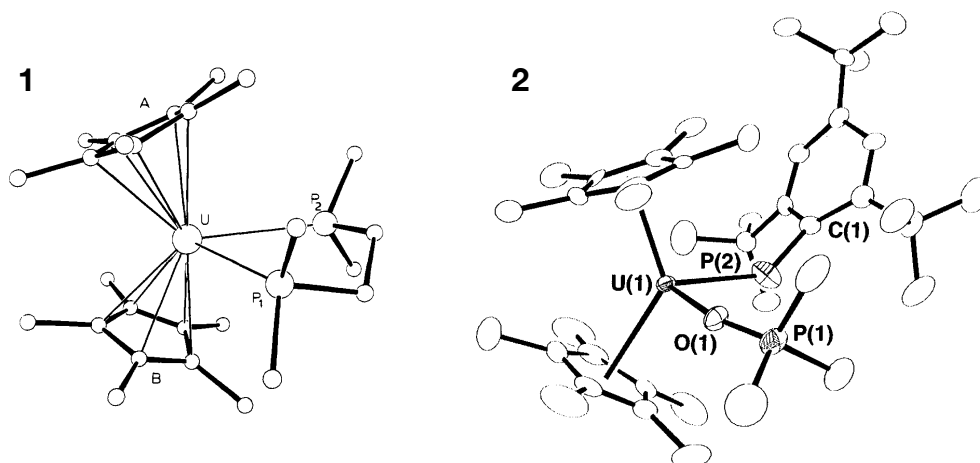


Figure 2.4: The structures of early examples of phosphorus-uranium complexes, shown as thermal ellipsoids as derived from X-ray crystallography. Structure 1, $\text{U}[\mu_5\text{-C}_5(\text{CH}_3)_5][(\text{CH}_3)_2\text{PCH}_2\text{CH}_2\text{P}(\text{CH}_3)_2]$ reported by M. R. Duttera *et al.* in 1984 and reproduced with permission from *the Journal of the American Chemical Society*.⁶⁸ Structure 2, $\text{U}[\mu_5\text{-C}_5(\text{CH}_3)_5][\text{OP}(\text{CH}_3)_3][\text{P}-2,4,6\text{-t-Bu}_3\text{C}_6\text{H}_2]$ reported by D. S. J. Arney *et al.* in 1996 and reproduced with permission from *the Journal of the American Chemical Society*.

heavier pnictogen analogues $\text{EU}[\text{Tren}^{\text{TIPS}}]$ ($\text{E} = \text{P}, \text{As}, \text{Sb}$ and Bi).⁶⁹ They performed calculations at the BP86 level of theory, using a Stuttgart ECP of 60 e^- on U, 46 e^- on Sb and 78 e^- on Bi. The 6-31G(d) basis set was used on all other atoms. All molecules were assumed to be singlet and closed-shell; other multiplicities were not considered. They found all molecules to have triple bonds, but the π bonding was found to be increasingly weak down group 15.

B. M. Gardner *et al.* reported phosphide and phosphinidene complexes not protected by such bulky R groups in 2014.⁷⁰ The synthetic scheme and structures of these complexes are shown in Figure 2.5. The sterically bulky ‘ $\text{Tren}^{\text{TIPS}}$ ’ ligand, as used for the nitride complexes discussed previously, was employed to compensate for the absence of kinetic stabilisation on phosphorus. Reaction of structure 1 with sodium phosphide afforded structure 2, a uranium phosphide with a $\text{U}-\text{P}$ bond length of 2.88 \AA , as confirmed by X-ray crystallography. Treatment of the uranium phosphide with benzyl potassium 2,2,2-cryptand did not produce an isolated phosphinidene since potassium was not fully encapsulated by 2,2,2-cryptand—as confirmed by X-ray crystallography (and shown as structure 3 of Figure 2.5). In an alternative approach, treatment of the uranium phosphide with benzyl potassium and benzo-15-crown-5 ether produced structure 4. The $\text{U}=\text{P}$ bond distance was found to be 2.613 \AA , about 0.05 \AA

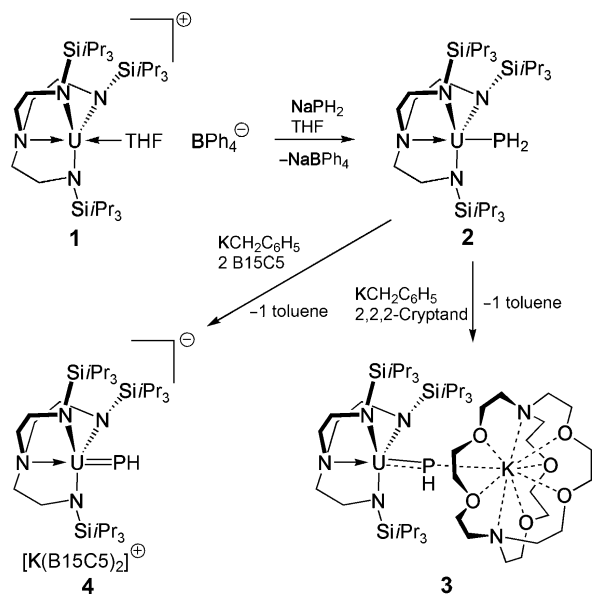


Figure 2.5: The synthesis of the uranium phosphide (structure 2) and phosphinidene (structure 4) identified by B. M. Gardner *et al.*. Reproduced with permission from *Angewandte Chemie - International Edition*.⁷⁰

shorter than the U=P bond length in **3**. DFT geometry optimisations were performed, using the same methodology as previous studies by D. M. King *et al.*, and were a good match for the observed parameters obtained by X-ray diffraction. NBO and QTAIM analyses confirmed the expected bonding descriptions. Structure **2** has a single bond, indicated by a Mayer bond index of 0.84, and a QTAIM ellipticity of $\varepsilon(\vec{r}) = 0.01$. Structures **3** and **4** both have double bonds with π character, with bond indices of 1.61 and 1.92 respectively and ellipticities of 0.22 and 0.20 respectively. The smaller bond index of structure **3** versus structure **4** reflects the coordination of phosphorus to potassium in structure **3**.

On extension of their work to arsenic, B. M. Gardner *et al.* identified analogous species to the phosphide and phosphinidene, and also a tetramer featuring ‘threefold bonding interactions’.⁶⁷ Because of the highly polarised nature of the bonds, featuring very little covalency, B. M. Gardener *et al.* use the terminology bonding interactions to represent the number of electron pairs donated. The reaction scheme is shown in Figure 2.6. DFT geometry optimisations with the same methodology as above were performed. For structure **4**, a pruned model was used to reduce computational complexity; isopropyl groups were replaced by

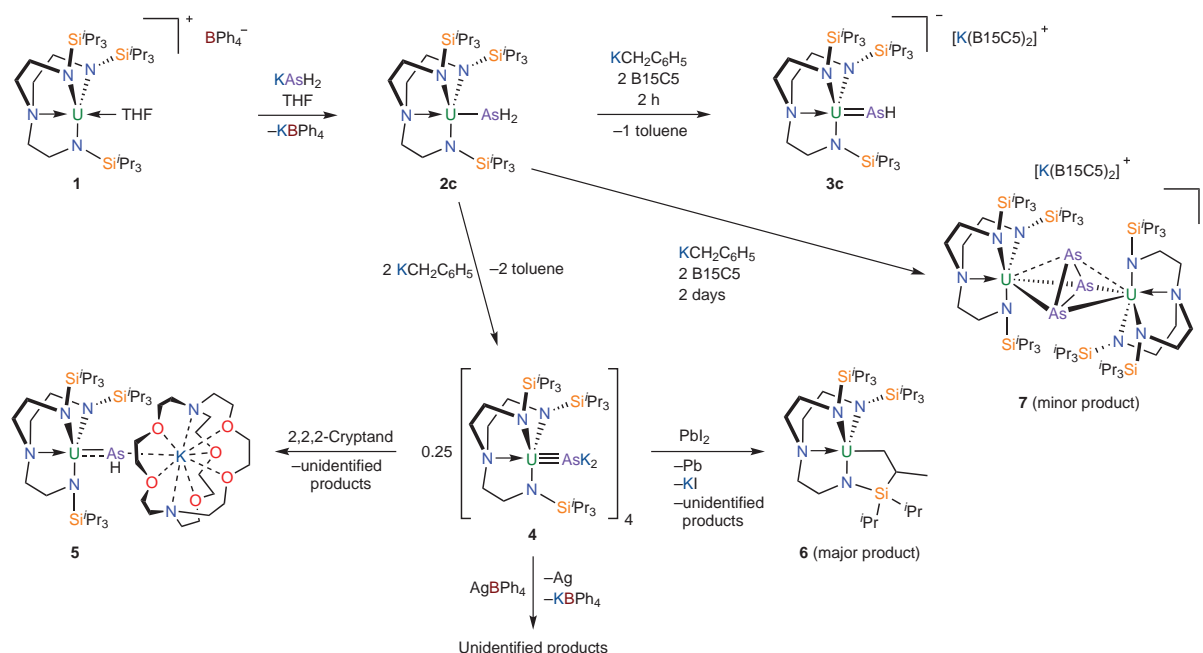


Figure 2.6: The synthesis of the uranium arsenide (structure 2c), uranium arsinidene (structure 3c) and tetrameric complex (structure 4) identified by B. M. Gardener *et al.* Reproduced with permission from *Nature Chemistry*.⁶⁷

hydrides (structure 4). Natural Bonding Orbitals were used to justify the one, two and threefold bonding interactions; structure 2 featuring a σ^2 U-As configuration, structure 3 having a $\sigma^2\pi^2$ configuration and structure 4 having a $\sigma^2\pi^4$ configuration. Structure 2c, with a single bonding interaction, has a U-As bond length of 3.05 Å and Mayer bond index of 0.69. Structure 3c has a bond length of 2.75 Å and bond index of 1.62. The tetrameric structure 4' has bond lengths of between 2.77 Å and 2.73 Å, and bond indices between 1.38 and 1.75. The varying bond indices and bond lengths highlight the polarisation present in the U-As bonding interaction, and the weakness of the third bonding interaction observed in the DFT calculation.

To complete the collection of pnictogen-uranium complexes, T. M. Rookes *et al.* identified a series of actinide-pnictide complexes for P, As, Sb and Bi. They again feature the ligand $\text{Tren}^{\text{TIPS}}$ and an analogue $\text{Tren}^{\text{DMTB}}$; $-\text{SiPr}_3^i$ is substituted for SiMe_2Bu^t . A more sterically hindered $-\text{Pn}(\text{SiMe}_3)_2$ pnictide is employed to kinetically stabilise the An-Pn bond. The U-Sb complex represented the first uranium-antimony molecular bond, and the U-Bi complex was the first identified two centre-two electron uranium-bismuth bond. In addition, thorium

analogues were synthesised for P, As and Sb, using the $\text{Tren}^{\text{TIPS}}$ ligand.⁷¹ The structures of the uranium complexes, obtained from X-ray crystallography, are shown in Figure 2.7. DFT

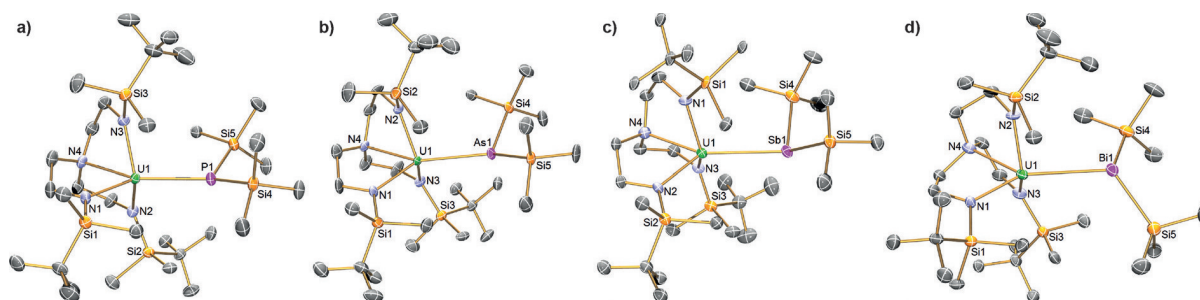


Figure 2.7: The structures of the $\text{U}[\text{Tren}^{\text{DMBS}}]\text{ESiMe}_3$ complexes, from X-ray crystallography, as reported by T. M. Rookes *et al.* E = P (a), As (b), Sb (c) and Bi (d). Reproduced with permission from *Angewandte Chemie - International Edition*.⁷¹

calculations (with the same methodology as above) present a broadly consistent picture down the group; an entirely ionic σ interaction with the bonding NBO 100% localised onto the pnictogen, and a slightly covalent character π NBO, increasing from 14% U character for phosphorus to 18% for bismuth. The Mayer bond index decreases from 0.92 for phosphorus to 0.78 for bismuth, suggesting a weakening of the single bonding interaction, but the $\text{Tren}^{\text{TIPS}}$ analogues all had bond indices of around 1.

2.3 Diuranium complexes

There is substantial interest in complexes containing multiple uranium centres; to explore novel bonding motifs,^{72–79} for their potential role in catalysis and small molecule activation (typically possible due to their novel bonding motifs),^{4,76,80–84} and for their magnetic properties.^{76,85–87} An overview of uranium-uranium bonds is first given below. Uranium-uranium bonds are relevant to this thesis firstly as an aid to understanding whether any uranium-uranium bonding exists in any of the diuranium complexes studied, and also as a well-studied example of the challenges performing high-level calculations on uranium-containing molecules. This is followed by a discussion of notable diuranium complexes, and a more in-depth discussion of diuranium complexes particularly relevant to this thesis; complexes featuring a U_2N_2 motif, and

complexes with a “U₂X₂” motif and their magnetic properties.

Uranium-uranium bonds

Multiple covalent metal-metal bonds have long been of interest. The first quadruple bond identified was a Re-Re bond in K₂[Re₂Cl₈] · 2 H₂O, by F. A. Cotton and C. B. Harris in 1965 and comprised of a σ bond, two π bonds and a δ bond.⁸⁸ Since, there have been numerous examples of multiple metal-metal bonds, predominantly in the middle of the d-block; for example, spectroscopic and theoretical evidence has shown that Mo₂ and W₂ have sextuple bonds, which, in 2007, B. O. Roos *et al.* found to be the greatest covalent bond order possible for homonuclear diatomics with an atomic number below 100.⁸⁹

The uranium dimer was first identified in high-temperature mass-spectrometric studies by L. N. Gorokhov *et al.* in 1974.⁹⁰ They calculated a U₂ binding energy of 52 ± 5 kcal mol⁻¹, however given the high temperature (around 2500°C), and that they assumed a U-U bond length of 3 and a vibrational frequency $\omega_e = 100$ cm⁻¹ this value may be overestimated.³⁹

L. Gagliardi and B. O. Roos found U₂ has a quintuple bond in a detailed theoretical study.⁹¹ They performed CASSCF, CASPT2 and CASPT2-SO calculations which identified a ground state with three full doubly-occupied bonding orbitals ($7s\sigma_g^2$, $6d\pi_u^2$), two full singly-occupied bonding orbitals ($6d\sigma_g^{0.97}$, $6d\delta_g^{0.98}$) and two partially occupied bonding orbitals ($5f\pi_u^{0.63}$, $5f\delta_g^{0.63}$) resulting in an effective bond-order of 4.2. Spin-orbit calculations give a ground state $\Omega = 8_g$ (where Ω is the total angular momentum projection on the internuclear axis). These molecular orbitals, along with their partially-occupied antibonding counterparts, are shown in Figure 2.8.

S. Knecht *et al.* performed fully relativistic calculations on U₂ in 2019, using the exact two-component (X2C) Hamiltonian which describes scalar relativistic and spin-orbit effects whilst reducing computational cost compared to the full four-component Dirac Hamiltonian.³⁹ They performed CASSCF calculations using a similar active space to that of L. Gagliardi and B. O. Roos, and also RASSCF calculations with a larger active space to include some dynamic

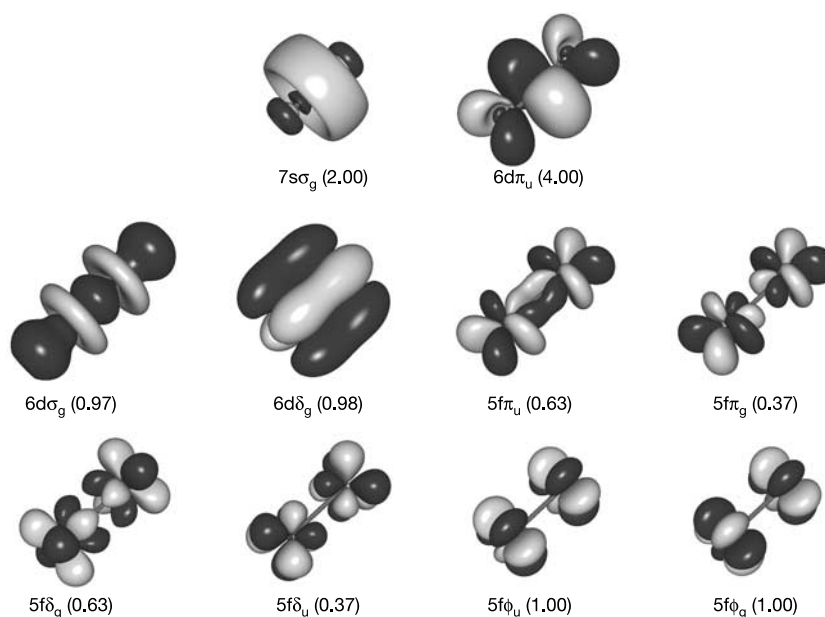


Figure 2.8: The active orbitals of U_2 . Symmetry labels and occupation numbers are given (for degenerate orbitals, the occupancy is of both orbitals). Reproduced with permission from *Nature*.⁹¹

correlation since fully relativistic CASPT2 was not feasible. They identify a $\Omega = 9_g$ ground state instead of the 8_g ground state identified by L. Gagliardi and B. O. Roos; the states mainly differ by the single occupation of a predominantly $5f_\delta$ orbitals in the 9_g state, and a $5f_\pi$ character orbital in the 8_g state. Because bonding and antibonding orbitals can mix at the spin-orbit level, S. Knecht *et al.* derived the ‘generalised’ EBO (gEBO), where each orbital is weighted according to its bonding and antibonding contributions. The gEBO of the 9_g ground state is 3.8 at the CASSCF level, and 3.7 at the RASSCF level, suggesting that U_2 has a quadruple bond.

The electronic structure of the uranium dimer highlights some of the challenges involved in calculations on actinide-containing molecules, and the tradeoffs necessary even for the smallest of molecules. The presence of sixteen energetically closely-spaced valence orbitals (5f, 6d, 7s and 7p), along with their varying overlap (5f overlaps considerably less) makes the electronic structure complicated, and even more so for molecules with multiple metal centres. Relativistic effects must be taken into consideration; L. Gagliardi and B. O. Roos use a second-order DKH Hamiltonian to account for scalar relativistic effects and performed

RASSI calculations for the effects of spin-orbit coupling. Describing spin-orbit coupling at a higher level, with the X2C Hamiltonian, necessitates neglecting some dynamic correlation as S. Knecht *et al.* were not able to perform CASPT2 calculations with the Hamiltonian. While S. Knecht *et al.* suggest that enough dynamic correlation is recovered in their RASSCF calculation, it is possible that fully relativistic calculations which fully include dynamic correlation again change the bonding description of U_2 .

The actinide dimers Ac_2 , Th_2 and Pa_2 were studied theoretically by B. O. Roos *et al.* in 2006,⁹² reporting effective bond orders of 1.7, 3.7 and 4.5 respectively. The uranium dimer has a lower bond order (4.2) than protactinium (4.5) due to the relative stabilisation of the 5f orbitals versus the 6d. The poorer overlap of the 5f orbitals disfavours covalency, hence the lower bond order. This trend is expected to continue for later actinides, in addition to the increased occupancy of antibonding orbitals. Therefore, the authors suggest that the protactinium dimer represents the greatest bond order of the actinide dimers, and thus the largest bond order in a homonuclear diatomic is 6, for Mo_2 and W_2 .

While many actinide metal-metal bonds have been reported theoretically, the number of which have been isolated experimentally is much more limited—partly due to the general preference to form actinide-ligand bonds over actinide-actinide. G. Cavigliasso and N. Kaltsoyannis explored this trend theoretically, performing DFT calculations on M_2X_6 , where $M = U, W$, and Mo and $X = Cl, F, OH, NH_2$, and CH_3 and analysing the systems with MO theory and energy decomposition. They suggest the relative paucity of experimentally isolated U-U bonds is due to the more destabilising contribution from Pauli and electrostatic effects, *versus* the transition metal analogues. This is despite a slight increase in the strength of the orbital mixing contribution of the bond energy for the U-U systems, which show substantial f-f overlap.

The uranium hydrides U_2H_4 and U_2H_2 were first isolated in solid argon by P. F. Souter *et al.*

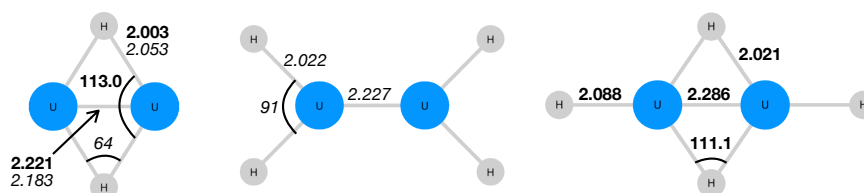


Figure 2.9: The structures of U_2H_2 (left), and U_2H_4 (centre, P. F. Souter *et al.*, and right, J. Raab *et al.*). Bond lengths in Å, angles in degrees. Structural parameters in bold are that calculated by J. Raab *et al.*⁹³ at the CASPT2 level of theory, italic are that from P. F. Souter *et al.* at the DFT/BP86 level of theory.

in 1996 (and were the first compound isolated which contained an actinide-actinide bond).⁹³ Their DFT calculations (at the BP86 level of theory, with a triple- ζ quality basis-set) suggested a D_{2h} structure with all hydrides μ_1 bound for U_2H_4 . However, calculations at a higher level of theory, CASPT2, 10 electrons in 12 orbitals as performed by J. Raab *et al.*, suggested a bridged structure—also D_{2h} (with a $^3B_{3u}$ ground state) but having two bridging hydrides and two terminal hydrides, as shown in Figure 2.9.⁹⁴ The effective bond order of the U-U bond in U_2H_2 was 3.97, at the CASPT2 level of theory. This bond order, and the orbital occupancies (predominantly $\sigma^2\sigma^2\delta^2\pi^4$), points to either a weak quintuple bond or a quadruple bond.

Multiple uranium centre complexes with bridging atoms/ligands frequently use polydentate or highly sterically bulky ligands to kinetically stabilise the complex and to create a pocket in which the ring can form. G. Feng *et al.* synthesised several uranium-nickel rings using the heptadentate ligand, $[\text{N}(\text{CH}_2\text{CH}_2\text{N}^i\text{Pr}_2)_3]^{3-}$.⁷⁸ The ligand has two binding sites on each arm, a hard amide, binding effectively to the actinide and a soft phosphide to bind with nickel. They synthesised complexes featuring U_2Ni_2 , $\text{U}_2\text{Ni}_2\text{Cl}_2$ and U_2Ni_3 motifs by varying the order in which the Ni(0) source, $\text{Ni}(\text{COD})_2$ and the reducing agent, KC_8 is added. They identify a uranium-uranium bonding interaction for the U_2Ni_2 and U_2Ni_3 species, with U–U Wiberg bond indices of 0.20 and 0.19, and optimised U–U interatomic distances of 4.4 and 4.6 Å respectively. They performed density functional theory (DFT) geometry optimisations using the B3PW91 functional, and large f-in-core effective core potentials (ECPs). They suggest that the uranium-uranium bonding interaction originates from a four-centre and five-centre two-electron

bond for U_2Ni_2 and U_2Ni_3 respectively. This is the HOMO for both which is an s/d_{z^2} hybrid on uranium donating into unoccupied Ni p . G. Feng *et al.* subsequently used a heptadentate ligand to isolate the first f-block–metal triple bond authenticated by crystal structure. The complex features a U_2Rh_4 core, with each uranium triply bonded to a single rhodium atom, with the heptadentate ligand again exploiting hard/soft interactions to coordinate with the uranium and rhodium respectively. DFT calculations (again using B3PW91) support the presence of a $\text{U}\equiv\text{Rh}$ triple bond, with a σ and two π bonding orbitals being observed, and a $\text{U}\equiv\text{Rh}$ Wiberg bond order of 2.61.

Fullerene cages were used to obtain highly novel diuranium carbide clusters; X. Zhang *et al.* encapsulated $\text{U}=\text{C}=\text{U}$ in a C_{80} fullerene,⁹⁵ and J. Zhuang *et al.* encapsulated U_2C_2 in C_{78} and C_{80} fullerenes. They performed detailed theoretical studies on both complexes, including multiconfigurational calculations, and identified that the $\text{U}=\text{C}=\text{U}$ unit was U(V) with substantial covalency between uranium and carbon. By contrast, the interaction in U_2C_2 was found to be largely ionic between the U(IV) and C_2^{2-} units; the $\text{C}\equiv\text{C}$ triple bond was slightly weakened by π backbonding with the uranium centres.

Diuranium-nitrogen complexes

The prospect of novel nitrogen reactivity and catalysis has driven much of the interest in diuranium-nitrogen complexes, given the strength of the N_2 triple bond, and also the strength of uranium-nitrogen bonds due to the unique role that 5f orbitals play in bonding in the actinides.^{4,59,80,96}

The first complex to feature a U_2N_2 core featured a dinitrogen ligand coordinated side-on to two U(III) centres, and was synthesised by P. Roussel and P. Scott in 1998 by exposing the parent U(III) complex to N_2 .⁷² The U(III) centres are sequestered by the ligand $\text{Tren}^{\text{DMSIB}}$; a tripodal ligand with three coordinating amides similar to $\text{Tren}^{\text{TIPS}}$, but with $\text{Si}^i\text{ButMe}_2$ instead of Si^iPr_3 —the structure of the complex is **A** in Figure 2.10. The length of the $\text{N}\equiv\text{N}$ bond, 1.109

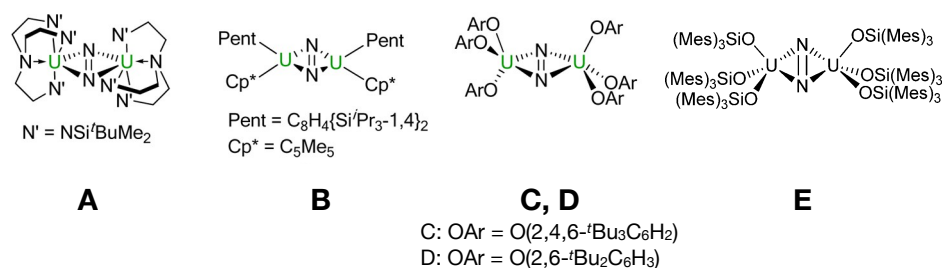


Figure 2.10: The structure of previously reported diuranium-N₂ complexes. Structure images adapted with permission from *Organometallics* 2013, 32, 15, 4214–4222.⁹⁷ Copyright 2013 American Chemical Society.

Å, is largely unperturbed from that of free N₂, 1.098 Å. Subsequent DFT calculations (using the functional BP86) on a model of the complex suggest substantial U–N π backbonding providing a significant electronic driver to elongate this bond; the authors suggest that this is offset by the substantial sterics of the Tren^{DMSIB} ligand not described by the simplified model.^{73,74}

Several complexes have since been obtained which reduce the coordinated N₂; either partially to give a N₂²⁻ containing complex,^{97–99} or to the nitride with complete cleavage of the N≡N bond.⁷⁵ In the case of the partially reduced complexes, all were obtained by reaction of the parent U(III) complex with U₂ however the reversibility and thermal stability of the dinitrogen complexes obtained varies, as does the N–N bond length. **A** and **B** dissociate *in vacuo*, **C** dissociates at 80 °C, **D** was only obtained in small quantities, but **E** was found to be stable to at least 100 °C. Complexes **B**, **C** and **D** have N–N bond lengths of between 1.163 and 1.236 Å showing clear signs of N₂ activation. Like **A**, complex **E** has a crystal structure bond length little perturbed to that of free N₂; the crystal structure of two isomers was obtained, 1.080 Å or 1.124 Å depending on the relative orientation of the siloxide ligands. S. Mansell *et al.* suggests that the crystal structure, itself based on the electronic density, underestimates the internuclear separation, and the Raman spectra support the two-electron reduction of N₂.⁹⁷

The first complex containing a U₂N₂ nitride motif was synthesised by Korobkov *et al.* in 2002.⁷⁵ The anionic complex, **F** in Figure 2.11, features the U₂N₂ ring sequestered by two tetranionic calix[4]-tetrapyrrole ligands and was obtained by treatment of a U(III) complex with

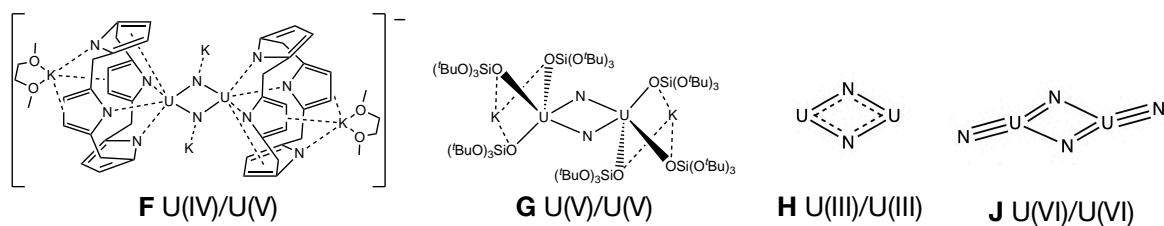


Figure 2.11: The structure of previously reported diuranium bis-nitride complexes. For **F**, ethyl groups on the bridging carbon of the calix[4]-tetrapyrrole are omitted for clarity.

$K(C_{10}H_8)$ in a N_2 atmosphere. The crystal structure they obtain is centrosymmetric; they suggest either that the complex is Class 1 mixed-valence, or that the complex is Class 2, with distinct U(IV) and U(V) centres and the two metals being disordered over both positions—however, the near-IR spectrum is supportive of the presence of a U(V) centre, supporting the complex being Class 2. The U–N bonds are substantially shorter than that obtained by Roussel and Scott, at an average of 2.09 Å, and the N–N distance of 2.46 Å indicates nitrides over coordination to end-on N_2 .

More recently, in 2013, Camp *et al.* identified a U_2N_2 -containing complex featuring two U(V) centres, **G** in Figure 2.11.⁷⁶ Two of the U–N bonds are 2.02 Å, with the other pair being 2.10 Å, suggesting multiple bonding character in the ring. The N–N distance of 2.48 Å again indicates no bonding interaction between the two ring nitrogens. The ring is encapsulated by six of the siloxide ligand $[OSi(O^tBu)_3]^-$, with the bulky tBu groups providing kinetic stabilisation. They reported an improved synthesis and a study of **C**'s magnetic properties in 2019.⁸² The magnetic susceptibility shows strong antiferromagnetic coupling between the two U(V) centres, with a critical temperature of 77 K. They suggest the short bond lengths observed are evidence of multiple bonding.

The molecules U_2N_2 and U_2N_4 were studied by Vlaisavljevich *et al.*⁷⁷ They isolated the molecules in an argon matrix and obtained IR absorption spectra. In addition, they performed a detailed theoretical study, performing DFT and multiconfigurational calculations on the molecules. DFT calculations, performed with the B3LYP functional, gave a D_{2h} , septet ground

state, with the six unpaired electrons occupying $5f_U$ character non-bonding orbitals, and a delocalised bonding system composed of four σ and two π orbitals. At the RASPT2 level, a multiconfigurational quintet ground state was obtained, with the ring bonding orbitals having a similar character to that of the DFT and significant contributions from $5f_U$ orbitals. By contrast, U_2N_4 was found to be a singlet with both DFT and CASPT2 and was found to be mostly monoconfigurational at the CASPT2 level. They found a significant alternation in the U–N ring bonds; one pair of is a single bond, with the other a double bond. By comparing to lanthanide and transition metal analogues La_2N_2 and W_2N_2 the role of f orbitals was further elucidated; La_2N_2 and U_2N_2 both being D_{2h} due to the availability of nonbonding nf orbitals but W_2N_2 has a C_{2v} structure due to the occupation of antibonding orbitals.

There are similarly few examples of diuranium complexes featuring bridging imido ligands; there are several examples of diuranium complexes featuring a single bridging imido ligand amongst others.^{76,100–103} There are only two examples of a bis-imido complex featuring no other bridging ligands, both of which feature the siloxide ligand $[OSi(O^tBu)_3]^-$; the U(V) complex $U_2(NMe)_2L_6$,¹⁰⁴ and the U(IV) complex $U_2(NH)_2L_6K_2$ ($L = [OSi(O^tBu)_3]^-$).⁸² The U(V) complex $U_2(NMe)_2L_6$, obtained by treatment of a U(IV) diuranium mono-nitride with MeOTf, was found to be rather unstable preventing further characterisation. The U(IV) $U_2(NH)_2L_6K_2$ was obtained by reacting the previously discussed U(V) bis-nitride complex $U_2N_2L_6K_2$ with H_2 . This reactivity is notable for uranium's potential role in small molecule catalysis, given that in the Haber-Bosch process hydrogen cleavage by a metal nitride species is likely to be an important step.^{82,105} The bis-imido complex retains the strong antiferromagnetic coupling observed in $U_2N_2L_6K_2$, with a slightly reduced critical temperature of 60 K.

Diuranium-chalcogen complexes

There is substantial interest, both theoretical and experimental, in complexes featuring a U_2O_2 diamond motif, for their magnetic properties and also to study 'cation-cation interactions'

(CCIs); cationic units, prototypically a dimer of U(V) uranyl UO_2^+ units bridged by an oxide ligand from each uranyl.^{4,85,87,106–110} Common motifs between two UO_2^+ units are shown in Figure 2.12. CCIs can be described as an attractive dipole interaction between two cationic

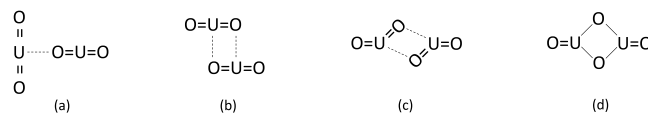


Figure 2.12: Possible UO_2^+ cation-cation interaction dimers. Reproduced with permission from *Inorg. Chem.* 2019, 58, 15, 10148–10159.¹¹⁰ Copyright 2019 American Chemical Society.

units, but as Figure 2.12 shows they exist in a spectrum; from a) and b) where the uranyl units are only weakly perturbed, to c) where the $\text{U}=\text{O}$ bond in the ring becomes more activated (typically by around 0.1 \AA) and the uranyl unit becomes slightly bent, and finally to d) where bond lengths within the ring are approximately equal and the uranyl unit substantially deviates from linearity. Due to their interesting electronic and magnetic properties, CCIs of the types c) and d) are what is focused on in this section of the thesis.

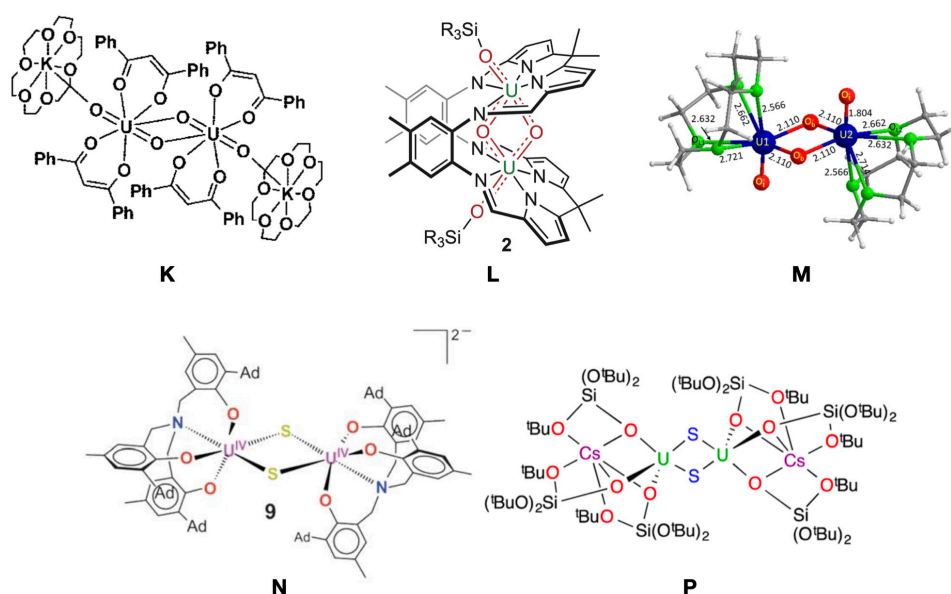


Figure 2.13: The structure of some previously reported diuranium bis-chalcenide complexes. **K** is adapted from the *Journal of the American Chemical Society*,⁸⁵ **L** from *Nature Chemistry*,¹⁰⁹ **M** from *Inorganic Chemistry*,¹¹⁰ **N** from *Chemical Science*, and **P** from the *Journal of the American Chemical Society*,¹¹¹ all with permission.

The first such U(V) dimer was isolated by Nocton *et al.* in 2008—they also isolated a similar tetramer earlier in 2006.^{85,112} They obtained the dimer $[\text{UO}_2(\text{dbm})_2\text{K}(18\text{C}_6)]_2$ (dbm =

dibenzoylmethanate), **K** in Figure by treatment of U(V) $\text{UO}_2(\text{py})_n^+$ (py = pyridine) with two equivalents of Kdbm salt. The $\text{U}_2\text{O}_2^{2+}$ core has U–O ring bond lengths of 1.941 and 2.384 Å, and a $\text{U}\equiv\text{O}$ external bond length of 1.850 Å, firmly type c (Figure 2.12). Study of the dimer's magnetic properties suggested weak antiferromagnetic coupling between the two f^1 centres; the critical temperature of the magnetic susceptibility was only 5 K. The magnetic moment at room temperature was $1.69 \mu_B$ per uranium centre. This is diminished compared to the monomeric $\text{UO}_2(\text{py})_n^+$ ($2.57 \mu_B$) and the theoretical value of a free $5f^1$ ion in the L-S coupling scheme ($2.54 \mu_B$). The authors suggest this is due to the covalency of the bridging ligands.

The dimer $[\text{UO}_2(\text{dbm})_2\text{K}(\text{18C6})]_2$ (and a related ' $\text{U}_3\text{O}_6^{3+}$ ' trimer) was studied theoretically by B. Teyar *et al.*⁸⁷ They performed DFT calculations, including broken-symmetry (BS) DFT calculations on the dimer, and a model. Their geometry optimisation, using the GGA functional BP86, was a reasonable match with the crystal structure; the shorter $\text{U}=\text{O}_{\text{ring}}$ bond length was slightly shortened by 0.01 Å, at 1.929 Å whereas the longer $\text{U}=\text{O}_{\text{ring}}$ bond was lengthened by 0.08 Å, at 2.462 Å. The U–U interatomic distance was lengthened by 0.09 Å, at 3.553 Å. The geometric discrepancy has important consequences for the magnetic properties of the complex they calculated. The exchange coupling parameter J is calculated at the BS-DFT level using the Yamaguchi formula:¹¹³

$$J_{12} = \frac{E_{BS} - E_{HS}}{\langle S_{HS}^2 \rangle - \langle S_{BS}^2 \rangle} \quad (2.1)$$

where E_{BS} and E_{HS} are the energies of the broken-symmetry and high-spin states respectively, and $\langle S^2 \rangle$ are their square of the total spin expectation values; a negative J represents antiferromagnetic coupling. B. Teyar *et al.* used the hybrid B3LYP functional to perform their BS-DFT calculations. At the BP86 optimised geometry, they obtained an exchange coupling constant J of -347.6cm^{-1} , which as they point out is far too negative for a weakly antiferromagnetically coupled molecule. By contrast, calculations where the U_2O_2 ring is frozen

at the geometry of the crystal structure gave $J = -24.1\text{cm}^{-1}$. Given this discrepancy, B. Teyar *et al.* performed a series of calculations on a model core where the U–O–U angle was varied, with bond lengths frozen at the crystal structure of the full molecule. They vary the U–O–U angle from 97.9° to 116.9° , with J varying from more strongly antiferromagnetic ($J = -56.1\text{cm}^{-1}$ at U–O–U = 97.9°) to very weakly ferromagnetic ($J = +1.6\text{cm}^{-1}$ at U–O–U = 116.9°). The calculations on the various core geometries highlight the extreme sensitivity of calculating the exchange coupling parameter, given the small energy differences involved.

P. Arnold *et al.* obtained a U(V) diuranium-oxo complex featuring a diamond U_2O_2 core, **L** in Figure 2.13, with average ring U–O bond lengths of either 2.094 \AA or 2.081 \AA , depending on the alkyl group on the ancillary silyl group on the ‘Pacman’ ligand.¹⁰⁹ They observe that the complex is remarkably stable, given that UO_2^+ CCI dimers are typically particularly liable to redox decomposition. Magnetic susceptibility data give a critical temperature of 17 K, and fitting of these data gives an experimental exchange coupling parameter $J = -33\text{cm}^{-1}$. They performed DFT calculations with the B3LYP functional. Their calculations suggested a single bond in the ring, with signs of weak delocalised π bonding. P. Arnold *et al.* performed geometry optimisations with triplet, broken-symmetry singlet, and closed-shell singlet couplings of the two $5f^1$ centres and find the broken-symmetry singlet to be the lowest in energy by 1.4 and $42.7\text{ kcal mol}^{-1}$ relative to the triplet and closed-shell singlet respectively. The 1.4 kcal mol^{-1} HS-BS energy difference corresponds to a theoretical $J = -490\text{cm}^{-1}$; far too large, despite optimised bond lengths being within 0.01 \AA . This may be because a full geometry optimisation was performed on the broken-symmetry state, but this again highlights the sensitivity of the small energy gap used in theoretically calculating exchange coupling parameters.

A U(VI) uranyl peroxide bridged dimer supported by three 12-crown-4 ether (12C4) ligands, **M** in Figure 2.13, was obtained in the gas phase by electrospray ionisation and characterised with DFT by S. Hu *et al.*¹¹⁰ Collision induced dissociation (CID) gave a U(V) “extreme CCI”

(via a U(V) species with only one 12-crown-4 ether). The species were identified with CID mass spectra in tandem with calculations at the DFT level, using PBE for computational efficiency when searching for candidate structures and further verifying with the hybrid B3LYP functional and *ab initio* calculations at the DLPNO-CCSD(T) level. The computed structure of the U(V) "extreme CCI" $[(\text{UO}_2)_2(12\text{C}4)_2]^{2+}$ is of type d) (Figure 2.12). Ring U–O bond lengths were computed to be equal at 2.110 Å, with calculated Gopinathan-Jug bond orders of 1.19 indicating delocalised bonding with slight multiple bonding character. BS-DFT calculations suggest weak ferromagnetic coupling, with an exchange coupling parameter $J = +6.9\text{cm}^{-1}$.

M. Falcone *et al.* isolated a U(IV) bis-oxide complex encapsulated by the previously discussed siloxide ligand $[\text{OSi}(\text{O}^t\text{Bu})_3]^-$ (=L), $\text{U}_2\text{O}_2\text{L}_6\text{K}_2$. The complex was amongst a series of others isolated, including a U(III) diuranium mono-nitride, and a U(IV) mono-oxide. The bis-oxide has an average U–O ring bond length of 2.137 Å, in line with other complexes discussed but slightly lengthened reflecting the reduced oxidation state on uranium.

The number of examples of diuranium complexes featuring bridging sulfur and heavier chalcogen ligands is much more limited. While there are several examples of η_2 bridging persulfide (S_2^{2-}) complexes^{114–117}, and some examples of bridging mono-sulfides,^{115,116} only two bis-sulfides, which feature a U_2S_2 diamond core, have been isolated.^{108,111}

O. Lam *et al.* isolated dianionic U(IV) bis-sulfide (**N** in Figure 2.13), bis-selenide and bis-telluride complexes, in addition to the related mono-chalcogenide U(IV) neutral analogues.¹⁰⁸ The family of complexes were ligated by a tripodal tris-aryloxide ligand, which features large aromatic groups on the arms to provide kinetic stabilisation. The U(IV) magnetic susceptibility of the mono-chalcogenide show clear signs of antiferromagnetism, however, the bis-chalcogenides are less clear; the magnetic moments of the complexes are less than that expected of a U(IV) centre which the authors suggest is the influence of the rather short U–E bonds.

L. Chatelain *et al.* obtained a U(IV) diuranium bis-sulfide, which features the siloxide ligand $[\text{OSi}(\text{O}^t\text{Bu})_3]^-$ ($=\text{L}$), having the structure $\text{U}_2\text{S}_2\text{L}_6\text{Cs}_2$,¹¹¹ **P** in Figure 2.13. The complex was obtained by reaction of a U(III) diuranium mono-nitride with CS_2 ; as the focus of the paper was the nitride, no magnetic characterisation of the bis-sulfide was reported.

Part II

Results

Post Hartree-Fock calculations of pnictogen-uranium bonding in EUF_3 (E = N-Bi)

Benjamin E. Atkinson, Han-Shi Hu and Nikolas Kaltsoyannis *Chem. Commun.*, 2018, **54**, 11100-11103 <https://doi.org/10.1039/C8CC05581E>

As has been found previously,⁶⁰ we identified NUF_3 as having a triple $\text{N}\equiv\text{U}$ bond, with a largely monoconfigurational electronic structure; the $\sigma^2\pi^4$ configuration represents 86.6% of the wavefunction. By contrast, previously reported calculations on PUF_3 and AsUF_3 gave a triply-bonded geometry,⁶¹ whereas the calculations in this work suggest a singly bonded geometry for both molecules, with antibonding π^* and non-bonding $5f_U$ orbitals significantly occupied. We propose this difference in conclusions is due to the smaller [6,6] active space used in the previous studies, which includes the σ , π , π^* and σ^* orbitals. In our calculations, a [6,16] active space was employed in order to include uranium f-orbitals and pnictogen d-orbitals; the smaller active space does not allow occupation of these non-bonding orbitals. Calculations on SbUF_3 and BiUF_3 (at the CASSCF level of theory) indicate a bonding environment consistent with PUF_3 and AsUF_3 ; a single bond with significant occupation of π^* and $5f_U$ orbitals.

Contribution statement

This work was written by myself with input and feedback from N.K. I performed calculations at the CASSCF and CASPT2 levels of theory, QTAIM analyses, and analysed the results, with supervision from N.K. and H-S.H., who jointly conceived the project.

Cite this: DOI: 10.1039/xxxxxxxxxx

Post Hartree-Fock calculations of pnictogen-uranium bonding in EUF_3 ($\text{E} = \text{N-Bi}$)

Benjamin E. Atkinson, Han-Shi Hu,[‡] and Nikolas Kaltsoyannis*

Received Date

Accepted Date

DOI: 10.1039/xxxxxxxxxx

www.rsc.org/Journalname

NUF_3 is identified as having a $\text{N} \equiv \text{U}$ triple bond, as has been previously found (Andrews *et al.*, *Angew. Chem. Int. Ed.*, 2008, 47, 5366). By contrast, while previously reported calculations on PUF_3 and AsUF_3 (Andrews *et al.*, *Inorg. Chem.*, 2009, 48, 6594) gave a $\text{E} \equiv \text{U}$ triple bond, our calculations suggest a single bond for both molecules, with antibonding π^* and non-bonding $5f_{\text{U}}$ orbitals significantly occupied, and highly multiconfigurational wavefunctions. We propose this difference to be due to the smaller [6,6] active space used (σ , π , π^* and σ^*) in the previous studies. In our calculations, a [6,16] active space was employed in order to include uranium f-orbitals and pnictogen d-orbitals.

Uranium's central role in nuclear power necessitates a detailed knowledge of its chemistry, including at the most fundamental level. Pnictogen-actinide chemistry is an understudied area, and in addition to being of fundamental interest, an understanding of uranium-nitrogen chemistry is important for developing future applications of the actinides, such as the potential for uranium nitride to be used as a replacement for uranium oxide fuels, given its higher melting point, thermal conductivity and increased density.¹

The terminal uranium nitride molecules which have been studied spectroscopically were summarised by King and Liddle in 2013; the molecules UN , UN_2 ,² NUNH (featuring both a double and triple U-N bond)³ and NUF_3 ⁴ were all isolated in inert gas matrices, and all feature $\text{U} \equiv ^{14}\text{N}$ stretching frequencies between 938–1051 cm^{-1} .¹ The first uranium nitride molecule isolable at ambient conditions was reported by King *et al.* in 2013, featuring the highly sterically hindered polydentate $\text{Tren}^{\text{TIPS}}$ lig-

and $(\text{N}(\text{CH}_2\text{CH}_2\text{NSi}^i\text{Pr}_3)_3)$.⁵ $\text{Tren}^{\text{TIPS}}$ has subsequently been successfully employed in isolating a range of pnictogen-actinide complexes, including $\text{U}(\text{Tren}^{\text{TIPS}})(\text{PH})$ featuring a double $\text{U}=\text{P}$ bond,⁶ and the tetrameric $[\text{U}(\text{Tren}^{\text{TIPS}})(\text{AsK}_2)]_4$ featuring a $\text{U} \equiv \text{As}$ triple bonding interaction.⁷

Andrews *et al.* also reported data for PUF_3 and AsUF_3 . They obtained argon matrix isolated IR spectra of the three molecules, with U-F stretches being observed in the 520–620 cm^{-1} region. The only pnictogen-uranium stretch observed was for NUF_3 (at 938 cm^{-1}); the P-U stretch and As-U stretch were not observed but were calculated to lie outside the window of the experimental spectra. Density functional theory (DFT) calculations were performed alongside complete active space-SCF (CASSCF) calculations with second-order perturbation theory (CASPT2). A 6 electrons in 6 orbitals ([6,6]) active space was employed, which included the σ , π , π^* and σ^* orbitals of the pnictogen-uranium bond. Effective U-E bond orders were 2.78, 2.39 and 2.21 for NUF_3 , PUF_3 and AsUF_3 respectively, indicating significant multiple bonding, with a weakening of π bonding down group 15.

In this contribution, we report superior post Hartree-Fock calculations on EUF_3 ($\text{E} = \text{N-Bi}$). Calculations were performed at the CASSCF⁸ and CASPT2 levels of theory,^{9,10} but with a substantially larger active space than previously used; 6 electrons in 16 orbitals. This was chosen to include the uranium 5f, 6d and 7s valence orbitals, along with the pnictogen np valence orbitals. For NUF_3 , the principal conclusion from the present larger active space calculations is very similar to that calculated by Andrews *et al.* with a [6,6] active space, *i.e.* there is a $\text{U} \equiv \text{N}$ triple bond. A U-N bond length of 1.753 Å was calculated, *vs.* 1.759 Å from L. Andrews *et al.* Geometric parameters are summarised in Fig. 1, and key vibrational frequencies in Table 1. The wavefunction is largely monoconfigurational with the $\sigma^2\pi^4$ configuration making up 86.6% of the wavefunction. The $^1\text{A}_1$ state was calculated to be the ground state; the first excited state, the $^3\text{A}''$ state, predominantly of $\sigma^1\pi^45f_{\text{U}}^1$ character, lies 1.60 eV higher in energy. The vast majority of the active electrons are inside the equivalent of Andrew's [6,6] active space (*i.e.* the σ and π bonding and anti-

School of Chemistry, The University of Manchester, Oxford Road, Manchester M13 9PL, United Kingdom; E-mail: nikolas.kaltsoyannis@manchester.ac.uk

[†] Electronic Supplementary Information (ESI) available: computational methodology, energies and natural orbital occupancies of excited states, full vibrational frequencies and optimised geometric parameters. See DOI: 10.1039/b000000x/

[‡] Present address: Department of Chemistry, Tsinghua University, Haidian District, Beijing 100084, China.

bonding orbitals) with only 0.042 electrons in the remaining 10 orbitals of the active space. This suggests that, for NUF_3 , the [6,6] active space is perfectly adequate.

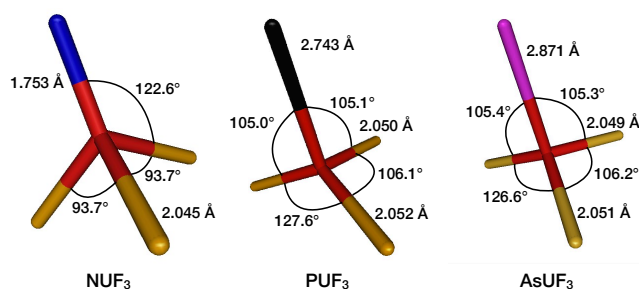


Fig. 1 The ground state geometries of NUF_3 (left, C_{3v} , 1A_1), PUF_3 (middle, C_s , $^1A'$) and AsUF_3 (right, C_s , $^1A'$). Bond lengths given in ångström, bond angles in degrees. Blue: nitrogen, black: phosphorus, pink: arsenic, red: uranium, yellow: fluorine.

The assignment of a triple bond for NUF_3 is clear; the effective bond order $BO_{\text{eff}} = 2.73$. This is firmly supported by the U-N bond critical point (BCP) ellipticity $\varepsilon = 0.00$ (Table 2). BCP ellipticities measure the extent to which the electron density is preferentially accumulated in a given plane containing the bond path connecting two chemically bonded atoms.¹¹ Cylindrically symmetric bonds (e.g. single or triple bonds) have ellipticities (close to) zero, while double bonds feature significantly non-zero ellipticity values. The triple bond is reflected in both the calculated and observed stretching frequencies. In argon matrix IR absorption spectra, Andrews *et al.* observed the N-U stretching frequency at 938 cm^{-1} , compared to a calculated 921 cm^{-1} (at the [6,6] CASPT2 level of theory). In this work, the N-U stretching frequency is calculated to be 928 cm^{-1} (Table 1), though given that argon matrix effects are not included in the gas phase calculations, this slight improvement in the agreement may be fortuitous. Two very small imaginary frequencies are present (at $9.52i\text{ cm}^{-1}$ and $0.73i\text{ cm}^{-1}$), though these are likely artefacts of the numerical frequency calculation, as is the 1 cm^{-1} difference between the two components of the E symmetry U-F stretch.

By contrast to NUF_3 , increasing the size of the active space has a significant effect on the geometry of PUF_3 . A [6,6] active space predicts a triple bond geometry with both the methodology of Andrews *et al.*,¹³ i.e. an all electron basis set with a second-order DKH hamiltonian ($r(\text{P-U}) = 2.40\text{ Å}$), and that employed in this work using a relativistic ECP ($r(\text{P-U}) = 2.44\text{ Å}$). A [6,16] active space, however, finds a singly-bonded geometry, with the π bonds partially broken ($r(\text{P-U}) = 2.74\text{ Å}$). The optimised geometry of PUF_3 is shown in Fig. 1. In comparison to NUF_3 , the UF_3 motif is much flatter, with a smaller E-U-F bond angle of 105° , vs. 123° for NUF_3 . The distortion from C_{3v} is a result of the increase of a single F-U-F angle to 128° (and a corresponding decrease of the other two).

The natural orbitals of the active space are shown in Fig. 2, and the orbital occupancy of the active space is $\sigma^{1.93}\pi^{2.14}\pi^*1.335f_{\text{U}}^{0.51}3d_{\text{P}}^{0.08}$, with configurations representing $\sigma^2\pi^2\pi^{*2}$ making up 30.8% of the wavefunction. The change in ground state geometry, from triply to singly bound, can be un-

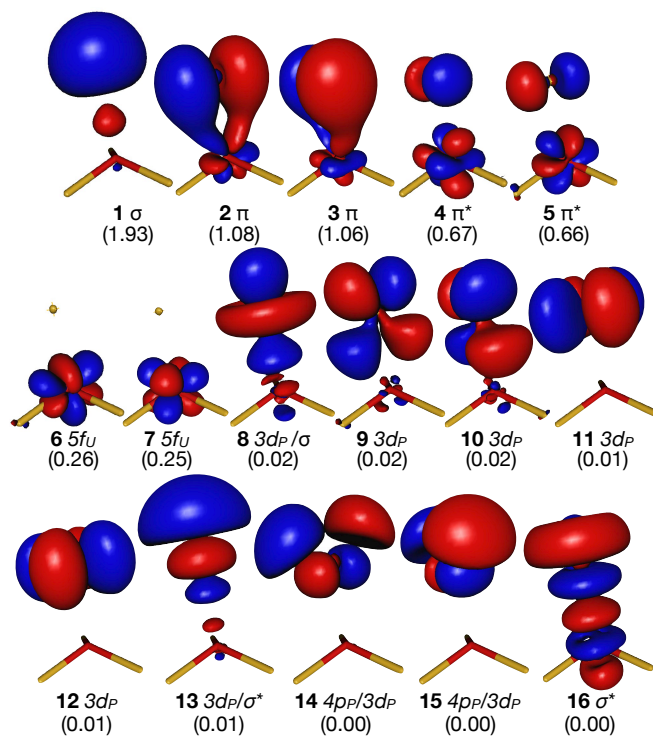


Fig. 2 The natural orbitals of the active space of PUF_3 ($^1A'$, CASPT2), shown at the 0.05 isosurface value. Occupancy number given in brackets.

derstood by the significant extent to which orbitals outside of this [6,6] active space are occupied. There are 0.52 electrons occupying nonbonding $5f_{\text{U}}$ orbitals, and 0.07 electrons in nonbonding $3d_{\text{P}}$. In the [6,6] active space, these electrons must occupy either the π bonding or antibonding orbitals, or the σ antibonding orbital, favouring the triple bonded electronic structure.[‡] The effective bond order $BO_{\text{eff}} = 1.35$ suggests either a single bond or a very weak double bond. The BCP ellipticity value (Table 2) strongly suggests a single bond assignment, and this is also supported by the delocalisation index $DI(\text{U}|\text{N}) = 0.79$. The latter metric is the Quantum Theory of Atoms-in-Molecules (QTAIM) measure of bond order.¹¹ In our systems, the delocalisation indices are rather lower than the formal bond orders, though that for the U-N bond is c. 2.6 times that for the U-P.

The $^1A'$ state was found to be the ground state, however, four other states ($^3A'$, $^3A''$, $^5A'$ and $^5A''$) were found to be within 0.07 eV of the ground state. For both the triplet and quintet multiplicities, the symmetric and antisymmetric wavefunction were close in energy, suggesting a slight distortion from an E symmetry C_{3v} state. The relative energies and orbital occupancies of the electronic states are summarised in Table S4 of the supplementary information. To establish if there are low-lying states of the same spatial and spin symmetry as the ground state, state-

[‡] Expanding the active space from [6,6] to [6,10] yields a geometry similar to the [6,16] calculation, though contains a mixture of U 5f-based, 6d-based, P 3p-based and 4d-based orbitals, i.e. it is not simply U 5f and P 3p in character. This suggests an active space larger than [6,10] is required.

Table 1 Key vibrational frequencies of NUF₃, PUF₃ and AsUF₃ (in cm⁻¹). Calculated frequencies are at the CASPT2 level of theory. Observed (obs.) frequencies, and those from the [6,6] active space are those calculated by Andrews *et al.*^{4,12}. Frequencies not observed in experimental spectra indicated by 'n.o.'.

	E-U stretch A ₁ /A'			U-F stretch A ₁ /A'			U-F stretch E/A'			U-F stretch E/A''		
	obs.	[6,16]	[6,6]	obs.	[6,16]	[6,6]	obs.	[6,16]	[6,6]	obs.	[6,16]	[6,6]
NUF ₃	938	928	921	613	630	634	540	547	548	533	546	548
PUF ₃	n.o.	239	404	581	592	619	536	544	560	542	530	560
AsUF ₃	n.o.	194	347	581,579	594	617	536,535	547	566	536,535	528	566

averaged CASSCF (SA-CASSCF) calculations were performed at the 1A' CASPT2 optimised geometry. Six states were identified within 0.5 eV, all of which had a similar bonding description. The occupation numbers of the state-averaged pseudo-natural orbitals were similar for each state; the σ occupation was 1.93 across all states, the occupation of the π orbitals varied between 1.96 and 2.06, and the occupation of largely 5f_U character orbitals, including the π^* orbitals, varied between 1.92 and 2.02. The relative energies and occupation numbers of the pseudo-natural orbitals of the SA-CASSCF calculation are shown in Table S19 of the supplementary information.

As with NUF₃, the frequency calculation of PUF₃ included two imaginary frequencies, though greater in magnitude at 46.1i cm⁻¹ and 50.1i cm⁻¹, likely as an artefact of the numerical frequency calculation, and/or due to the constraint to C_s symmetry. The argon matrix IR spectra obtained by Andrews *et al.* did not observe the P-U stretch, only the three U-F stretching frequencies.⁴ As such, there is no direct experimental evidence of the P≡U triple bond. The frequency calculation of the singly-bonded geometry (at the [6,16] CASPT2 level of theory) does, however, appear to have a better fit with the observed U-F stretching frequencies, as summarised in Table 1. However, a definite geometric assignment cannot be made for the single bonded geometry based on this improvement in fit, suggesting that the U-F stretching frequencies are not enough of a fingerprint to make unambiguous assignments of other parameters in the molecule.

Like PUF₃, a change in the description of the bonding is seen on increasing the size of the active space at the CASPT2 level of theory for AsUF₃; triply bonded for a [6,6] active space ($r(\text{As-U}) = 2.54 \text{ \AA}$ as calculated by Andrews *et al.*¹²) and singly bonded for a [6,16] active space CASPT2 calculation ($r(\text{As-U}) = 2.87 \text{ \AA}$). The CASPT2 global minimum was identified as a ¹A' state, with active space orbital occupancies of $\sigma^{1.94}\pi^{2.09}\pi^*1.335f_U^{0.57}4d_{As}^{0.07}$, giving an effective bond order of 1.34 (the isosurfaces of the active space natural orbitals are shown in Fig. 3). The configurations which represent $\sigma^2\pi^2\pi^{*2}$ make up 35.2% of the total wavefunction. Like PUF₃, the σ bond is highly polarised to phosphorus, and AsUF₃ continues the trend of worsening overlap in the π bonds down group 15. The QTAIM delocalisation index $DI(U|As) = 0.76$ (versus 0.79 for phosphorus) suggests, like phosphorus, a single bond with only slight weak π bonding character, as does the ϵ (Table 2).

Similarly to PUF₃, there are several low lying excited states of different wavefunction symmetry; ¹A', ³A', ³A'', ⁵A' and ⁵A'' are all within 0.06 eV of each other. Again, for the triplet and quintet multiplicities, the A' and A'' states are near degenerate suggesting a slight distortion from a doubly degenerate C_{3v} E-

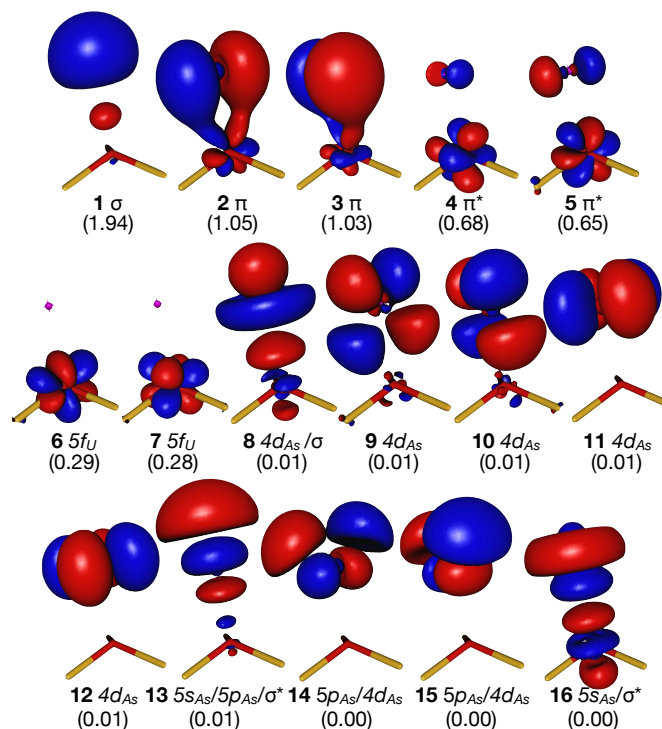


Fig. 3 The natural orbitals of the active space of AsUF₃ (¹A', CASPT2), shown at the 0.05 isosurface value. Occupancy number given in brackets.

symmetry state.

A CASPT2 frequency calculation on AsUF₃ resulted in a similar improvement to PUF₃, as shown in Table 1. However, three imaginary frequencies were observed, at 84.11i cm⁻¹, 69.44i cm⁻¹ and 32.62i cm⁻¹, and are possibly artefacts of the numerical frequency calculation or a result of the constraint to C_s symmetry. Again, the As-U stretch was not observed by Andrews *et al.*; only U-F stretches were. And, as before, we can not make geometric assignments from this improvement in fit.

Table 2 QTAIM delocalisation indices and atomic charges of NUF₃, PUF₃ and AsUF₃ in their CASPT2 ground state. *For $DI(U|F)$ and $q(F)$, the figures shown are averages.

	NUF ₃	PUF ₃	AsUF ₃
$DI(E U)$	2.037	0.787	0.758
$DI(U F)^*$	0.651	0.646	0.653
$q(U)$	+3.233	+2.977	+2.963
$q(E)$	-0.875	-0.580	-0.570
$q(F)^*$	-0.786	-0.799	-0.797
$\epsilon(E-U \text{ BCP})$	0.000	0.006	0.023

Despite the change in the pnictogen-uranium bonding environment, there is little change in the uranium-fluorine bonding of NUF_3 , PUF_3 and AsUF_3 . As shown in Fig. 1, the U-F bond length increases slightly from 2.045 Å in NUF_3 to 2.052 Å for PUF_3 and 2.051 Å for AsUF_3 . As Table 2 shows, the U|F delocalisation index and atomic charge of fluorine are essentially invariant from N to As; the change in atomic charge of uranium is almost entirely due to the change in the pnictogen.

For SbUF_3 and BiUF_3 , geometry optimisations have been performed at the CASSCF level of theory. For SbUF_3 the ground state is $^5A''$, with orbital occupancies of $\sigma^{1.94}\pi^{1.99}\pi^{*1.00}5f_U^{1.00}5d_{Sb}^{0.07}$. The ground state of BiUF_3 is $^1A'$, with orbital occupancies of $\sigma^{1.94}\pi^{2.16}\pi^{*1.58}5f_U^{0.24}6d_{Bi}^{0.08}$. The singlet, triplet and quintet, A' and A'' states lie within 0.02 eV and 0.04 eV of each other for SbUF_3 and BiUF_3 respectively. The CASSCF bonding description for both of the heavier pnictogens is consistent with that for PUF_3 and AsUF_3 at both the CASSCF and CASPT2 levels. On the basis of the CASSCF and CASPT2 optimisations of AsUF_3 and PUF_3 (as shown in Tables S12, S13, S15 and S16 of the supplementary information), we would expect a small contraction in the E-U bond length of about 0.1 Å at the CASPT2 level for SbUF_3 and BiUF_3 , but the ground state bonding description would be expected to be essentially unchanged.

The calculations presented are in contrast to those recently reported by Wang *et al.* on $[\text{EFe}(\text{CO})_3]^-$ (E = N-Bi), who found $\text{E}\equiv\text{Fe}$ triple bonds in all cases.¹⁴ They performed single-point CASSCF calculations whose wavefunctions were predominantly composed of a single configuration (c. 90% for E = As-Bi), in support of their closed-shell DFT calculations. This serves to highlight the impact of the many actinide valence orbitals in influencing their chemistry.

In summary, the calculations presented here support the previously published literature in finding a $\text{U}\equiv\text{N}$ triple bond in NUF_3 . However, for PUF_3 and AsUF_3 , the crucial role of the active space in CASSCF/CASPT2 calculations is highlighted, as for both molecules the bonding description differs on change from a [6,6] active space (*i.e.* the σ , π , π^* and σ^* orbitals), to [6,16], where nonbonding uranium f-orbitals and pnictogen d-orbitals have occupancies of about 0.50 and 0.07 respectively for both PUF_3 and AsUF_3 . Both PUF_3 and AsUF_3 , at the CASPT2 level of theory, are identified as having a polarised single σ bond with an essentially entirely broken π bond. Calculations at the CASSCF level of theory for SbUF_3 and BiUF_3 paint a largely similar picture, with the same single bonded geometry being observed. The plethora of closely-spaced excited states for the heavier pnictogen systems reflects the complexity of the electronic structure and highlights the importance of multiconfigurational methods. It is important to note that the effects of spin-orbit coupling (SOC) have not been accounted for in this work. Given the closely-spaced states found, it is very likely that a SOC-CASPT2 calculation would result in a large mixing of spin-orbit free states. However, as the bonding picture in all the low-lying states identified is essentially the same, spin-orbit coupling will not materially affect the principal conclusions of this work, *i.e.* that there is a significant reduction in the U-E bond order from E = N to E = P-Bi.

We are grateful to The University of Manchester for a PhD

studentship to B.E.A., a postdoctoral fellowship to H.-S.H., and for computational resources from the University's Computational Shared Facility. We also thank the Environmental Molecular Sciences Laboratory at the Pacific Northwest National Laboratory for a grant of computer time on the CASCADE facility (Proposal Number 49254).

Conflicts of interest

There are no conflicts to declare.

Notes and references

- 1 D. M. King and S. T. Liddle, *Coord. Chem. Rev.*, 2014, **266-267**, 2–15.
- 2 D. W. Green and G. T. Reedy, *J. Chem. Phys.*, 1976, **65**, 2921–2922.
- 3 X. Wang, L. Andrews, B. Vlaisavljevich and L. Gagliardi, *Inorg. Chem.*, 2011, **50**, 3826–3831.
- 4 L. Andrews, X. Wang, R. Lindh, B. O. Roos and C. J. Marsden, *Angew. Chem. Int. Ed.*, 2008, **47**, 5366–5370.
- 5 D. M. King, F. Tuna, E. J. McInnes, J. McMaster, W. Lewis, A. J. Blake and S. T. Liddle, *Nat. Chem.*, 2013, **5**, 482–488.
- 6 B. M. Gardner, G. Balázs, M. Scheer, F. Tuna, E. J. McInnes, J. McMaster, W. Lewis, A. J. Blake and S. T. Liddle, *Angew. Chem. Int. Ed.*, 2014, **53**, 4484–4488.
- 7 B. M. Gardner, G. Balázs, M. Scheer, F. Tuna, E. J. McInnes, J. McMaster, W. Lewis, A. J. Blake and S. T. Liddle, *Nat. Chem.*, 2015, **7**, 582–590.
- 8 B. O. Roos, P. R. Taylor and P. E. Sielaff, *Chem. Phys.*, 1980, **48**, 157–173.
- 9 H. J. Werner and P. J. Knowles, *J. Chem. Phys.*, 1985, **82**, 5053–5063.
- 10 K. Andersson, P. Å. Malmqvist, B. O. Roos, A. J. Sadlej and K. Wolinski, *J. Phys. Chem.*, 1990, **94**, 5483–5488.
- 11 C. F. Matta and R. J. Boyd, in *An Introduction to the Quantum Theory of Atoms in Molecules*, Wiley-Blackwell, 2007, ch. 1, pp. 1–34.
- 12 L. Andrews, X. Wang and B. O. Roos, *Inorg. Chem.*, 2009, **48**, 6594–6598.
- 13 T. A. Keith, *AIMAll (Version 17.11.14)*, 2017.
- 14 J.-Q. Wang, C. Chi, H.-S. Hu, L. Meng, M. Luo, J. Li and M. Zhou, *Angew. Chem. Int. Ed.*, 2018, **57**, 542–546.

Supplementary information

Computational Methodology

The def2-TZPP basis set¹ (obtained from the EMSL Basis Set Exchange^{2,3}) was used for all elements except uranium. The def2-TZPP basis set is all electron for F, N, P and As; for Sb, a 28 electron effective core potential (ECP) is used and for Bi a 60 electron ECP. For uranium, the 60-electron quasi-relativistic ECP of the Stuttgart/Cologne Group was used along with the associated atomic natural orbital basis set.^{4,5,6} Calculations were performed with Molpro version 2015.1,⁷ using the CASSCF program 'Multi',^{8,9} and the second-order multiconfigurational perturbation theory program 'rs2c'.¹⁰

Geometry optimisations at the CASSCF level of theory were performed for all molecules NUF₃-BiUF₃; geometry optimisations at the CASPT2 level of theory were performed for NUF₃, PUF₃ and AsUF₃. Geometry optimisations were first performed in C_s symmetry, but the optimised geometry of NUF₃ was approximately C_{3v}, and was re-optimised in that point group. CASPT2 geometry optimisations and harmonic frequency calculations were numerical, due to the lack of analytical gradients in the rs2c program. A level shift of 0.1 was applied for NUF₃, and 0.3 for PUF₃ and AsUF₃ (unless otherwise noted in the SI). Wavefunctions were calculated in C_s symmetry (regardless of the point group of the geometry optimisation) with both space-symmetric and antisymmetric wavefunctions optimised at the singlet, triplet and quintet multiplicities--the effects of spin-orbit coupling were not taken into account.

Quantum Theory of Atoms-in-Molecules (QTAIM)¹¹ analyses were performed with AIMALL,¹² using .wfx files generated by the Molden2AIM program.¹³

Calculated states of EUF₃ at CASSCF (E = N...Bi) and CASPT2 (E = N, P, As) levels of theory. A [6,16] active space is used in all cases. All states are geometrically optimised. Electronic energy relative to the global minimum, electronic energy, natural orbital occupancies, effective bond orders and E-U bond lengths (in ångstrom) given.

Electronic States

Table S1: **NUF₃ CASSCF/def2-TZVPP (N, F), SDD (U)**, optimised geometry

	$\Delta E_{el} / eV$	E_{el} / Ha	σ	π	π^*	σ^*	$f(n.b)$	BO_{eff}	$r(N-U) / \text{\AA}$
$^1A'$	0.000	-828.483	1.901	3.805	0.166	0.087	0.000	2.727	1.750
$^3A''$	1.903	-828.413	0.970	3.774	0.194	0.029	0.999	2.260	1.926
$^1A''$	1.953	-828.411	0.976	3.717	0.251	0.020	1.000	2.211	1.962
$^3A'$	2.035	-828.408	1.863	2.849	0.134	0.123	0.993	2.227	1.984
$^5A'$	2.128	-828.405	1.959	1.982	0.000	0.026	1.998	1.957	2.327
$^5A''$	2.576	-828.388	0.991	2.943	0.289	0.000	1.714	1.822	2.221

Table S2: **NUF₃ CASPT2/def2-TZVPP (N, F), SDD (U)**, optimised geometry, level shift = 0.1

	$\Delta E_{el} / eV$	E_{el} / Ha	σ	π	π^*	σ^*	$f(n.b)$	BO_{eff}	$r(N-U) / \text{\AA}$
$^1A'$	0.000	-829.754	1.903	3.809	0.161	0.086	0.000	2.733	1.753
$^3A''^*$	1.602	-829.695	0.970	3.800	0.160	0.030	1.000	2.290	1.886
$^3A'$	1.987	-829.681	1.872	1.862	1.111	0.124	0.992	1.249	1.990
$^1A''^o$	2.087	-829.678	0.976	3.752	0.216	0.022	0.998	2.245	1.926
$^5A''^*$	2.598	-829.659	1.960	1.985	0.302	0.017	1.699	1.813	2.286
$^5A'^*$	2.614	-829.658	1.960	1.985	1.564	0.017	0.437	1.182	2.278

*level shift = 0.2 °level shift = 0.5

Table S3: **PUF₃ CASSCF/def2-TZVPP (P, F), SDD (U)**, optimised geometry

	$\Delta E_{el} / eV$	E_{el} / Ha	σ	π	π^*	σ^*	$f(n.b)$	BO_{eff}	$r(P-U) / \text{\AA}$
$^1A'$	0.000	-1114.714	1.932	2.198	1.533	0.017	0.253	1.290	2.855
$^5A''$	0.014	-1114.714	1.931	1.982	1.347	0.018	0.653	1.274	2.883
$^3A'$	0.024	-1114.713	1.932	2.031	1.492	0.017	0.460	1.226	2.879
$^1A''$	0.100	-1114.710	1.931	1.173	1.808	0.017	1.000	0.639	2.873
$^3A''$	0.166	-1114.708	1.940	2.008	0.971	0.021	1.000	1.478	2.860
$^5A'$	0.184	-1114.707	1.942	1.979	1.533	0.018	0.467	1.184	2.865

Table S4: **PUF₃ CASPT2/def2-TZVPP** (P, F), SDD (U), optimised geometry, level shift = 0.3

	$\Delta E_{el} / eV$	E_{el} / Ha	σ	π	π^*	σ^*	$f(n.b)$	BO_{eff}	$r(P-U) / \text{\AA}$
$^1A'$	0.000	-1115.949	1.931	2.141	1.333	0.0167	0.510	1.362	2.743
$^3A''$	0.031	-1115.948	1.931	2.012	0.971	0.0171	1.000	1.478	2.770
$^3A'$	0.034	-1115.948	1.931	2.025	0.961	0.0072	0.998	1.494	2.771
$^5A''$	0.063	-1115.947	1.931	1.982	0.312	0.0177	1.688	1.792	2.800
$^5A'$	0.068	-1115.947	1.931	1.982	0.784	0.0177	1.216	1.556	2.796
$^1A''$	0.229	-1115.941	1.931	2.193	0.788	0.017	1.000	1.659	2.771

Table S5: **AsUF₃ CASSCF/def2-TZVPP** (As, F), SDD (U), optimised geometry

	$\Delta E_{el} / eV$	E_{el} / Ha	σ	π	π^*	σ^*	$f(n.b)$	BO_{eff}	$r(As-U) / \text{\AA}$
$^5A''$	0.000	-3008.183	1.943	1.985	0.327	0.015	1.673	1.793	2.999
$^5A'$	0.002	-3008.183	1.943	1.985	0.505	0.015	1.496	1.704	2.996
$^3A'$	0.007	-3008.183	1.943	2.014	1.440	0.015	0.532	1.251	2.996
$^3A''$	0.014	-3008.182	1.943	2.000	0.986	0.015	1.000	1.471	3.001
$^1A'$	0.080	-3008.180	1.943	2.305	1.674	0.023	0.000	1.275	2.951
$^1A''$	0.296	-3008.172	1.946	1.129	0.861	0.021	1.990	1.096	2.973

Table S6: **AsUF₃ CASPT2/def2-TZVPP** (As, F), SDD (U), optimised geometry, level shift = 0.3

	$\Delta E_{el} / eV$	E_{el} / Ha	σ	π	π^*	σ^*	$f(n.b)$	BO_{eff}	$r(As-U) / \text{\AA}$
$^1A'$	0.000	-3009.364	1.943	2.085	1.334	0.014	0.567	1.340	2.871
$^3A''$	0.022	-3009.363	1.943	2.009	0.977	0.014	1.000	1.480	2.893
$^3A'$	0.039	-3009.362	1.943	2.020	1.310	0.010	0.655	1.321	2.901
$^5A''$	0.042	-3009.362	1.943	1.985	0.315	0.015	1.686	1.799	2.910
$^5A'$	0.053	-3009.362	1.943	1.985	0.503	0.010	1.498	1.708	2.905
$^1A''^*$	0.306	-3009.353	1.943	2.028	0.958	0.014	1.000	1.500	2.890

*level shift = 0.5

Table S7: **SbUF₃** CASSCF/def2-TZVPP (Sb, F), SDD (U), optimised geometry

	$\Delta E_{el} / eV$	E_{el} / Ha	σ	π	π^*	σ^*	$f(n.b)$	BO_{eff}	$r(Sb-U) / \text{\AA}$
$^5A''$	0.000	-1013.252	1.943	1.985	1.000	0.016	1.000	1.456	3.220
$^5A'$	0.001	-1013.252	1.943	1.985	1.000	0.016	1.000	1.456	3.219
$^1A'$	0.008	-1013.251	1.943	2.131	1.608	0.015	0.246	1.225	3.208
$^3A'$	0.010	-1013.251	1.943	2.004	1.702	0.015	0.279	1.115	3.221
$^3A''$	0.014	-1013.251	1.943	1.995	1.000	0.015	0.990	1.462	3.225
$^1A''$	0.096	-1013.248	1.942	2.128	0.855	0.016	1.000	1.600	3.220

Table S8: **BiUF₃** CASSCF/def2-TZVPP (As, F), SDD (U), optimised geometry

	$\Delta E_{el} / eV$	E_{el} / Ha	σ	π	π^*	σ^*	$f(n.b)$	BO_{eff}	$r(Bi-U) / \text{\AA}$
$^1A'$	0.000	-987.556	1.937	2.164	1.574	0.030	0.242	1.248	3.277
$^1A''$	0.023	-987.555	1.938	2.009	1.232	0.029	0.740	1.343	3.282
$^3A'$	0.027	-987.555	1.939	2.012	1.479	0.027	0.489	1.223	3.261
$^3A''$	0.033	-987.554	1.939	1.995	1.255	0.027	0.730	1.326	3.282
$^5A''$	0.041	-987.554	1.943	1.979	1.372	0.023	0.628	1.263	3.276
$^5A'$	0.042	-987.554	1.943	1.979	1.507	0.024	0.493	1.196	3.274

Frequency Calculations ([6,16] CASPT2)

Table S9: Frequency calculations at the CASPT2 level of theory. Frequency calculations are numerical, and performed without wavefunction symmetry. Frequencies given in cm⁻¹

	$U-E$ <i>stretch</i> a_1/a'	$U-F$ <i>stretch</i> a_1/a'	$U-F$ <i>stretch</i> e/a'	$U-F$ <i>stretch</i> e/a''	$U-F$ <i>bend</i> a_1/a'	$U-F$ <i>bend</i> e/a'	$U-F$ <i>bend</i> e/a''	$E-U-F$ <i>bend</i> e/a'	$E-U-F$ <i>bend</i> e/a''	#imag. freq.
$NUF_3 \ ^1A_1$	928.44	630.44	546.75	546.18	144.48	138.88	138.80	9.52i	0.73i	2
$PUF_3 \ ^1A'$	260.22	591.61	544.10	530.44	107.69	5.53	100.00	50.09i	46.08i	2
$AsUF_3 \ ^1A'$	193.65	594.34	546.79	528.13	107.85	32.62i	91.73	84.11i	69.44i	3

Optimised Geometries

Z matrix variables of the optimised geometries are given in ångstrom for bond lengths and degrees for angles. Z-matrix all of the form:

U,
E, U, B1,
F1, U, B2, E, A1,
F2, U, B3, E, A2, F1, D1, 0,
F3, U, B3, E, A2, F1, -D1, 0,

Table S10: **NUF₃ CASSCF [6,16]** optimised geometries

	${}^1A'$	${}^1A''$	${}^3A'$	${}^3A''$	${}^5A'$	${}^5A''$
$B1/\text{\AA}$	1.74966363	1.96207590	1.98376709	1.92583599	2.32732023	2.22068830
$B2/\text{\AA}$	2.06247224	2.07064231	2.06034721	2.06169677	2.06327373	2.06528070
$B3/\text{\AA}$	119.26670015	117.53550905	119.97127633	123.22698633	113.12592329	105.03934627
$A1/^\circ$	2.06248584	2.07057741	2.07937513	2.07464437	2.06518285	2.06760061
$A2/^\circ$	119.31825159	117.68409939	109.11952786	114.19898228	104.62218407	111.79501377
$DI/^\circ$	119.98346235	119.99151795	115.59685227	120.33368540	117.22853506	120.44948587

Table S11: **NUF₃ CASPT2 [6,16]** optimised geometries

	${}^1A'$	${}^1A''$	${}^3A'$	${}^3A''$	${}^5A'$	${}^5A''$
$B1/\text{\AA}$	1.75315792	1.92604004	1.99004607	1.88435033	2.27835083	2.28650344
$B2/\text{\AA}$	2.04485854	2.05302879	2.04665842	2.03788217	2.05331815	2.05374786
$B3/\text{\AA}$	2.04485854	2.04921027	2.06635945	2.06054510	2.05942704	2.05624541
$A1/^\circ$	122.58314996	99.04872772	121.25316610	141.90245469	103.52253600	109.92919824
$A2/^\circ$	122.58314996	127.45327165	107.87668701	107.35099811	106.45590828	104.58243365
$DI/^\circ$	119.97200364	113.23606871	114.30883104	124.78557197	116.13020533	122.95979828

Table S12: **PUF₃ CASSCF [6,16]** optimised geometries

	${}^1A'$	${}^1A''$	${}^3A'$	${}^3A''$	${}^5A'$	${}^5A''$
$B1/\text{\AA}$	2.85487233	2.87307254	2.87898686	2.86018471	2.86483680	2.88262101
$B2/\text{\AA}$	2.06330151	2.06754338	2.05713816	2.05488434	2.05870044	2.05577362
$B3/\text{\AA}$	2.06329881	2.05661772	2.06312145	2.06274954	2.06042015	2.06202954
$A1/^\circ$	108.08441646	106.12601358	108.25828906	107.67882184	107.50633008	109.81992138
$A2/^\circ$	108.07221905	109.18338207	107.83836643	108.02790589	107.50986207	107.03349551
$DI/^\circ$	119.98188899	119.91887086	122.26806489	122.39787190	116.46055934	122.65750282

Table S13: **PUF₃ CASPT2 [6,16]** optimised geometries

	${}^1A'$	${}^1A''$	${}^3A'$	${}^3A''$	${}^5A'$	${}^5A''$
$B1/\text{\AA}$	2.74344624	2.77127150	2.78567990	2.76986521	2.79582952	2.79991948
$B2/\text{\AA}$	2.04944358	2.05392432	2.04084123	2.04419397	2.04532166	2.04437239
$B3/\text{\AA}$	2.05246669	2.04555281	2.05383880	2.05142110	2.05020489	2.04899668
$A1/^\circ$	105.10446315	103.45650116	105.79445974	105.19041589	108.15012735	109.83601344
$A2/^\circ$	104.97744266	109.10153060	104.84078912	106.76007393	105.47665484	105.47531864
$DI/^\circ$	111.74179511	119.29915794	125.39655946	123.15852805	123.49864932	123.22404395

Table S14: **PUF₃ CASPT2 [6,6]** optimised geometry

	¹ A'
<i>B1</i> / Å	2.44583209
<i>B2</i> / Å	2.03441332
<i>B3</i> / Å	2.03441332
<i>A1</i> / °	120.58416314
<i>A2</i> / °	120.58416314
<i>D1</i> / °	120.00000000

Table S15: **AsUF₃ CASSCF [6,16]** optimised geometries

	¹ A'	¹ A''	³ A'	³ A''	⁵ A'	⁵ A''
<i>B1</i> / Å	2.95095386	2.97344563	2.99638316	3.00106915	2.99639075	2.99898403
<i>B2</i> / Å	2.05856220	2.05443031	2.05806991	2.05269929	2.05760834	2.05360612
<i>B3</i> / Å	2.05858915	2.06531671	2.05900099	2.06069238	2.05928422	2.05996764
<i>A1</i> / °	109.10003689	108.87121501	109.31699988	108.62761259	108.18297141	110.03184374
<i>A2</i> / °	109.07630568	108.75416391	107.07313858	107.88872382	107.19792721	107.34404512
<i>D1</i> / °	119.96581826	123.88872103	115.85400273	122.63188038	115.93625359	122.65071001

Table S16: **AsUF₃ CASPT2 [6,16]** optimised geometries

	¹ A'	¹ A''	³ A'	³ A''	⁵ A'	⁵ A''
<i>B1</i> / Å	2.87103834	2.89019864	2.90714091	2.89300332	2.90458440	2.91016953
<i>B2</i> / Å	2.04893379	2.04300197	2.04081681	2.04339804	2.04624629	2.04341232
<i>B3</i> / Å	2.05169932	2.04990351	2.04656500	2.05069225	2.05130089	2.04884815
<i>A1</i> / °	105.31355176	105.26257931	110.27643340	105.97650475	104.97318200	110.04834229
<i>A2</i> / °	105.38649558	107.04913704	105.18514065	106.70908361	105.91751855	105.64739257
<i>D1</i> / °	112.10479959	123.07590962	115.08441516	123.29710737	113.39243801	123.29995138

Table S17: **SbUF₃ CASSCF [6,16]** optimised geometries

	¹ A'	¹ A''	³ A'	³ A''	⁵ A'	⁵ A''
<i>B1</i> / Å	3.20816964	3.21966056	3.22119937	3.22533659	3.21908393	3.22033463
<i>B2</i> / Å	2.05773287	2.06274178	2.05507969	2.04979538	2.05488595	2.05060653
<i>B3</i> / Å	2.05767308	2.05136075	2.05627145	2.05782646	2.05661818	2.05747406
<i>A1</i> / °	108.63503163	107.45328614	109.48034612	109.06850427	108.55017177	110.18561632
<i>A2</i> / °	108.58549558	109.17680721	107.38137318	108.19846413	107.59897703	107.78332464
<i>D1</i> / °	120.05135064	120.23443643	115.69668696	122.61913254	115.82500088	122.64493084

Table S18: **BiUF₃ CASSCF [6,16]** optimised geometries

	¹ A'	¹ A''	³ A'	³ A''	⁵ A'	⁵ A''
<i>B1</i> / Å	3.26067651	3.28187390	3.27730259	3.28142156	3.27416886	3.27630339
<i>B2</i> / Å	2.06026239	2.05271034	2.05774247	2.05213107	2.05670185	2.05249744
<i>B3</i> / Å	2.06024022	2.06002321	2.05815706	2.05994190	2.05826193	2.05909817
<i>A1</i> / °	108.50661518	107.76367729	109.23817717	108.46948235	108.10335375	110.11807776
<i>A2</i> / °	108.44222008	108.33175721	107.51542263	108.19084219	107.87322869	107.84112289
<i>D1</i> / °	120.01642730	122.32915801	116.58485815	122.44965955	116.19337716	122.55055062

Table S19: **PUF₃ SA-CASSCF [6,16]** pseudo-natural orbital occupancies for each state, electronic energies and relative energies. All states ¹A' symmetry, performed at the CASPT2 optimised geometry.

State	A'										A''						<i>5f_U</i> + <i>π</i> *	<i>Eel</i> / Ha	<i>ΔE</i> / eV
	<i>σ</i>	<i>π</i>	<i>π</i> *	<i>5f_U</i>	<i>5f_U</i>	<i>5f_U</i>	<i>3d_P</i>	<i>3d_P</i>	<i>3d_P</i>	<i>3d_P</i>	<i>π</i>	<i>f</i>	<i>π</i> *	<i>5f_U</i>	<i>3d_P</i>	<i>3d_P</i>			
1	1.93	1.03	0.55	0.40	0.01	0.00	0.02	0.02	0.01	0.00	1.03	0.51	0.44	0.02	0.01	0.01	1.92	-1114.701	0.00
2	1.93	1.02	0.45	0.51	0.01	0.00	0.02	0.02	0.01	0.00	1.01	0.54	0.41	0.02	0.01	0.01	1.95	-1114.701	0.01
3	1.93	0.99	0.21	0.34	0.31	0.14	0.02	0.02	0.01	0.00	1.02	0.41	0.53	0.04	0.01	0.01	1.98	-1114.694	0.19
4	1.93	1.03	0.22	0.44	0.10	0.19	0.02	0.02	0.01	0.00	1.02	0.13	0.38	0.46	0.01	0.01	1.93	-1114.689	0.33
5	1.93	1.02	0.44	0.04	0.44	0.05	0.02	0.02	0.01	0.00	1.02	0.19	0.31	0.47	0.01	0.01	1.95	-1114.687	0.40
6	1.93	0.98	0.15	0.25	0.26	0.35	0.02	0.01	0.01	0.00	0.98	0.53	0.09	0.40	0.01	0.01	2.02	-1114.685	0.45

References

- 1 F. Weigend and R. Ahlrichs, *Phys. Chem. Chem. Phys.*, 2005, **7**, 3297.
- 2 D. Feller, *J. Comput. Chem.*, 1996, **17**, 1571–1586.
- 3 K. L. Schuchardt, B. T. Didier, T. Elsethagen, L. Sun, V. Gurumoorthi, J. Chase, J. Li and T. L. Windus, *J. Chem. Inf. Model.*, 2007, **47**, 1045–1052.
- 4 X. Cao, M. Dolg and H. Stoll, *J. Chem. Phys.*, 2003, **118**, 487–496.
- 5 X. Cao and M. Dolg, *THEOCHEM*, 2004, **673**, 203–209.
- 6 W. Küchle, M. Dolg, H. Stoll and H. Preuss, *J. Chem. Phys.*, 1994, **100**, 7535–7542.
- 7 H.-J. Werner, P. J. Knowles, G. Knizia, F. R. Manby, M. Schütz *et al.*, *MOLPRO, version 2015.1*, 2015.
- 8 P. J. Knowles and H. J. Werner, *Chem. Phys. Letters*, 1985, **115**, 259–267.
- 9 H. J. Werner and P. J. Knowles, *J. Chem. Phys.*, 1985, **82**, 5053–5063.
- 10 P. Celani and H. J. Werner, *J. Chem. Phys.*, 2000, **112**, 5546–5557.
- 11 R. F. Bader, *Atoms in molecules: a quantum theory*, Clarendon Pr., 1990.
- 12 O. P. K. U. Todd A. Keith, TK Gristmill Software, *AIMAll (Version 17.11.14)*, 2017.
- 13 W. Zou, D. Nori-Shargh and J. E. Boggs, *J. Phys. Chem. A*, 2013, **117**, 207–212.

High oxidation state electron-poor metal-to-ligand backbonding in a crystalline uranium(V)-dinitrogen complex

Erli Lu, **Benjamin E. Atkinson**, Ashley J. Wooles, Josef T. Boronski, Laurence R. Doyle, Floriana Tuna, Jonathan D. Cryer, Philip J. Cobb, Inigo J. Vitorica-Yrezabal, George F. S. Whitehead, Nikolas Kaltsoyannis & Stephen T. Liddle, *Nat. Chem.*, 2019, **11**, 806–811, <https://doi.org/10.1038/s41557-019-0306-x>

This introduction includes aspects of the paper and supplementary information to summarise my contribution to this work.

Neutral π -acceptor ligands such as N_2 and CO are a common feature of coordination chemistry. Blyholder first described the molecular orbital description of its binding mechanism for CO; donation from the σ HOMO of CO into an unoccupied metal d orbital, and back-donation of a π symmetry d orbital into the unoccupied CO π^* orbital.¹¹⁸ This bonding mechanism favours low oxidation state metal centres, being sufficiently electron rich to back-donate and radially extended to overlap effectively with the ligand.

The uranium(V)-dinitrogen complex identified in this work, shown in Figure 4.1, was

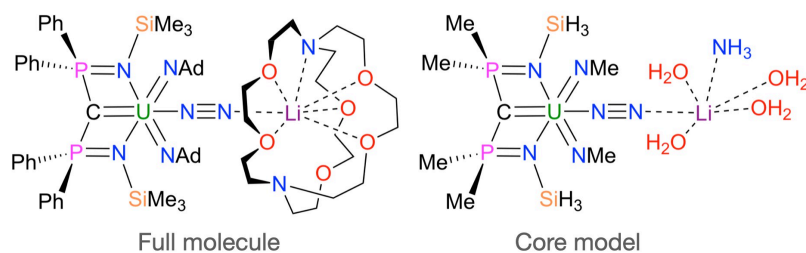


Figure 4.1: The structure of the U(V)–N₂ complex identified in this work (left), and the structure of the core model used in post-Hartree Fock calculations (right).

synthesised by Erli Lu and coworkers in the Liddle group at the University of Manchester. It is an unusual example of dinitrogen end-on coordinated to an electron poor U(V) centre. This is possible due to the coordination environment which makes the U(V) centre unusually electron rich. DFT, NBO and QTAIM calculations (performed by S. Liddle) confirm the presence of a weak U–N₂ π backbond, however the U–N₂ bond length is long at 2.60 Å. NBO gives a single bonding U–N orbital with 31% U character, and 69% N. QTAIM gives $\varepsilon(r) = 0.39$, confirming presence of single pi backbond. But a geometry optimisation with the PBE functional gives a U–N₂ bond length of 2.39 Å.

I performed calculations at varying levels of theory to account for this discrepancy. I performed potential energy surface scans along the U1–N1 vector, both on the full molecule and on a simplified model, shown on the right in Figure 4.1 (full computational methodology is given in the Supplementary Information). A full geometry optimization was performed with UPBE, giving a U1–N1 bond distance of 2.393 Å. From this geometry, a relaxed potential energy scan was performed whereby the U1–N1 bond distance was increased in steps of 0.050 Å, to 2.743 Å, and decreased to 2.293 Å. At each point, all other geometric parameters were optimized. This is shown in Fig. 4 of the main text as ‘Relaxed / UPBE’.

In addition, rigid potential energy scans were performed, where the N₂[Li(2,2,2–cryptand)] fragment was displaced from the crystal structure geometry in the U1–N1 axis, with UPBE and RHF (XRD / UPBE, RHF respectively in Fig. 4). The RHF scan has its minimum at 2.50 Å; in better agreement with experiment than the UPBE calculations but still some 0.1 Å away from

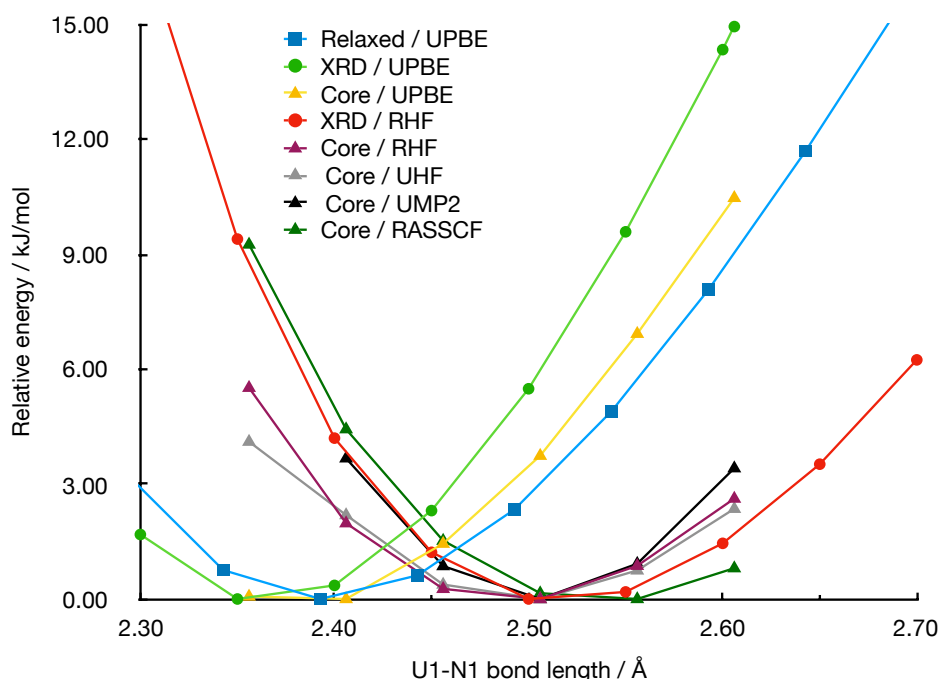


Figure 4.2: Relative energy (kJ mol^{-1}) vs U1-N1 distance (\AA). ‘XRD’ and ‘Relaxed’ calculations are on the full molecule **2**; ‘Core’ is the model shown in Figure 4.1 (**2 core**). All scans are rigid, i.e. in which all geometric parameters other than the U1-N1 distance are frozen, except the Relaxed / UPBE scan, in which other geometric parameters are optimised at each point.

the crystal structure geometry.

Further to this, calculations were performed on a ‘core’ model, **2 core**, shown in Figure 4.1. From the crystal structure geometry, phenyl and adamantyl groups were replaced with methyl groups. SiMe_3 was replaced with SiH_3 , and only coordinating atoms of the cryptands were kept, with hydrogens added to balance charges. Hydrogen geometries were optimised at each geometry, at the restricted HF level of theory, with other atoms being kept at their crystal structure coordinates. The U1-N1 bond length was shortened in 0.05 \AA increments, from the crystal structure geometry, 2.608 \AA , to 2.358 \AA , with the $\text{N}_2\text{Li}(\text{H}_2\text{O})_4\text{NH}_3$ fragment being translated in the U1-N1 axis. The UPBE and RHF scans on this core geometry suggest that this model is a good representation of the full molecule; the slightly shallower potential at shorter bond lengths in the RHF scans is likely a result of the reduction in steric bulk. The introduction of dynamic correlation at the UMP2 level of theory (based on a UHF reference) results in a slightly steeper potential, compared with the UHF scan but an unchanged minimum

point (at the 0.05 Å resolution of these scans).

RASSCF calculations on the core model were also performed. An ideal active space would conceivably include all bonding and antibonding orbitals in the uranium coordination sphere; this would be a [25,25] CASSCF calculation (the 2 U–N_{imido} σ, 4 U–N_{imido} π, 2 U–N_{amide} σ, 2 U–N_{amide} π, the C–U σ and π bonding orbitals, the corresponding antibonding orbitals, and the N₂ π* SOMO). This is however intractably large, so we performed a single initial RASSCF [17,17] calculation including only the π orbitals, and where all 114 non-active orbitals were frozen at the RHF reference.

The only orbitals to show significant static correlation (antibonding orbitals with occupancy numbers >0.02) were the U–N_{imido} π orbitals, so this is the active space we employed in the potential energy scans; 9 electrons in 9 active orbitals. We used the conventional three active space formalism; RAS1 includes the 4 U–N_{imido} π bonding orbitals, RAS2 includes N₂ π* SOMO, and RAS3 contains the 4 U–N_{imido} π* antibonding orbitals. Double excitations are allowed out of RAS1, and triple excitations into RAS3. This corresponds to (9,2,3;4,1,4) in the conventional Sauri notation.¹⁶ A RHF reference was used, and 78 orbitals frozen at this reference.

The natural orbitals of the active space and their occupation numbers at the minimum energy point on the scan, 2.56 Å, are shown in Figure 4.3, and their occupation numbers at each point are shown in Table S1. As Figure 4.2 shows, the points at 2.51 Å, 2.56 Å and 2.61 Å are very close in energy; 2.51 Å is 0.15 and 2.61 Å is 0.80 kJ mol⁻¹ higher in energy than the minimum 2.56 Å. Introduction of more correlation energy with a larger active space, the increased steric bulk of the full molecule, or crystal packing forces could all shift the minimum to that of the crystal structure geometry—or indeed a combination of the three.

Calculations at higher levels of theory (MP2, RASSCF) give a longer U1–N₂ bond length, closer to that observed in the crystal structure compared to DFT calculations. Scans at all

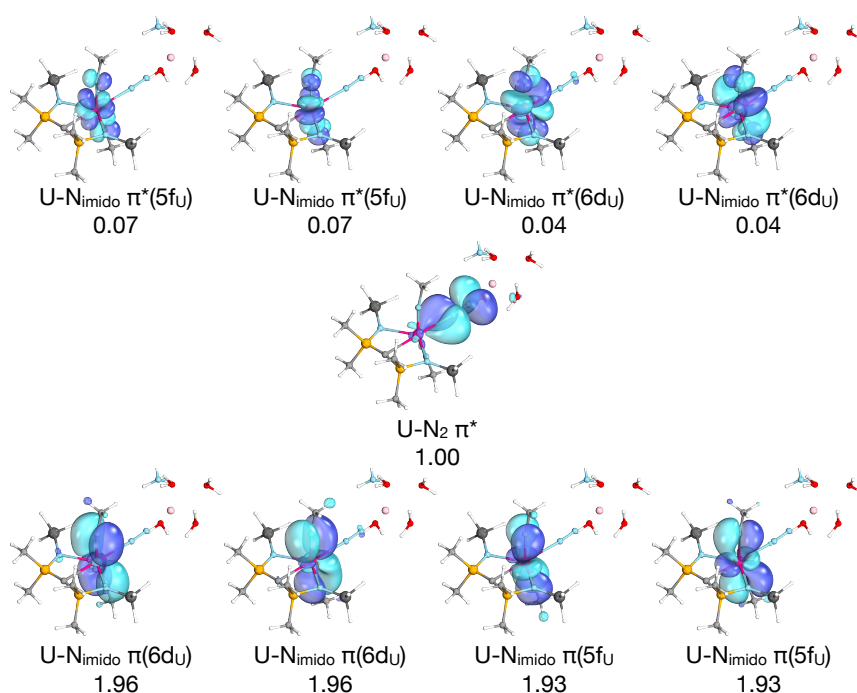


Figure 4.3: The natural orbitals of the RASSCF calculation on 2 core at $U1-N1 = 2.56 \text{ \AA}$, the minimum energy point on the scan. Bottom row: RAS1, middle: RAS2, top: RAS3. The isosurfaces enclose 90% of the orbital electron density. Occupation numbers are shown in Table S1

levels of theory demonstrate that the potential is very shallow, reflecting the weakness of the bond between N_2 , a poor π acceptor, and the $U(V)$ centre. Because the potential is so shallow, a small discrepancy in the energetics of the DFT potential results in a large difference in bond length compared to that observed in the crystal structure.

Contribution statement

I performed energy-scan calculations and analysed the results, with input and feedback from N.K. I performed rigid and relaxed energy scan calculations at the DFT and HF levels of theory, and derived a model of the complex to reduce computational cost, and tested its validity at the DFT and HF level. I performed MP2 and RASSCF calculations on this model. E.L. and J.T.B. prepared and characterised the compound and its precursors. E.L., A.J.W., I.J.V.-Y. and G.F.S.W. collected, solved, refined and analysed the crystallographic data. E.L., L.R.D., J.D.C. and P.J.C. recorded and interpreted the Raman data. F.T. recorded and interpreted the EPR data. S.T.L. originated the central idea, supervised the work, analysed the data, performed the

DFT, NBO and QTAIM calculations and analysed the results, and wrote the manuscript with contributions from all the authors.

For brevity, cartesian coordinates are removed from the included version of the supplementary information and are available online at <https://doi.org/10.1038/s41557-019-0306-x>.

Back-bonding between an electron-poor, high-oxidation-state metal and poor π -acceptor ligand in a uranium(V)–dinitrogen complex

Erli Lu, Benjamin E. Atkinson, Ashley J. Wooles, Josef T. Boronski, Laurence R. Doyle, Floriana Tuna, Jonathan D. Cryer, Philip J. Cobb, Inigo J. Vitorica-Yrezabal, George F. S. Whitehead, Nikolas Kaltsoyannis, and Stephen T. Liddle*

School of Chemistry, The University of Manchester, Oxford Road, Manchester, M13 9PL, UK.

*Email: steve.liddle@manchester.ac.uk

Abstract

A fundamental bonding model in coordination and organometallic chemistry is the synergic, donor–acceptor interaction between a metal and a neutral π -acceptor ligand where the ligand σ -donates to the metal, which π -back-bonds to the ligand. This interaction typically involves a metal with an electron-rich, mid-, low-, or even negative, oxidation state and a ligand with a π^ orbital. Here, we report that treatment of a uranium–carbene complex with an organo-azide produces a uranium(V)–bis(imido)–dinitrogen complex, stabilised by a lithium counter-ion. This complex, which has been isolated in crystalline form, involves an electron-poor, high-oxidation-state uranium(V) $5f^1$ ion that is π -back-bonded to the poor π -acceptor ligand dinitrogen. We propose that this is made possible by a combination of cooperative heterobimetallic uranium–lithium effects and the presence of suitable ancillary ligands rendering the uranium ion unusually electron-rich. This electron-poor back-bonding could have implications for the field of dinitrogen activation.*

Introduction

In coordination and organometallic chemistry, a well-established fundamental bonding model is that neutral π -acceptor ligands, such as isoelectronic dinitrogen (N_2) and carbon monoxide (CO), can ligate end-on to metals in a synergic donor-acceptor interaction.¹ In this classical bonding model σ -donation from the ligand lone pair to the metal is complemented by metal π -back-bonding to a formally vacant π^* acceptor molecular orbital of the ligand resulting in weak ligand activation, Fig. 1. It naturally follows that a key requirement of metal-to-ligand back-bonding is that the metal must be in a medium to low, or even negative, formal oxidation state so that it is sufficiently electron-rich to possess the requisite valence electrons for back-bonding. An inherent consequence of this scenario is that a low oxidation state metal centre will exhibit more radially extended valence orbitals compared to higher oxidation states, thus enabling effective spatial overlap with the ligand π^* orbitals. Thus, a high oxidation state and electron-poor metal is usually inherently ill-suited, if not incapable, of engaging in π -back-bonding to π -acceptor ligands.

For N_2 complexes, although $[U(N)_2(N_2)_n]$ ($n = 1-5$) species formally containing uranium in oxidation state +VI have been spectroscopically detected when trapped under cryogenic matrix isolation conditions,^{2,3} no classical molecular N_2 -complex isolable on macroscopic scale is known above a metal oxidation state of +III, otherwise strong activation to give reduced N_2^{n-} ($n = 2, 4$) with high oxidation state metals occurs.^{3,4} CO is a better π -acceptor ligand than N_2 , so metal oxidation state +IV but electron-rich carbonyl anions such as $[PtCl_5(CO)]^{1-}$, $[OsF_5(CO)]^{1-}$, $[OsCl_5(CO)]^{1-}$ are known,⁵⁻⁷ yet despite the fact these M(IV) ions are electron-rich they are exceedingly rare and only the latter is structurally authenticated.⁷ Transient or matrix isolation-trapped M(IV) $[M(O)_2(CO)_n]$ ($M = Rh, n = 1$; $M = Mo, W, n = 4$) species have been detected spectroscopically,^{8,9} and the formally +VI osmium dication $[OsO_2(CO)_4]^{2+}$ has been reported, but was too unstable to be isolated and fully characterised.¹⁰ Very recently the Fe(IV) dication $[Fe(\eta^5-C_5Me_5)_2(CO)]^{2+}$ was structurally authenticated,¹¹ but is stabilised via C_5Me_5 -to-CO ligand-to-ligand

π -back-bonding. This bonding type is a departure from the classical model, and appears to be unique to metallocene complexes, being similarly proposed for d^0 M(IV) $[M(\eta^5\text{-C}_5\text{Me}_5)_2(\text{H})_2(\text{CO})]$ (M = Zr, Hf) species detected spectroscopically at low temperature.^{12,13} In summary, all the species discussed in this paragraph are, despite their high oxidation states, either d-electron rich, kinetically trapped at low temperatures, or utilise ligand-to-ligand not metal-to-ligand back-bonding, and they represent quite different bonding situations to non-classical, cationic carbonyl complexes where the M-CO σ -bonding component dominates the bonding picture with little or no π -back-bonding contributions.^{14,15}

For early actinides, outside of cryogenic matrix isolation conditions^{2,3} N_2 derivatives tend to be strongly activated and reduced to side-on-bound $(\text{N}_2)^{n-}$ by polymetallic-mediated reductions,¹⁶⁻¹⁹ or complete cleavage to nitrides occurs.^{20,21} Very few isolable, structurally characterised end-on CO, N_2 , or NO actinide complexes are known,²²⁻²⁹ and all terminal end-on complexes are supported by *tris*(cyclopentadienyl) ligand sets.^{22-25,27-29} The back-bonding in these systems stems not from metal orbitals but cyclopentadienyl ligand orbitals,³⁰ reminiscent of transition metal analogues,¹¹ or in the case of NO formal full reduction to $(\text{NO})^{1-}$ occurs,²⁹ so these are quite different from the classical metal-to-ligand back-bonding model.¹ Notably, all uranium complexes with end-on CO or N_2 involve electron-rich $5f^3$ uranium(III).^{22-25,28} Although 5f orbitals are radially more expanded than ‘core-like’ 4f orbitals, they only just penetrate the valence region, so such metal-to-ligand interactions and π -acceptor ligand activation is weak, as evidenced by their reversible coordination and dominance of ligand-to-ligand back-bonding. However, it should be noted that even though actinide-metallocenes represent a non-classical case of donor-acceptor bonding,³⁰ they fundamentally comply with the classical requirements of electron rich metal ions in a medium to low metal oxidation state.

We recently reported the synthesis of the silyl-phosphino-carbene uranium(IV) complex $[\text{U}(\text{BIPM}^{\text{TMS}})\{\text{C}(\text{SiMe}_3)(\text{PPh}_2)\}(\text{Cl})][\text{Li-2,2,2-cryptand}]$ (**1**, $\text{BIPM}^{\text{TMS}} = \text{C}(\text{PPh}_2\text{NSiMe}_3)_2$) that contains two types of covalent $\text{U}=\text{C}$ carbene double bond.³¹ In order to establish the fundamental properties of **1** we have examined its reactivity towards a wide range of substrates. Here, we report that treatment of **1** with an organo-azide produces a $5f^1$ high oxidation state uranium(V)-*bis*(imido) $\{\text{U}(\text{NR})_2\}^{1+}$ derivative. This carbene to *bis*(imido) motif transformation is unknown in carbene chemistry, and the uranium(V)-*bis*(imido) complex that is formed contains an end-on bound molecule of N_2 which bridges end-on to a lithium counter-ion. This isolable, crystalline complex features a +V high oxidation state metal classically back-bonded to a neutral π -acceptor ligand despite formally involving an electron-poor metal with only one valence electron. This unusual situation occurs with an electron in a 5f-orbital, ostensibly one of least radially expanded orbitals of the Periodic Table.

Results and Discussion

Synthesis. Treatment of **1** with one equivalent of 1-adamantyl-azide (AdN_3) in benzene results in immediate effervescence of N_2 and the red solution turning black. After work-up blackish-red crystals of $[\text{U}(\text{BIPM}^{\text{TMS}})(\text{NAd})_2(\mu\text{-}\eta^1\text{:}\eta^1\text{-N}_2)(\text{Li-2,2,2-cryptand})]$ (**2**) are obtained from toluene in 28% crystalline yield (by uranium content), Fig. 2. Complex **2** is formed irrespective of whether the reaction is conducted under N_2 or Ar, suggesting that the coordinated N_2 derives from the azide. Analysis of the reaction mother liquor by Nuclear Magnetic Resonance (NMR) spectroscopy reveals that more than one uranium-containing product is formed. The by-products have resisted all attempts to isolate and characterise them, but hydrolysis of the mother liquor and analysis by NMR spectroscopy and chromatographic methods reveals the presence of $\text{BIPM}^{\text{TMS}}\text{H}_2$, $\text{Me}_3\text{SiCH}_2\text{PPh}_2$, and $\text{LiCl-2,2,2-cryptand}$ in an approximate 1:2:1 ratio. This gives mass balance for the reaction and accounts for the superficially low yield of **2**, since the theoretical maximum in a scenario where sacrificial uranium-containing by-products form is substantially lower than 100%. The reaction that

produces **2** is clearly complex and most likely involves ligand scrambling, but **2** is consistently the sole isolable uranium complex from multiple reactions.

Structural characterisation. The solid-state molecular structure of **2** was determined by X-ray crystallographic studies, Fig. 3. The salient feature of **2** is the presence of a molecule of N₂ bridging between uranium and lithium ions, the latter of which is encapsulated within a 2,2,2-cryptand ligand in an irregular six-coordinate geometry. The coordination sphere of uranium is completed by a tridentate BIPM^{TMS} carbene ligand *trans* to the N₂ ligand, and two mutually *trans*-imido units resulting in a distorted octahedral geometry.

The U1-N1 distance of 2.605(8) Å is longer than the sum of single bond covalent radii of uranium and nitrogen (2.41 Å),³² and the strongly activated U-N₂ bond length of 2.220(9) Å in [{(Ph)(Bu^t)N}₃Mo(μ-η¹:η¹-N₂)U{N(Bu^t)(C₆H₃-3,5-Me₂)₃}₃],³³ but, by the 3σ-criterion, compares reasonably well to the U-N distance of 2.492(10) Å reported for weakly activated [(η⁵-C₅Me₅)₃U(N₂)].²⁸ Interestingly, there is little variation of the U-N_α-N_β angles in those three molecules, being 175.1(7), 173.8(7), and 180°, respectively, presumably reflecting that they are all back-bonded linkages no matter whether they result from metal- or ligand-to-ligand back-bonded electron density. We suggest that the U1-N1 distance can be considered long as a result of weak back-bonding, the fact that it resides *trans* (175.9(2)°) to the strong carbene donor of the BIPM^{TMS} ligand, and that the uranium ion is bonded to several stronger donor ligands overall. The N1-N2 distance of 1.139(9) Å is elongated slightly compared to the N-N distance in free-N₂ (1.0975 Å),¹ again indicating weak back-bonding, and is shorter than the 1.23(1) Å distance in [{(Ph)(Bu^t)N}₃Mo(μ-η¹:η¹-N₂)U{N(Bu^t)(C₆H₃-3,5-Me₂)₃}₃],³³ but is indistinguishable from the 1.120(14) Å N-N distance in [(η⁵-C₅Me₅)₃U(N₂)].²⁸

The U1-N5 and U1-N6 distances of 1.906(6) and 1.897(6) Å, respectively, are typical of uranium-bis(imido) units,³⁴ though we note the N5-U1-N6 angle (159.1(2)°) departs substantially from linearity, presumably to avoid steric clashing between the bulky Ad and BIPM^{TMS} ligand substituents. The U1-C1 distance of 2.461(7) Å in **2** compares well to the analogous distance of 2.400(3) Å in the uranium(VI)-carbene-imido-oxo complex [U(BIPM^{TMS})(NC₆H₂-2,4,6-Me₃)(O)(DMAP)] (DMAP = 4-dimethylaminopyridine),³⁵ but considering the formal uranium(V/VI) oxidation states of these two complexes the U=C bonds are long reflecting the presence of several multiple bond donor ligands. For example, in the uranium(V)-carbene complex [U(BIPM^{TMS})(Cl)₂(I)] the U=C distance is 2.268(10) Å,³⁶ and we suggest the long U=C bond in **2** arises from the uranium ion being electron rich from the two imido ligands and that the *bis*(imido) combination is the primary bonding motif with binding of the BIPM^{TMS} being secondary.

The N2-Li1 distance of 2.008(15) Å compares well to the sum of the single bond covalent radii of nitrogen and lithium (2.04 Å),³² and is indeed reminiscent of Li-NR₂ distances generally, suggesting that the N₂ carries partial anionic character resulting from back-bonding from the 5f¹ uranium(V) ion. During crystallographic refinement of **2** the possibility that the N₂ could be other diatomic small molecules (C₂, CN, CO, NO, O₂) or a disordered chloride was considered in detail, but is ruled out by a combination of incompatibility with the crystallographic metrical data, chemical unfeasibility of their occurrence, and the oxidation state formulation confirmed by the characterisation data below.

Spectroscopic and magnetic characterisation. The NMR spectra that could be obtained for **2**, noting its poor solubility once isolated, are well resolved and essentially within diamagnetic ranges (Supplementary Information Fig. 1-4), however this is common for uranium(V) complexes which are weakly paramagnetic and the data for **2** are consistent with those of related uranium(V)-BIPM complexes.³⁶⁻³⁸ The Raman spectrum of **2** (Supplementary Information Fig. 5) exhibits a broad

$\nu(\text{N}_2)$ absorption centred at $\sim 1940\text{ cm}^{-1}$, which compares reasonably well to a computed $\nu(\text{N}_2)$ value of 2038 cm^{-1} from a Density Functional Theory (DFT) analytical frequencies calculation of **2** using atomic coordinates from the experimentally determined crystal structure (see below). Additionally, it has been shown^{39,40} that $\nu(\text{N}_2)$ is proportional to $d(\text{N}_2)$ to the 3/2-power as:

$$\nu(\text{N}_2) = -1840[d(\text{N}_2)]^{3/2} + 4130 \text{ (Eqn 1.)}$$

Using Eqn 1 and the N1-N2 distance of $1.139(9)\text{ \AA}$ in **2**, a $\nu(\text{N}_2)$ frequency centred at 1890 cm^{-1} is predicted, and noting that by the 3σ -criterion the N1-N2 distance spans the range $1.112\text{--}1.166\text{ \AA}$ the $\nu(\text{N}_2)$ frequency is predicted to, and does, fall in the range $1813\text{--}1972\text{ cm}^{-1}$. Considering that the N1-N2 solid-state distance is determined in close proximity to the heavy uranium and that N_2 -containing molecules, including N_2 itself, frequently deviate by up to 300 cm^{-1} from predictions^{39,40} based on Eqn 1, the fit for **2** is remarkably good. The $\nu(\text{N}_2)$ frequency of **2** is $\sim 390\text{ cm}^{-1}$ lower (Δ) than that of free N_2 (2331 cm^{-1}) (*1*), indicating weak, but not insignificant, back-bonding and activation. For comparison, the $\nu(\text{N}_2)$ frequency of $[(\eta^5\text{-C}_5\text{Me}_5)_3\text{U}(\text{N}_2)]$ is 2207 cm^{-1} ($\Delta = 124\text{ cm}^{-1}$, $\nu(\text{N}_2)$ predicted to be 1949 cm^{-1} by Eqn 1),²⁸ suggesting very weak back-bonding in that case, whereas the $\nu(\text{N}_2)$ frequency of $[\{(3,5\text{-Me}_2\text{-C}_6\text{H}_3)(\text{Ad})\text{N}\}_3\text{Mo}(\mu\text{-}\eta^1\text{:}\eta^1\text{-N}_2)\text{U}\{\text{N}(\text{Bu}^t)(\text{C}_6\text{H}_3\text{-}3,5\text{-Me}_2)\}_3]$ is 1568 cm^{-1} ($\Delta = 763\text{ cm}^{-1}$) suggesting strong back-bonding in that case.³³ These spectroscopic data correlate with the observed stabilities of **2** and $[(\eta^5\text{-C}_5\text{Me}_5)_3\text{U}(\text{N}_2)]$,²⁸ where the latter requires a pressure of 80 psi to form, with N_2 release observed when the pressure is returned to 14.7 psi (1 atm), whereas the former forms at 1 atm pressure and does not release N_2 even when placed under dynamic vacuum (0.01 mm Hg), nor exchange with $^{15}\text{N}_2$ when refluxed in toluene under $^{15}\text{N}_2$, which instead results in decomposition to unidentifiable products and any remaining **2** shows no sign of $^{15}\text{N}_2$ -incorporation. Further confirming this trend, the related carbonyl complex $[(\eta^5\text{-C}_5\text{Me}_5)_3\text{U}(\text{CO})]$ exhibits a $\nu(\text{CO})$ frequency that is 221 cm^{-1} lower than free CO ,²⁵ and this compound liberates CO only after several hours under vacuum. The attenuated total reflectance infrared (ATR-IR) spectrum of **2** (Supplementary Information Fig. 6) exhibits several weak

absorptions in the range 1900-2100 cm^{-1} , but none of these could be definitively assigned as a $\nu(\text{N}_2)$ absorption, and attempts to perform ^{15}N -labelling studies proved intractable.

The ultraviolet/visible/near-infrared (UV/Vis/NIR) electronic absorption spectrum of **2** (Supplementary Information Fig. 7) is dominated by strong charge transfer bands that tail from the UV region to $\sim 12,000 \text{ cm}^{-1}$. The NIR region exhibits weak ($\epsilon = 10\text{-}20 \text{ L mol}^{-1} \text{ cm}^{-1}$) Laporte forbidden f-f absorptions in the range 5555-11,000 cm^{-1} that are characteristic of intra-configurational transitions from the ground $^2\text{F}_{5/2}$ to excited $^2\text{F}_{7/2}$ term multiplets of uranium(V).⁴¹ These absorptions are modelled well by Time-Dependent DFT, revealing that they all involve electronic promotions within the U-N₂ unit (Supporting Information Fig. 8).

The uranium(V) formulation of **2** is supported by Electron Paramagnetic Resonance (EPR) spectroscopy. The solid-state X-band EPR spectrum of **2** at 5 K (Supplementary Information Fig. 9) exhibits a resonance peak at $g_z = 3.80$, which is similar to the axial g_z feature of terminal uranium(V)-nitrides supported by tripodal ligands ($g \sim 3.7$);⁴² as for those nitrides, no $g_{x,y}$ features are observed for **2** within the available magnetic field range, 0-18,000 Gauss, suggesting that $g_{x,y} < 0.4$. This resonance peak is observable only below 50 K, consistent with 5f-electron character since rapid relaxation can occur due to the high orbital angular momenta of 5f-orbitals.

Unequivocal confirmation of the +V oxidation state assignment of **2** comes from variable-temperature superconducting quantum interference device (SQUID) magnetometry, Fig. 4 and Supplementary Information Fig. 10. A powdered sample of **2** exhibits a magnetic moment of 2.33 Bohr magneton units (μ_B) at 298 K (2.28 μ_B in solution), in close agreement with a theoretical magnetic moment of 2.54 μ_B for a single uranium(V) ion. Characteristic of uranium(V), the magnetic moment decreases slowly, until at 50 K ($\mu_{\text{eff}} = 2.04 \mu_B$) the magnetic moment decreases

rapidly, reaching $0.94 \mu_B$ at 2 K since this ion is an open shell magnetic doublet at all temperatures.⁴¹⁻⁴⁴

Computational characterisation. In order to probe the nature of the bonding in **2** we performed DFT calculations (see Supplementary Information Tables 1-32). In general, the computed bond lengths and angles of the geometry optimised structure are within 0.05 \AA and 2° of the experimental crystal structure. However, the U1-N1 distance of 2.439 \AA in the geometry optimised gas-phase structure is $\sim 0.16 \text{ \AA}$ shorter than the distance in the experimental solid-state crystal structure. Furthermore, inspection of a space filling representation of **2** (Supplementary Information Fig. 11) clearly shows that the $\text{N}_2\text{-Li-2,2,2-cryptand}$ fragment could approach closer to the $\text{U(BIPM}^{\text{TMS}}\text{)(NAd)}_2$ unit of **2** without any obvious steric clashing. Moreover, an analytical frequencies calculation on the geometry optimised coordinates computes a N_2 stretch of 1712 cm^{-1} , which does not compare well with the experimentally determined value.

In order to probe this further, we performed potential energy surface scans along the U1-N1 vector, both on the full molecule and on a simplified model (**2 core**) in which phenyl and adamantyl groups are replaced with methyl groups, SiMe_3 is substituted for SiH_3 and only the coordinating atoms of the cryptand are retained (Supplementary Information Fig. 12). Several levels of theory have been employed, and the results are summarised in Fig. 5. DFT Perdew-Burke-Ernzerhof (PBE) scans give minimum energies between $2.35\text{-}2.41 \text{ \AA}$, whereas Hartree-Fock (HF) scans show minima at around 2.50 \AA . Second-order Møller-Plesset perturbation theory (MP2) calculations yield similar conclusions to HF. Restricted Active Space-Self Consistent Field (RASSCF) calculations have also been performed; the choice of active space is discussed in detail in the Supplementary Information, and the natural orbitals are shown in Supplementary Information Fig. 13 and their occupancies, at each point in the scan, in Supplementary Information Table 1. These calculations give an energy minimum at 2.56 \AA , with a significantly shallower potential compared to the already rather shallow

HF and DFT scans; the point at 2.61 Å is only 0.80 kJ mol⁻¹ higher in energy. It may be that including further correlation shifts the minimum even closer to the crystal structure geometry, as may the additional sterics of the full molecule. We note that the very shallow potentials shown in Fig. 4 are well within the range of crystal packing forces,⁴⁵ and hence conclude that the discrepancy of the experimental vs computed U1-N1 distance is either the result of solid-state crystal packing effects that are not accounted for in gas phase calculations and/or correlation energy effects not well described by DFT.

Noting the experimental vs computed U1-N1 discrepancy, to obtain an experimentally relevant description of the electronic structure of **2** DFT studies were performed using the crystallographic coordinates and not geometry optimised ones. The good agreement of TD-DFT and analytical frequencies calculations using those coordinates to experimental observations provides validation of this approach. The computed Multipole Derived Charges (MDC-q) on the U1, C1, Li1, and N₂ units are +3.36, -2.14, +0.66, and -0.51. In a purely ionic bonding situation these values would be +5, -2, +1, and 0, so the computed data reflect charge donation to the U1 and Li1 ions from the ligands and back-bonding from uranium to the N₂ ligand. Consistent with this, the computed spin densities on U1 and N₂ unit are -0.6 and -0.51, confirming transfer of ~0.5 of an electron from the formal 5f¹ U1 to N₂. In further support of this back-bonding picture, the U1-N1 and N₂ computed Nalewajski-Mrozek bond orders are 0.66 and 2.75, respectively, showing a weak U-N₂ back-bond and modest reduction of the N₂ bond order (3 in free N₂). As suggested by the U1-C1 distance, the U1-C1 bond is poorly developed with a bond order of 0.92, reflecting the presence of the two imido groups with U1-N5 and U1-N6 bond orders of 2.57 and 2.59 that are consistent with strong triple bonds. For comparison the U1-N3 and U1-N4 bond orders are 0.77 and 0.79, respectively, and a highly polar N2-Li1 interaction is confirmed by a computed bond order of 0.13.

The highest occupied Kohn-Sham molecular orbital (HOMO) of **2** is the U-N₂ back-bond, Fig. 6. This is consistent with the formal 5f¹ +V oxidation state of the uranium ion in **2** and back-bonding to N₂. The U-C_{carbene} double bond is principally represented by HOMO-1 (π) and HOMO-2 (σ) (Supplementary Information Fig. 14). The U-N_{imido} bonding interactions are represented by HOMO-3 to HOMO-11, but these MOs are extensively mixed. Therefore, in order to obtain a clearer and chemically more intuitive description of the bonding in **2** we turned to Natural Bond Orbital (NBO) theory.

NBO calculations on **2** (Supplementary Information Fig. 15) reveal one U-N₂ back-bonding interaction that is composed of 31% U1 and 69% N1 character. As expected, the N component is essentially pure 2p-orbital character from the π^* -orbital manifold of N₂ and the uranium contribution is 95% 5f and 5% 6d character. The N₂ lone pair donation to U is described in an NBO of exclusively N-character (62% 2s and 38% 2p character), in-line with its dative, and weak, nature. Confirming analysis of the Kohn-Sham electronic structure, NBO returns a $\sigma^2\pi^2$ U-C double bond interaction and also two $\sigma^2\pi^2\pi^2$ U-N_{imido} triple bond interactions. The U=C bonds are quite polar, being composed of 10% uranium and 90% carbon character with the uranium component dominated by 5f character (80:20 5f:6d), whereas the U-N_{imido} bonds have 20% uranium and 80% nitrogen character with a 5f:6d ratio of 70:30.

DFT and NBO methods are orbital-based, and in order to probe the chemical bonding in **2** in an alternative way we examined the topology of the electron density using Quantum Theory of Atoms in Molecules (QTAIM). A U1-N1 3,-1 bond critical point (BCP) was found, with an electron density $\rho(r)$ of 0.04 e bohr⁻³. In QTAIM analysis covalent bond tends to have $\rho(r) > 0.1$ so the value for **2** is consistent with a polar bonding interaction, which is also reflected by the total energy density $H(r)$ (-0.01) at the BCP. The presence of the back-bond is unequivocally confirmed by examination of the bond ellipticity, $\epsilon(r)$. Single (σ^2 , e.g. H₃CCH₃) and triple ($\sigma^2\pi^2\pi^2$, e.g. HC \equiv CH)

bonds exhibit spherical distributions of electron density around the bond path at the BCP and so $\epsilon(r) \sim 0$, however double bonds ($\sigma^2\pi^2$, e.g. $\text{H}_2\text{C}=\text{CH}_2$) are asymmetric and so $\epsilon(r) > 0$, being 0.45 for $\text{H}_2\text{C}=\text{CH}_2$.⁴⁶ Here, the $\epsilon(r)$ value for the U1-N1 bond in **2** is 0.39, confirming a single π -back-bond. For comparison, the U1-C1, av. U-N_{imido}, and N1-N2 $\rho(r)/H(r)/\epsilon(r)$ data are 0.08/−0.03/0.24, 0.20/−0.14/0.01, and 0.6/−0.91/0.01, respectively. Taken together with all the other data, the consistent picture that emerges is a U-N₂ donor-acceptor interaction with a π -back-bond that only weakly activates the $\text{N}\equiv\text{N}$ triple bond, and polarised covalent U-C_{carbene} double and U-N_{imido} triple bonds.

Discussion. Complex **2** represents a departure from the traditional requirements of synergic, donor-acceptor metal-to-ligand interactions. This situation arises in an electron-poor, high oxidation state complex, involving the poor π -acceptor N_2 , utilising a single electron in a 5f-orbital, which is one of the least radially expanded orbitals, and therefore one of the least likely candidates for this scenario to occur. So how can this situation arise? We propose two factors that may be responsible. The heterobimetallic uranium-lithium combination may cooperatively assist in trapping the N_2 , and certainly heteropolymetallic cooperative effects are increasingly being recognised as crucial to binding and activating N_2 in heterogeneous Haber Bosch chemistry and in homogeneous molecular analogues.^{1,47} Recognising that electron-poor, high oxidation state metals can also back-bond to N_2 by tuning the ligand environment could have implications for N_2 -activation chemistry given the vast scale that industrial Haber Bosch and biomimetic nitrogenase processes operate on.⁴⁸ The uranium ion in **2** is bonded to two imido ligands and the tridentate BIPM^{TMS} carbene ligand. We suggest that with at least three strong multiply bonded π -donor ligands, the formally electron-poor 5f¹ uranium ion in **2** is evidently uncommonly capable of engaging in π -back-bonding even to a poor π -acceptor ligand. Uranium(V) is usually considered to be quite oxidising,⁴¹ but here the uranium is in such an electron rich ligand environment that it is now essentially reducing in nature. The isolation of crystalline **2**, and the prior report of meta-stable $[\text{OsO}_2(\text{CO})_4]^{2+}$ (reference 10) that contains one less

metal-ligand multiple bond linkage than stable **2**, suggests that such unusual bonding might be realised more widely by electron-poor metals when coordinated by very electron-rich ancillary ligands.

Conclusions and Summary

To conclude, we have found that reaction of a uranium-carbene complex with an organo-azide results in isolation of a crystalline uranium(V)-*bis*(imido)-dinitrogen complex. This complex features a +V high oxidation state metal classically back-bonded to a neutral π -acceptor ligand, and this is despite formally involving an electron-poor metal with only one valence electron that is ostensibly one of the least radially extended in the Periodic Table combined with a very poor π -acceptor ligand. We propose that this scenario arises due to a combination of cooperative heterobimetallic effects and that the uranium ion in this complex is unusually electron-rich to the point that a usually oxidising metal centre is now reducing in nature. This suggests that with suitable ancillary ligands isolable complexes with the unusual bonding situation reported here might be realised more widely when electron-poor metals are coordinated by very electron-rich ancillary ligands. Lastly, N₂-activation chemistry usually relies on the use of low-valent reducing metal ions, but this work suggests that in the suitable situations high oxidation state metals might also play a role in the binding and activation of dinitrogen.

Acknowledgements

We gratefully acknowledge funding and support from the UK Engineering and Physical Sciences Research Council (grants EP/M027015/, and EP/P001386/1), European Research Council (grant CoG612724), Royal Society (grant UF110005), the National EPSRC UK EPR Facility, The University of Manchester, and the UK National Nuclear Laboratory. B.E.A and N.K are also grateful to the University of Manchester for computational resources and associated support services from the Computational Shared Facility.

Data Availability

The X-ray crystallographic data for **2** have been deposited at the Cambridge Crystallographic Data Centre (CCDC), under deposition number CCDC 1869009. These data can be obtained free of charge from The Cambridge Crystallographic Data Centre (www.ccdc.cam.ac.uk/data_request/cif). All other data supporting the findings of this study are available within the Article and its Supplementary Information, or from the corresponding author upon reasonable request.

Author Contributions

E.L. and J.B. prepared and characterised the compound and its precursors. B.E.A. and N.K. performed the energy-scan calculations and analysed the results. E.L., A.J.W., I.J.V.-Y., and G.F.S.W. collected, solved, refined, and analysed the crystallographic data. E.L., L.R.D., J.D.C., and P.C. recorded and interpreted the Raman data. F.T. recorded and interpreted the EPR data. S.T.L. originated the central idea, supervised the work, analysed the data, performed the DFT, NBO, and QTAIM calculations and analysed the results, and wrote the manuscript with contributions from all authors.

Additional Information

Supplementary information and chemical compound information are available in the online version of the paper. Reprints and permissions information is available at www.nature.com/reprints. Correspondence and requests for materials should be addressed to S.T.L.

Competing Interests

The authors declare no competing interests.

References

1. Fryzuk, M. D. & Johnson, S. A. The continuing story of dinitrogen activation. *Coord. Chem. Rev.* **200-202**, 379-409 (2000).
2. Kushto, G. P., Souter, P. F. & Andrews, L. An infrared spectroscopic and quasirelativistic theoretical study of the coordination and activation of dinitrogen by thorium and uranium atoms. *J. Chem. Phys.* **108**, 7121 (1998).
3. Andrews, L., Wang, X., Gong, Y., Vlasisavljevich, B. & Gagliardi, L. Infrared spectra and electronic structure calculations for the $\text{NUN}(\text{NN})_{1-5}$ and $\text{NU}(\text{NN})_{1-6}$ complexes in solid argon. *Inorg. Chem.* **52**, 9989-9993 (2013).
4. Burford, R. J. & Fryzuk, M. D. Examining the relationship between coordination mode and reactivity of dinitrogen. *Nat. Rev. Chem.* **1**, 0026 (2017).
5. Dell'Amico, D. B., Calderazzo, F., Marchetti, F. & Merlino, S. Synthesis and molecular structure of $[\text{Au}_4\text{Cl}_8]$, and the isolation of $[\text{Pt}(\text{CO})\text{Cl}_5]^-$ in thionyl chloride. *J. Chem. Soc. Dalton Trans.* 2257-2260 (1982).
6. Bernhardt, E. & Preetz, W. Synthesis and spectroscopic characterization of fluorocarbonyl osmates, normal coordinate analysis and crystal structure of *fac*- $[\text{OsF}_3\text{Br}_2(\text{CO})]^{2-}$. *Z. Anorg. Allg. Chem.* **624**, 694-700 (1998).
7. Höhling, M. & Preetz, W. Synthesis and crystal structure of tetraphenylarsonium pentachlorocarbonyl osmate(IV), $(\text{Ph}_4\text{As})[\text{OsCl}_5(\text{CO})]$. *Z. Naturforsch.* **B52**, 978-980 (1997).
8. Wovchko, E. A. & Yates, J. T. Activation of O_2 on a photochemically generated Rh^{I} site on an Al_2O_3 surface: low temperature O_2 dissociation and CO oxidation. *J. Am. Chem. Soc.* **120**, 10523-10527 (1998).
9. Crayston, J. A., Almond, M. J., Downs, A. J., Poliakoff, M. & Turner, J. J. Formation of *trans*- $\text{M}(\text{O})_2(\text{CO})_4$ (M = Mo and W): intermediates in the photooxidation of matrix-isolated $\text{M}(\text{CO})_6$. *Inorg. Chem.* **23**, 3051-3056 (1984).

10. Bernhardt, E., Willner, H., Jonas, V., Thiel, W., & Aubke, F. The tetrakis(carbonyl)dioxoosmium(VI) cation: *trans*-[OsO₂(CO)₄]²⁺. *Angew. Chem. Int. Ed.* **39**, 168-171 (2000).
11. Malischewski, M., Seppelt, K., Sutter, J., Munz, D. & Meyer, K. A ferrocene-based dicationic iron(IV) carbonyl complex. *Angew. Chem. Int. Ed.* **57**, 14597-14601 (2018).
12. Marsella, J. A., Curtis, C. J., Bercaw, J. E. & Caulton, K. G. Low-temperature infrared study of d⁰ carbonyl complexes. *J. Am. Chem. Soc.* **102**, 7244-7246 (1980).
13. Guram, A. S., Swenson, D. C. & Jordan, R. F. Synthesis and characterization of Cp₂Zr(CH{Me}{6-ethylpyrid-2-yl})(CO)⁺, a d⁰ metal alkyl carbonyl complex. Coordination chemistry of the four-membered azazirconacycle Cp₂Zr(η²-C,N-CH{Me}{6-ethylpyrid-2-yl})⁺. *J. Am. Chem. Soc.* **114**, 8991-8996 (1992).
14. Hurlburt, P. K. *et al.* Nonclassical metal carbonyls: [Ag(CO)]⁺ and [Ag(CO)₂]⁺. *J. Am. Chem. Soc.* **116**, 10003-10014 (1994).
15. Lupinetti, A. J., Frenking, G. & Strauss, S. H. Nonclassical metal carbonyls: appropriate definitions with a theoretical justification. *Angew. Chem. Int. Ed.* **37**, 2113-2116 (1998).
16. Roussel, P. & Scott, P. Complex of dinitrogen with trivalent uranium. *J. Am. Chem. Soc.* **120**, 1070-1071 (1998).
17. Cloke, F. G. N. & Hitchcock, P. B. Reversible binding and reduction of dinitrogen by a uranium(III) pentalene complex. *J. Am. Chem. Soc.* **124**, 9352 (2002).
18. Mansell, S. M., Kaltsoyannis, N. & Arnold, P. L. Small molecule activation by uranium tris(aryloxides): experimental and computational studies of binding of N₂, coupling of CO, and deoxygenation insertion of CO₂ under ambient conditions. *J. Am. Chem. Soc.* **133**, 9036-9051 (2011).
19. Mansell, S. M., Farnaby, J. H., Germeroth, A. I. & Arnold, P. L. Thermally stable uranium dinitrogen complex with siloxide supporting ligands. *Organometallics* **32**, 4214-4222 (2013).

20. Korobkov, I., Gambarotta, S. & Yap, G. P. A. A highly reactive uranium complex supported by the calix[4]tetrapyrrole tetraanion affording dinitrogen cleavage, solvent deoxygenation, and polysilanol depolymerisation. *Angew. Chem. Int. Ed.* **41**, 3433-3436 (2002).
21. Falcone, M., Chatelain, L., Scopelliti, R., Zivkovic, I. & Mazzanti, M. Nitrogen reduction and functionalization by a multimetallic uranium nitride complex. *Nature* **547**, 332-335 (2017).
22. Brennan, J. G., Andersen, R. A. & Robbins, J. L. Preparation of the first molecular carbon monoxide complex of uranium, $(\text{Me}_3\text{SiC}_5\text{H}_4)_2\text{UCO}$. *J. Am. Chem. Soc.* **108**, 335-336 (1986).
23. Parry, J., Carmona, E., Coles, S. & Hursthouse, M. Synthesis and single crystal X-ray diffraction study on the first isolable carbonyl complex of an actinide, $(\text{C}_5\text{Me}_4\text{H})_3\text{U}(\text{CO})$. *J. Am. Chem. Soc.* **117**, 2649-2650 (1995).
24. Del Mar Conejo, M. *et al.* Carbon monoxide and isocyanide complexes of trivalent uranium metallocenes. *Chem. Eur. J.* **5**, 3000-3009 (1999).
25. Evans, W. J., Kozimor, S. A., Nyce, G. W. & Ziller, J. W. Comparative reactivity of sterically crowded nf^3 $(\text{C}_5\text{Me}_5)_3\text{Nd}$ and $(\text{C}_5\text{Me}_5)_3\text{U}$ complexes with CO: formation of a nonclassical carbonium ion versus an f element metal carbonyl complex. *J. Am. Chem. Soc.* **125**, 13831-13835 (2003).
26. Castro-Rodriguez, I. & Meyer, K. Carbon dioxide reduction and carbon monoxide activation employing a reactive uranium(III) complex. *J. Am. Chem. Soc.* **127**, 11242-11243 (2005).
27. Langeslay, R. R. *et al.* Synthesis, structure, and reactivity of the sterically crowded Th^{3+} complex $(\text{C}_5\text{Me}_5)_3\text{Th}$ including formation of the thorium carbonyl, $[(\text{C}_5\text{Me}_5)_3\text{Th}(\text{CO})][\text{BPh}_4]$. *J. Am. Chem. Soc.* **139**, 3387-3398 (2017).
28. Evans, W. J., Kozimor, S. A. & Ziller, J. W. A monometallic f element complex of dinitrogen: $(\text{C}_5\text{Me}_5)_3\text{U}(\eta^1\text{-N}_2)$. *J. Am. Chem. Soc.* **125**, 14264-14265 (2003).
29. Siladke, N. A. *et al.* Synthesis, structure, and magnetism of an f element nitrosyl complex, $(\text{C}_5\text{Me}_4\text{H})_3\text{UNO}$. *J. Am. Chem. Soc.* **134**, 1243-1249 (2012).

30. Maron, L., Eisenstein, O. & Andersen, R. A. The bond between CO and $\text{Cp}'_3\text{U}$ in $\text{Cp}'_3\text{U}(\text{CO})$ involves back-bonding from the $\text{Cp}'_3\text{U}$ ligand-based orbitals of π -symmetry, where Cp' represents a substituted cyclopentadienyl ligand *Organometallics* **28**, 3629-3635 (2009).
31. Lu, E., Boronski, J. T., Gregson, M., Wooles, A. J. & Liddle, S. T. Silyl-phosphino-carbene complexes of uranium(IV). *Angew. Chem. Int. Ed.* **57**, 5506-5511 (2018).
32. Pyykkö, P. Additive covalent radii for single-, double-, and triple-bonded molecules and tetrahedrally bonded crystals: A summary. *J. Phys. Chem. A* **119**, 2326-2337 (2015).
33. Odom, A. L., Arnold, P. L. & Cummins, C. C. Heterodinuclear uranium/molybdenum dinitrogen complexes. *J. Am. Chem. Soc.* **120**, 5836-5837 (1998).
34. Hayton, T. W. *et al.* Synthesis of imido analogs of the uranyl ion. *Science* **310**, 1941-1943 (2005).
35. Lu, E. *et al.* Synthesis, characterization, and reactivity of a uranium(VI) carbene imido oxo complex. *Angew. Chem. Int. Ed.* **53**, 6696-6700 (2014).
36. Cooper, O. J. *et al.* Uranium-carbon multiple bonding: facile access to the pentavalent uranium carbene $[\text{U}\{\text{C}(\text{PPh}_2\text{NSiMe}_3)_2\}(\text{Cl})_2(\text{I})]$ and comparison of $\text{U}^{\text{V}}=\text{C}$ and $\text{U}^{\text{IV}}=\text{C}$ double bonds. *Angew. Chem. Int. Ed.* **50**, 2383-2386 (2011).
37. Mills, D. P. *et al.* Synthesis of a uranium(VI)-carbene: reductive formation of uranyl(V)-methanides, oxidative preparation of a $[\text{R}_2\text{C}=\text{U}=\text{O}]^{2+}$ analogue of the $[\text{O}=\text{U}=\text{O}]^{2+}$ uranyl ion ($\text{R} = \text{Ph}_2\text{PNSiMe}_3$), and comparison of the nature of $\text{U}^{\text{IV}}=\text{C}$, $\text{U}^{\text{V}}=\text{C}$ and $\text{U}^{\text{VI}}=\text{C}$ double bonds. *J. Am. Chem. Soc.* **134**, 10047-10054 (2012).
38. Cooper, O. J. *et al.* The nature of the $\text{U}=\text{C}$ bond: Pushing the stability of high oxidation state uranium carbenes to the limit. *Chem. Eur. J.* **19**, 7071-7083 (2013).
39. Cohen, J. D., Mylvaganam, M., Fryzuk, M. D. & Loehr, T. M. Resonance raman studies of dinuclear zirconium complexes with a bridging dinitrogen ligand. Possible N_2 -coordination models for nitrogenase. *J. Am. Chem. Soc.* **116**, 9529-9534 (1994).

40. Laplaza, C. E. *et al.* Dinitrogen cleavage by three-coordinate molybdenum(III) complexes: mechanistic and structural data. *J. Am. Chem. Soc.* **118**, 8623-8638 (1996).
41. Liddle, S. T. The renaissance of non-aqueous uranium chemistry. *Angew. Chem. Int. Ed.* **54**, 8604-8641 (2015).
42. King, D. M. *et al.* Molecular and electronic structure of terminal and alkali metal-capped uranium(V)-nitride complexes. *Nat. Commun.* **7**, 13773 (2016).
43. Castro-Rodríguez, I. & Meyer, K. Small molecule activation at uranium coordination complexes: control of reactivity *via* molecular architecture. *Chem. Commun.* 1353-1368 (2006).
44. Kindra, D. R. & Evans, W. J. Magnetic susceptibility of uranium complexes. *Chem. Rev.* **114**, 8865-8882 (2014).
45. Minasian, S. G., Krinsky, J. L. & Arnold, J. Evaluating f-element bonding from structure and thermodynamics. *Chem. Eur. J.* **17**, 12234-12245 (2011).
46. Bader, R. F. W., Slee, T. S., Cremer, D. & Kraka, E. Description of conjugation and hyperconjugation in terms of electron distributions. *J. Am. Chem. Soc.* **105**, 5061-5068 (1983).
47. MacLeod, K. C. & Holland, P. L. Recent developments in the homogeneous reduction of dinitrogen by molybdenum and iron. *Nat. Chem.* **5**, 559-565 (2013).
48. Foster, S. L. *et al.* Catalysts for nitrogen reduction to ammonia. *Nat. Cat.* **1**, 490-500 (2018).

Figures and Schemes:

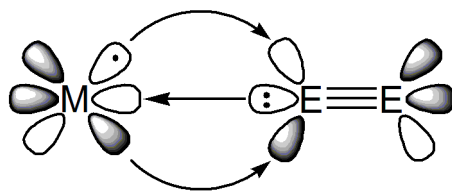


Figure 1 | The classical donor-acceptor bonding model for a transition metal (M) and a neutral diatomic $E\equiv E$ ($N\equiv N$ or $C\equiv O$) π -acceptor ligand. This model describes the requirement for a metal in a mid, low, or even negative oxidation state, to possess one or more metal valence electrons, to have a spatial reach of d-orbitals to overlap with ligand orbitals, and a ligand with a lone pair to donate to the metal and one or more accessible π^* orbitals to receive electron density from back-bonding. This work reports an example where the metal is high oxidation state and electron poor back-bonding with a spatially-limited f-electron to the poor π -acceptor ligand N_2 .

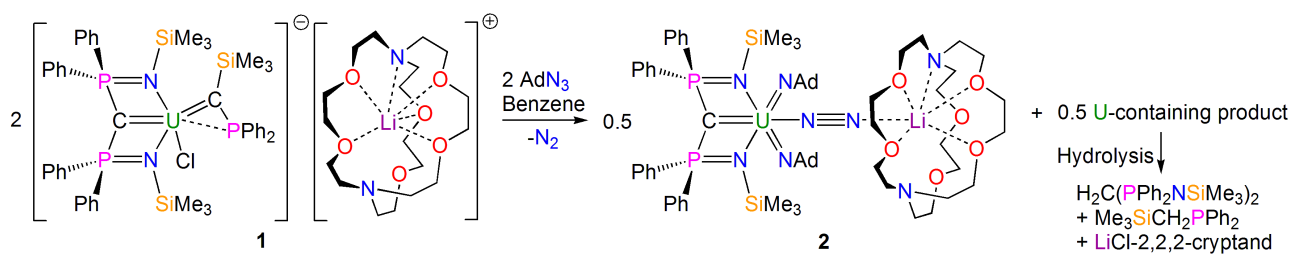


Figure 2 | Synthesis of compound 2 from precursor 1. The uranium(IV)-bis(carbene) compound **1** reacts with 1-adamantyl-azide in a 1:1 ratio to give the uranium(V)-carbene-bis(imido)-dinitrogen-lithium-cryptand complex **2**. This reaction is accompanied by the elimination of N_2 and formation of at least one other uranium by-product. Analysis of the hydrolysed mother liquor containing the uranium by-product reveals the presence of $\text{BIPM}^{\text{TMS}}\text{H}_2$, $\text{Me}_3\text{SiCH}_2\text{PPh}_2$, and LiCl -2,2,2-cryptand in an approximate 1:2:1 ratio.

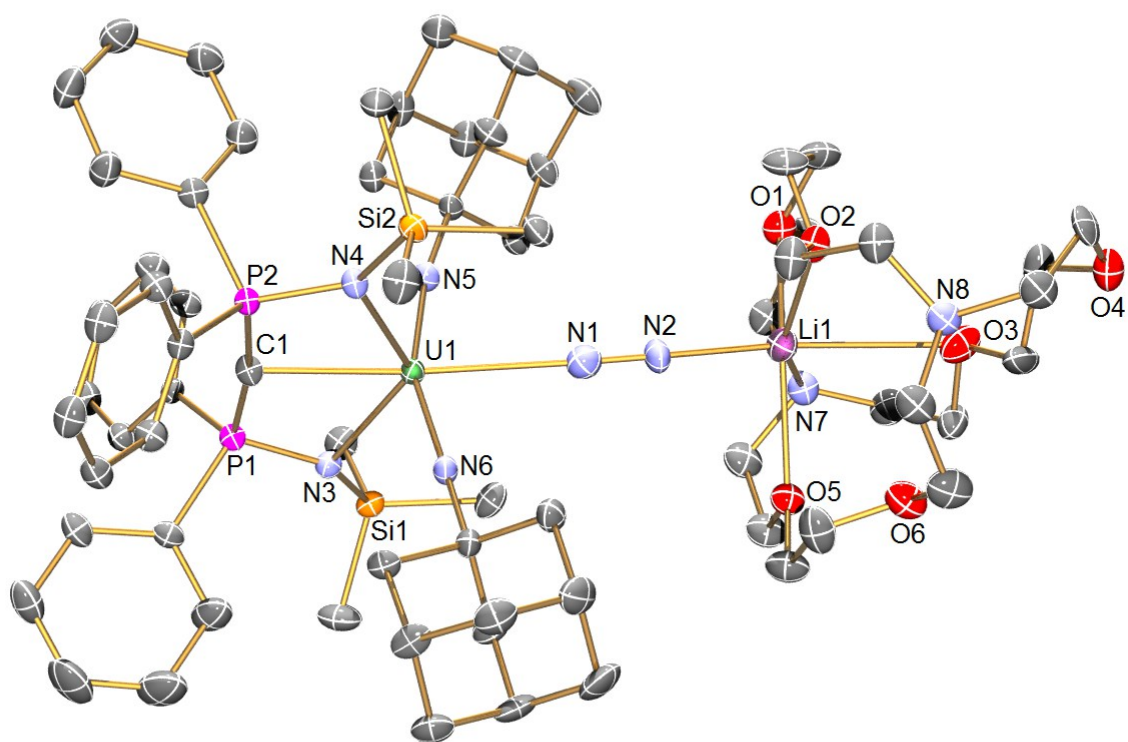


Figure 3. Molecular structure of 2 at 150 K with 40% probability ellipsoids. Selected distances (Å) and angles (°) are U1-N1, 2.605(8); U1-C1, 2.461(7); U1-N3, 2.452(6); U1-N4, 2.451(6); U1-N5, 1.906(6); U1-N6, 1.897(6); N1-N2, 1.139(9); N2-Li1, 2.008(15); C1-U1-N1, 175.9(2); U1-N1-N2, 175.1(7); N1-N2-Li1, 175.4(8); P1-C1-P2, 169.9(5); N5-U1-N6, 159.1(2); N3-U1-N4, 127.26(19); C1-U1-N5 99.9(3); C1-U1-N6, 101.0(2); N1-U1-N5 78.2(2); N1-U1-N6 81.0(2).

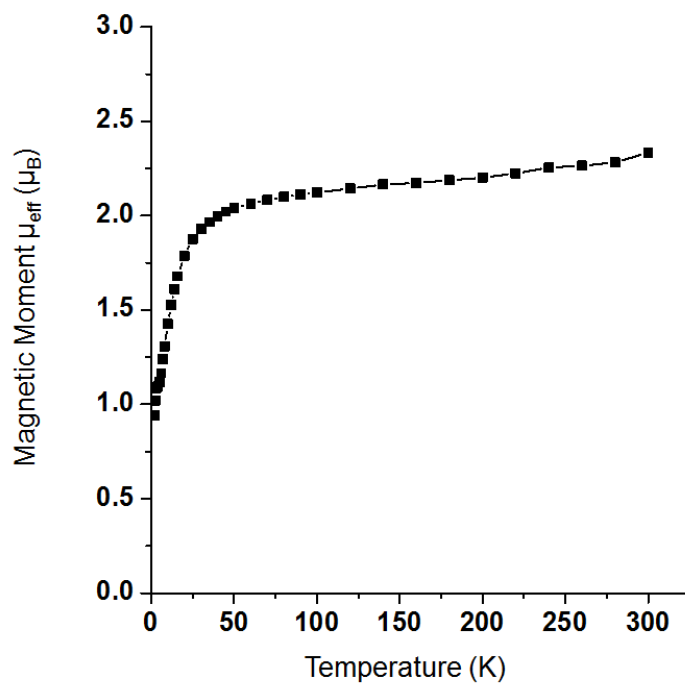


Figure 4 | Variable-temperature effective magnetic moment data for 2. Data are plotted as μ_{eff} (μ_B) as a function of temperature (K) for powdered **2**, measured on a superconducting quantum interference device (SQUID) magnetometer in an applied magnetic field of 0.1 T. The line connecting the data points is a guide to the eye only.

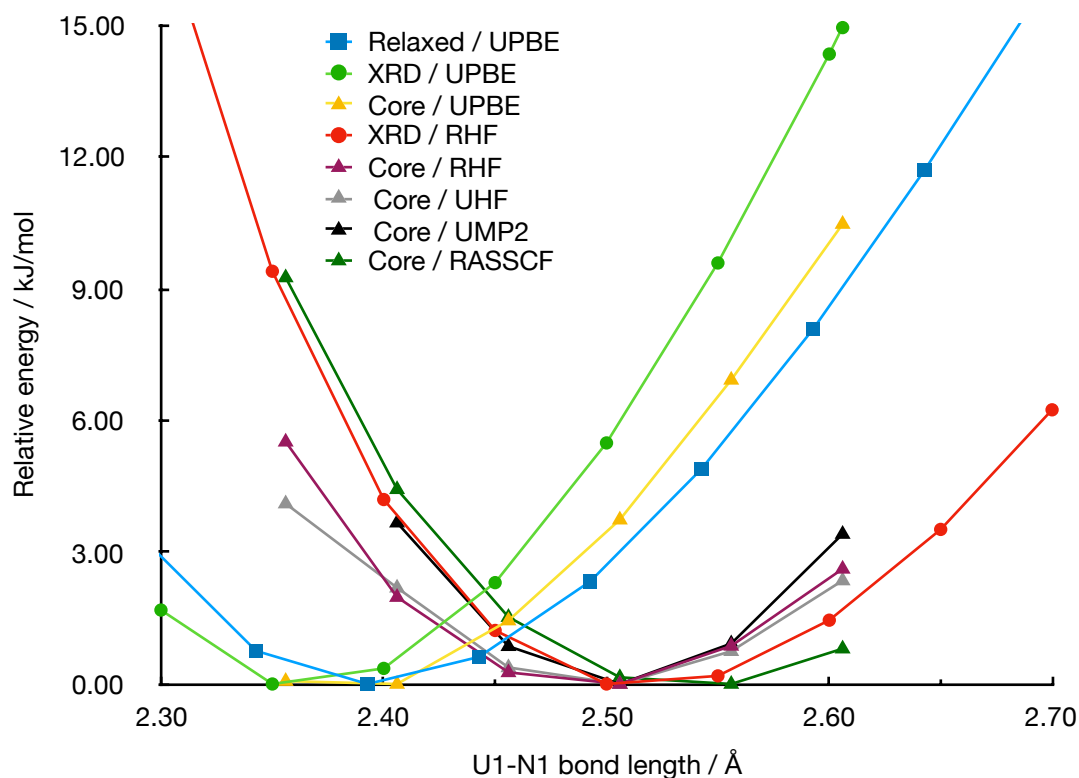


Figure 5 | Computed potential energy surface scans of the relative energy (kJ mol^{-1}) vs the U1-N1 distance (\AA) of **2.** ‘XRD’ and ‘Relaxed’ calculations are on the full molecule **2**. ‘Core’ is the model shown in Fig. 12 of the Supporting Information (**2 core**). All scans are rigid, *i.e.* in which all the geometric parameters of the non-hydrogen atoms are frozen, other than the U1-N1 distance, except the Relaxed / UPBE scan, in which all other geometric parameters are optimised at each point. For the rigid scans on **2 core**, the hydrogen atom positions are optimised at each point of the scan.

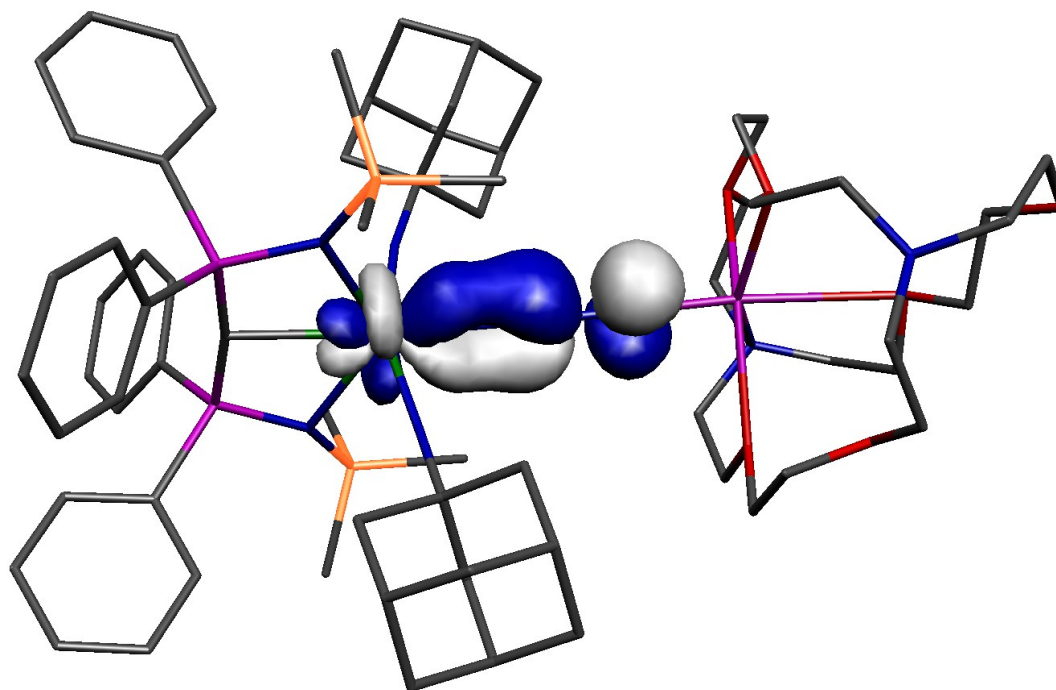


Figure 6 | The singularly-occupied, α -spin highest occupied Kohn-Sham molecular orbital (338a, -1.715 eV) of **2. This molecular orbital represents the U-N₂ back-bonding interaction. Hydrogen atoms are omitted for clarity.**

**High Oxidation State Electron-Poor Metal-to-Ligand Backbonding in a Crystalline
Uranium(V)-Dinitrogen Complex**

Erli Lu, Benjamin E. Atkinson, Ashley J. Wooles, Josef T. Boronski, Laurence R. Doyle, Floriana
Tuna, Jonathan D. Cryer, Philip J. Cobb, Inigo J. Vitorica-Yrezabal, George F. S. Whitehead,
Nikolas Kaltsoyannis, and Stephen T. Liddle*

School of Chemistry, The University of Manchester, Oxford Road, Manchester, M13 9PL, UK.

*Email: steve.liddle@manchester.ac.uk

Experimental Details

General Procedures

All manipulations were carried out using Schlenk techniques, or an MBraun UniLab glovebox, under an atmosphere of dry nitrogen or argon. Solvents were dried by passage through activated alumina towers and degassed before use. All solvents were stored over potassium mirrors except for ethers, which were stored over activated 4 Å sieves. Deuterated solvent was distilled from potassium, degassed by three freeze-pump-thaw cycles and stored under nitrogen. $[\text{U}\{\text{C}(\text{PPh}_2\text{NSiMe}_3)_2\}\{\text{=C}(\text{PPh}_2)(\text{SiMe}_3)\}][\text{Li}(2,2,2\text{-cryptand})]$ (**1**) was prepared as described previously.¹ 1-Azidoadamantane was purchased from Sigma-Aldrich and was dried under dynamic vacuum for 12 hours prior to use.

^1H , ^7Li , ^{13}C , and ^{31}P , NMR spectra were recorded on a Bruker 400 spectrometer operating at 400.2, 155.5, 100.6, and 162.0 MHz respectively; chemical shifts are quoted in ppm and are relative to SiMe_4 (^1H and ^{13}C), external 85% H_3PO_4 (^{31}P), or external 0.1 M LiCl in D_2O (^7Li). FTIR spectra were recorded on a Bruker Alpha spectrometer with Platinum-ATR module. UV/Vis/NIR spectra were recorded on a Perkin Elmer Lambda 750 spectrometer. Data was collected in 1 mm path length cuvette loaded in an MBraun UniLab glovebox and was run versus toluene reference solvent. Raman spectra were recorded on a Horiba XploRA Plus Raman microscope with a 638 nm laser with a power of ≤ 1.5 mW. The power was adjusted using a power filter for each complex to inhibit sample decomposition. Variable-temperature magnetic moment data were recorded in an applied dc field of 0.1 T on a Quantum Design MPMS XL7 superconducting quantum interference device magnetometer using doubly recrystallised powdered samples. Care was taken to ensure complete thermalisation of the sample before each data point was measured and samples were immobilised in an eicosane matrix to prevent sample reorientation during measurements. Specifically, 54.0 mg of finely ground **2** was immobilised in a matrix of 37.4 mg of eicosane within a 4 mm diameter tube sealed under vacuum. The sample holder background was subtracted using data from a blank and a diamagnetic correction

was applied using Pascal Table of Constants.² Variable temperature EPR spectra were measured at X-band (ca. 9.4 GHz) on a Bruker EMX 300 spectrometer equipped with an ER4119HS-W1 resonator. Elemental microanalyses were carried out by Mr Martin Jennings at the Micro Analytical Laboratory, School of Chemistry, The University of Manchester.

Preparation of [U(BIPM^{TMS})(NAd)₂(μ-η¹:η¹-N₂)(Li-2,2,2-cryptand)] (2)

Method A: At ambient temperature and under nitrogen atmosphere, a solution of 1-azidoadamantane in benzene (59.7 mg, 0.337 mmol, 2 ml) was added to a stirring suspension of **1** in benzene (500 mg, 0.337 mmol, 3 ml). Immediate effervescence was observed along with dissolution of **1**. The black mixture was allowed to stir at ambient temperature for 1 hour. All volatiles were removed under vacuum. The residue was extracted with toluene (3 × 2 ml); the volume was concentrated to approximately 3 ml and kept under –35 °C. After 12 hours the first crop of **2** was collected as blackish red crystals. The mother liquor was further concentrated to approximately 2 ml and was kept under –35 °C for 12 hours to produce the second crop of **2**. The blackish red crystals from the two crops were combined, washed with pentane (3 × 1 ml) under –35 °C, and dried under vacuum to afford **2** as a blackish red crystalline solid. Yield: 143.4 mg, 28%. *Method B:* The procedure was carried out in an identical manner to Method A, but the reaction was carried out under argon atmosphere. Complex **2** was produced as 2 crops of blackish red crystals. Yield: 132.2 mg, 26%. Single crystals of **2** suitable for X-ray diffraction were obtained from a mixture of toluene/benzene solution at –35 °C. Anal. Calcd for C₆₉H₁₀₄N₈O₆P₂Si₂ULi·(C₆H₆)₂: C, 59.02; H, 7.16; N, 6.63%. Found: C, 59.77; H, 7.17; N, 5.59%. ¹H NMR (C₆D₆, 298 K): δ 8.24 (m, 7 H, ArH), 7.25 (m, 8 H, ArH), 7.19 (m, 4 H, ArH), 7.12 (m, 5 H, ArH), 7.07-7.01 (m, 8 H, ArH), 3.44 (br, 10 H, OCH₂ or NCH₂), 3.26 (br, 12 H, OCH₂ or NCH₂), 2.22 (br, 10 H, OCH₂, NCH₂ or C-H of 1-adamantyl), 2.11 (s, 6 H, OCH₂, NCH₂ or C-H of 1-adamantyl), 2.09 (br, 6 H, OCH₂, NCH₂ or C-H of 1-adamantyl), 1.41 (m, br, 10 H, OCH₂, NCH₂ or C-H of 1-adamantyl), 1.34 (s, br, 10 H, OCH₂, NCH₂ or C-H of 1-adamantyl), 0.76 (s, 18 H, -SiMe₃). ³¹P{¹H} NMR (C₆D₆, 298 K): δ –17.91 (s). ¹³C{¹H} NMR (C₆D₆, 298 K): δ 145.15,

137.49, 132.50, 128.93, 125.29 (ArC), 99.98 (U=C), 73.14, 68.90, 68.05, 54.59, 53.58, 36.64, 31.37, 21.04 (NC/CH/CH₂ of 1-adamantyl or CH₂ of 2, 2, 2-cryptand), 3.91 (-SiMe₃). ⁷Li{¹H} NMR (C₆D₆, 298 K): δ -1.31 (s, br). The ²⁹Si NMR spectrum did not exhibit any resonances, which is attributed to the low solubility of **2** in benzene once isolated in crystalline form combined with the unfavourable $-\gamma$ NMR property of the ²⁹Si nucleus. Evans Method (C₆D₆, 298 K): 2.28 μ_B . ATR-IR ν/cm^{-1} : 3050 (w), 2898 (s), 2843 (s), 1976 (m), 1495 (m), 1449 (m), 1433 (s), 1368 (s), 1299 (s), 1237 (s), 1104 (m), 1078 (m), 1027 (w), 1017 (w), 982 (s), 959 (s), 945 (m), 928 (m), 830 (m), 798 (w), 749 (m), 729 (m), 710 (s), 694 (s), 675 (s), 657 (s), 633 (s), 616 (s), 601 (s), 520 (s), 509 (s), 484 (s), 466 (s), 420 (s). Raman ν/cm^{-1} (Neat, ≤ 5 mW): 3057 (m), 2891 (br, w), 1941 (br, w), 1586 (s), 1100 (br, m), 1285 (br, w), 629 (s). It should be noted that due to the sensitivity of the complex, any irradiating laser with power of > 1.5 mW causes visually observable signs of decomposition. On the other hand, multiple accumulation/long exposure time using reduced power laser are not available either, due to the thermal instability of the complex at room temperature, as well as due to its air/moisture sensitivity in the Raman cell. Attempts at dispersing **2** to suppress decomposition were unsuccessful.

Single Crystal X-ray Diffraction Details

Crystals were examined using an Agilent Supernova diffractometer equipped with an Eos CCD area detector and a Microfocus source with Mo K α radiation ($\lambda = 0.71073$ Å). Intensities were integrated from data recorded on narrow (0.5°) frames by ω rotation. Cell parameters were refined from the observed positions of all strong reflections the data set. Gaussian grid face-indexed absorption corrections with a beam profile correction were applied. The structure was solved by direct methods using SHELXT³ and the dataset was refined by full-matrix least-squares on all unique F^2 values, with anisotropic displacement parameters for all non-hydrogen atoms, and with constrained riding hydrogen geometries; $U_{iso}(H)$ was set at 1.2 (1.5 for methyl groups) times U_{eq} of the parent atom. The largest features in final difference syntheses were close to heavy atoms and were of no chemical significance. CrysAlisPro⁴ was used for control and integration, and SHELXL,⁵ Olex2⁶ and

PLATON⁷ were employed for structure refinement. ORTEP-3⁸ and POV-Ray⁹ were employed for molecular graphics. Crystals of **2** were found to be consistently twinned, but this was straightforwardly ameliorated using the following two-component twin law:

2-axis (0 0 1) [0 1 3], Angle () [] = 1.83 Deg, Freq = 46

(-1.000 0.000 0.000) (h1) (h2) Nr Overlap = 3476

(0.000 -1.000 0.000) * (k1) = (k2) BASF = 0.15

(0.077 0.676 1.000) (l1) (l2) DEL-R = -0.011

Lattice benzene molecules are each disordered over two orientations. In each case the occupancies were allowed to freely refine converging to final ratios of 0.59:0.41 and 0.46:0.54. 1,2-C-C bond distances in the benzene rings were restrained to be approximately 1.39 Å, and 1,3- and 1,4-C-C distances were restrained to be approximately equal. Each benzene ring was restrained to be approximately planar. Enhanced rigid bond and similarity thermal restraints were applied to all atoms in the lattice solvent. The C60-C61 distance in the cryptand unit was restrained to be approximately 1.55 Å. The C36 and C50 atoms in adamantyl units each exhibit unusual atomic displacement parameters. Enhanced rigid bond and similarity thermal restraints were applied to these atoms and all adjacent atoms. All other details are unexceptional and can be found in the cif file.

Computational Details

General

Unrestricted geometry optimisations for **2** were performed using coordinates derived from crystal structure as the start-point. No constraints were imposed on the structures during the geometry optimisations. However, the geometry optimised structure of **2** was found to contain a U1-N1 bond distance of 2.439 Å that is ~0.16 Å shorter than the distance in the experimental solid-state crystal structure. Furthermore, an analytical frequencies calculation on the geometry optimised coordinates computes a N₂ stretch of 1712 cm⁻¹, which does not compare well with the experimentally determined value. Therefore, a single point energy calculation was conducted on coordinates derived from the crystal structure of **2** and all computed data refer to this model. The calculations were performed using the Amsterdam Density Functional (ADF) suite version 2012.01.^{10,11} The DFT optimisations employed Slater type orbital (STO) triple- ζ -plus polarisation all-electron basis sets (from the ZORA/TZP database of the ADF suite). Scalar relativistic approaches were used within the ZORA Hamiltonian for the inclusion of relativistic effects and the local density approximation (LDA) with the correlation potential due to Vosko *et al* was used in all of the calculations.¹² Gradient corrections were performed using the functionals of Becke and Perdew.^{13,14} The TD-DFT calculation of **2** computed the first 200 transitions within ADF. Frequency calculations were carried out with the analytical frequencies approach within ADF. Natural Bond Order (NBO) analyses were carried out with NBO 5.0.¹⁵ MOLEKEL¹⁶ was used to prepare the three-dimensional plots of the electron density. The Atoms in Molecules analysis^{17,18} was carried out with Xaim-1.0.¹⁹

To account for the ~0.16 Å discrepancy of the U1-N1 bond length, relaxed potential energy scan calculations were performed at several levels of theory. Spin-unrestricted DFT, Hartree-Fock (UHF) and second-order Møller–Plesset perturbation theory (UMP2) calculations were performed in Gaussian version 09, Revision D.01, and version 16, Revision A.03.²⁰ Spin-restricted HF (RHF), and restricted active space-self consistent field^{21,22} (RASSCF) calculations were performed with Molpro 2018.2,²³ in integral direct mode.²⁴ DFT calculations were performed using the gradient corrected PBE functional²⁵ and used Grimme's D3 damping function.²⁶ On uranium, the 60 electron quasi-

relativistic effective core potential of the Stuttgart/Cologne Group was used, along with the associated valence basis set (of approximately quadruple- ζ quality).²⁷⁻²⁹ On all other elements, the def2-TZVPP basis set was used, obtained from the EMSL basis set library.^{30,31} For the XRD/RHF scan, the cc-pVDZ basis set was used on elements other than uranium.³²⁻³⁴

A full geometry optimisation was performed with UPBE, giving a U1-N1 bond distance of 2.393 Å. From this geometry, a relaxed potential energy scan was performed whereby the U1-N1 bond distance was increased in steps of 0.050 Å, to 2.743 Å, and decreased to 2.293 Å. At each point, all other geometric parameters were optimised, shown in Fig. 4 of the main text as ‘Relaxed / UPBE’. In addition, rigid potential energy scans were performed, where the $\text{N}_2[\text{Li}(2,2,2\text{-cryptand})]$ fragment was displaced from the crystal structure geometry in the U1-N1 axis, with UPBE and RHF (XRD / UPBE, RHF respectively in Fig. 4). The RHF scan has its minimum at 2.50 Å; in better agreement with experiment than the UPBE calculations but still some 0.1 Å away from the crystal structure geometry.

Further to this, calculations were performed on a ‘core’ model, **2 core**, shown in Fig. S12. From the crystal structure geometry, phenyl and adamantyl groups were replaced with methyl groups. SiMe_3 was replaced with SiH_3 , and only coordinating atoms of the cryptands were kept, with hydrogens added to balance charges. Hydrogen geometries were optimised at each geometry, at the restricted HF level of theory, with other atoms being kept at their crystal structure coordinates. The U1-N1 bond length was shortened in 0.05 Å increments, from the crystal structure geometry, 2.608 Å, to 2.358 Å, with the $\text{N}_2\text{Li}(\text{H}_2\text{O})_4\text{NH}_3$ fragment being translated in the U1-N1 axis. The UPBE and RHF scans on this core geometry suggest that this model is a good representation of the full molecule; the slightly shallower potential at shorter bond lengths in the RHF scans is likely a result of the reduction in steric bulk. The introduction of dynamic correlation at the UMP2 level of theory (based on a UHF reference)

results in a slightly steeper potential, compared with the UHF scan but an unchanged minimum point (at the 0.05 Å resolution of these scans).

RASSCF calculations on the core model were also performed. An ideal active space would conceivably include all bonding and antibonding orbitals in the uranium coordination sphere; this would be a [25,25] CASSCF calculation (the 2 U-N_{imido} σ, 4 U-N_{imido} π, 2 U-N_{amide} σ, 2 U-N_{amide} π, the C-U σ and π bonding orbitals, the corresponding antibonding orbitals, and the N₂ π* SOMO). This is however intractably large, so we performed a single initial RASSCF [17,17] calculation including only the π orbitals, and where all 114 non-active orbitals were frozen at the RHF reference. The only orbitals to show significant static correlation (antibonding orbitals with occupancy numbers >0.02) were the U-N_{imido} π orbitals, so this is the active space we employed in the potential energy scans; 9 electrons in 9 active orbitals. We used the conventional three active space formalism; RAS1 includes the 4 U-N_{imido} π bonding orbitals, RAS2 includes N₂ π* SOMO, and RAS3 contains the 4 U-N_{imido} π* antibonding orbitals. Double excitations are allowed out of RAS1, and triple excitations into RAS3. This corresponds to (9,2,3;4,1,4) in the conventional Sauri notation.³⁵ A RHF reference was used, and 78 orbitals frozen at this reference. The natural orbitals of the active space at the minimum energy point on the scan, 2.56 Å, are shown in Fig. S13, and their occupation numbers at each point are shown in Table S1. As Fig. 4 in the main text shows, the points at 2.51 Å, 2.56 Å and 2.61 Å are very close in energy; 2.51 Å is 0.15 and 2.61 Å is 0.80 kJ mol⁻¹ higher in energy than the minimum 2.56 Å. Introduction of more correlation energy with a larger active space, the increased steric bulk of the full molecule, or crystal packing forces could all shift the minimum to that of the crystal structure geometry – or indeed a combination of the three.

Characterisation Data

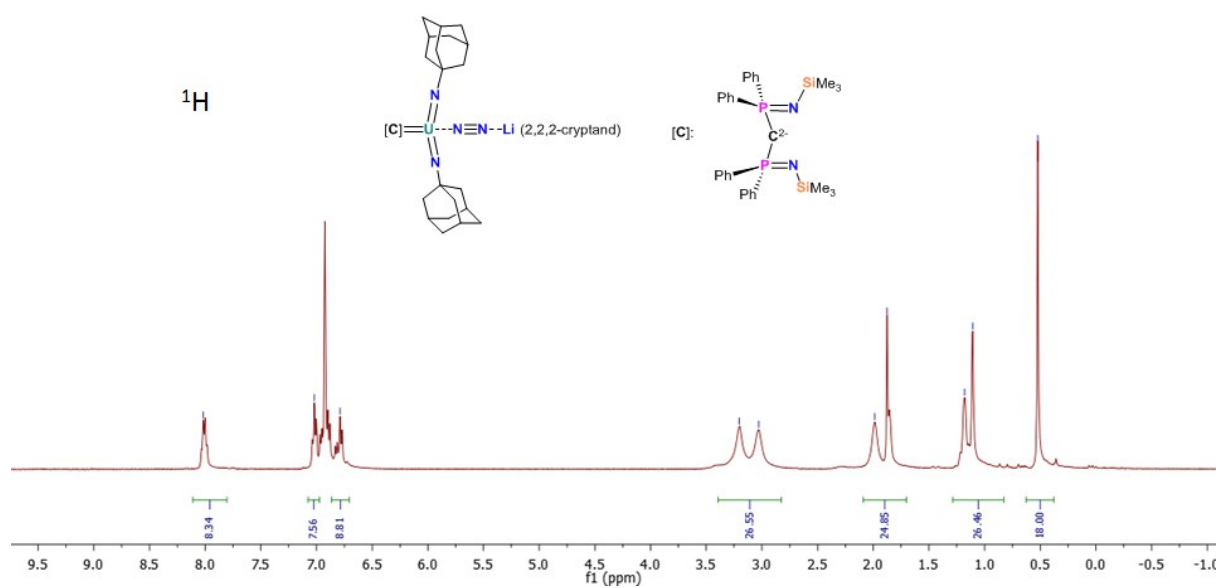


Figure S1. ^1H NMR spectrum of **2** (C_6D_6 , 25 °C).

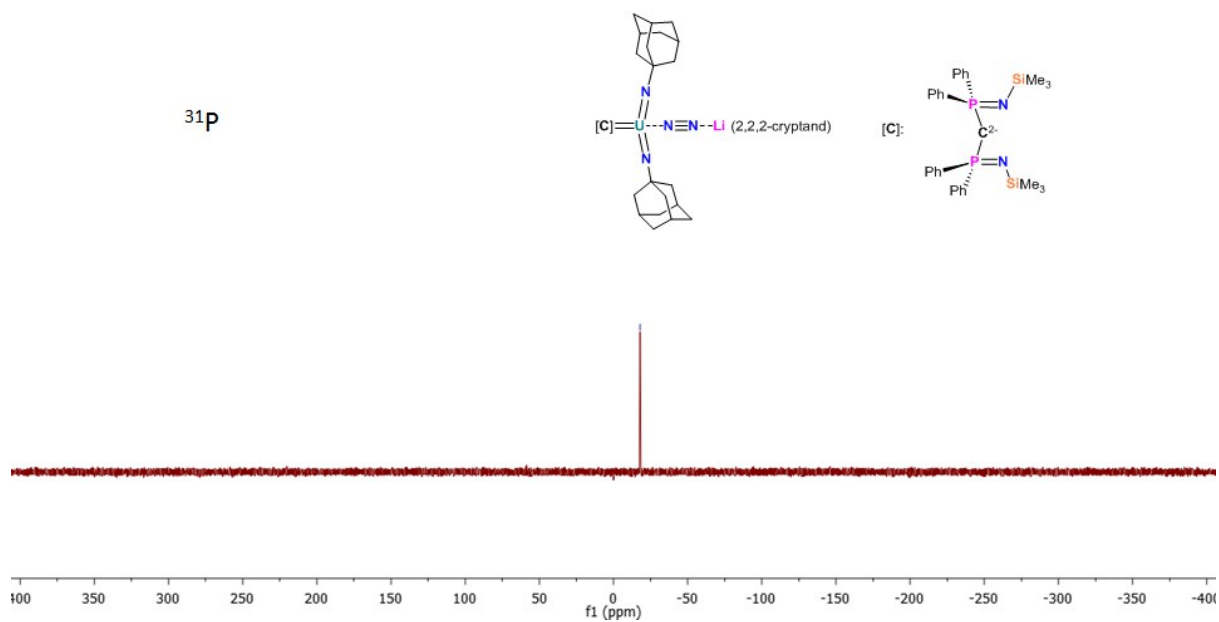


Figure S2. $^{31}\text{P}\{^1\text{H}\}$ NMR spectrum of **2** (C_6D_6 , 25 °C).

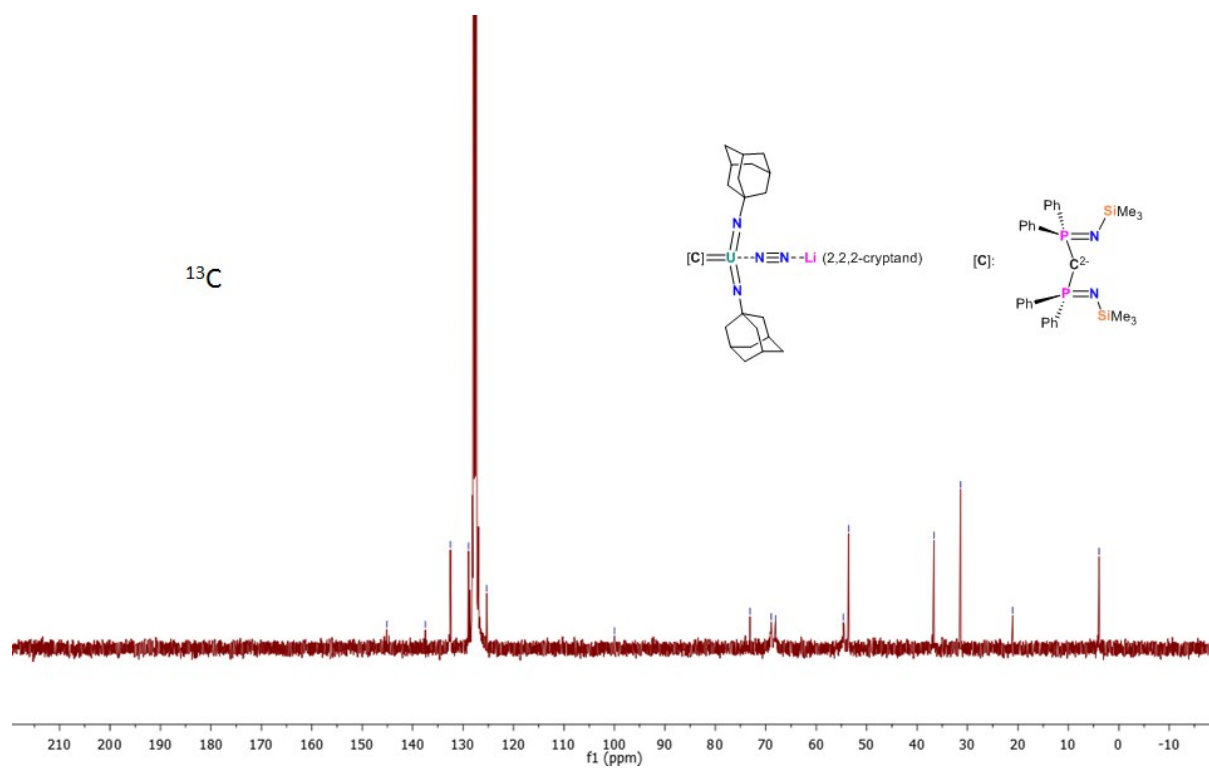


Figure S3. $^{13}\text{C}\{^1\text{H}\}$ NMR spectrum of **2** (C_6D_6 , 25 °C).

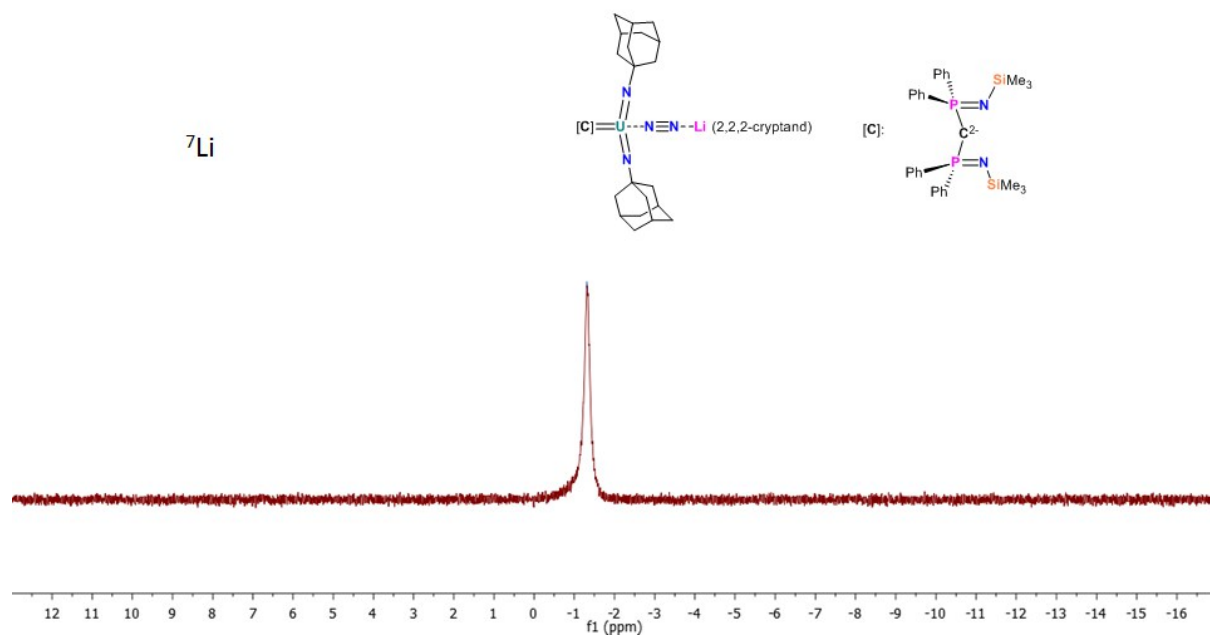


Figure S4. $^7\text{Li}\{^1\text{H}\}$ NMR spectrum of **2** (C_6D_6 , 25 °C).

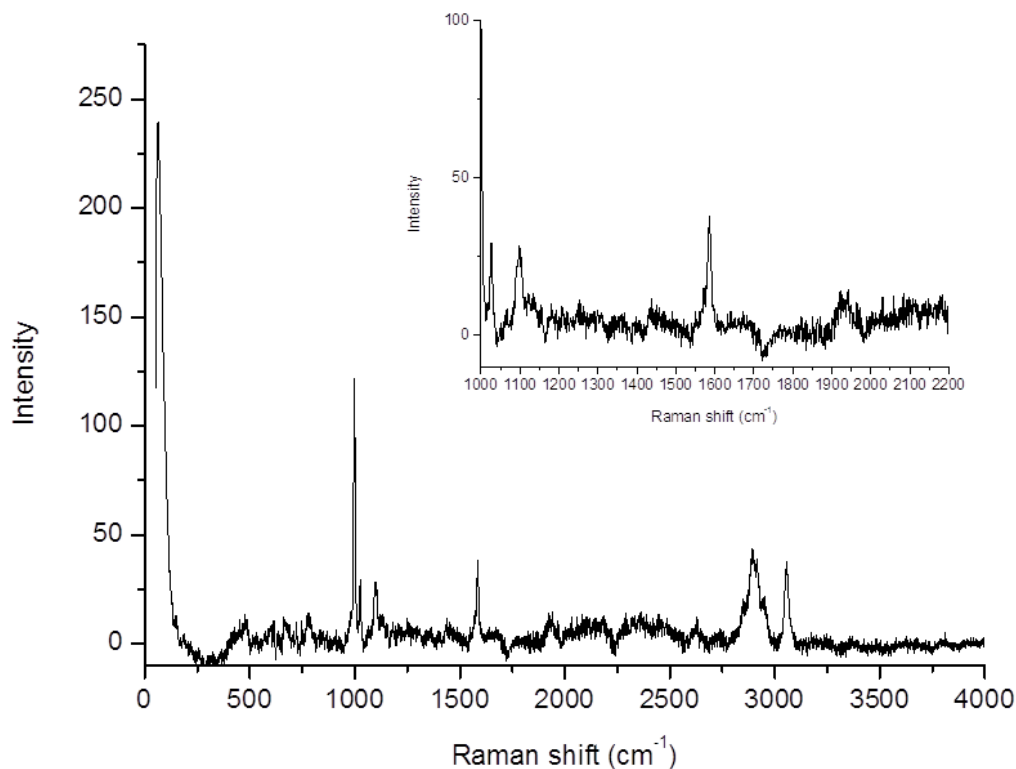


Figure S5. Raman spectrum of **2**. Inset is the enlarged view of the 1500 to 2200 cm^{-1} range. The strong features at 950-1200, ~ 1600 , and 2750-3100 are predominantly due to the $\{\text{C}(\text{PPh}_2\text{NSiMe}_3)_2\}^{2-}$ and 2,2,2-crypt ligands.

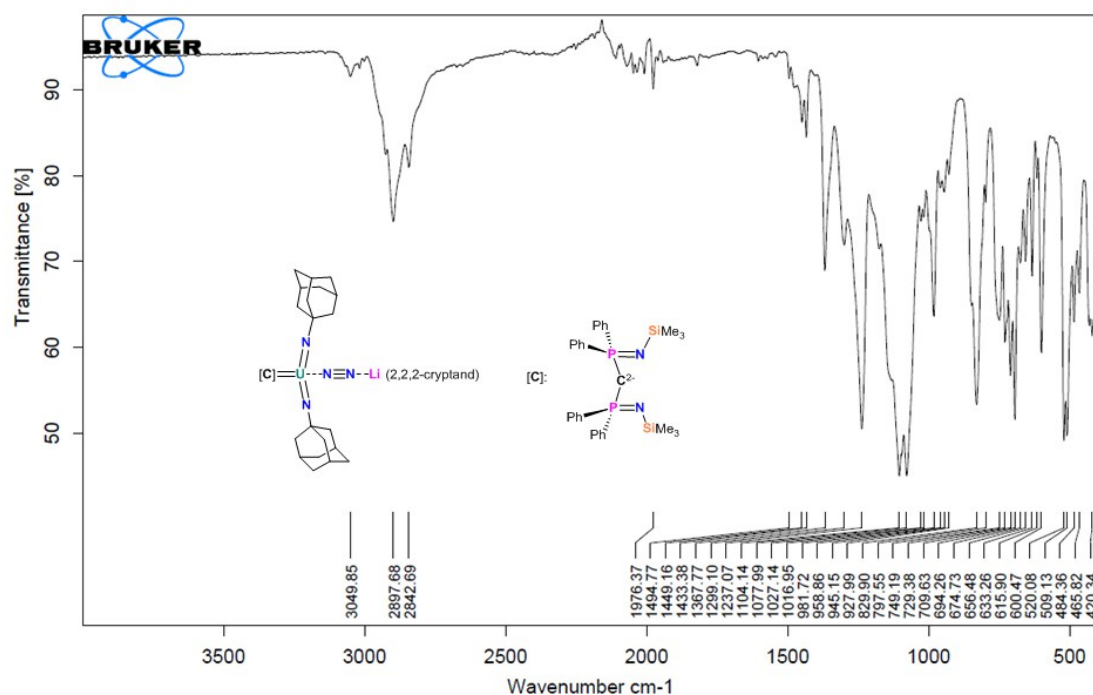


Figure S6. FTIR spectrum of **2**.

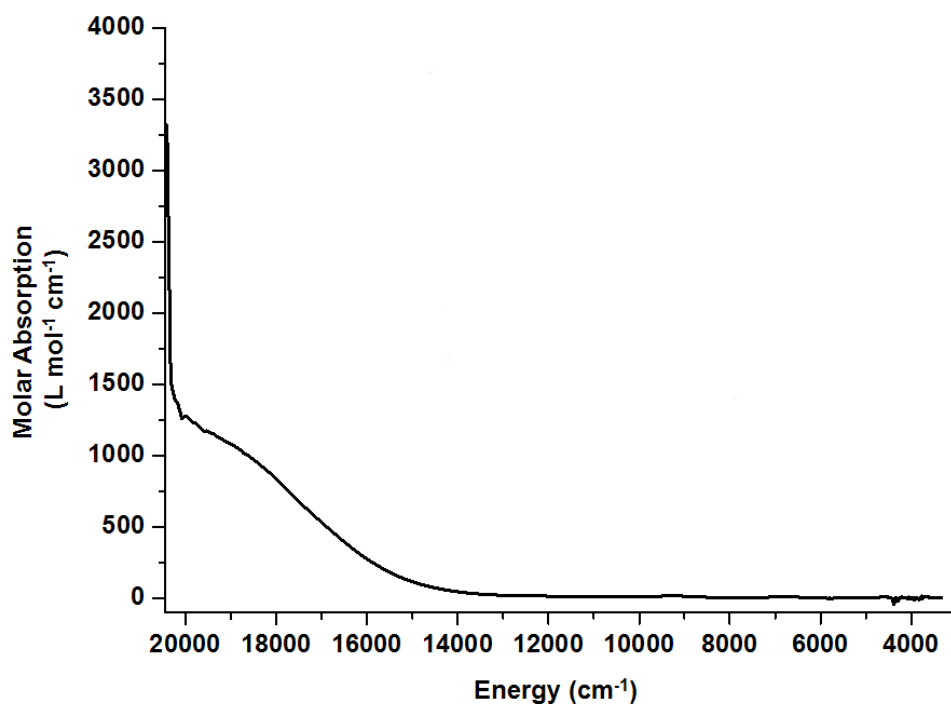


Figure S7. Electronic absorption spectrum of **2**. 30 mM in THF in 1 mm quartz cell. A zoom-in of the near-infrared region with TD-DFT modelled transitions can be found below.

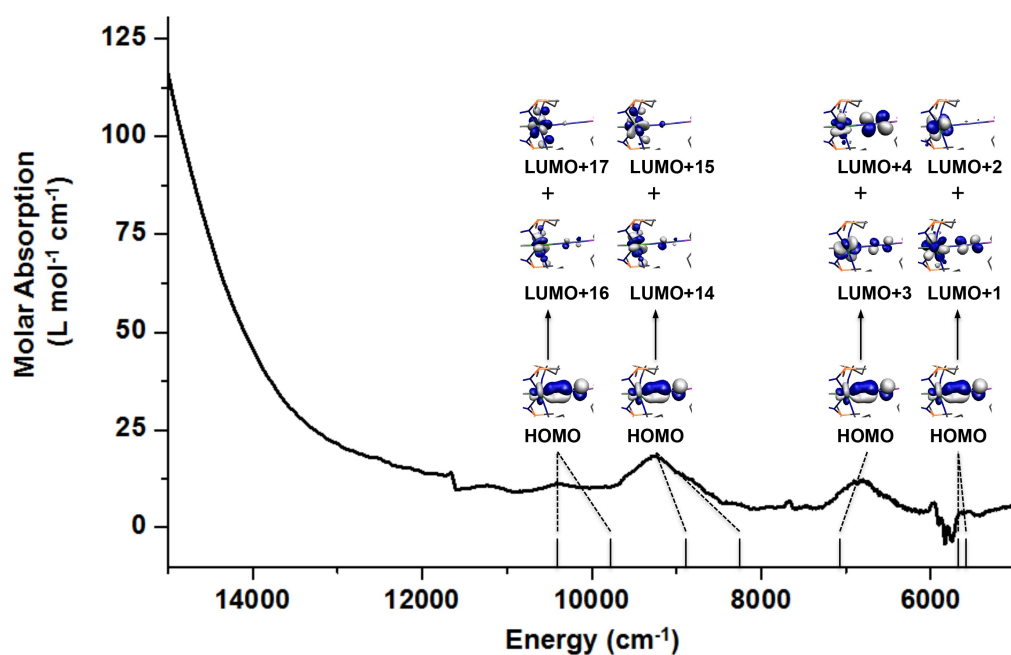


Figure S8. Zoom-in showing the near-infrared portion of the optical spectrum of **2** with computed transitions as vertical black lines and the majority components (>80%) of those transitions illustrated.

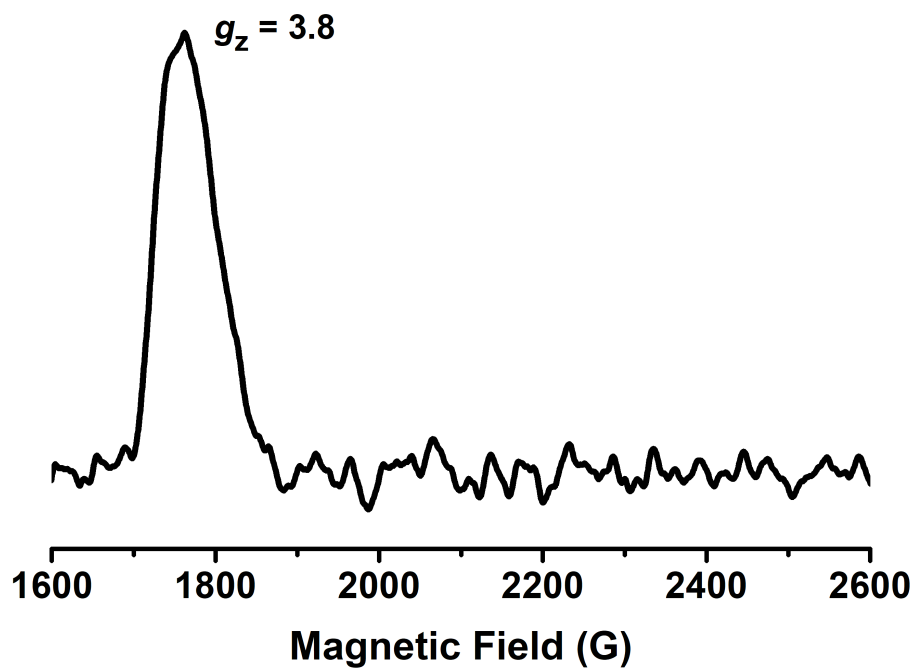


Figure S9. X-band EPR spectrum of **2**.

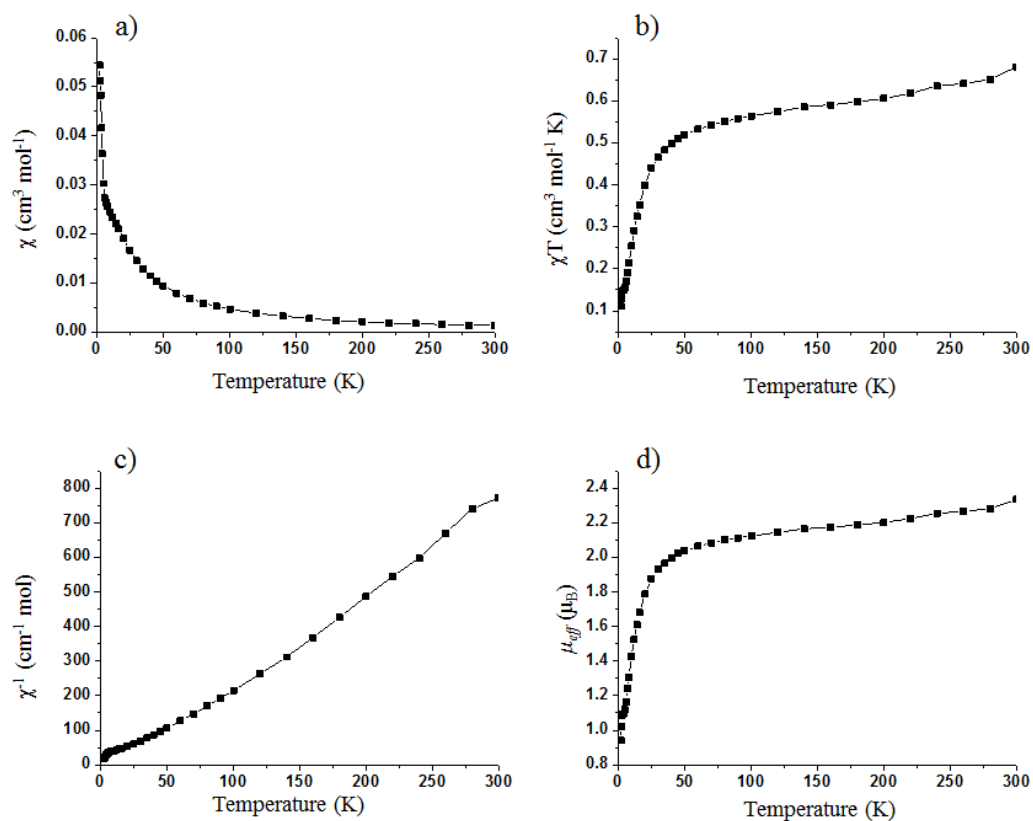


Figure S10. Variable-temperature SQUID magnetic data for powdered **2** in a 0.1 T applied magnetic field, presented as: (a) χ vs T; b) χT vs T; c) χ^{-1} vs T; d) μ_{eff} vs T.

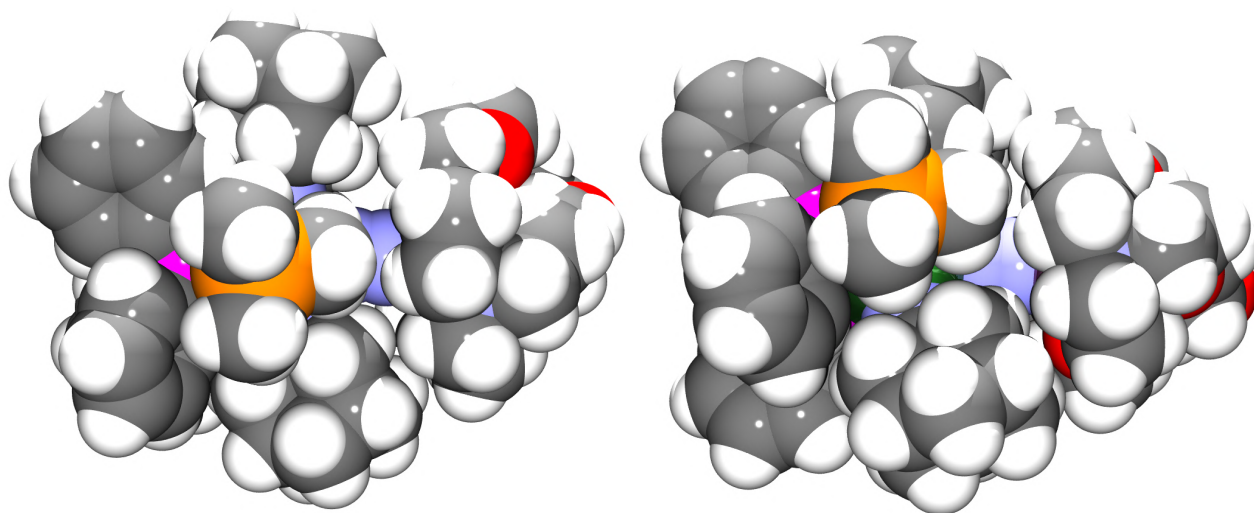


Figure S11. Space filling plots of **2** from two different angles highlighting that the N₂-Li-2,2,2-cryptand fragment could approach closer to the U(BIPM^{TMS})(NAd)₂ unit.

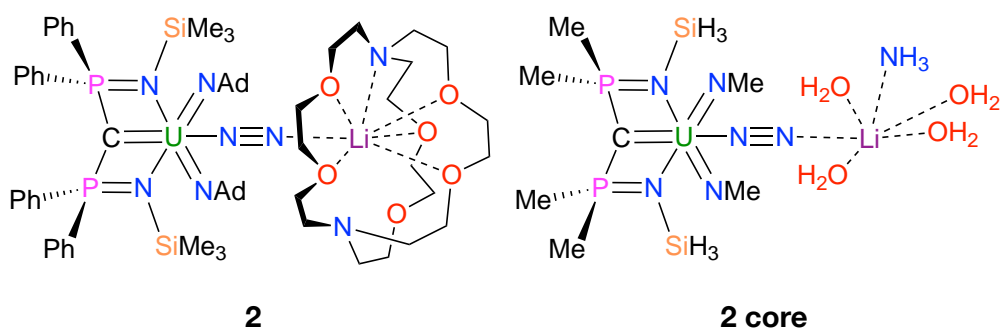


Figure S12. The structure of **2**, left, and the model **2 core**, used in potential energy scans, right

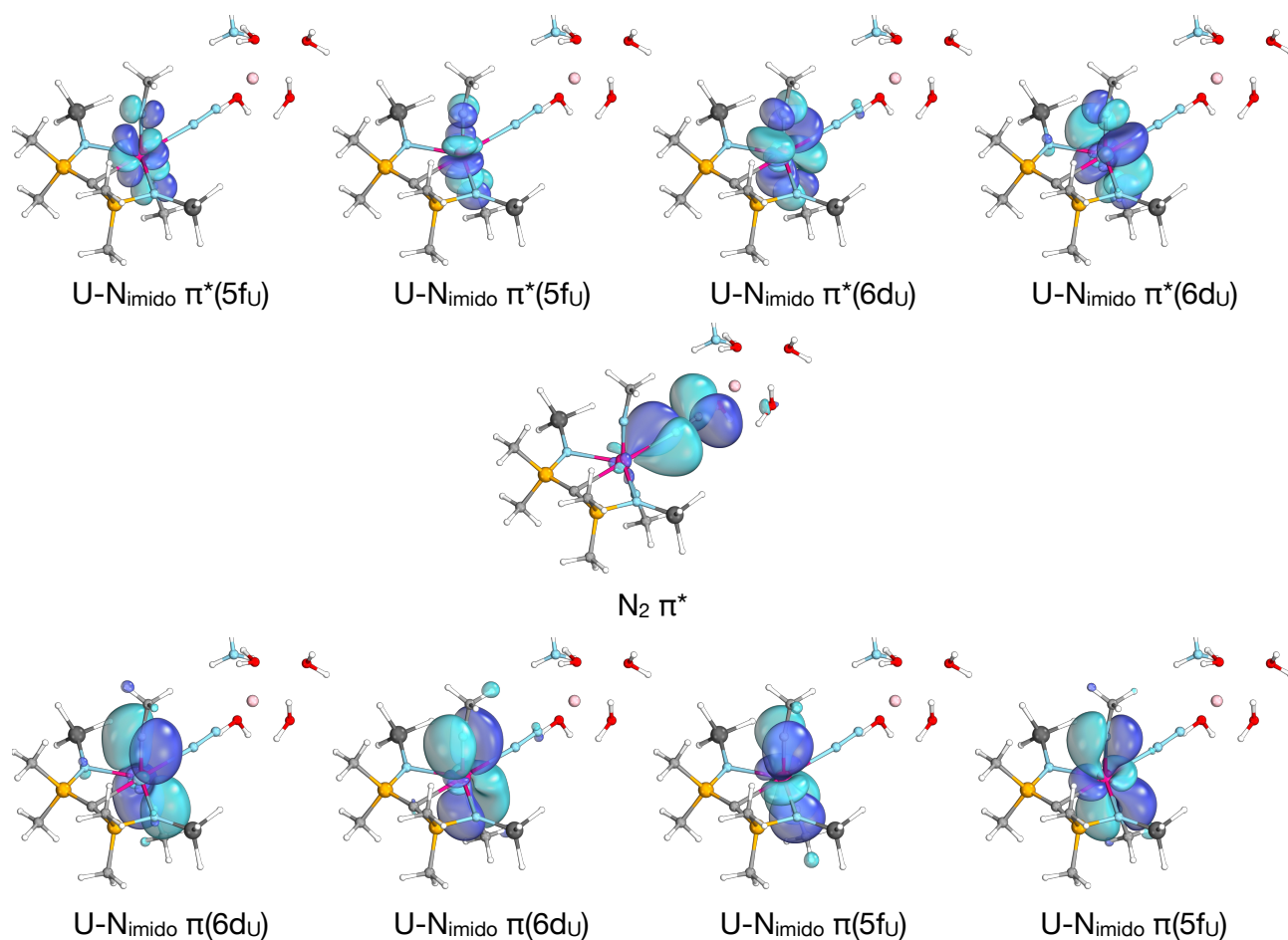


Figure S13. The natural orbitals of the RASSCF calculation on **2 core** at U1-N1 = 2.56 Å, the minimum energy point on the scan. Bottom row: RAS1, middle: RAS2, top: RAS3. The isosurfaces enclose 90% of the orbital electron density. Occupation numbers are shown in Table S1. Orbitals plotted with IboView.³⁶

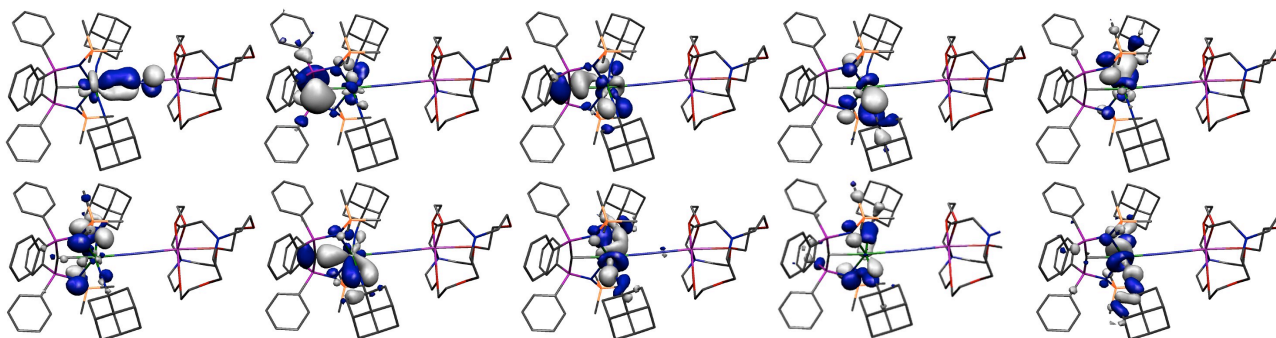


Figure S14. Kohn Sham molecular orbital representations of the principal frontier orbitals representing the uranium-N₂, -carbene, and -imido interactions. Top left to bottom right: HOMO (388a, -1.715 eV), HOMO-1 (387a, -3.349 eV), HOMO-2 (386a, -3.649 eV), HOMO-3 (385a, -3.920 eV), HOMO-4 (384a, -3.995 eV), HOMO-5 (383a, -4.153 eV), HOMO-6 (382a, -4.263 eV), HOMO-7 (381a, -4.676 eV), HOMO-10 (378a, -5.012 eV), HOMO-11 (377a, -5.245 eV).

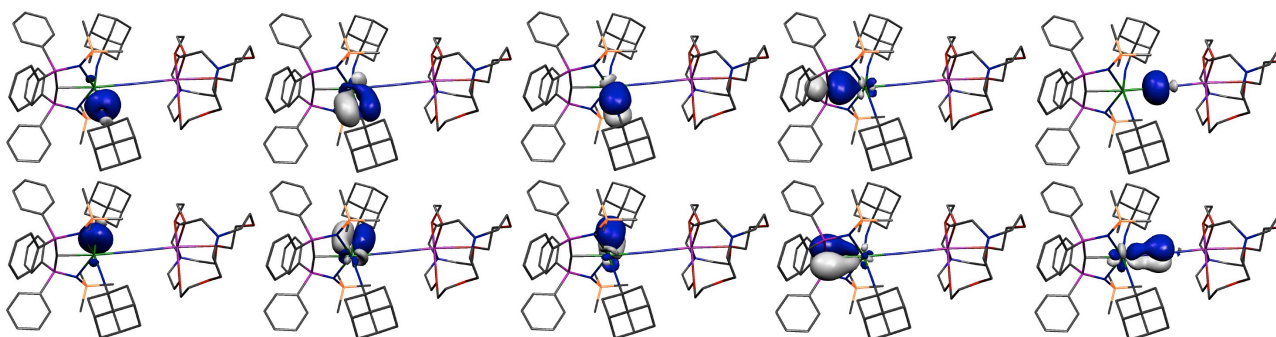


Figure S15. NBO representations of the uranium-N₂, -carbene, and -imido interactions. Top left to bottom right: U=Nσ, U=Nπ, U=Nπ, U=Cσ, U-N₂σ, U=Nσ, U=Nπ, U=Nπ, U=Cπ, U-N₂π.

Table S1. Occupation numbers of the natural orbitals of the RASSCF calculations on **2 core**, at each point on the scan. The structure of **2 core** is shown in Fig. S14, and the isosurfaces of the natural orbitals shown in Fig. S15.

	U1-N1 Bond length / Å					
	2.36	2.41	2.46	2.51	2.56	2.61
U-N _{imido} $\pi(6d_U)$	1.963	1.963	1.963	1.963	1.963	1.963
U-N _{imido} $\pi(6d_U)$	1.959	1.959	1.958	1.958	1.958	1.958
U-N _{imido} $\pi(5f_U)$	1.935	1.935	1.934	1.934	1.934	1.933
U-N _{imido} $\pi(5f_U)$	1.932	1.931	1.931	1.931	1.930	1.930
N ₂ π^*	1.000	1.000	1.000	1.000	1.000	1.000
U-N _{imido} $\pi^*(5f_U)$	0.070	0.070	0.071	0.071	0.072	0.072
U-N _{imido} $\pi^*(5f_U)$	0.066	0.066	0.067	0.067	0.068	0.068
U-N _{imido} $\pi^*(6d_U)$	0.041	0.041	0.041	0.041	0.041	0.041
U-N _{imido} $\pi^*(6d_U)$	0.035	0.035	0.035	0.035	0.035	0.035

For brevity, tables S2-S28 which gave computational geometries are not shown in this version included in the thesis and are available online at <http://doi.org/10.1038/s41557-019-0306-x>

Table S29. Energy of points in the relaxed energy scan

r(U1-N1) / Å	Energy / Hartree	Relative energy / kJ mol⁻¹
2.2927	-5324.136563	3.28
2.3427	-5324.137523	0.75
2.3927	-5324.137811	0.00
2.4427	-5324.137576	0.62
2.4927	-5324.136920	2.34
2.5427	-5324.136921	2.34
2.5927	-5324.135943	4.90
2.6427	-5324.134733	8.08
2.6927	-5324.133354	11.70
2.7427	-5324.131865	15.61

Table S30. Energy of points in the XRD scans

r(U1-N1) / Å:	XRD / UPBE		XRD / RHF	
	Energy / Hartree	Relative energy / kJ mol⁻¹	Energy / Hartree	Relative energy / kJ mol⁻¹
2.30	-5322.971423	1.68	-5299.454257	17.32
2.35	-5322.972064	0.00	-5299.457275	9.40
2.40	-5322.971929	0.36	-5299.459255	4.20
2.45	-5322.971185	2.31	-5299.460391	1.22
2.50	-5322.969973	5.49	-5299.460855	0.00
2.55	-5322.968412	9.59	-5299.460785	0.18
2.60	-5322.966599	14.35	-5299.460302	1.45
2.65	-5322.964617	19.55	-5299.459514	3.52
2.70	-5322.962527	25.04	-5299.458477	6.25

Table S31. Energy of points in the spin-unrestricted core scans

r(U1-N1) / Å:	Core / UPBE		Core / UHF		Core / UMP2	
	Energy / Hartree	Relative energy / kJ mol⁻¹	Energy / Hartree	Relative energy / kJ mol⁻¹	Energy / Hartree	Relative energy / kJ mol⁻¹
2.36	-2717.034374	0.07	-2708.634864	4.11	-	-
2.41	-2717.034399	0.00	-2708.635594	2.19	-2713.257353	3.67
2.46	-2717.033849	1.44	-2708.636286	0.38	-2713.258425	0.86
2.51	-2717.032974	3.74	-2708.636429	0.00	-2713.258752	0.00
2.56	-2717.031761	6.93	-2708.636145	0.75	-2713.258401	0.92
2.61	-2717.030409	10.48	-2708.635532	2.36	-2713.257451	3.42

Table S32. Energy of points in the spin-restricted core scans

r(U1-N1) / Å:	Core / RHF		Core / RASSCF	
	Energy / Hartree	Relative energy / kJ mol⁻¹	Energy / Hartree	Relative energy / kJ mol⁻¹
2.36	-2708.612186	5.52	-2708.758769	9.26
2.41	-2708.613533	1.98	-2708.760606	4.44
2.46	-2708.614186	0.26	-2708.761715	1.52
2.51	-2708.614287	0.00	-2708.762238	0.15
2.56	-2708.613957	0.87	-2708.762295	0.00
2.61	-2708.613288	2.62	-2708.761989	0.80

References

1. E. Lu, J. T. Boronski, M. Gregson, A. J. Wooles, S. T. Liddle, *Angew. Chem. Int. Ed.* **2018**, *57*, 5506.
2. G. A. Bain, J. F. Berry, *J. Chem. Edu.* **2008**, *85*, 532.
3. G.M. Sheldrick, *Acta Cryst. Sect. A* **2015**, *A71*, 3.
4. CrysAlisPRO version 39.46, Oxford Diffraction /Agilent Technologies UK Ltd, Yarnton, England.
5. G.M. Sheldrick, *Acta Cryst. Sect. C* **2015**, *C71*, 3.
6. O.V. Dolomanov, L.J. Bourhis, R.J. Gildea, J.A.K. Howard, H. Puschmann, *J. Appl. Cryst.* **2009**, *42*, 339.
7. A.L. Spek, *Acta Cryst. Sect. D* **2009**, *D65*, 148.
8. L.J. Farugia, *J. Appl. Cryst.* **2012**, *45*, 849.
9. Persistence of Vision (TM) Raytracer, Persistence of Vision Pty. Ltd., Williamstown, Victoria, Australia.
10. C. Fonseca Guerra, J. G. Snijders, G. Te Velde, E. J. Baerends, *Theor. Chem. Acc.* **1998**, *99*, 391.
11. G. Te Velde, F. M. Bickelhaupt, S. J. van Gisbergen, A. C. Fonseca Guerra, E. J. Baerends, J. G. Snijders, T. Ziegler, *J. Comput. Chem.* **2001**, *22*, 931.
12. S. H. Vosko, L. Wilk, M. Nusair, *Can. J. Phys.* **1980**, *58*, 1200.
13. A. D. Becke, *Phys. Rev. A* **1988**, *38*, 3098.
14. J. P. Perdew, *Phys. Rev. B* **1986**, *33*, 8822.
15. NBO 5.0: E. D. Glendening, J. K. Badenhoop, A. E. Reed, J. E. Carpenter, J. A. Bohmann, C. M. Morales, F. Weinhold, (Theoretical Chemistry Institute, University of Wisconsin, Madison, WI, 2001); <http://www.chem.wisc.edu/~nbo5>.
16. S. Portmann, H. P. Luthi, *Chimia* **2000**, *54*, 766.

17. R. F. W. Bader, *Atoms in Molecules: A Quantum Theory*, Oxford University Press, New York, 1990.
18. R. F. W. Bader, *J. Phys. Chem. A* **1998**, *102*, 7314.
19. <http://www.quimica.urv.es/XAIM>.
20. Gaussian 09, Revision D.03, and Gaussian 16, Revision A.02, M. J. Frisch, G. W. Trucks, H. B. Schlegel, G. E. Scuseria, M. A. Robb, J. R. Cheeseman, G. Scalmani, V. Barone, G. A. Petersson, H. Nakatsuji, X. Li, M. Caricato, A. Marenich, J. Bloino, B. G. Janesko, R. Gomperts, B. Mennucci, H. P. Hratchian, J. V. Ortiz, A. F. Izmaylov, J. L. Sonnenberg, D. Williams-Young, F. Ding, F. Lipparini, F. Egidi, J. Goings, B. Peng, A. Petrone, T. Henderson, D. Ranasinghe, V. G. Zakrzewski, J. Gao, N. Rega, G. Zheng, W. Liang, M. Hada, M. Ehara, K. Toyota, R. Fukuda, J. Hasegawa, M. Ishida, T. Nakajima, Y. Honda, O. Kitao, H. Nakai, T. Vreven, K. Throssell, J. A. Montgomery, Jr., J. E. Peralta, F. Ogliaro, M. Bearpark, J. J. Heyd, E. Brothers, K. N. Kudin, V. N. Staroverov, T. Keith, R. Kobayashi, J. Normand, K. Raghavachari, A. Rendell, J. C. Burant, S. S. Iyengar, J. Tomasi, M. Cossi, J. M. Millam, M. Klene, C. Adamo, R. Cammi, J. W. Ochterski, R. L. Martin, K. Morokuma, O. Farkas, J. B. Foresman, D. J. Fox, Gaussian, Inc., Wallingford CT, 2016.
21. H. -J. Werner and P. J. Knowles, *J. Chem. Phys.* **1985**, *82*, 5053.
22. P. J. Knowles and H. -J. Werner, *Chem. Phys. Lett.* **1985**, *115*, 259.
23. MOLPRO, version 2019.1, a package of ab initio programs, H.-J. Werner, P. J. Knowles, G. Knizia, F. R. Manby, M. Schütz, and others , *see* <http://www.molpro.net>.
24. M. Schütz, R. Lindh, and H.-J. Werner, *Mol. Phys.* **96**, 719 (1999).
25. J. P. Perdew, K. Burke, M. Ernzerhof, *Phys. Rev. Lett.* **1996**, *77*, 3865.
26. S. Grimme, J. Antony, S. Ehrlich, H. Krieg, *J. Chem. Phys.* **2010**, *132*, 154104.
27. X. Cao, M. Dolg, H. Stoll, *J. Chem. Phys.* **2003**, *118*, 487.
28. X. Cao, M. Dolg, *THEOCHEM* **2004**, *673*, 203.
29. W. Küchle, M. Dolg, H. Stoll, H. Preuss, *J. Chem. Phys.* **1994**, *100*, 7535.

30. F. Weigend, R. Ahlrichs, *Phys. Chem. Chem. Phys.* **2005**, 7, 3297.
31. K. L. Schuchardt, B. T. Didier, T. Elsethagen, L. Sun, V. Gurumoorthi, J. Chase, J. Li, T. L. Windus, *J. Chem. Inf. Model.* **2007**, 47(3), 1045-1052.
32. T. H. Dunning, *J. Chem. Phys.* **1989**, 90, 1007-1023.
33. R. A. Kendall, T. H. Dunning and R. J. Harrison, *J. Chem. Phys.* **1992**, 96, 6796-6806.
34. D. E. Woon and T. H. Dunning, *J. Chem. Phys.* **1993**, 98, 1358-1371.
35. V. Sauri, L. Serrano-Andrés, A. R. M. Shahi, L. Gagliardi, S. Vancoillie and K. Pierloot, *J. Chem. Theory Comput.* **2011**, 7, 153-168.
36. G. Knizia and J. E. M. N. Klein, *Angew. Chem. Int. Ed.* **2015**, 54 5518.

Synthesis, characterisation and electronic structure of U_2N_2 complexes

Benjamin E. Atkinson, Matthew Gregson, David M. King, Stephen T. Liddle and Nikolas Kaltsoyannis

The tripodal ligand $\text{Tren}^{\text{TIPS}}$ has been previously used to obtain novel uranium bonding motifs such as a uranium-nitride triple bond, a uranium arsenic bonding interaction, and terminal pnictide complexes.^{1,66,67,71} The uranium nitride $\text{UNTren}^{\text{TIPS}}$ was the first terminal uranium isolable in ambient conditions, and features a $\text{U}\equiv\text{N}$ triple bond. The complexes studied in this work were obtained in the Liddle group at the University of Manchester by reaction of $\text{UNTren}^{\text{TIPS}}$ with lithium. Both diuranium complexes feature a U_2N_2 ring; in one case, the two uraniums are bridged by two nitrides, and in the other by a nitride and imido.

The bare molecule U_2N_2 was studied by Vlaisavljevich *et al.*, who identified a delocalised 12-electron bonding system in the ring in a matrix isolation and theoretical study.⁷⁷ While there have been two previous examples of isolable complexes featuring U_2N_2 rings, they have not yet been studied computationally.^{75,76,82} I performed a detailed study of the U(IV) diuranium bis-nitride complex, comparing the electronic structure to that of the bare molecule. I identified a 12-electron bonding system similar in character to that of the bare molecule, with 4 σ and 2 π bonding orbitals in the ring.

Contribution statement

I devised and performed calculations at the DFT, CASSCF and CASPT2 levels of theory, NBO and QTAIM analyses, and analysed the results, with supervision from NK. I drafted the manuscript with input from all authors. MG and DMK prepared and characterised the compounds, STL came up with the research idea and STL and NK directed the work, analysed the data.

Synthesis, characterisation and electronic structure of U₂N₂ complexes

Benjamin E. Atkinson, Matthew Gregson, David M. King, Nikolas Kaltsoyannis* and
Stephen T. Liddle*

Department of Chemistry, University of Manchester, Oxford Road, Manchester M13
9PL, UK

Abstract

We report the synthesis, characterisation and computational investigation of the electronic structure of two diuranium complexes. Both are obtained from reduction of a previously-reported U(V) uranium nitride complex, and both feature U₂N₂ rings. The first has a bridging imido and nitride, and the second two bridging nitrides. The electronic structure of the latter is compared to that of the bare U₂N₂ molecule in a detailed computational study, including density functional theory and multiconfigurational calculations. The U-N bond in the U₂N₂ ring features a single bond and a partial delocalised π bond, and there is minimal U-U interaction.

1 Introduction

Uranium's central role in nuclear power has long driven interest in its chemistry, including at the most fundamental level. Uranium-nitrogen chemistry is of particular interest because of the potential for uranium nitride to be used in generation IV reactors, given its higher melting point and density than the conventional UO_2 .^[1] Additionally, because of the potential of amido and imido ligands in nitrogen fixation catalysis, there is interest in actinide complexes featuring novel, and multiple, uranium-nitrogen bonds.^[2–8] Sterically hindered ligands have been highly successful in exposing novel bonding motifs in uranium-pnictogen chemistry.^[7–11] The tetradentate, tripodal $\text{Tren}^{\text{TIPS}}$ ligand, $[\text{N}(\text{CH}_2\text{CH}_2\text{NSi}(\text{iPr})_3)_3]^{3-}$, featured in the first terminal uranium-nitride with a $\sigma^2\pi^4 \text{U}\equiv\text{N}$ triple bond;^[12,13] the tripodal ligand forms a well-defined pocket for the terminal uranium nitride to reside in. The $\text{Tren}^{\text{TIPS}}$ ligand has also been used to support a variety of other uranium-pnictogen bonds, such as uranium-arsenic single, double and triple bonding interactions,^[14] and terminal pnictide ($\text{E}=\text{N}, \text{P}, \text{As}$) complexes.^[15,16]

The first molecule to feature a U_2N_2 motif was isolated in 1998 by Roussel and Scott.^[17] The ring is encapsulated by two ligands very similar to $\text{Tren}^{\text{TIPS}}$, with $\text{Si}^{\text{i}}\text{BuMe}_2$ in place of $\text{Si}^{\text{i}}\text{Pr}_3$ (' $\text{Tren}^{\text{DMSIB}}$ '), to give $\text{U}_2\text{N}_2[\text{Tren}^{\text{DMSIB}}]_2$, **a** in Figure 1. The length of the $\text{N}\equiv\text{N}$ bond, 1.11 Å, is essentially unperturbed from free N_2 (1.10 Å); the complex has side-on coordination of two $\text{U}(\text{III})$ units to N_2 . This is reflected in the length of the $\text{U}-\text{N}$ bonds (average 2.42 Å), and DFT calculations which revealed a $\text{U } 5f \rightarrow \text{N } \pi$ backbond.^[18,19]

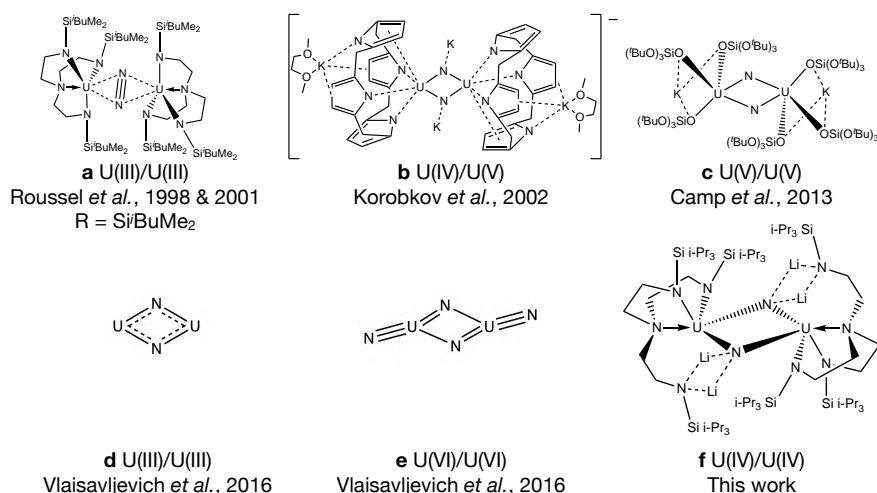


Figure 1: The structure of previously reported molecules with a U_2N_2 motif, **a-e**, and **f**, the complex which is the principal focus of this work. For **b**, ethyl groups on the bridging carbon of the calix[4]-tetrapyrrole are omitted for clarity

The first complex containing a U_2N_2 nitride motif was synthesised by Korobkov *et al.* in 2002.^[20] The anionic complex, **b** in Figure 1, features the U_2N_2 ring sequestered by two tetranionic calix[4]-tetrapyrrole ligands. The crystal structure is centrosymmetric; either the complex is Class 1 mixed-valence, or Class 2, with distinct U(IV) and U(V) centres with the two metals being disordered over both positions. The U-N bonds are substantially shorter than those obtained by Roussel and Scott, at an average of 2.09 Å, and the N-N distance of 2.46 Å clearly indicates the presence of nitrides. More recently, in 2013, Camp *et al.* identified a U_2N_2 -containing complex featuring two U(V) centres, **c** in Figure 1.^[7] Two of the U-N bonds are 2.02 Å, with the other pair being 2.10 Å, suggesting multiple bonding character in the ring. The N-N distance of 2.48 Å again indicates no bonding interaction between the two ring nitrogens. Barluzzi *et al.* reported an improved synthesis and a study of **c**'s magnetic properties in 2019.^[21]

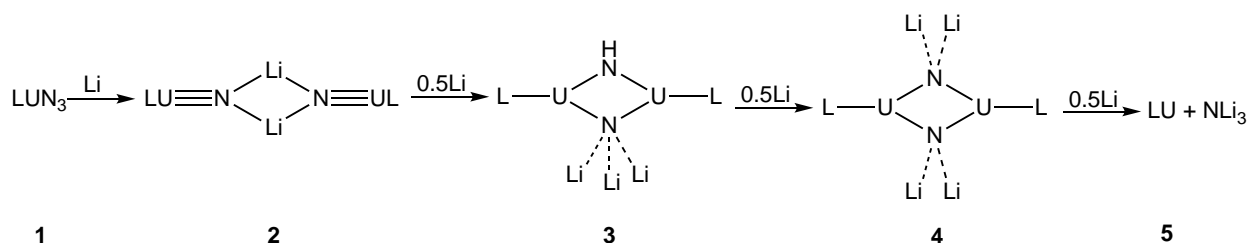
U_2N_2 (**d** in Figure 1) and U_2N_4 (**e**) were studied by Vlaisavljevich *et al.*.^[22] They obtained argon matrix-isolated IR absorption spectra and performed high-level calculations. DFT geometry optimisation of U_2N_2 gave a D_{2h} septet ground state, with the

six unpaired electrons occupying $5f_U$ character non-bonding orbitals, and a delocalised σ and π bonding system. At the RASPT2 level, a multiconfigurational quintet was observed. By contrast, U_2N_4 has a singlet ground state at both the DFT and CASPT2 levels, the latter showing it to be mostly monoconfigurational, with a significant alternation in the U-N ring bonds, one pair of which are single bonds and the other double bonds.

Herein, we report the synthesis and characterisation of two diuranium complexes obtained from the reduction of a uranium nitride with lithium; a complex featuring a U_2N_2 rhombic ring and two U(IV) centres, and a related U(IV)/U(IV) complex featuring both a nitride and imido bridging nitrogen. We also report calculations at the DFT level of theory on **3** and **4** (Scheme 1), and with the complete, and restricted, active space-self consistent field approaches on **4**. These calculations are used to investigate the electronic structure, including the extent of any U-U interaction, and to make comparisons with the previous work on molecular U_2N_2 and U_2N_4 .

2 Results and Discussion

We previously obtained the U(IV)-N₃ complex **1**; treatment of **1** with one equivalent of lithium gives the lithium-capped U(V) nitride **2** (scheme 1).^[13,23] Subsequent reduction of **2** with 0.5 Li equivalents gave the U(IV) diuranium imido/nitride complex **3**, U₂NHNLi₃[Tren^{TIPS}]₂, and further treatment of **3** with Li gave the U(IV) diuranium nitride complex **4**, U₂N₂Li₄[Tren^{TIPS}]₂. We additionally obtained **3** from **4** with either benzo-9-crown-3 or AgBH₄.



Scheme 1: Synthesis of **3** and **4** by stepwise reduction of **2** with lithium (L = Tren^{TIPS}).

The structures of **3** and **4** were determined by X-ray diffraction and are shown in Figure 2. Ring bond lengths of **3**, which has *C*₂ symmetry, are 2.22 Å (U1-N1) and 2.17 Å (U1-N2). Based on the crystal structure, **3** could conceivably have been a mixed U(IV)/U(V) U₂N₂ complex, or U(IV)/U(IV) with a nitride and imido nitrogen. We therefore performed hybrid DFT (PBE0) geometry optimisations on **3**; that of the U(IV)/U(V) form gave bond lengths of 2.02 Å (U1-N2) and 2.13 Å (U1-N1), whereas U(IV)/U(IV) gave 2.21 Å and 2.15 Å. This suggests that a mixed oxidation state U₂N₂ core, as observed by Korobkov *et al.* (**b** in Figure 1) is disfavoured versus a U(IV)/U(IV) system. Quantum Theory of Atoms-in-Molecules (QTAIM)^[24] and Natural Bond Orbital (NBO) bonding metrics and charges are given in Table 1. The significantly weaker U-N_{imido} bond is reflected in both the Wiberg Bond Index (WBI) and delocalisation index

$\delta(\text{U}, \text{N}_{\text{imido}})$ (0.84 and 0.86 respectively) versus that of the $\text{U}-\text{N}_{\text{nitride}}$ bond (1.13 and 1.05 respectively).

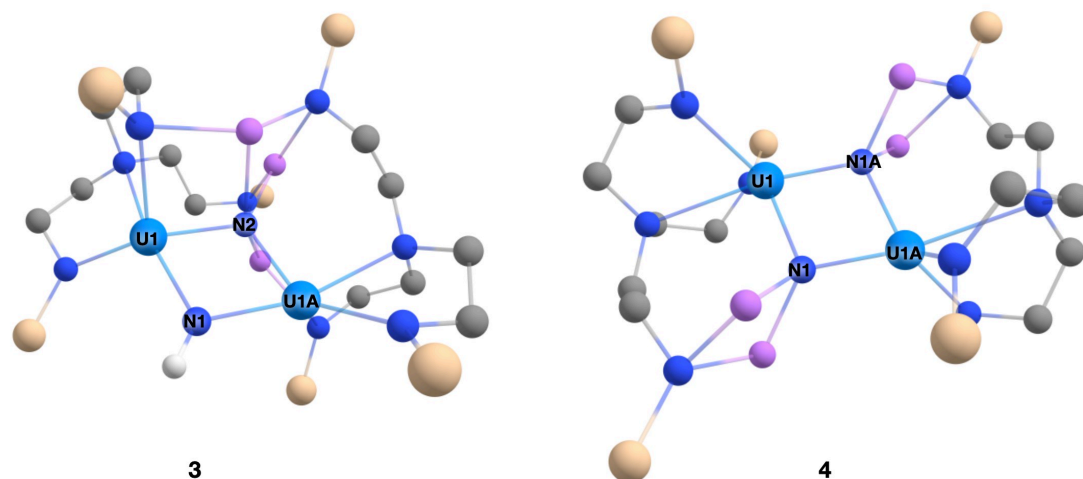


Figure 2: Molecular structure of **3** (left) and **4** (right). For clarity, isopropanyl groups and alkyl hydrogens are omitted. Light blue: uranium, dark blue: nitrogen, brown: silicon, grey: carbon, white: hydrogen. For **3**, selected distances are: U1-N1 . For **4**, selected distances are: U1-N1 2.181 Å, U1-N1A 2.148 Å, U1-U1A: 3.367 Å.

Table 1: NBO and QTAIM bond indices and charges, for the optimised geometry of **3** with the PBE0 functional, and the full molecule (**4**) and SiH₃ model (**4A**), at the crystal structure geometry (XRD) and the optimised geometry (opt), with both PBE and PBE0 functionals. For **3**, U-N_{ring}^a are the U-N_{nitride} bonds and U-N_{ring}^b are the U-N_{imido} bonds (both pairs of bonds equal due to C₂ symmetry) and * is the N_{imido} charge, and for **4** U-N_{ring}^a is the shorter pair of bonds, U-N_{ring}^b is the longer pair (opposite pairs of bonds are equal due to C_i symmetry).

	Bond Indices						Charges					
	WBI (NBO)			QTAIM $\delta(A,B)$			NBO Natural		Mulliken		QTAIM	
	U-N _{ring} ^a	U-N _{ring} ^b	U-U	U-N _{ring} ^a	U-N _{ring} ^b	U-U	U	N _{ring}	U	N _{ring}	U	N _{ring}
PBE0:												
3-opt ⁵ A _g	1.13	0.84	0.19	1.05	0.86	0.15	1.64	-1.43, -1.30*	1.19	-0.93, -0.71*	2.30	-1.75, -1.53*
4-XRD ⁵ A _g	1.15	1.05	0.23	1.13	1.08	0.22	1.64	-1.50	1.36	-0.95	2.01	-1.68
4-opt ⁵ A _g	1.18	1.03	0.23	1.15	1.05	0.20	1.58	-1.47	1.36	-0.95	2.06	-1.68
4A-XRD ⁵ A _g	1.17	1.14	0.22	1.14	1.08	0.21	1.62	-1.47	1.51	-0.96	2.07	-1.72
4A-opt ⁵ A _g	1.23	1.14	0.28	1.21	1.13	0.27	1.32	-1.34	1.67	-0.89	1.94	-1.56
PBE:												
4-XRD ⁵ A _g	1.25	1.13	0.51	1.23	1.15	0.45	1.32	-1.31	1.07	-0.81	1.89	-1.58
4-opt ⁵ A _g	1.29	1.11	0.46	1.25	1.13	0.39	1.26	-1.28	1.08	-0.79	1.89	-1.57
4A-XRD ⁵ A _u	1.25	1.16	1.13	1.24	1.18	1.01	1.32	-1.30	1.21	-0.81	1.90	-1.63
4A-opt ⁵ A _g	1.32	1.22	0.57	1.29	1.19	0.53	1.09	-1.18	1.37	-0.76	1.83	-1.52

In the XRD structure of **4**, which has C_i symmetry, there is a slight alternation in the U-N_{ring} bond lengths, of 2.15 Å (U1-N1) and 2.18 Å (U1-N1A), see Table 2. The alternation is much smaller than Vlaisavljevich *et al.* observed for U₂N₄, so the electronic structure of the U₂N₂ ring in U₂N₂Li₄[Tren^{TIPS}]₂ might be expected to be more similar to U₂N₂²⁺ than U₂N₄²⁻ (given the two Tren^{TIPS} 3- ligands, and four Li⁺ cations). Geometry optimisations of **4** were performed using both PBE and PBE0, both on the full molecule (**4-opt**), and a model where isopropyl groups are replaced with hydrogens in the Tren^{TIPS} ligand (**4A-opt**). In addition, calculations were performed where heavy atoms were fixed at their crystal structure geometries, with only hydrogens optimised (**4-XRD** and **4A-XRD**). As summarised in Table 2, the geometry optimisations on the full molecule (**4-opt**) are a good match for the crystal structure; PBE0 gives better agreement, with bond lengths

in the U_2N_2 ring being within 0.02 Å of experiment, and $\text{U-N}_{\text{amide}}$ and $\text{U-N}_{\text{amine}}$ being within 0.05 Å. For PBE, key bond lengths are within 0.05 Å.

Table 2: Bond lengths, in ångstrom, of the U_2N_2 ring and its coordinating atoms, for the crystal structure (XRD) and geometry optimisations on the full molecule (**4**) and the model wherein Si^iPr_3 groups are replaced by SiH_3 (**4A**)

	U-U	U-N _{ring}	U-N _{amide}	U-N _{amine}
4 XRD	3.367	2.148, 2.181	2.359, 2.379	2.810
PBE 4 -opt	3.399	2.129, 2.185	2.331, 2.356	2.765
PBE 4A -opt	3.307	2.101, 2.143	2.316, 2.373	2.896
PBE0 4 -opt	3.385	2.136, 2.189	2.327, 2.354	2.768
PBE0 4A -opt	3.323	2.110, 2.143	2.331, 2.367	2.843

In full geometry optimisation (with both PBE and PBE0) of the model **4A**-opt, where Si^iPr_3 groups are replaced by SiH_3 , both ring U-N bonds shorten by about 0.05 Å. As Figure 3 shows, however, the loss of the steric bulk of the isopropyl groups results in the U_2N_2 ring tilting, relative to the coordinating Li^+ ions.

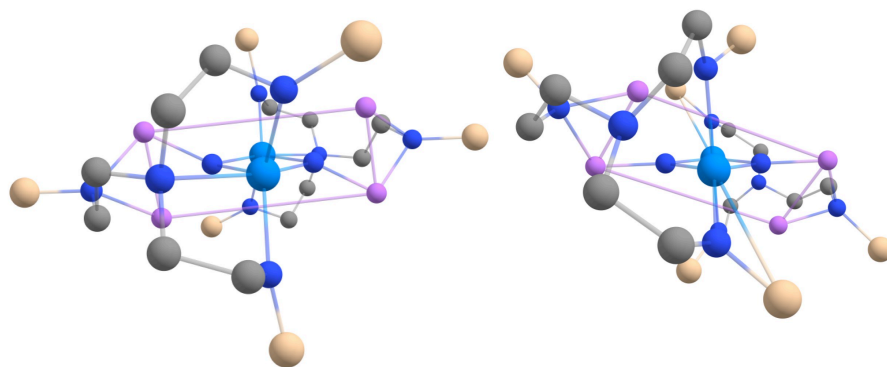


Figure 3: The geometries of **4A** with heavy atoms frozen at the crystal structure geometry (**4A**-XRD, left) and fully optimised SiH_3 model (**4A**-opt right), viewed along the uranium atoms. The loss of steric bulk results in a tilting of lithium atoms relative to the U_2N_2 ring. Light blue: uranium, dark blue: nitrogen, brown: silicon, grey: carbon, white: hydrogen. Hydrogens omitted for clarity, and lines are drawn between lithium atoms to highlight the distortion.

In all DFT calculations, the ground state multiplicity is a quintet as would be expected from two $5f^2$ U(IV) atoms; the singly-occupied orbitals are predominantly of $5f_{\text{U}}$

character—as shown in Figure 4. Lower multiplicity single-point calculations were performed, although in some cases could not be converged; their energies are reported in Tables S1 and S2 of the supplementary information and are significantly higher in energy than the quintet ground state. The WBI and $\delta(A,B)$ are reasonably consistent between the two functionals in the case of the U-N_{ring} bonds, as shown in Table 1; PBE gives a 6-9% higher WBI/ $\delta(U, N_{\text{ring}})$ versus PBE0. The U-N bond indices indicate a partial double bond, with one pair of bonds, U-N_{ring}^a having slightly larger bonding metrics than the other, U-N_{ring}^b. This structure is indicative of a ring motif more like U₂N₂ than U₂N₄.

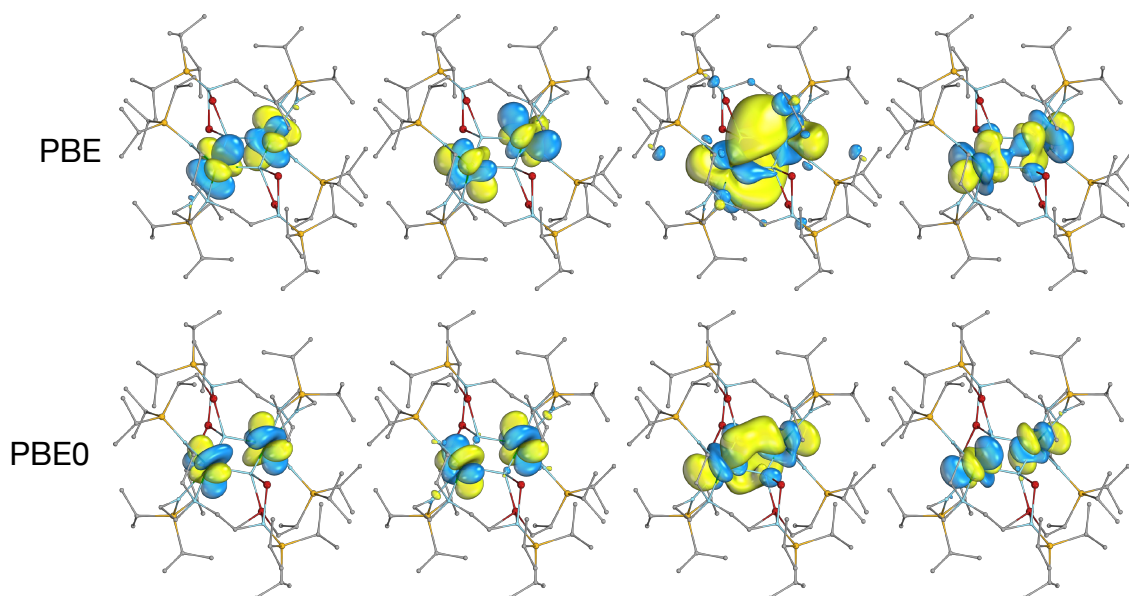


Figure 4: the singly-occupied α -spin Kohn Sham MOs of the 5A_g ground state of **4-opt** (top: PBE, bottom PBE0). The isosurfaces enclose 90% of the orbitals. Hydrogen atoms omitted for clarity.

There is a significant difference between the PBE and PBE0 values for the U-U WBIs and $\delta(U,U)$, with PBE being about double that calculated for PBE0. This likely reflects the more radially extended PBE 5f_U orbitals shown in Figure 4, which show increased 5f_U overlap. In the QTAIM calculations, there is a ring critical point at the centre of the U₂N₂ ring, so there is no bond critical point between the two uranium atoms. The PBE calculation on **4A-XRD** is out of step with the other systems, with a U-U WBI bond index

of 1.13 and $\delta(\text{U},\text{U})$ of 1.01. This is likely a result of the calculated $^5\text{A}_u$ ground state, though given the lack of consistency with other calculations is likely not reflective of the full molecule.

It is interesting to note that the U-U WBI obtained in the PBE0 calculations, 0.23 for **4-opt**, is about the same as that observed in the U_2Ni_2 and U_2Ni_3 rings studied by Feng *et al.* (using the hybrid B3PW91 functional), which they suggest indicates a U-U ‘bonding interaction’.^[25] In the U_2N_2 ring we report, the U-U distance is 3.39 Å, versus around 4.3-4.5 Å for the uranium-nickel systems. The difference in U-U distance suggests that the ring geometry is driven by the U-N bonds and that any uranium-uranium interaction is weak by comparison. That the WBI is small, and virtually unchanged on shortening by around 1 Å, suggests there is minimal metal-metal bonding present.

The bonding description we identify for **4**—a small alternation of the U-N bonds, and, at the DFT level, a high-spin state with largely nonbonding $5f_{\text{U}}$ electrons—is more similar to that of U_2N_2 than U_2N_4 , where distinct single and triple bonds are observed. Mindful that Vlaisavljevich *et al.* identify a highly multiconfigurational electronic structure for U_2N_2 at the RASPT2 level whereas a singlet, largely monoconfigurational CASSCF ground state was identified for U_2N_4 ,^[22] we therefore performed further calculations using multiconfigurational techniques to explore whether our DFT description holds at higher levels of theory. In order to reduce the computational cost, we performed the calculations on the **4A-XRD** model system.

Our RASSCF active space follows that used by Vlaisavljevich *et al.* on molecular U_2N_2 ,^[22] considering the U_2N_2 core as $\text{U}_2\text{N}_2^{2+}$; we include the four nonbonding $5f_{\text{U}}$ electrons in RAS2, the 6 σ and π U_2N_2 bonding orbitals in RAS1 and corresponding antibonding orbitals in RAS3, with single and double excitations allowed out of RAS1

into RAS3. To inform this choice, and especially to identify the number of nonbonding nonbonding $5f_U$ orbitals to include in RAS2, we first performed some preliminary CASSCF and CASPT2 calculations, only including $5f_U$ orbitals in our active space. Given the 3H_4 U(IV) ground state term, we might expect nine low-lying states.^[26] To see if this the case, we performed a 20 state average (SA) 5A_g (the DFT ground state) [4,14] CASPT2 calculation. However, there is no obvious jump in energies at the 9th state (Table S3). We observe a small jump at the 12th state of 0.05 eV, however, an 11 state calculation would necessitate 12 $5f_U$ orbitals in the active space, which proved too large when including the U_2N_2 bonding and antibonding orbitals. We therefore chose to focus on a 5 state average, including the ground state and other near-degenerate states while including 10 $5f_U$ orbitals; the difference in the [4,10] and [4,14] CASSCF energies is 0.05 eV for 5 states, rising to 0.09 eV for 6 and 0.20 eV for 11 states (Table S4). Summarising: our active space for our RASSCF and RASPT2 calculation then corresponds to (16,2,2;6,10,6) in the Sauri notation.^[27]

We performed 5-SA RASSCF calculations for singlet, triplet and quintet spin multiplicities in A_g and A_u symmetries, and MS-RASPT2 calculations on these references. The relative MS-RASPT2 energies are given in Table 3, and relative and absolute MS-RASPT2 and SA-RASSCF energies given in Tables S5 and S6 respectively. There are 9 states within 0.03 eV and 18 states within 0.1 eV. These states differ only in the occupation of the nonbonding $5f_U$ orbitals in RAS2; the occupation of the bonding orbitals in RAS1 and antibonding orbitals in RAS3 is essentially identical in each state, meaning that the U_2N_2 ring bonding is the same. Note that the effects of spin-orbit coupling have been neglected. Calculation of enough excited states to perform a RAS State Interaction (RASSI) would likely be challenging, given the large number of low-lying states

identified in this study, and also that Vlaisavljevich *et al.* were unable to calculate enough states to perform such a calculation on the bare U_2N_2 molecule. Since all states identified have very similar qualitative electronic structures, our conclusions would very likely be unaltered at the RASSI level.

Table 3: The relative energies of the MS-RASPT2 calculations on **4A-XRD**, for each space symmetry and spin multiplicity, in eV. The $^1\text{A}_g$ ground state is highlighted in bold.

State:	$^1\text{A}_g$	$^1\text{A}_u$	$^3\text{A}_g$	$^3\text{A}_u$	$^5\text{A}_g$	$^5\text{A}_u$
1	0.000	0.011	0.020	0.009	0.002	0.010
2	0.018	0.078	0.089	0.027	0.022	0.082
3	0.060	0.086	0.092	0.067	0.061	0.084
4	0.103	0.154	0.161	0.110	0.103	0.150
5	0.145	0.225	0.234	0.154	0.145	0.226

The change in ground state multiplicity, $^1\text{A}_g$ at the MS-RASPT2 level vs. $^5\text{A}_g$ with DFT, suggests weak antiferromagnetic coupling between the two U(IV) centres; the 1.7 meV difference between the lowest energy $^1\text{A}_g$ and $^5\text{A}_g$ MS-RASPT2 states corresponds to an exchange coupling parameter of -7.0 cm^{-1} ; consistent with the weak antiferromagnetism observed, with a Weiss constant of -8 K (Figure S1).

The RASSCF active natural orbitals of the state which most contributes (66.3%) to the $^1\text{A}_g$ MS-RASPT2 ground state are shown in Figure 5. The natural orbitals do not suggest any significant direct U-U bond; in and out-of-phase linear combinations of $5f_U$ orbitals are almost exactly equally occupied, and bonding orbitals in RAS1 are dominated by nitride contributions.

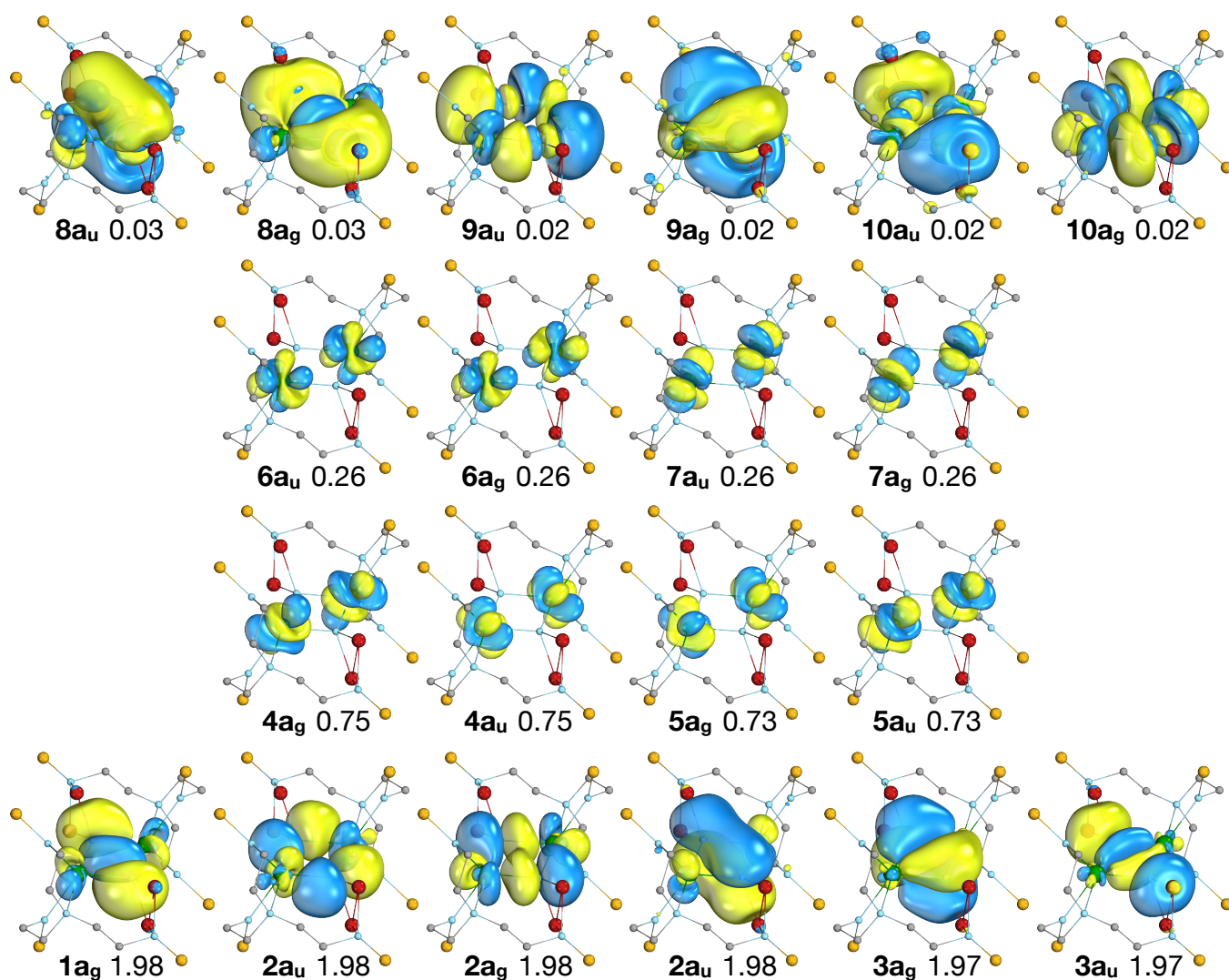


Figure 5: The natural orbitals, their symmetries and occupation numbers of the SA-RASSCF state which most contributes (66.3%) to the 1A_g MS-RASPT2 ground state of **4A**. Orbitals with occupancies > 0.01 shown. The isosurfaces enclose 90% of the orbitals. RAS1: bottom row, RAS2: middle rows, RAS3: top row. Note that the natural orbitals of the other states which contribute to the 1A_g MS-RASPT2 ground state are very similar to those shown here, differing only in the occupation of the RAS2 orbitals (see Table S7 of the supplementary information).

The active orbitals are highly localised on the U_2N_2 ring; the bonding orbitals (RAS1) are at least 90% localised on the U_2N_2 ring. Analysis of the composition of the bonding orbitals (Figure 6 and Table S8) highlights the larger contributions of the $6d$ orbitals compared with the $5f$. The remaining orbitals are similarly highly localised; the

nonbonding RAS2 orbitals are at least 94% $5f_U$ (Table S9) and antibonding RAS3 orbitals at least 85% localised on the U_2N_2 ring (Table S10).

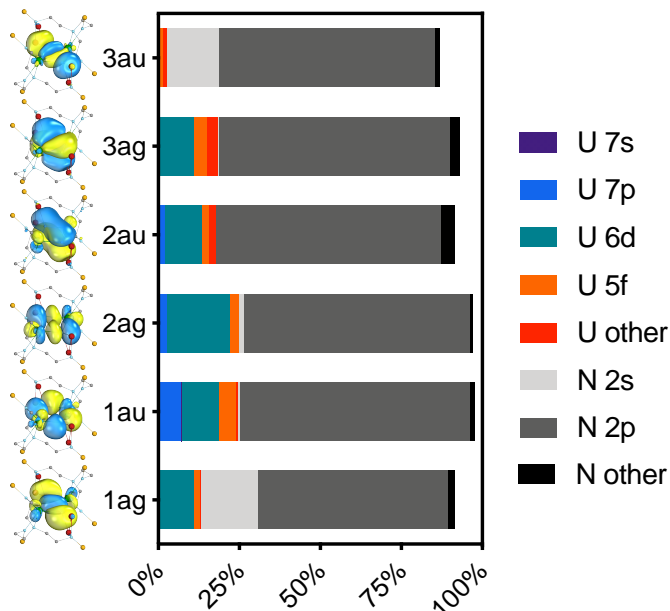


Figure 6: Mulliken analysis of the RAS1 bonding orbitals shown in Figure 5.

The character of the six ring bonding orbitals is similar to that of U_2N_2 , featuring 4 delocalised σ bonds and 2 delocalised π bonds, and agrees with the qualitative bonding description provided by Vlaisavljevich *et al.*^[22] The effective bond order (EBO) for a 2-centre bond, is $(N_B - N_{AB})/2$, where N_B and N_{AB} are the total occupation numbers of bonding and antibonding orbitals respectively. For **4A-XRD**, the average effective U-N EBO in the ring is 1.47. However, there is a small population on uranium of 3.5% for orbital 3au (Figure 6), and the corresponding antibonding orbital in RAS3, 10au, of 8.9% (Table S10). Sharma *et al.* suggested a threshold of 10% uranium population in their recent study of uranium-transition metal complexes;^[28] given this, it may therefore be more appropriate to classify these orbitals as nonbonding in which case we arrive at an EBO of 1.22.

3 Conclusions

In this contribution, we report the synthesis and characterisation of two novel diuranium nitride complexes, including the first U(IV)/U(IV) complex featuring a U_2N_2 ring, obtained by reduction of a U(V) uranium nitride. Calculations on $\text{U}_2\text{N}_2\text{Li}_4[\text{Tren}^{\text{TIPS}}]_2$ and a computational model have been performed at varying levels of theory, ranging from GGA and hybrid DFT to C/RASSCF and MS-RASPT2. Although a $^5\text{A}_g$ ground state is found by DFT, a $^1\text{A}_g$ ground state emerges at the MS-RASPT2 level, with weak antiferromagnetic coupling between the two uranium centres, in agreement with experiment. The electronic structure is similar to that of the previously-reported bare U_2N_2 ring, with delocalised σ and π bonding, and essentially nonbonding $5f_{\text{U}}$ electrons; RASPT2 finds that the six bonding orbitals in RAS1, and corresponding antibonding orbitals in RAS3, have similar character and occupation to those of U_2N_2 . This supports QTAIM and NBO analyses of the DFT calculations, which indicate a U-N_{ring} σ bond, with weak delocalised π bonding in the ring. U-U bonding is found to be negligible and hence the ring geometry is driven by the U-N_{ring} bonding, in addition to the surrounding coordination environment.

Supplementary Information

Acknowledgements

We are grateful to the EPSRC and The University of Manchester for a PhD studentship to B.E.A., and for computational resources from the University's Computational Shared

Facility, including the use of The HPC Pool funded by the Research Lifecycle Programme at The University of Manchester.

References

- [1] D. M. King, S. T. Liddle, *Coord. Chem. Rev.* **2014**, 266–267, 2–15.
- [2] M. J. Bezdek, I. Pappas, P. J. Chirik, in *Nitrogen Fixat.* (Ed.: Y. Nishibayashi), Springer International Publishing, Cham, **2017**, pp. 1–21.
- [3] G. W. Margulieux, M. J. Bezdek, Z. R. Turner, P. J. Chirik, *J. Am. Chem. Soc.* **2017**, 139, 6110–6113.
- [4] M. J. Bezdek, P. J. Chirik, *Angew. Chemie - Int. Ed.* **2018**, 57, 2224–2228.
- [5] K. C. MacLeod, S. F. McWilliams, B. Q. Mercado, P. L. Holland, *Chem. Sci.* **2016**, 7, 5736–5746.
- [6] I. Pappas, P. J. Chirik, *J. Am. Chem. Soc.* **2016**, 138, 13379–13389.
- [7] C. Camp, J. Pécaut, M. Mazzanti, *J. Am. Chem. Soc.* **2013**, 135, 12101–12111.
- [8] M. Falcone, L. Barluzzi, J. Andrez, F. Fadaei Tirani, I. Zivkovic, A. Fabrizio, C. Corminboeuf, K. Severin, M. Mazzanti, *Nat. Chem.* **2019**, 11, 154–160.
- [9] E. Lu, B. E. Atkinson, A. J. Wooles, J. T. Boronski, L. R. Doyle, F. Tuna, J. D. Cryer, P. J. Cobb, I. J. Vitorica-Yrezabal, G. F. S. Whitehead, et al., *Nat. Chem.* **2019**, 11, 806–811.
- [10] M. R. Duttera, V. W. Day, T. J. Marks, *J. Am. Chem. Soc.* **1984**, 106, 2907–2912.
- [11] D. S. J. Arney, R. C. Schnabel, B. C. Scott, C. J. Burns, *J. Am. Chem. Soc.* **1996**, 118, 6780–6781.
- [12] D. M. King, F. Tuna, E. J. L. McInnes, J. McMaster, W. Lewis, A. J. Blake, S. T. Liddle, *Science (80-.)*. **2012**, 337, 717–720.
- [13] D. M. King, F. Tuna, E. J. L. McInnes, J. McMaster, W. Lewis, A. J. Blake, S. T. Liddle, *Nat. Chem.* **2013**, 5, 482–488.

- [14] B. M. Gardner, G. Balázs, M. Scheer, F. Tuna, E. J. L. McInnes, J. McMaster, W. Lewis, A. J. Blake, S. T. Liddle, *Nat. Chem.* **2015**, *7*, 582–590.
- [15] B. M. Gardner, G. Balázs, M. Scheer, F. Tuna, E. J. L. McInnes, J. McMaster, W. Lewis, A. J. Blake, S. T. Liddle, *Angew. Chemie - Int. Ed.* **2014**, *53*, 4484–4488.
- [16] D. M. King, J. McMaster, F. Tuna, E. J. L. McInnes, W. Lewis, A. J. Blake, S. T. Liddle, *J. Am. Chem. Soc.* **2014**, *136*, 5619–5622.
- [17] P. Roussel, P. Scott, *J. Am. Chem. Soc.* **1998**, *120*, 1070–1071.
- [18] N. Kaltsoyannis, P. Scott, **1998**, *3*, 1665–1666.
- [19] P. Roussel, W. Errington, N. Kaltsoyannis, P. Scott, *J. Organomet. Chem.* **2001**, *635*, 69–74.
- [20] I. Korobkov, S. Gambarotta, G. P. A. Yap, *Angew. Chemie Int. Ed.* **2002**, *41*, 3433–3436.
- [21] L. Barluzzi, L. Chatelain, F. Fadaei-Tirani, I. Zivkovic, M. Mazzanti, *Chem. Sci.* **2019**, *10*, 3543–3555.
- [22] B. Vlaisavljevich, L. Andrews, X. Wang, Y. Gong, G. P. Kushto, B. E. Bursten, *J. Am. Chem. Soc.* **2016**, *138*, 893–905.
- [23] D. M. King, P. A. Cleaves, A. J. Wooles, B. M. Gardner, N. F. Chilton, F. Tuna, W. Lewis, E. J. L. McInnes, S. T. Liddle, *Nat. Commun.* **2016**, *7*, 1–14.
- [24] R. F. Bader, *Atoms in Molecules: A Quantum Theory*, Clarendon Pr., **1990**.
- [25] G. Feng, M. Zhang, D. Shao, X. Wang, S. Wang, L. Maron, C. Zhu, *Nat. Chem.* **2019**, 18–23.
- [26] V. Kaufman, L. F. Radziemski Jr., *J. Opt. Soc. Am.* **1976**, *66*, 599–600.
- [27] V. Sauri, L. Serrano-Andrés, A. R. M. Shahi, L. Gagliardi, S. Vancoillie, K. Pierloot, *J. Chem. Theory Comput.* **2011**, *7*, 153–168.

- [28] P. Sharma, D. R. Pahls, B. L. Ramirez, C. C. Lu, L. Gagliardi, *Inorg. Chem.* **2019**, 58, 10139–10147.

Synthesis, characterisation and electronic structure of U₂N₂ complexes

Supplementary Information

Benjamin E. Atkinson, Matthew Gregson, David M. King, Stephen T. Liddle and
Nikolas Kaltsoyannis

Department of Chemistry, University of Manchester

1 Preparation of U₂N₂Li₄[Tren^{TIPS}]₂

A) A solution of [(Tren^{TIPS})U(N₃)] (3.57 g, 4.00 mmol) in toluene (10 ml) was added to a cold (−78 °C) slurry of Li metal (0.20 g, 28.57 mmol) in toluene (20 ml). The mixture was allowed to slowly warm to room temperature and then stirred for 5 days. Each day the mixture was sonicated for 1 hr. After this time the mixture turned deep blue/red and a red precipitate had formed. The red precipitate was isolated by filtration (via cannula) and extracted into boiling toluene (60 ml), which was filtered through a frit. The residue was washed with boiling toluene (2 x 10 ml). The filtrate was concentrated to ~30 ml and stored at −30 °C to yield [{(Tren^{TIPS})UNLi₂}₂] as a red crystalline solid. The product was isolated by filtration, washed with pentane (2 x 10 ml) and dried *in vacuo*.

B) A solution of [{(Tren^{TIPS})UNLi}₂] (3.48 g, 2.00 mmol) in toluene (10 ml) was added to a cold (−78 °C) slurry of Li metal (0.04 g, 5.8 mmol) in toluene (20 ml). The mixture was allowed to slowly warm to room temperature and then stirred for 5 days. Each day the mixture was sonicated for 1 hr. The red precipitate was extracted into boiling toluene (60 ml) and filtered through a frit. The residue was washed with boiling toluene (2 x 10 ml). The filtrate was stored at −30 °C to yield [{(Tren^{TIPS})UNLi₂}₂] as a red crystalline solid. The product was isolated by filtration, washed with pentane (2 x 10 ml)

and dried *in vacuo*. Yield 2.05 g, 58%. Anal. calcd for C₆₆H₁₅₀N₁₀Li₄Si₆U₂: C, 45.14; H, 8.61; N, 7.97. Found: C, 45.45; H, 8.57; N, 7.88. FTIR ν/cm^{-1} (Nujol): 1631 (w), 1377 (w), 1300 (w) 1261 (w), 1052 (bs), 1025 (s), 990 (w), 933 (s), 917(m) 882 (s), 738 (s), 671 (m), 620 (m), 564 (w), 513 (w). ¹H, ²⁹Si NMR and UV-Vis/NIR could not be obtained due to the insolubility of in aromatic solvent once isolated and decomposition in polar solvent.

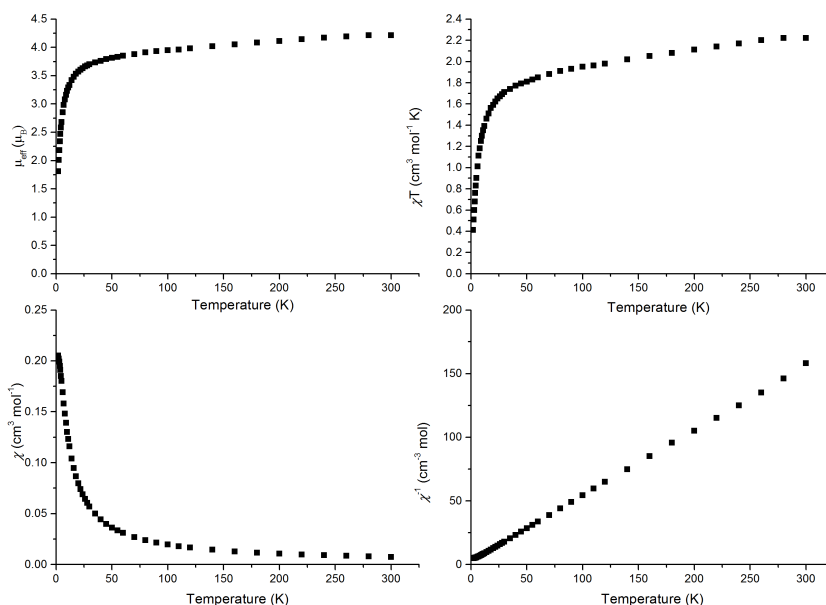


Figure S1: Magnetic data of U₂N₂Li₄[Tren^{TIPS}]₂

2 Preparation of U₂NHNLi₃(Tren^{TIPS})₂

A) Toluene (15 ml) was added to a mixture of [{(Tren^{TIPS})UNLi₂}₂] (0.44 g, 0.25 mmol) and Benzo-9-crown-3 (0.18 g, 1 mmol). The resulting red mixture was gently heated to dissolve both reagents, then filtered and the volume was reduced to ca. 5 ml. Storage of the mixture at -30°C afforded red crystals of [{(Tren^{TIPS})UN}₂Li₃]. Yield: 0.056 g, 13%.

B) Toluene (10 ml) was added to a pre-cooled (-78°C) mixture of [{(Tren^{TIPS})UNLi₂}₂] (0.20 g, 0.11 mmol) and [AgBPh₄] (0.048 g, 0.11 mmol). The resulting red suspension was allowed to warm to room temperature, sonicated for 1 hr then stirred for 72 hrs. Volatiles were removed *in vacuo* and the resulting red solid recrystallised from hot toluene (2 ml) to afford red crystals of [{(Tren^{TIPS})UN}₂Li₃] on

storing at room temperature. Yield: 0.105 g, 53%. Anal. Calcd for $C_{66}H_{150}Li_3N_{10}Si_6U_2$: C, 45.30; H, 8.65; N, 8.01%. Found: C, 45.34; H, 8.67; N, 7.88%.

This gave crystal UMG25 which is $[(Tren^{TIPS})UN]_2Li_3$ with an unidentifiable Q peak. CHN data is fine but the squid looks like U(IV)

FTIR ν/cm^{-1} (ATR): 2937 (m), 2855 (s), 2830 (m), 1494 (w), 1456 (m), 1241 (s), 1185 (w), 1074 (m), 1065 (m), 988 (s), 915 (s), 881 (s), 816 (m), 778 (m), 737 (s), 670 (m), 572 (s), 514 (w), 493 (m), 414(w). 1H , ^{29}Si NMR and UV-Vis/NIR could not be obtained due to the insolubility of in aromatic solvent once isolated and decomposition in polar solvent.

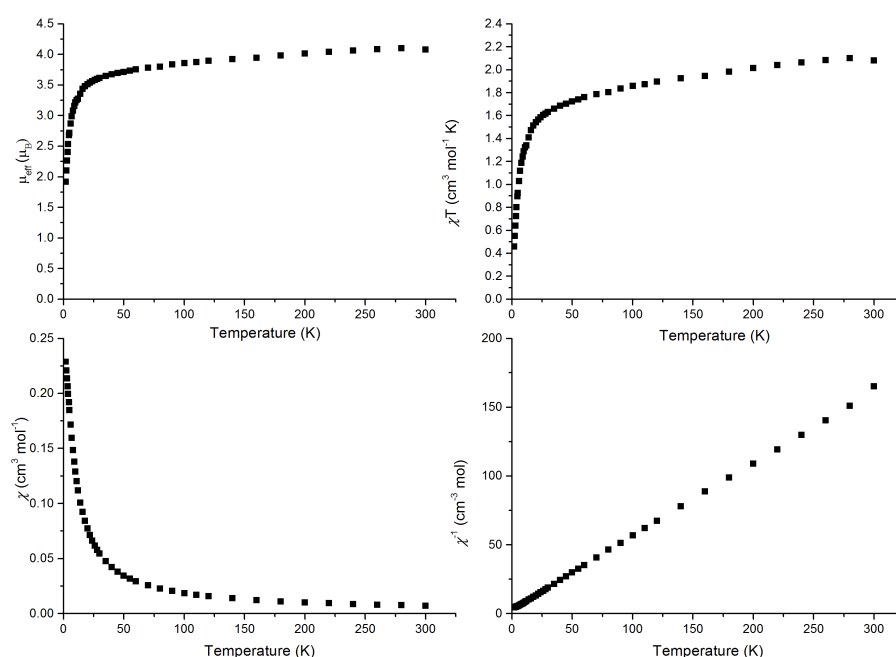


Figure S2: Magnetic data of **3**, $U_2NHNLi_3(Tren^{TIPS})_2$

3 Computational methodology

DFT calculations on **4** were performed with Gaussian 16 revision A.03^[1], and with Turbomole 7.3 for **3**.^[2] Calculations were spin unrestricted and used the GGA functional PBE,^[3] as well as the hybrid PBE0.^[4] The 60e⁻ relativistic effective core potential (RECP) of the Stuttgart/Cologne group (ECP60MWB) was used alongside the associated

segmented basis set,^[5–7] and on other elements the cc-pVDZ basis set was used.^[8–10] Grimme's D3 dampening function was used to account for dispersion interactions.^[11] Integration grids and convergence criteria were left at their default in Gaussian 16, and in Turbomole the m4 integration grid was used, with convergence criteria being left at their default.

CASSCF and RASSCF calculations were performed on model systems using OpenMolcas 18.09^[12] Calculations were performed in C_i symmetry, reflecting the symmetry of the XRD crystal structure. The ANO-RCC basis set was used; on uranium, and the ring nitrogen atoms, the VTZP contraction was used and VDZ on all other atoms. The second-order Douglas-Kroll-Hess Hamiltonian was used to account for scalar relativistic effects. Cholesky decomposition was used, with the high decomposition threshold. CASPT2 and MS-CASPT2 calculations used an imaginary shift of 0.2 in addition to the default IPEA shift of 0.25. Mulliken composition of the active natural orbitals was analysed with Molpy.^[13]

Quantum Theory of Atoms-in-Molecules (QTAIM)^[14] analyses were performed with AIMALL,^[15] Natural Bond Orbital (NBO) analyses were performed with NBO 6.0.^[16]

Supplementary Tables

Table S1: Absolute and relative energies of **4** and **4A** with the functional PBE, for several multiplicities at the quintet optimised geometry. * = failed to converge.

	4-opt		4-XRD		4A-opt		4A-XRD	
2S+1	E / Ha	ΔE / eV	E / Ha	ΔE / eV	E / Ha	ΔE / eV	E / Ha	ΔE / eV
1	*	*	*	*	-3749.25622	1.233	*	*
3	-5869.45155	0.483	-5869.44815	0.360	-3749.28408	0.475	-3749.22947	0.535
5	-5869.46929	0.000	-5869.46136	0.000	-3749.30153	0.000	-3749.24913	0.000

Table S2: Absolute and relative energies of **4** and **4A** with the functional PBE, for several multiplicities at the quintet optimised geometry. * = failed to converge.

	4-opt		4-XRD		4A-opt		4A-XRD	
2S+1	E / Ha	ΔE / eV	E / Ha	ΔE / eV	E / Ha	ΔE / eV	E / Ha	ΔE / eV
1	-5870.08694	2.708	*	*	-3749.42771	2.249	-3749.36165	2.695
3	-5870.17328	0.358	-5870.15591	0.451	-3749.44555	1.763	-3749.39699	1.733
5	-5870.18644	0.000	-5870.17248	0.000	-3749.51035	0.000	-3749.46067	0.000

Table S3: Absolute and relative energies CASPT2 energies of **4A-XRD** (5A_g , 20-SA [4,14] CASSCF reference).

State	E / Ha	ΔE / eV
1	-58695.481170.00	
2	-58695.481110.00	
3	-58695.479950.03	
4	-58695.479880.04	
5	-58695.479850.04	
6	-58695.479750.04	
7	-58695.479160.05	
8	-58695.479040.06	
9	-58695.478700.07	
10	-58695.478170.08	
11	-58695.477850.09	
12	-58695.476070.14	
13	-58695.474230.19	
14	-58695.474200.19	
15	-58695.474090.19	
16	-58695.473640.20	
17	-58695.473000.22	
18	-58695.472700.23	
19	-58695.472530.24	
20	-58695.472300.24	

Table S4: The CASSCF absolute energies in Hartree with a [4,14] and [4,10] active space, and the difference in energy between the two active spaces, in eV. Absolute energies are shifted up by 58690 Hartree. Energies shown for a 20, 11, 6 and 5 state average on **4A**-XRD (5A_g).

State:Ha	20 SA			11 SA			6 SA			5 SA		
	E[4,14] Ha	/E[4,10] Ha	/ΔE / eV	E[4,14] Ha	/E[4,10] Ha	/ΔE / eV	E[4,14] Ha	/E[4,10] Ha	/ΔE / eV	E[4,14] Ha	/E[4,10] Ha	/ΔE / eV
1	-0.53102	-0.53120	-0.01	-0.53339	-0.53222	0.03	-0.53427	-0.53367	0.02	-0.53453	-0.53403	0.01
2	-0.52976	-0.52953	0.01	-0.53209	-0.53053	0.04	-0.53249	-0.53193	0.02	-0.53266	-0.53209	0.02
3	-0.52857	-0.52796	0.02	-0.53086	-0.52893	0.05	-0.53079	-0.53027	0.01	-0.53087	-0.53023	0.02
4	-0.52688	-0.52593	0.03	-0.52702	-0.52627	0.02	-0.52788	-0.52587	0.05	-0.52779	-0.52590	0.05
5	-0.52562	-0.52432	0.04	-0.52572	-0.52465	0.03	-0.52611	-0.52417	0.05	-0.52593	-0.52399	0.05
6	-0.52545	-0.52231	0.09	-0.52558	-0.52268	0.08	-0.52584	-0.52252	0.09			
7	-0.52496	-0.52072	0.12	-0.52495	-0.52104	0.11						
8	-0.52459	-0.52067	0.11	-0.52456	-0.52038	0.11						
9	-0.52422	-0.51798	0.17	-0.52429	-0.51714	0.19						
10	-0.52375	-0.51702	0.18	-0.52373	-0.51673	0.19						
11	-0.52318	-0.51630	0.19	-0.52309	-0.51546	0.21						
12	-0.52280	-0.51339	0.26									
13	-0.52134	-0.51326	0.22									
14	-0.52095	-0.51286	0.22									
15	-0.52038	-0.51166	0.24									
16	-0.51982	-0.51068	0.25									
17	-0.51945	-0.50913	0.28									
18	-0.51901	-0.50906	0.27									
19	-0.51888	-0.50812	0.29									
20	-0.51849	-0.50547	0.35									

Table S5: The absolute (Ha) and relative (eV) energies of the MS-RASPT2 calculations on **4A**-XRD, for each space symmetry and spin multiplicity. Absolute energies are shifted up by 58695 Hartree.

State:	¹ A _g		¹ A _u		³ A _g		³ A _u		⁵ A _g		⁵ A _u	
	E / Ha	ΔE / eV	E / Ha	ΔE / eV	E / Ha	ΔE / eV	E / Ha	ΔE / eV	E / Ha	ΔE / eV	E / Ha	ΔE / eV
1	-0.4528	0.0000	-0.4524	0.0112	-0.4521	0.0196	-0.4524	0.0090	-0.4527	0.0017	-0.4524	0.0103
2	-0.4521	0.0179	-0.4499	0.0777	-0.4495	0.0889	-0.4518	0.0272	-0.4520	0.0216	-0.4498	0.0816
3	-0.4506	0.0595	-0.4496	0.0855	-0.4494	0.0922	-0.4503	0.0672	-0.4505	0.0609	-0.4497	0.0840
4	-0.4490	0.1029	-0.4471	0.1542	-0.4469	0.1609	-0.4487	0.1096	-0.4490	0.1028	-0.4472	0.1504
5	-0.4475	0.1446	-0.4445	0.2254	-0.4442	0.2341	-0.4471	0.1536	-0.4474	0.1452	-0.4445	0.2257

Table S6: The absolute (Ha) and relative (eV) energies of the SA-RASSCF calculations on **4A**-XRD, for each space symmetry and spin multiplicity. Absolute energies are shifted up by 58695 Hartree.

State:	¹ A _g		¹ A _u		³ A _g		³ A _u		⁵ A _g		⁵ A _u	
	E / Ha	ΔE / eV	E / Ha	ΔE / eV	E / Ha	ΔE / eV	E / Ha	ΔE / eV	E / Ha	ΔE / eV	E / Ha	ΔE / eV
1	-0.6944	0.0084	-0.6913	0.0929	-0.6914	0.0897	-0.6945	0.0058	-0.6947	0.0000	-0.6917	0.0827
2	-0.6925	0.0595	-0.6860	0.2366	-0.6861	0.2337	-0.6926	0.0576	-0.6927	0.0538	-0.6863	0.2272
3	-0.6906	0.1122	-0.6849	0.2677	-0.6850	0.2648	-0.6907	0.1095	-0.6909	0.1042	-0.6852	0.2586
4	-0.6863	0.2284	-0.6839	0.2937	-0.6840	0.2921	-0.6864	0.2262	-0.6866	0.2214	-0.6841	0.2888
5	-0.6844	0.2811	-0.6828	0.3248	-0.6828	0.3229	-0.6845	0.2786	-0.6846	0.2734	-0.6829	0.3197

Table S7: The occupation numbers of the natural orbitals for each root of the 1A_g SA-RASSCF calculation on **4A**-XRD

Root:	Orbital symmetry:	RAS1			RAS2					RAS3		
1	a _g	1.974941	1.978228	1.979562	0.132297	0.864374	0.000280	0.883054	0.132114	0.019071	0.022107	0.024979
	a _u	1.977365	1.974681	1.979150	0.872186	0.131708	0.000241	0.132193	0.853635	0.019788	0.025194	0.022852
2	a _g	1.974960	1.978255	1.979568	0.426622	0.561836	0.006958	0.815791	0.197892	0.019088	0.022378	0.024992
	a _u	1.977365	1.974684	1.979147	0.568341	0.430304	0.006855	0.196098	0.790811	0.019934	0.025247	0.022875
3	a _g	1.974989	1.978292	1.979576	0.734487	0.258218	0.000317	0.751834	0.261021	0.019088	0.022308	0.025000
	a _u	1.977371	1.974688	1.979155	0.262105	0.745485	0.000275	0.259551	0.728330	0.019864	0.025176	0.022871
4	a _g	1.974965	1.978238	1.979576	0.065760	0.835375	0.153852	0.536700	0.414465	0.019023	0.021872	0.024972
	a _u	1.977399	1.974661	1.979094	0.842425	0.065037	0.410875	0.155042	0.523146	0.019679	0.025005	0.022838
5	a _g	1.974986	1.978264	1.979582	0.515704	0.535886	0.146921	0.469114	0.334837	0.019039	0.021999	0.024994
	a _u	1.977403	1.974662	1.979096	0.550010	0.515886	0.145323	0.331305	0.457414	0.019717	0.025006	0.022851

Table S8: Composition analysis of the RAS1 active orbitals of the SA-RASSCF state which most contributes (66.3%) to the 1A_g MS-RASPT2 ground state of **4A**.

	1a _g	1a _u	2a _g	2a _u	3a _g	3a _u
U total	13.066	24.546	24.934	17.837	18.251	2.609
U 7s	-1.196	7.145	-0.236	-0.008	0.161	0.087
U 6p	0.222	-0.071	3.068	2.062	0.032	-1.609
U 6d	11.940	11.687	19.308	11.361	10.858	-0.640
U 5f	1.764	5.060	2.583	2.286	3.914	3.526
N total	78.259	73.173	72.024	73.686	74.777	84.323
N 2s	17.663	0.644	1.491	0.011	0.406	16.209
N 2p	58.656	70.961	69.799	69.265	71.412	66.406
U + N	91.325	97.719	96.958	91.522	93.028	86.932
U / (N + U)	14.307	25.119	25.716	19.489	19.619	3.002
Occupation	1.980	1.979	1.978	1.977	1.975	1.975

Table S9: Composition analysis of the RAS2 active orbitals of the SA-RASSCF state which most contributes (66.3%) to the 1A_g MS-RASPT2 ground state of **4A**.

	4a _g	4a _u	5a _g	5a _u	6a _g	6a _u	7a _g	7a _u
U total	99.448	99.512	99.354	99.443	99.069	98.307	98.323	99.449
U 7s	2.072	0.057	0.133	1.466	0.244	0.351	0.320	0.167
U 6p	0.077	0.065	0.004	-0.091	-0.042	-0.001	0.135	0.197
U 6d	2.200	0.766	1.217	1.069	1.241	0.272	1.231	0.375
U 5f	94.805	98.241	97.583	96.518	97.354	96.881	95.816	98.294
N total	0.386	0.158	0.314	0.165	0.354	0.712	0.696	0.104
N 2s	-0.007	-0.008	0.000	-0.002	0.000	0.017	0.000	0.009
N 2p	0.226	0.108	0.270	0.046	0.240	0.558	0.481	0.022
U + N	99.834	99.670	99.668	99.608	99.423	99.019	99.019	99.553
U / (N + U)	99.613	99.842	99.685	99.835	99.644	99.281	99.297	99.896
Occupation	0.752	0.746	0.735	0.728	0.262	0.261	0.260	0.258

Table S10: Composition analysis of the RAS2 active orbitals of the SA-RASSCF state which most contributes (66.3%) to the 1A_g MS-RASPT2 ground state of **4A**.

	8a _g	8a _u	9a _g	9a _u	10a _g	10a _u
U total	19.019	18.865	26.844	22.746	8.928	34.130
U 7s	0.001	0.691	13.053	0.245	1.091	0.071
U 6p	1.914	0.951	-4.281	0.048	1.326	3.551
U 6d	15.673	15.843	15.469	18.118	0.929	29.930
U 5f	0.927	1.860	4.079	2.234	4.843	2.747
N total	71.791	70.982	67.508	69.352	75.934	63.689
N 2s	0.054	1.322	0.057	-0.000	1.355	0.027
N 2p	23.992	15.666	20.232	21.040	9.090	19.540
U + N	90.809	89.847	94.352	92.098	84.862	97.818
U / (N + U)	20.943	20.997	28.451	24.697	10.521	34.891
Occupation	0.025	0.025	0.023	0.022	0.020	0.019

Supplementary References

- [1] Gaussian 16, Revision A.03, M. J. Frisch, G. W. Trucks, H. B. Schlegel, G. E. Scuseria, M. A. Robb, J. R. Cheeseman, G. Scalmani, V. Barone, G. A. Petersson, H. Nakatsuji, X. Li, M. Caricato, A. V. Marenich, J. Bloino, B. G. Janesko, R. Gomperts, B. Mennucci, H. P. Hratchian, J. V. Ortiz, A. F. Izmaylov, J. L. Sonnenberg, D. Williams-Young, F. Ding, F. Lipparini, F. Egidi, J. Goings, B. Peng, A. Petrone, T. Henderson, D. Ranasinghe, V. G. Zakrzewski, J. Gao, N. Rega, G. Zheng, W. Liang, M. Hada, M. Ehara, K. Toyota, R. Fukuda, J. Hasegawa, M. Ishida, T. Nakajima, Y. Honda, O. Kitao, H. Nakai, T. Vreven, K. Throssell, J. A. Montgomery, Jr., J. E. Peralta, F. Ogliaro, M. J. Bearpark, J. J. Heyd, E. N. Brothers, K. N. Kudin, V. N. Staroverov, T. A. Keith, R. Kobayashi, J. Normand, K. Raghavachari, A. P. Rendell, J. C. Burant, S. S. Iyengar, J. Tomasi, M. Cossi, J. M. Millam, M. Klene, C. Adamo, R. Cammi, J. W. Ochterski, R. L. Martin, K. Morokuma, O. Farkas, J. B. Foresman, and D. J. Fox, Gaussian, Inc., Wallingford CT, **2016**..
- [2] TURBOMOLE V7.3 2015, a development of University of Karlsruhe and Forschungszentrum Karlsruhe GmbH, **2019**, TURBOMOLE GmbH; available from turbomole.com..
- [3] J. P. Perdew, K. Burke, M. Ernzerhof, *Phys. Rev. Lett.* **1996**, 77, 3865–3868.
- [4] J. P. Perdew, M. Ernzerhof, K. Burke, *J. Chem. Phys.* **1996**, 105, 9982–9985.
- [5] X. Cao, M. Dolg, H. Stoll, *J. Chem. Phys.* **2003**, 118, 487–496.
- [6] X. Cao, M. Dolg, *J. Mol. Struct. THEOCHEM* **2004**, 673, 203–209.
- [7] W. Küchle, M. Dolg, H. Stoll, H. Preuss, *J. Chem. Phys.* **1994**, 100, 7535–7542.

- [8] T. H. Dunning, *J. Chem. Phys.* **1989**, *90*, 1007–1023.
- [9] R. A. Kendall, T. H. Dunning, R. J. Harrison, *J. Chem. Phys.* **1992**, *96*, 6796–6806.
- [10] D. E. Woon, T. H. Dunning, *J. Chem. Phys.* **1993**, *98*, 1358–1371.
- [11] K. K. Pandey, P. Patidar, S. K. Patidar, R. Vishwakarma, *Spectrochim Acta A Mol Biomol Spectrosc* **2014**, *133*, 846–855.
- [12] I. Fdez. Galván, M. Vacher, A. Alavi, C. Angeli, F. Aquilante, J. Autschbach, J. J. Bao, S. I. Bokarev, N. A. Bogdanov, R. K. Carlson, et al., *J. Chem. Theory Comput.* **2019**, *15*, 5925–5964.
- [13] Molpy, S. Vancoillie, **2017**, available from github.com/steabert/molpy
- [14] R. F. Bader, *Atoms in Molecules: A Quantum Theory*, Clarendon Pr., **1990**.
- [15] AIMAll (Version 19.10.12), Todd A. Keith, TK Gristmill Software, Overland Park KS, USA, **2019**, available from aim.tkgristmill.com.
- [16] E. D. Glendening, J. K. Badenhoop, A. E. Reed, J. A. Carpenter, J. E. Bohmann, C. M. Morales, C. R. Landis, F. Weinhold, **2013**.

U₂N₂ rings in diuranium complexes: a comparative computational study

Benjamin E. Atkinson and Nikolas Kaltsoyannis

In my previous work on the U(IV) U₂N₂ ring-containing complex U₂N₂Tren^{TIPS}, described in Chapter 5, I identified two other complexes previously isolated which have U₂N₂ ring motifs. Their structures are **B**[−] and **C** in Figure 6.1, shown alongside U₂N₂Tren^{TIPS}, **A**.

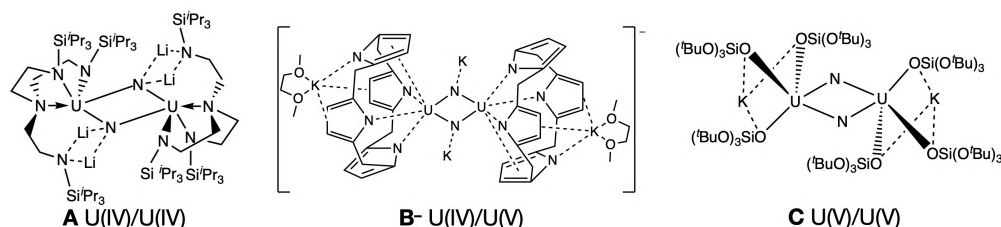


Figure 6.1: The structure of U₂N₂ ring-containing complexes previously isolated. For **B**, ethyl groups on the bridging carbon of the calix[4]-tetrapyrrole are omitted for clarity.

These previously reported complexes form a series; **A** is U(IV)/U(IV), **B**[−] is mixed U(IV)/U(V) and **C** is U(V). I performed DFT calculations on these three complexes, and identify similar bonding in each; a delocalised 12 electron bonding system. Further to this, I performed calculations on charged models of these complexes, varying the oxidation state on uranium from U(IV) to U(VI), in order to explore the influence of both oxidation state and coordination environment. Covalency increases as oxidation state on uranium increases, but the U(VI) systems have substantially less delocalised bonding; instead of approximately equal bonds

in the U_2N_2 ring, pairs of single and triple bonds are found.

Furthermore, I performed multiconfigurational calculations on $\text{U(V)} \mathbf{C}$, and $\text{U(VI)} \mathbf{C}_2^+$. Strong ferromagnetic coupling was observed for \mathbf{C} ,⁸² and RASPT2 calculations supported this with a calculated exchange-coupling parameter of -68.8 cm^{-1} . RASPT2 calculations on \mathbf{C} and \mathbf{C}_2^+ allow for further comparison to the multiconfigurational calculations on \mathbf{A} .

The change in bonding in the U_2N_2 ring, from U(IV)/U(V) to U(VI) , was confirmed experimentally by L. Barluzzi and coworkers in the Mazzanti group, École Polytechnique Fédérale de Lausanne. They obtained the U(VI) complex $\text{U}_2\text{N}_2\text{L}_6\text{THF}$ ($\text{L} = [\text{OSi}(\text{O}^t\text{Bu})_3]^-$), a neutral analogue of $\text{U(VI)} \mathbf{C}_2^+$, which features a pair of triple bonds and single bonds in the ring. The shorter pair of U_2N_2 ring bonds are 1.97 and 1.85 Å, and the longer pair are 2.25 and 2.29 Å. These bonds are slightly perturbed by the THF coordinated to the U_2N_2 ring, which also induces a slight puckering of the ring, with the U-N-N-U dihedral being 155° , *versus* 180° of the unperturbed ring. The crystal structure of this complex is shown in Figure 6.2.

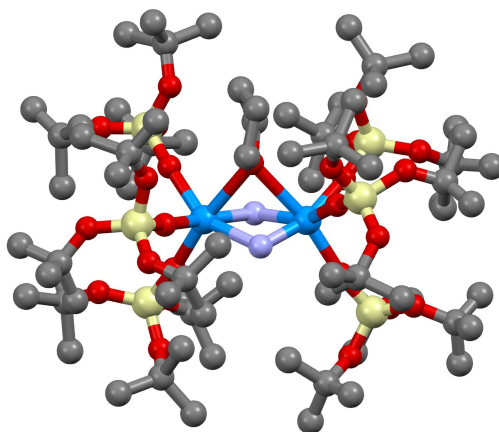


Figure 6.2: The crystal structure of $\text{U}_2\text{N}_2\text{L}_6\text{THF}$ ($\text{L} = [\text{OSi}(\text{O}^t\text{Bu})_3]^-$). Hydrogens omitted for clarity. L. Barluzzi and M. Mazzanti, personal correspondence.

Contribution statement

I devised the project, and performed calculations at the DFT, CASSCF and CASPT2 levels of theory, IBO, NBO and QTAIM analyses, analysed the results and wrote the manuscript, with

supervision and input from Prof. Nikolas Kaltsoyannis.

U₂N₂ rings in diuranium complexes: a comparative computational study

Benjamin E. Atkinson and Nikolas Kaltsoyannis
Department of Chemistry, University of Manchester

Abstract

Three diuranium bis-nitride complexes have been previously experimentally reported. We report theoretical calculations, using Density Functional Theory and multiconfigurational techniques, on these three complexes and charged counterparts, to explore their bonding and the influence of oxidation state and coordination environment. We find covalency increases at high oxidation state, and this is mainly the result of larger 5f_U character. U(IV) and U(V) systems feature delocalised bonding, however U(VI) systems differ with pairs of triple and single bonds in the ring.

Introduction

There is continued interest in uranium nitride chemistry, out of fundamental interest but also because of their potential for nitrogen fixation catalysis, and uranium nitride's potential role in future nuclear reactors.^[1,2,11,12,3–10] Kinetically stabilising, often polydentate ligands have been a highly useful tool in generating novel bonding motifs. For example the Tren^{TIPS} ligand, [N(CH₂CH₂NSi(ⁱPr₃)₃)]³⁻, was used to make the first isolable molecular uranium-nitride featuring a U≡N triple bond, UNTren^{TIPS}, in addition to a variety of other novel bonding motifs.^[13–21]

Similarly, molecules containing multiple uranium centres are an area of interest due to the novelty of their bonding, and also their potential in catalysis and small molecule activation. Additionally, there is interest in their magnetic properties, and the effects of bridging ligands on the magnetic interactions of the metal centres.^[22–24] Siloxide ligands which feature large

alkyl groups, especially (^tBuO₃)SiO[−], have been particularly successful in isolating a variety of diuranium complexes, including many with a U₂X₂ diamond core (X=N, O, NH, NMe, S).^[5,8,25,26] For example, the U(IV) complex U₂(NH)₂K₂L₆ (L = (^tBuO₃)SiO[−]) was obtained by reaction of H₂ with the U(V) nitride U₂N₂K₂L₆,^[9] and the U(IV) U₂S₂K₂L₆ was obtained from reaction of CS₂ with a U(III) mono-nitride U₂NCs₃L₆ (alongside other unidentified products).^[25]

There have been several examples of N₂ coordinated in a diuranium complex, typically reduced to N₂^{2−} by a U(III) complex.^[1–3,27–29] The first reported diuranium bis-nitride complex, synthesised in 2002 by Korobkov *et al.* is notable in that it was obtained by reacting a U(III) complex with N₂ and K(C₁₀H₈) resulting in the complete cleavage of the N₂ bond.^[4] The anionic compound they obtained features a U(IV)/U(V) U₂N₂ motif sequestered by two tetranionic calix[4]-pyrrole ligands (**B**[−] in Figure 1). The crystal structure is centrosymmetric, with opposite pairs of ring bonds having bond lengths of 2.08 and 2.10 Å. The authors suggest that it is possible that the complex is mixed-valence, or that there are distinct U(IV) and U(V) centres which are disordered over both positions—the near-IR spectrum they obtain supports the presence of discrete oxidation states, rather than a mixed oxidation state geometry.

The siloxide ligand (^tBuO₃)SiO[−] (=L) was used to isolate a U(V) bis-nitride complex U₂N₂K₂L₆, obtained first from treatment of U(III) [UL₄][K(18c6)] with CsN₃.^[5] Subsequently, an improved synthesis was reported, alongside analysis of the complex's magnetic properties.^[26] The complex, **C** in Figure 1, features ring bond lengths of 2.02 and 2.10 Å, and strong antiferromagnetic coupling was observed, with the critical temperature of the magnetic susceptibility being 77 K.

We previously reported the synthesis, characterisation and theoretical study of a U(IV) bis-nitride complex encapsulated by the Tren^{TIPS} ligand, U₂N₂Li₄[Tren^{TIPS}]₂ (**A** in Figure 1), with ring bond lengths of 2.15 and 2.18 Å.^[30] Our theoretical study of its electronic structure

suggested delocalised σ and π bonding in the U_2N_2 ring, similar to that previously reported for the bare U_2N_2 molecule.^[7]

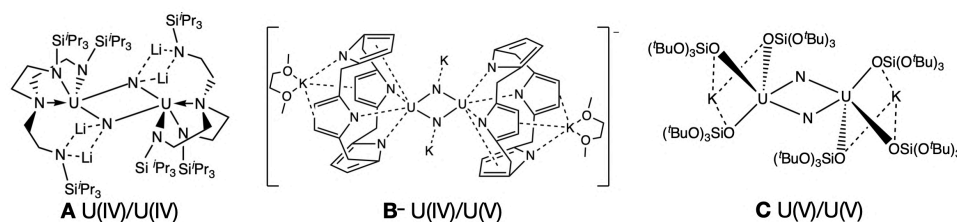


Figure 1: The geometries of the three previously reported complexes containing a U_2N_2 ring, studied in this work. For clarity, the ethyl groups on the bridging carbon of the calix[4]-pyrrole are omitted on **B⁻**

In this contribution, we present a theoretical study of the three complexes previously reported featuring a U_2N_2 ring, **A**, **B⁻**, and **C**, comparing their electronic structure. The three structures are in a series, with **A**, **B⁻**, and **C** being $U(V)/U(V)$, $U(V)/U(IV)$ and $U(IV)/U(IV)$ respectively. We additionally report calculations on other charged systems, to explore the role of oxidation state and complexation environment in their bonding. We further report multiconfigurational calculations on **C** to compare to our previous work on **A**.

Computational Methodology

Density functional theory (DFT) calculations were performed with Turbomole 7.3.^[31] All open-shell calculations were spin unrestricted, using the hybrid functional PBE0.^[32,33] The cc-pVDZ basis set was used on all atoms, other than uranium on which cc-pVDZ-PP basis was used^[34] (with the associated 60 relativistic effective core potential^[35]). To calculate magnetic properties, cc-pVTZ-PP was used on uranium and cc-pVTZ on ring nitrogen atoms, at the crystal structure geometry with only the positions of hydrogen atoms optimised (with the DZ basis set) in addition to the DFT optimised geometries. Grimme's D3 dampening function was used to account for dispersion interactions, with the m4 integration grid. For anionic calculations, the aug-cc-pVDZ basis was used on ring nitrogen atoms. On uranium, cc-pVDZ-PP was used, with an additional set of even-tempered diffuse functions constructed using Molpro 2018.2,^[36] the exponents of these diffuse functions are given in the

supplementary information. True minima were confirmed with frequency calculations, though in some cases small ($<17i\text{ cm}^{-1}$) imaginary frequencies corresponding to ligand twisting were found, which could not be eliminated and we believe are due to the integration grid and the very flat potential of these twisting motions. Dianion calculations have some KS orbitals with positive eigenvalues, however have sensible qualitative character and geometries and bond metrics are in line with other charges.

Complete/restricted active space-self consistent field (C/RASSCF) calculations, and C/RASSCF with second-order perturbation theory (C/RASPT2), including MS-C/RASPT2, were performed with OpenMolcas 18.09.^[37] The ANO-RCC basis set was used; using the VTZP contraction on uranium and on the ring nitrogen atoms, and VDZ otherwise.^[38–40] The second order Douglas-Kroll-Hess Hamiltonian was used to account for scalar relativistic effects, and Cholesky decomposition to save on computational time and disk space, using the high decomposition threshold, and an imaginary shift of 0.2 in addition to the default IPEA shift of 0.25 to avoid intruder states in C/RASPT2 calculations. Molpy was used to generate molden files, and to perform Mulliken analysis of the active orbitals.

Quantum Theory of Atoms-in-Molecules (QTAIM) analyses were performed with AIMALL, with .wfx files generated by Molden2AIM.^[41,42] NBO 7.0 was used to obtain natural charges and Wiberg bond indices (WBI) in the natural atomic orbital basis.^[43] Molecular orbital visualisation, and intrinsic bonding orbital (IBO) analyses were performed with IBOView.^[44] Minimum quality bases for uranium and caesium were constructed from the cc-pVTZ-PP basis, in the same manner as previously described for other elements.^[44] Rudel *et al.* recently used IBO analysis on uranium by constructing Hartree-Fock orbitals from the def-TZVP basis (without polarisation functions) but obtained similar results to cc-pVTZ-PP.^[45] The uranium minimum quality basis included 7s, 6p, 6d and 5f valence orbitals. The four-exponent option was used for IBO analysis, and orbital composition was obtained from IBO localisation in *Proper*, a component of Turbomole; charges were within 0.001 of that calculated by IBOView.

Results and Discussion

Experimentally isolated systems

We performed geometry optimisations on the three complexes with the hybrid PBE0 functional; Reta *et al.* previously identified PBE as the best performing functional for uranium compounds in a variety of oxidation states^[46] but our previous work on **A** suggested PBE0 performed slightly better for this diuranium complex. For **A** and **C**, there is a good match with the crystal structure geometries,^[4,5,30] summarised in Table 1. Key U-N and U-L bond lengths are at most 0.05 Å from that of the crystal structure. Note that due to a change in basis set and ECP, our optimised bond lengths of **A** differ very slightly to our previous work.^[30] Calculations on **B⁻** suggest a preference for discrete U(IV) and U(V) centres; the C_i mixed oxidation state isomer was found to be 0.62 eV higher in energy than the C_1 discrete isomer, consistent with the near-IR spectrum obtained experimentally which suggested the presence of a discrete U(V) centre.^[4] At the U(V) centre, **B⁻** has an average U-N_{ring} bond length of 1.98 Å, and 2.15 Å at the U(IV) centre. The observed crystal structure is centrosymmetric, by inverting the DFT geometry through its centre of mass, overlaying the geometries and taking average positions we get U-N_{ring} bond lengths of 2.05 and 2.07 Å, 0.03 Å shorter than the crystal structure, though the U-U interatomic distance is 0.06 Å shorter than the crystal structure, at 3.30 Å.

Table 1: Key interatomic distances, in ångstrom, of **A**, **B⁻**, and **C** of the U₂N₂ ring at the crystal structure (XRD) geometry and the DFT optimised geometry. U^a is the U(V) centre and U^b is the U(IV) centre on **B⁻**, for **A** and **C** the two centres are equivalent due to the C_i symmetry. **B⁻** is C_1 and so has four distinct U-N_{ring} bonds, DFT (av.) refers to the bond length obtained overlaying the inverted DFT geometry and averaging atomic positions to reflect the crystal structure geometry.

	A		B⁻			C	
	XRD	DFT (⁵ A _g)	XRD	DFT (⁴ A)	DFT (av.)	XRD	DFT (³ A _u)
U ^a -N _{ring} ^a	2.148	2.145	2.077	1.972	2.054	2.022	2.004
U ^b -N _{ring} ^a	2.181	2.204	2.098	1.989	2.074	2.101	2.084
U ^b -N _{ring} ^b	2.148	2.145	2.077	2.138	2.054	2.022	2.004
U ^a -N _{ring} ^b	2.181	2.204	2.098	2.162	2.074	2.101	2.084
U-U	3.367	3.407	3.355	3.298	3.298	3.296	3.248
N-N	2.723	2.702	2.485	2.484	2.484	2.480	2.484

The ground state reflects the oxidation state of the uranium atoms, with the multiplicity of **A**, **B**[−], and **C** being ⁵A_g, ⁴A and ³A_u respectively. The singly occupied molecular orbitals (SOMOs), shown in Figure 2, are 5f_U in character (at least 83.4, 86.3, and 96.7 % by Mulliken population for **A**, **B**[−], and **C** respectively) and predominantly nonbonding. For **A** and **C** with an even number of 5f_U electrons, in- and out-of-phase linear combinations are equally occupied. For **B**[−], the orbitals are largely localised onto each uranium centre; two on the U(IV) centre and one on U(V).

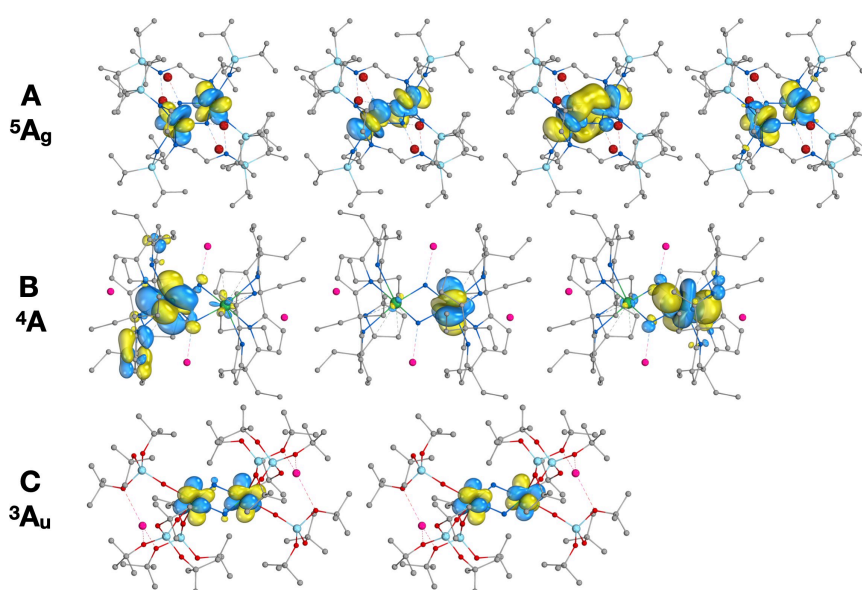


Figure 2: Singly occupied α -spin Kohn Sham MOs of **A** (top), **B**[−] (middle) and **C** (bottom). The isosurfaces enclose 90% of the orbital. Hydrogen atoms, and the dimeethoxyethanes which cap K⁺ in **B**, omitted for clarity. Grey: carbon, dark blue: nitrogen, red: lithium (**A**), oxygen (**B** + **C**)

Intrinsic bonding orbital (IBO) analysis reveals a comparable bonding motif in all three complexes, but differ in their degrees of covalency. Because IBOs minimise the number of atoms an orbital's charge is distributed over, they localise on each nitride, showing the nitrides bonding with each uranium. Figure 3 a) shows the IBOs for one nitride; due to the C_i symmetry of **A** and **C**, there is a degenerate set of IBOs for the opposite nitride, and for **B**[−] the bond lengths at each uranium centre are similar so the set of IBOs on the opposite nitrogen are approximately equivalent. IBO analysis derives a consistent pattern of four nitride valence orbitals; a predominantly 2s orbital with small uranium contributions, two

orbitals which are predominantly U-N σ , with a small U-N π contribution with the other uranium, and a delocalised π bonding orbital. The IBO composition is shown in Figure 3 b), and Tables S1, S13 and S20 of the Supplementary Information. This shows bonding orbitals becoming more covalent as oxidation state on U increases, with the largely nonbonding 2s orbital remaining approximately constant. The IBOs are well localised onto the ring, being at least 96% localised on the U-N-U unit (other than the nonbonding N 2s orbital of **A**, 92% localised with some small Li charge). As shown, the increase in covalency is driven by increase in 5f contributions (6.1, 11.3 and 14.0 % for **A**, **B**⁻, and **C** respectively), with 6d contributions remaining approximately constant (16.0, 15.8 and 15.4 % respectively). As we discussed in our previous work on **A**,^[30] the electronic structure in the ring is similar to that of the bare molecule as studied by Vlasisavljevich *et al.*; a delocalised bonding system with four σ and two π bonding orbitals in the ring, with (approximately, in the case the complexes studied in this work) equal U-N_{ring} bonds.^[7] While the delocalised bonding is similar in all three complexes, it becomes increasingly covalent, due to the improved energy match of 5f_U orbitals with nitride 2p.

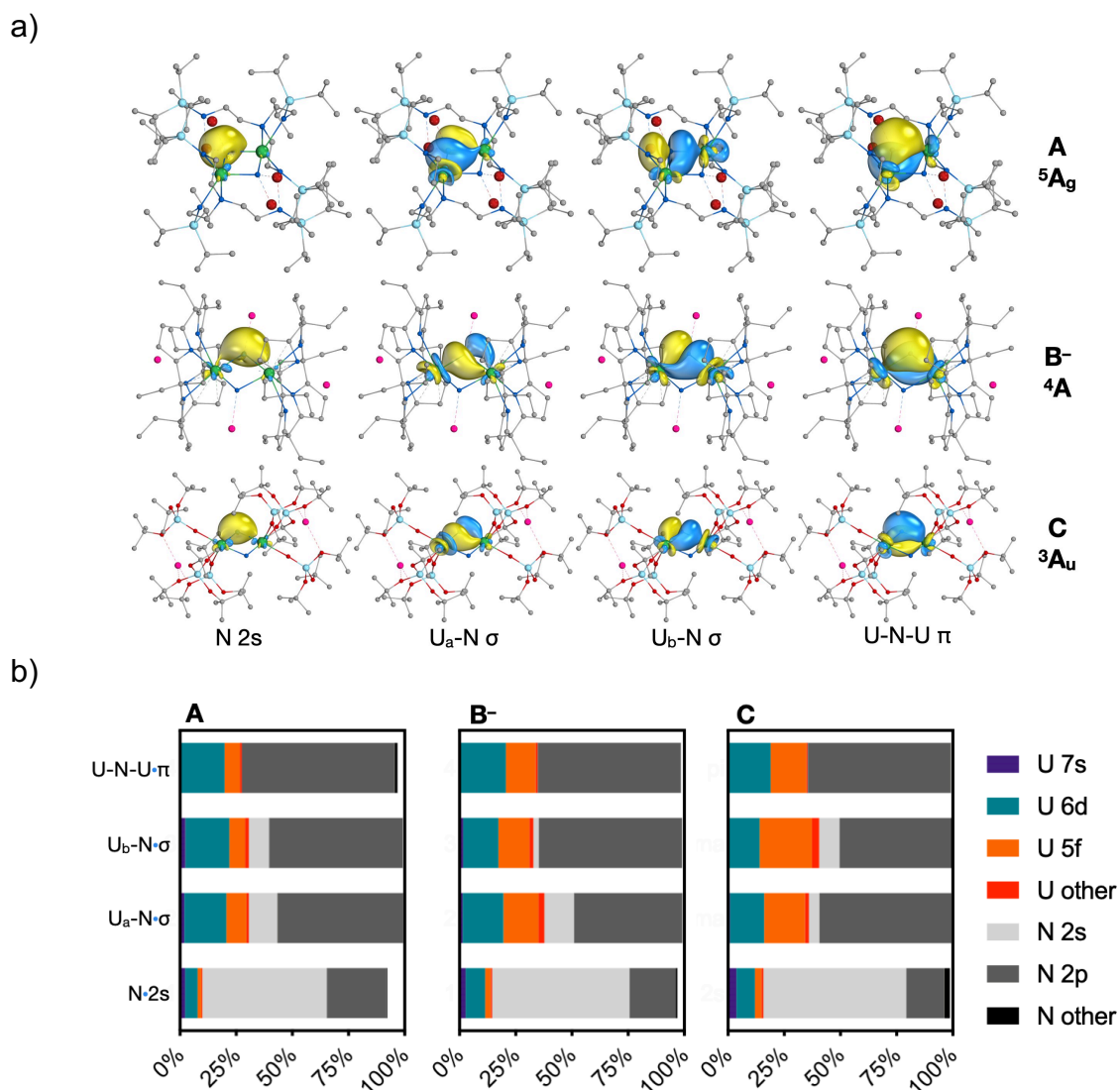


Figure 3: a) α IBOs of **A** (top), **B⁻** (middle) and **C** (bottom) in the U_2N_2 ring. The isosurfaces enclose 90% of the orbital. Hydrogen atoms, and the dimeethoxyethanes which cap K^+ in **B⁻**, omitted for clarity. b) The composition of IBOs shown in a), in the IAO basis.

In addition to the IBO analysis, we used QTAIM to obtain delocalisation indices $\delta(A|B)$ and charges, and we obtained charges and Wiberg bond orders from NBO, detailed in Table 2. As the IBO analysis describes, covalency increase as the oxidation state on uranium increases; the average $\delta(U|N_{\text{ring}})$ is 1.03 for **A**, 0.96 at the U(IV) centre of **B⁻**, 1.50 at the U(V) centre of **B⁻**, and 1.32 for **C**, with the Wiberg bond orders following a similar trend.

The U-U bonding metrics follow a similar trend, with $\delta(U|U)$ increasing from 0.17 for **A**, to 0.26 for **B⁻** and 0.33 for **C**. The U-U Wiberg bond orders (0.18, 0.17 and 0.34 for **A**, **B⁻**, and

C respectively) differ slightly, with **B**[−] slightly lower than **A**. The character of the SOMOs (Figure 2) suggests there is no 5f_U U-U bonding, with in- and out-of-phase linear combinations both occupied for **A** and **C**, and the SOMOs of **B**[−] largely localised to a single uranium centre. The QTAIM analysis gives a ring critical point at the centre of the U₂N₂ ring in all three cases, meaning there is no bond critical point between the two uranium atoms. Only the U-N-U IBOs discussed above have significant (>2 %) character on both uranium atoms—remaining IBOs are either core electrons or uranium-ligand bonds. This suggests that any U-U bonding interaction is mediated by the stronger delocalised U-N-U bonding system.

Table 2: QTAIM and NBO bond indices and charges, for **A**, **B**[−], and **C** in the U₂N₂ ring. **A** and **C** have C_i symmetry so opposite U-N_{ring} bond lengths in the ring are equal and atoms have the same charge.

	Bond Indices				Charges			
	WBI (NBO)		QTAIM δ(A,B)		NBO Natural		QTAIM	
	U-N _{ring}	U-U	U-N _{ring}	U-U	U	N _{ring}	U	N _{ring}
A ⁵ A _g U(IV)/U(IV)	1.057, 0.905	0.182	1.087, 0.969	0.168	1.759	-1.667	2.304	-1.82
B [−] ⁴ A _u U(IV)/U(V)	1.323, 1.269	0.173	1.527, 1.470	0.264	2.055,	-1.688, -2.430,	-1.468,	
	0.754, 0.717		0.984, 0.931		1.913	1.673	2.285	-1.460
C ³ A _u U(V)/U(V)	1.468, 1.188	0.342	1.452, 1.197	0.328	1.773	-1.080	2.640	-1.330

Charged Systems

To further explore the role of the coordination environment and oxidation state, we performed a series of calculations on charged analogues of these systems. We performed calculations on complexes with uranium oxidation states U(IV) – U(VI), *i.e.* 0 to +4 for **A**, and -2 to +2 for **B** and **C**. The U-N_{ring} bond lengths of these U(IV) – U(VI) systems are shown in Figure 4 and Tables S29-31 of the Supplementary Information. Complexes with an even charge have C_i symmetry, and as with **B**[−], odd-charged complexes adopt C₁ geometries with each uranium having a discrete oxidation state. This is confirmed by the expected number of 5f_U SOMOs which are localised on each uranium, shown in Figures S1-S13 of the Supplementary Information. In some cases, the 5f_U orbitals become delocalised into the ligands, however the oxidation state is confirmed by the IBOs localised onto a single

uranium centre (shown alongside the SOMOs in Figures S1-S13 of the Supplementary Information)

As Figure 4 shows, there is a slight shortening of the average U-N_{ring} bond length for all three complexes as the U oxidation state increases. The average bond lengths of **B** and **C** are rather similar, with U-N_{ring} bond lengths of **A** being on average 0.08 Å longer than **B** and **C**. This is likely the influence of both the slightly softer Tren^{TIPS} ligand (versus the tetranionic calix[4]-pyrrole of **B**, and the siloxide ligands of **C**) and the presence of four Li⁺ cations coordinated to the nitrides in the ring.

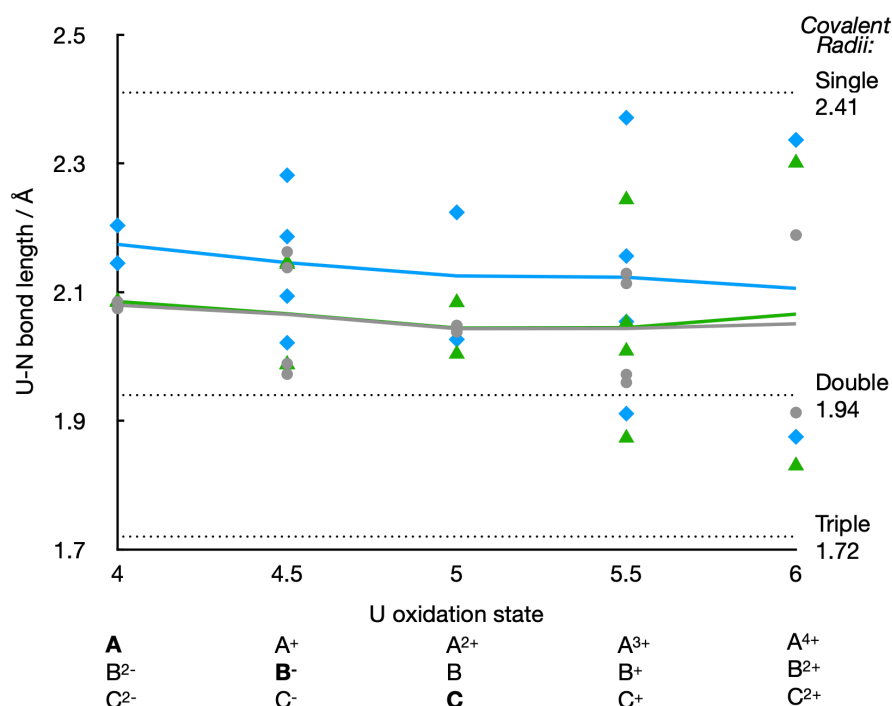


Figure 4: The U-N_{ring} bond lengths, in ångstrom, as a function of uranium oxidation state.; **A** blue, diamond; **B**, grey, circle; **C**, green, triangle. The connecting line gives the average bond length. The charge of each system is shown below, with the experimentally obtained complex shown in bold. The sum of U-N Pyykkö covalent radii are indicated.^[47]

Another clear trend is an increase in the range of bond lengths in the ring as uranium oxidation state increases. For U(IV) **B**²⁻ and **C**²⁻, all four U-N_{ring} bonds are essentially equal, and for **A** they differ by 0.06 Å, whereas for U(VI) **A**⁴⁺, **B**²⁺ and **C**²⁺, there is a 0.46, 0.28 and 0.47 Å difference between the pair of shorter bonds and the pair of longer bonds in the ring.

The U(V) systems are an intermediate case, the difference between the shorter and longer pair of bonds being 0.20, 0.01 and 0.08 Å for **A**²⁺, **B** and **C** respectively. There is a smaller range of bond lengths for **B** versus **A** and **C**, likely due to the less flexible calix[4]-pyrrole ligand and the nitride-capping K⁺ cations. For example, for the U(VI)/U(V) systems **B**⁺ adopts a structure with bond lengths approximately equal at each uranium (U(VI) 1.96, 1.97 Å and U(V) 2.13, 2.11 Å) whereas **C**⁺ features a U(VI) centre with a weak triple bond and a longer bond, and similarly a longer and shorter bond at U(V) (U(VI) 1.87, 2.01 Å and U(V) 2.05, 2.24s Å).

By comparison of the three U(V)/U(V) systems, **A**²⁺, **B** and **C**, we can explore the role of the ligand and coordination environment. All are ³A_u, with 2 5f_U character SOMOs (shown in Figures S3, S7 and S11 for **A**²⁺, **B** and **C** respectively, and also Figure 2 for **C**), as expected for two U(V) centres. While **B** and **C** have similar average U-N_{ring} bond lengths at 2.04 Å, they differ in **C** by 0.08 Å but only 0.01 Å for **B** (as shown in Table 3), reflective of the rigidity of the calix[4]-pyrrole ligand as discussed above. **A**²⁺ has a longer average U-N_{ring} bond length at 2.12 Å, and a greater difference at 0.2 Å. This is likely the influence of the two coordinating Li⁺ cations on each nitride, which induces more polarised bonding – reflected in the more negative charge on N_{ring}; -1.60 for **A**²⁺, versus -1.36 and -1.33 for **B** and **C**, respectively. The reduced covalency is seen in the lengthening of a single pair of bonds, at 2.22 Å (reflected in the WBI, 0.88, and δ(U|N_{ring}), 0.90), with the other pair similar to the bonds observed in **B** and **C**. As previously observed, this reduced covalency manifests itself as reduced 5f contributions to bonding IBOs; the three bonding IBOs of all three U(V)/U(V) systems are at least 98% localised to the U-N-U unit, with 65.5, 62.3, and 61.3 % population on N for **A**²⁺, **B** and **C** respectively, with 6d_U populations being 17.9, 16.6 and 17.7 %, and 5f_U being 13.4, 17.3 and 17.9 %. The bonding IBOs of **C** are shown in Figure 3, **A**²⁺, **B** in Figures S16, S21 and IBO composition shown in Table S5, S14 and S23 of the Supplementary Information.

Table 3: Bond lengths, and QTAIM and NBO bond indices and charges, for 3A_u U(V)/U(V) **A**²⁺, **B**, and **C** in the U₂N₂ ring. All three complexes have C_i symmetry so opposite U-N_{ring} bond lengths in the ring are equal and atoms have the same charge

	Bond length U-N _{ring} / Å	Bond Indices				Charges			
		WBI (NBO)		QTAIM δ(A,B)		NBO Natural		QTAIM	
		U-N _{ring}	U-U	U-N _{ring}	U-U	U	N _{ring}	U	N _{ring}
A ²⁺	2.026, 2.224	1.414, 0.879	0.225	1.419, 0.897	0.207	1.867	-1.338	2.529	-1.601
B	2.038, 2.048	1.309, 1.283	0.314	1.298, 1.270	0.317	1.661	-1.174	2.463	-1.365
C	2.004, 2.084	1.468, 1.188	0.342	1.452, 1.197	0.328	1.773	-1.080	2.640	-1.330

Conversely, by comparing the same coordination environment we can study the role of oxidation state. The U₂N₂ ring IBOs of U(IV) **C**²⁻, U(V) **C**, and U(VI) **C**²⁺ are shown in Figure 5, and bond lengths and bond indices are shown in Table 4. As Figure 5 shows, the IBOs of **C**²⁻ and **C**²⁺ differ to previously shown IBOs. **C**²⁻ differs from the other U(IV) systems in having highly symmetric σ IBOs, rather than the U-N σ, with a small U-N π contribution on the other uranium as seen on **A** and **B**²⁻ (and the U(V) systems). As would be expected, the composition of the IBOs suggests covalency increases with oxidation state (the average character on N is 63.7, 61.3, and 59.3 % for the three bonding IBOs of **C**²⁻, **C** and **C**²⁺ respectively with the IBOs at least 98 localised to U-N-U). This increase in covalency is driven by increased 5f_U character (11.7, 17.9 and 23.9 % for **C**²⁻, **C** and **C**²⁺ respectively), however there is also a decrease in 6d_U character (21.2, 17.7 and 14.9 % for **C**²⁻, **C** and **C**²⁺ respectively). The increase in 6d_U character may explain the switch in character of the IBOs, as 6d_U orbitals are less well suited to this π overlap in the plane of the U₂N₂ ring.

Unusually, the NBO WBI and QTAIM δ(U|N_{ring}) differ significantly for **C**²⁻, with NBO suggesting a substantially lower bond order (average 0.76) compared to QTAIM (average 1.21), driven by the substantially more negative charge on nitrogen (Table 4). It should be cautioned that **C**²⁻ has several positive Kohn-Sham orbital eigenvalues, the predominantly 5f_U SOMOs and a single bonding orbital (as does **B**²⁻, and as is common for anionic DFT calculations) however their character is qualitatively sensible (shown in Figure S9 of the Supplementary Information). We additionally performed calculations on a neutral U(IV)/U(IV)

model of **C**, by replacing K^+ with Ca^{2+} . This model behaves similarly to the dianion in the character of its IBOs (shown in Figure S29 of the Supplementary Information) and QTAIM $\delta(U|N)$ (average 1.23), but the NBO Wiberg bond order is much larger and inline with the QTAIM metric, at an average of 1.20 in the ring. This suggests the highly ionic bonding picture in the NBO analysis of **C**²⁻ may be erroneous.

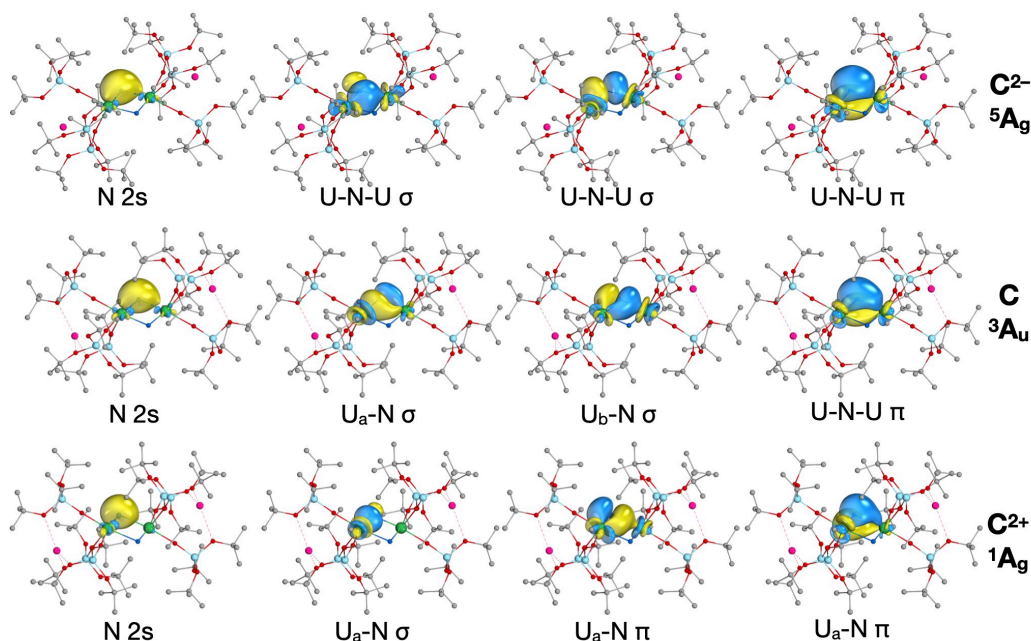


Figure 5: α IBOs of U(IV) **C**²⁻ (top), U(V) **C** (middle) and U(VI) **C**²⁺ (bottom) in the U_2N_2 ring. The isosurfaces enclose 90% of the orbital. Hydrogen atoms omitted for clarity.

Table 4: Bond lengths, and QTAIM and NBO bond indices and charges, for **C**²⁻, **C**, and **C**²⁺ in the U_2N_2 ring. All three complexes have C_i symmetry so opposite U-N_{ring} bond lengths in the ring are equal and atoms have the same charge.

	Bond length	Bond Indices				Charges			
		WBI (NBO)		QTAIM $\delta(A,B)$		NBO Natural		QTAIM	
	U-N _{ring} / Å	U-N _{ring}	U-U	U-N _{ring}	U-U	U	N _{ring}	U	N _{ring}
C²⁻ U(IV)	2.085, 2.086	0.755, 0.755	0.183	1.212, 1.205	0.263	2.154	-2.054	2.324	-1.555
C U(V)	2.004, 2.084	1.468, 1.188	0.342	1.452, 1.197	0.328	1.773	-1.080	2.640	-1.330
C²⁺ U(VI)	1.830, 2.301	2.230, 0.692	0.287	2.086, 0.653	0.264	1.728	-0.694	2.807	-1.905

The U(IV)/U(IV) and U(V)/U(V) systems can be compared to the bare U_2N_2 molecule, as studied by Vlaisavljevich *et al*,^[7] given the delocalised bonding observed and approximately

equal bond lengths. The U(VI)/U(VI) systems however have distinctly different bond lengths in the ring, which on the basis of covalent radii (Figure 4) are weak triple bonds. This is similar to what was previously reported by Vlasisavljevich *et al.* for the U(VI) molecule U_2N_4 , which was described as a dimer of two UN_2 molecules with a pair of triple bonds in the ring, and a pair of single bonds linking the two UN_2 units.

This observation of the change in the electronic structure of the U(VI)/U(VI) systems is confirmed by IBO analysis. The U_2N_2 ring IBOs of \mathbf{C}^{2+} are shown in Figure 5, and those for \mathbf{A}^{4+} and \mathbf{B}^{2+} shown in Figures S17 and-S23 of the Supplementary Information. There is a change in the character of these bonding orbitals, with a 2 centre-2 electron σ bond (54% U, 44% N, with less than 2% character on the other U) and two π bonding orbitals with only small contributions from the other uranium. The triple bond $\delta(\text{U}|\text{N}_{\text{ring}})$ and WBI (2.23 and 2.09 respectively) are about three times that of the weaker single bond (0.65 and 0.69 respectively).

Multiconfigurational Calculations

In order to gain a more detailed picture of the electronic structure of \mathbf{C} , and explore some of its magnetic properties, we performed calculations at the RASSCF and MS-RASPT2 levels of theory. We followed the same methodology as our previous study on \mathbf{A} ,^[30] which in turn was based on the active space used by Vlasisavljevich *et al.* on the bare U_2N_2 molecule.^[7] We performed calculations on a model to save on computational time, whereby *t*-butyl groups are replaced with hydrogens. We used the crystal structure geometry, with hydrogens being geometry optimised at the PBE0 level.

We included 6 bonding orbitals in RAS1, with the corresponding antibonding orbitals in RAS3. Double excitations were allowed out of RAS1, and into RAS3. The two nonbonding $5f_{\text{U}}$ electrons were included in RAS2; in order to identify the number of orbitals to include in RAS2 we performed preliminary [2,14] CASPT2 calculations, based on a 10 state-average (SA) CASSCF reference including only $5f_{\text{U}}$ orbitals in the active space, the energies of which

are reported in Tables S41 (CASSCF) and S42 (CASPT2) of the Supplementary Information. This identifies 8 orbitals needed to describe low lying states, which we included in RAS2 (less than 0.38 eV, beyond which there is a jump in energy). This corresponds to (14,2,2;6,8,6) in Sauri notation.^[48] To include all low-lying configurations of these orbitals given symmetry constraints in C_i symmetry, we performed a 6 state-average for 1A_u and 3A_g , and 10 state-average for 1A_g and 3A_u .

The relative energies of our MS-RASPT2 calculation are given in Table 5, and absolute energies given in Table S41 of the Supplementary information. The MS-RASPT2 ground state is 1A_g , consistent with the observation of antiferromagnetic coupling in **C** by Falcone *et al.*^[49] The 9 meV energy difference between the lowest energy 1A_g and 3A_u state gives an exchange coupling parameter J of -68.8 cm^{-1} .

Table 5: Relative energies of the MS-RASPT2 calculation on **C**, in eV.

State:	1A_g	1A_u	3A_g	3A_u
1	0.000	0.002	0.013	0.009
2	0.011	0.180	0.200	0.025
3	0.182	0.337	0.357	0.195
4	0.291	0.362	0.382	0.286
5	0.335	0.481	0.485	0.318
6	0.355	0.623	0.617	0.358
7	0.484			0.484
8	0.582			0.589
9	0.677			0.677
10	0.941			0.930

The natural orbitals of the RASSCF root which makes up 83.8% of the MS-RASPT2 ground state are shown in Figure 6. The occupancies and character of the orbitals in the active space is similar to what we previously observed for **A**.^[30] The six bonding orbitals in RAS1 are similar in character to what we observed for **A**, and also the qualitative bonding description derived by Vlasisavljevich *et al* of four delocalised σ bonding orbitals, and two delocalised π bonding orbitals in the ring.^[7] The two $5f_u$ electrons in RAS2 are multiconfigurational, and in- and out-of-phase linear combinations are equally occupied.

Occupation of the antibonding orbitals in RAS3 is again similar to **A** and molecular U_2N_2 , being between 0.02 and 0.03.

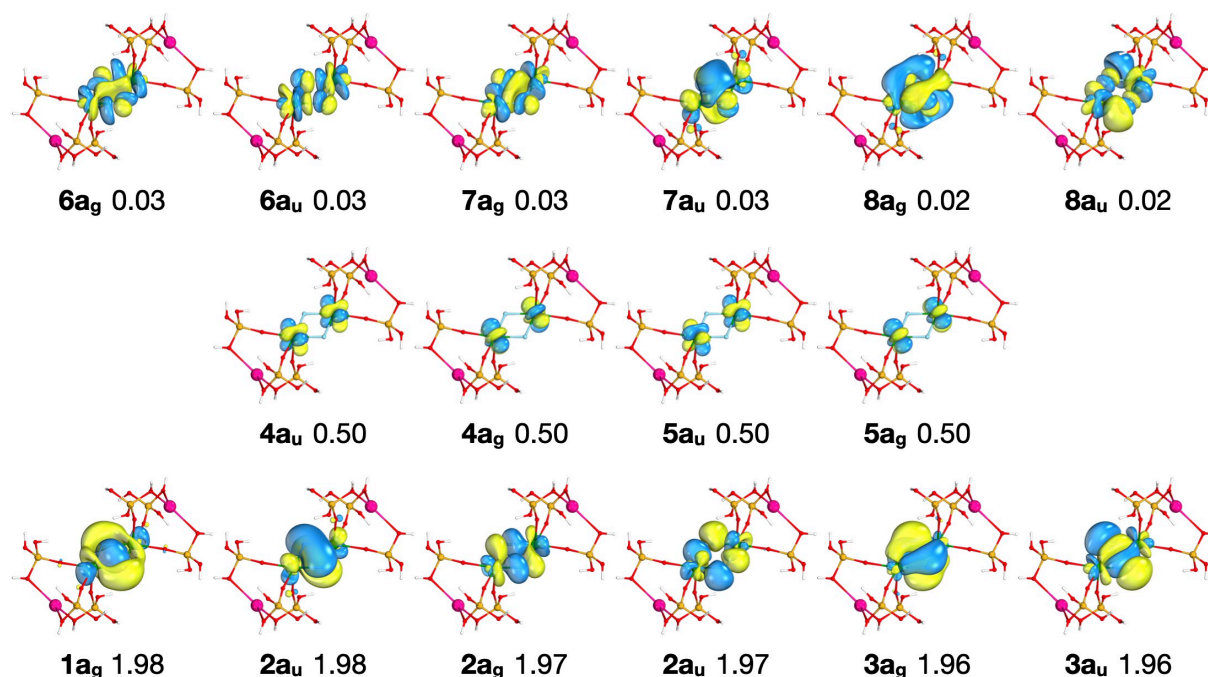


Figure 6: The active natural orbitals, their symmetries and occupation numbers of the $1A_g$ RASSCF root which most contributes (83.8%) to the MS-RASPT2 ground state. Only orbitals with occupation numbers > 0.01 shown. The orbital isosurfaces encapsulate 90% of the orbital. Top: RAS3, middle: RAS2, bottom: RAS1.

We additionally performed a CASSCF calculation on \mathbf{C}^{2+} , at the DFT optimised geometry of \mathbf{C}^{2+} (with *t*-butyl groups again replaced with hydrogens whose positions are optimised at the PBE0 level). Given the U(VI)/U(VI) oxidation state, there are no $5f_U$ electrons and thus the active space used was [6,12] to include the 6 ring bonding orbitals and corresponding antibonding orbitals. The active orbitals are shown in Figure 7 – the occupation of antibonding orbitals is larger than for **C** or **A**, though this is partly due to the lack of restrictions on excitations from bonding orbitals to antibonding orbitals in the CASSCF calculation. To aid comparability we performed a RASSCF calculation with no orbitals in RAS2, *i.e.* (12,2,2;6,0,6). The occupation numbers of the corresponding orbitals are shown in brackets in Figure 7, and are more similar to **C**.

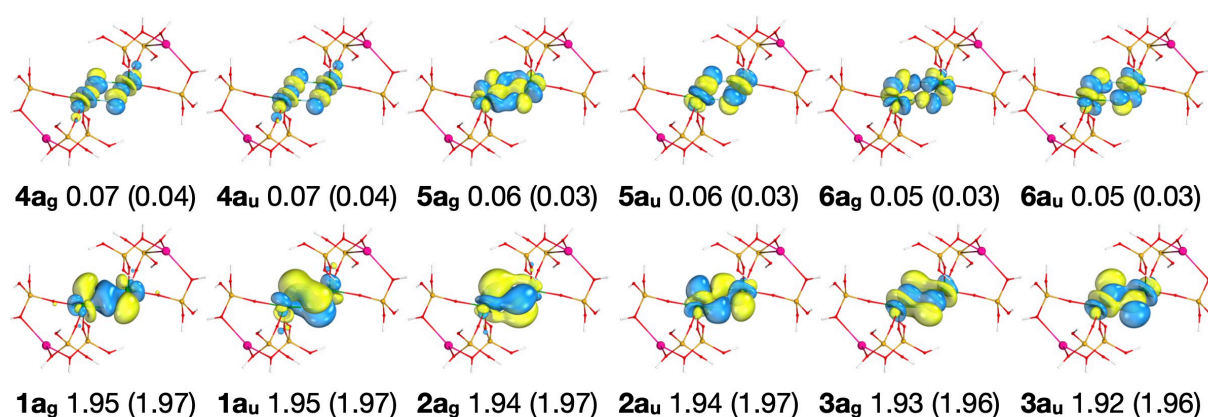


Figure 7: The active natural orbitals, their symmetries and occupation numbers of the $1A_g$ [6,12] CASSCF calculation on C^{2+} . The occupation numbers of the RASSCF calculation are given in parentheses. The orbital isosurfaces encapsulate 90% of the orbital electron density.

We performed a Mulliken composition analysis on the active orbitals of **C** and C^{2+} ;

composition of the bonding orbitals of **A**, **C** and C^{2+} is shown in Figure 8 and composition of all orbitals are shown in Tables S46-S48 of the Supplementary Information. The RAS1 bonding orbitals are highly localised to the U_2N_2 ring, at least 97% for **C** and at least 99% for C^{2+} . As Figure 8 shows, increase in the uranium oxidation state substantially increases covalency. The average $5f_U$ character of the bonding orbitals is 3.2, 11.7 and 24.5 % for U(IV)/U(IV) **A**, U(V)/U(V) **C** and U(V)/U(V) C^{2+} respectively, whereas the average $6d_U$ character is 10.9, 11.8 and 10.6 % respectively, remaining approximately constant. This highlights the increase in covalency is driven by the $5f$ orbitals becoming a better size-match for nitride $2p$. Our analysis has shown at all oxidation states, the bonding system is a 6 bonding orbital system, but the increase of the Wiberg bond order at higher oxidation states suggests increased overlap driven covalency, as opposed to energy-degeneracy driven.

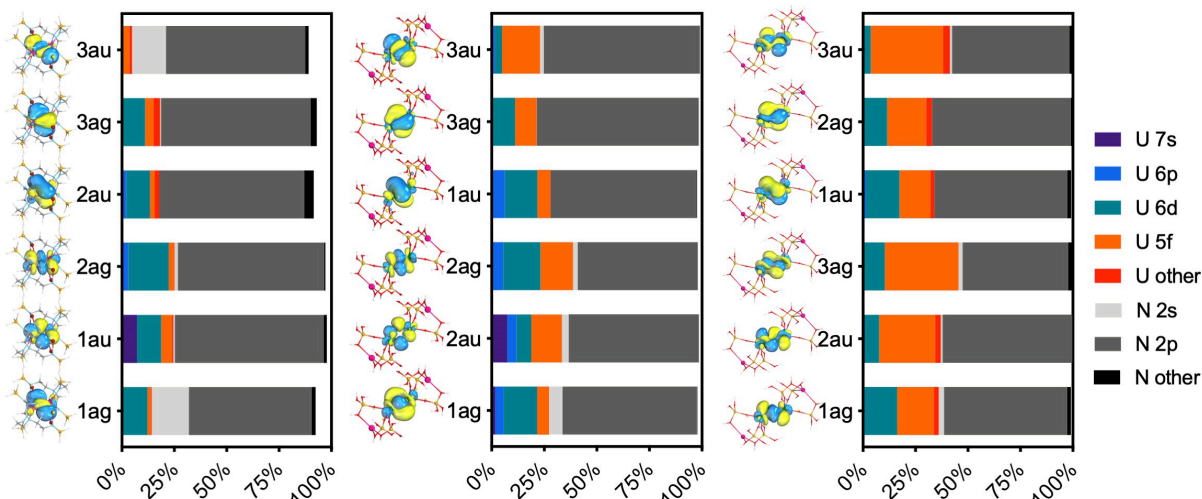


Figure 8: Mulliken orbital composition of the U_2N_2 bonding orbitals of **A**, left, **C**, middle, and **C**²⁺, right.

Given the character of the six bonding orbitals remains the same, the effective bond order (EBO, which for a 2 centre bond is $(N_B - N_{AB})/2$, where N_B and N_{AB} are the total occupation numbers of bonding and antibonding orbitals respectively) remains essentially identical; the average U-N effective bond order in the ring is 1.47 for **A**, 1.46 for **C** and 1.41 for **C**²⁺ (or 1.45 for the RASSCF occupancies). This highlights the crudeness of the EBO in comparing these systems, as covalency and the strength of bonding plainly increases from **A** to **C** and **C**²⁺, given the increase in bonding metrics at the DFT level, the shortening of bond lengths, and the increase in covalency in the Mulliken composition analysis. Sharma *et al.* suggested a threshold of 10% uranium population for an orbital to be considered bonding,^[50] in which case the average EBO of **A** becomes 1.22 as we previously reported[ref] however all six bonding orbitals for **C** and **C**²⁺ pass this threshold. Because the six orbitals are delocalised across the U_2N_2 ring, we cannot give EBOs to each of the U-N bonds. This is especially pertinent to **C**²⁺ since our DFT calculations give a pair of triple bonds and a pair of single bonds in the ring, however qualitatively there is substantially more bonding character between the pair of $\text{U}\equiv\text{N}$ triple bonds vs. the single bonds.

Conclusion

All three complexes studied in this work feature a similar U_2N_2 motif, featuring delocalised bonding in the ring, with remaining electrons occupying nonbonding $5f_{\text{U}}$ orbitals. The similarity of the bonding motifs is confirmed by IBO analysis, which gives a total of four σ and two π bonding orbitals in the U_2N_2 ring. The three experimentally obtained molecules, U(IV)/U(IV) **A**, U(V)/U(IV) **B**[−], and U(V)/U(V) **C** differ in the degree of covalency; higher U oxidation states have more covalent bonding in the U_2N_2 ring, and this is predominantly driven by the increased $5f_{\text{U}}$ character of the bonding orbitals, as $5f$ becomes a better energy match at higher oxidation states. This trend is explored in calculations on charged systems in order to vary the U oxidation state of these three complexes. U(IV) and U(V) systems preserve the delocalised U_2N_2 motif, with greater covalency still driven by increased $5f_{\text{U}}$ character of the bonding orbitals. However U(VI) systems feature distinctly different bonding in the ring, with a pair of triple bonds and a pair of single bonds rather than delocalised bonding. We additionally performed multiconfigurational calculations on **C** and **C**²⁺, to compare to our previous work on **A**. The six bonding of **C** orbitals have similar character to **A** (and to the bare U_2N_2 molecule^[7]), but substantially more covalent reflecting the higher U oxidation state. The ¹A_g MS-RASPT2 ground state suggests antiferromagnetic coupling and an exchange coupling parameter J of -68.8 cm^{-1} , matching the experimentally observed magnetic properties. The U(VI) **C**²⁺ features distinct bonding, matching what was observed with the DFT calculations, with substantial $5f_{\text{U}}$ character in the bonding orbitals.

Supplementary Information

Supplementary Information is available; SOMOs, IBOs, IBO compositions, ring bond lengths, NBO and QTAIM metrics, motion of small imaginary frequencies, multiconfigurational calculations data tables. Coordinates, in xyz format, are available online at <http://dx.doi.org/10.17632/5nwh67d8cx.1>

Acknowledgements

We are grateful to the EPSRC and The University of Manchester for a PhD studentship to B.E.A., and for computational resources from the University's Computational Shared Facility, including the use of the HPC Pool funded by the Research Lifecycle Programme at The University of Manchester.

References

- [1] P. Roussel, P. Scott, *J. Am. Chem. Soc.* **1998**, *120*, 1070–1071.
- [2] N. Kaltsoyannis, P. Scott, *Chem. Commun.* **1998**, *3*, 1665–1666.
- [3] P. Roussel, W. Errington, N. Kaltsoyannis, P. Scott, *J. Organomet. Chem.* **2001**, *635*, 69–74.
- [4] I. Korobkov, S. Gambarotta, G. P. A. Yap, *Angew. Chemie Int. Ed.* **2002**, *41*, 3433–3436.
- [5] C. Camp, J. Pécaut, M. Mazzanti, *J. Am. Chem. Soc.* **2013**, *135*, 12101–12111.
- [6] D. M. King, S. T. Liddle, *Coord. Chem. Rev.* **2014**, *266–267*, 2–15.
- [7] B. Vlaisavljevich, L. Andrews, X. Wang, Y. Gong, G. P. Kushto, B. E. Bursten, *J. Am. Chem. Soc.* **2016**, *138*, 893–905.
- [8] M. Falcone, L. Chatelain, M. Mazzanti, *Angew. Chemie - Int. Ed.* **2016**, *55*, 4074–4078.
- [9] L. Barluzzi, M. Falcone, M. Mazzanti, *Chem. Commun.* **2019**, *55*, 13031–13047.
- [10] C. T. Palumbo, R. Scopelliti, I. Zivkovic, M. Mazzanti, *J. Am. Chem. Soc.* **2020**, *142*, 3149–3157.

- [11] P. L. Arnold, T. Ochiai, F. Y. T. Lam, R. P. Kelly, M. L. Seymour, L. Maron, *Nat. Chem.* **2020**, 12, 654–659.
- [12] A. R. Fox, S. C. Bart, K. Meyer, C. C. Cummins, *Nature* **2008**, 455, 341–349.
- [13] D. M. King, F. Tuna, E. J. L. McInnes, J. McMaster, W. Lewis, A. J. Blake, S. T. Liddle, *Science (80-.)*. **2012**, 337, 717–720.
- [14] B. M. Gardner, J. C. Stewart, A. L. Davis, J. McMaster, W. Lewis, A. J. Blake, S. T. Liddle, *Proc. Natl. Acad. Sci.* **2012**, 109, 9265–9270.
- [15] D. M. King, F. Tuna, E. J. L. McInnes, J. McMaster, W. Lewis, A. J. Blake, S. T. Liddle, *Nat. Chem.* **2013**, 5, 482–488.
- [16] B. M. Gardner, G. Balázs, M. Scheer, F. Tuna, E. J. L. McInnes, J. McMaster, W. Lewis, A. J. Blake, S. T. Liddle, *Angew. Chemie - Int. Ed.* **2014**, 53, 4484–4488.
- [17] D. M. King, J. McMaster, F. Tuna, E. J. L. McInnes, W. Lewis, A. J. Blake, S. T. Liddle, *J. Am. Chem. Soc.* **2014**, 136, 5619–5622.
- [18] B. M. Gardner, G. Balázs, M. Scheer, F. Tuna, E. J. L. McInnes, J. McMaster, W. Lewis, A. J. Blake, S. T. Liddle, *Nat. Chem.* **2015**, 7, 582–590.
- [19] T. M. Rookes, E. P. Wildman, G. Balázs, B. M. Gardner, A. J. Wooles, M. Gregson, F. Tuna, M. Scheer, S. T. Liddle, *Angew. Chemie - Int. Ed.* **2018**, 57, 1332–1336.
- [20] R. Magnall, G. Balázs, E. Lu, F. Tuna, A. J. Wooles, M. Scheer, S. T. Liddle, *Angew. Chemie - Int. Ed.* **2019**, 58, 10215–10219.
- [21] L. Chatelain, E. Louyriac, I. Douair, E. Lu, F. Tuna, A. J. Wooles, B. M. Gardner, L. Maron, S. T. Liddle, *Nat. Commun.* **2020**, 11, 1–12.
- [22] G. Nocton, P. Horeglad, J. Pécaut, M. Mazzanti, *J. Am. Chem. Soc.* **2008**, 130,

16633–16645.

- [23] D. P. Mills, F. Moro, J. McMaster, J. van Slageren, W. Lewis, A. J. Blake, S. T. Liddle, *Nat. Chem.* **2011**, 3, 454–460.
- [24] B. Teyar, S. Boucenina, L. Belkhiri, B. Le Guennic, A. Boucekkine, M. Mazzanti, *Inorg. Chem.* **2019**, 58, 10097–10110.
- [25] L. Chatelain, R. Scopelliti, M. Mazzanti, *J. Am. Chem. Soc.* **2016**, 138, 1784–1787.
- [26] L. Barluzzi, L. Chatelain, F. Fadaei-Tirani, I. Zivkovic, M. Mazzanti, *Chem. Sci.* **2019**, 10, 3543–3555.
- [27] F. G. N. Cloke, P. B. Hitchcock, *J. Am. Chem. Soc.* **2002**, 124, 9352–9353.
- [28] S. M. Mansell, N. Kaltsoyannis, P. L. Arnold, *J. Am. Chem. Soc.* **2011**, 133, 9036–9051.
- [29] S. M. Mansell, J. H. Farnaby, A. I. Germeroth, P. L. Arnold, *Organometallics* **2013**, 32, 4214–4222.
- [30] B. E. Atkinson, M. Gregson, D. M. King, N. Kaltsoyannis, S. T. Liddle, *unpublished* **2020**.
- [31] University of Karlsruhe and Forschungszentrum Karlsruhe GmbH, **2019**.
- [32] J. P. Perdew, K. Burke, M. Ernzerhof, *Phys. Rev. Lett.* **1996**, 77, 3865–3868.
- [33] J. P. Perdew, M. Ernzerhof, K. Burke, C.-O. Almbladh, A. C. Pedroza, U. von Barth, A. V. Arbuznikov, H. Bahmann, A. Rodenberg, A. V. Arbuznikov, et al., *J. Chem. Phys.* **1996**, 109, 9982–9985.
- [34] K. A. Peterson, *J. Chem. Phys.* **2015**, 142, 074105.

- [35] M. Dolg, X. Cao, *J. Phys. Chem. A* **2009**, *113*, 12573–12581.
- [36] H.-J. Werner, P. J. Knowles, G. Knizia, F. R. Manby, M. Schütz, P. Celani, W. Györfy, D. Kats, T. Korona, R. Lindh, et al., **2018**.
- [37] I. Fdez. Galván, M. Vacher, A. Alavi, C. Angeli, F. Aquilante, J. Autschbach, J. J. Bao, S. I. Bokarev, N. A. Bogdanov, R. K. Carlson, et al., *J. Chem. Theory Comput.* **2019**, *15*, 5925–5964.
- [38] B. O. Roos, V. Veryazov, P.-O. Widmark, *Theor. Chem. Acc.* **2004**, *111*, 345–351.
- [39] B. O. Roos, R. Lindh, P.-Å. Malmqvist, V. Veryazov, P.-O. Widmark, *J. Phys. Chem. A* **2004**, *108*, 2851–2858.
- [40] B. O. Roos, R. Lindh, P.-Å. Malmqvist, V. Veryazov, P.-O. Widmark, *Chem. Phys. Lett.* **2005**, *409*, 295–299.
- [41] T. A. Keith, **2017**.
- [42] W. Zou, D. Nori-Shargh, J. E. Boggs, *J. Phys. Chem. A* **2013**, *117*, 207–212.
- [43] E. D. Glendening, C. R. Landis, F. Weinhold, *J. Comput. Chem.* **2019**, *40*, 2234–2241.
- [44] G. Knizia, *J. Chem. Theory Comput.* **2013**, *9*, 4834–4843.
- [45] S. S. Rudel, H. L. Deubner, M. Müller, A. J. Karttunen, F. Kraus, *Nat. Chem.* **2020**, DOI 10.1038/s41557-020-0505-5.
- [46] D. Reta, F. Ortu, S. Randall, D. P. Mills, N. F. Chilton, R. E. P. Winpenny, L. Natrajan, B. Edwards, N. Kaltsoyannis, *J. Organomet. Chem.* **2018**, *857*, 58–74.
- [47] P. Pyykkö, *J. Phys. Chem. A* **2015**, *119*, 2326–2337.

- [48] V. Sauri, L. Serrano-Andrés, A. R. M. Shahi, L. Gagliardi, S. Vancoillie, K. Pierloot, *J. Chem. Theory Comput.* **2011**, *7*, 153–168.
- [49] M. Falcone, L. Barluzzi, J. Andrez, F. Fadaei Tirani, I. Zivkovic, A. Fabrizio, C. Corminboeuf, K. Severin, M. Mazzanti, *Nat. Chem.* **2019**, *11*, 154–160.
- [50] P. Sharma, D. R. Pahls, B. L. Ramirez, C. C. Lu, L. Gagliardi, *Inorg. Chem.* **2019**, *58*, 10139–10147.

Supplementary Information

U₂N₂ rings in diuranium complexes: a comparative computational study

Benjamin E. Atkinson and Nikolas Kaltsoyannis
Department of Chemistry, University of Manchester

1 DFT Singly Occupied Molecular Orbitals	2
2 Intrinsic Bonding Orbitals	7
3 Ring bond lengths	17
5 QTAIM bond indices and charges	18
6 NBO bond indices and charges	20
7 Imaginary Frequencies	22
8 Multiconfigurational Calculations	26

1 DFT Singly Occupied Molecular Orbitals

Singly occupied molecular orbitals of all open-shell systems studied. In some cases the $5f_U$ electron becomes somewhat delocalised in the KS MOs, in these cases the localised IBO is shown confirms the expected character for the uranium oxidation state of the system.

1.1 A^n $[U_2N_2Li_4TrenTIPS_2]^n$

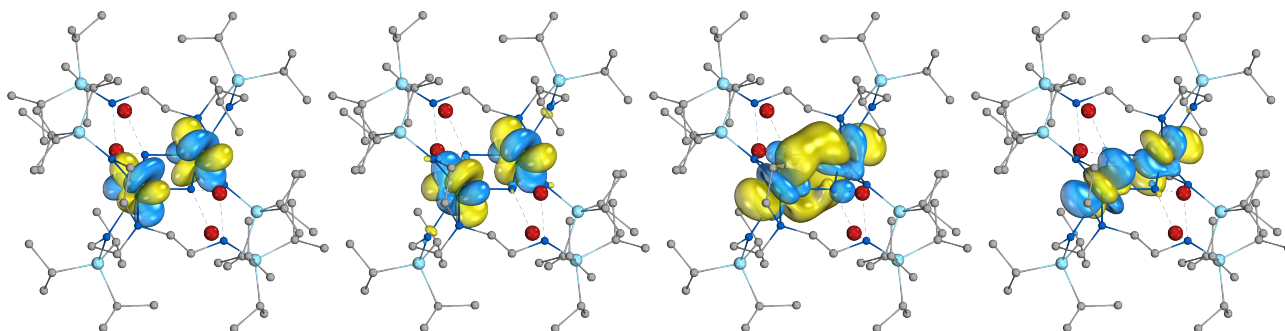


Figure S1: α U_2N_2 SOMOs of U(IV)/U(IV) **A** and their KS energy eigenvalues in Hartree

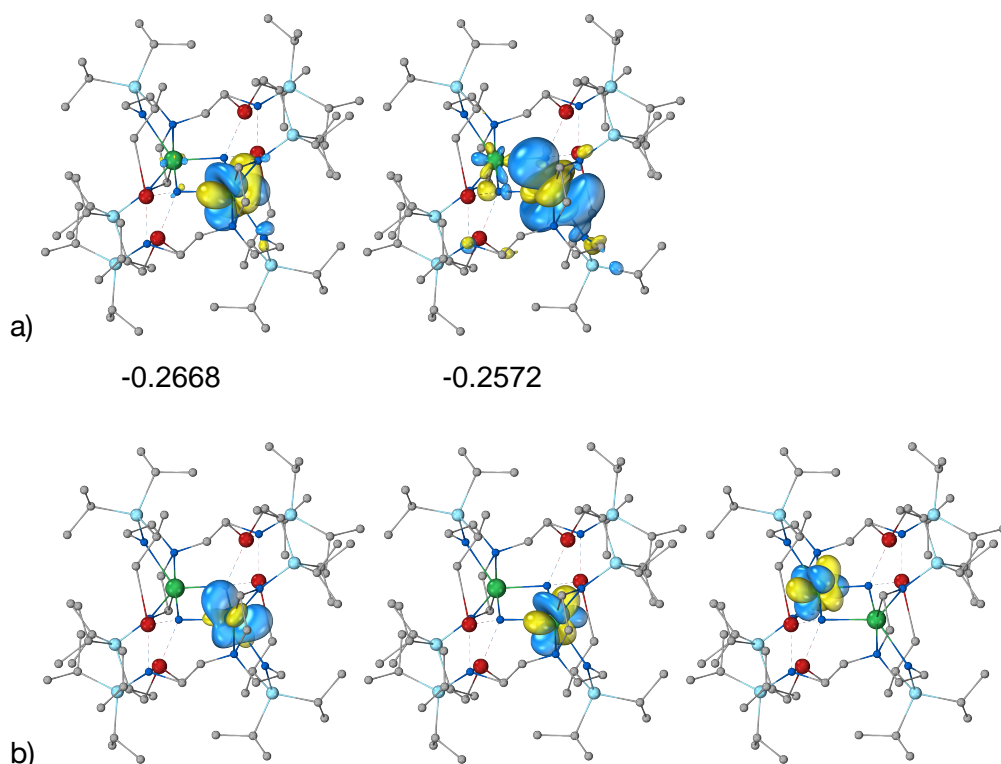


Figure S2: α U_2N_2 SOMOs of U(V)/U(IV) **A**⁺ and their KS energy eigenvalues in Hartree (a, top row). The $5f$ electron on the U(V) centre is delocalised, likely due to energy degeneracy with the amide ligand orbitals, so the $5f_U$ IBOs are additionally shown (b, bottom row).

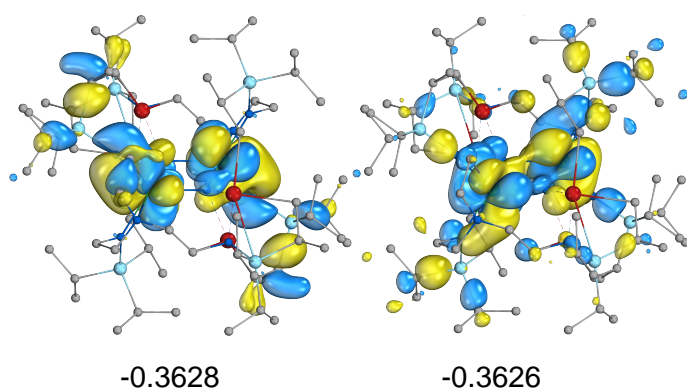


Figure S3: α U_2N_2 SOMOs of $\text{U(V)/U(V)} \mathbf{A}^{2+}$ and their KS energy eigenvalues in Hartree

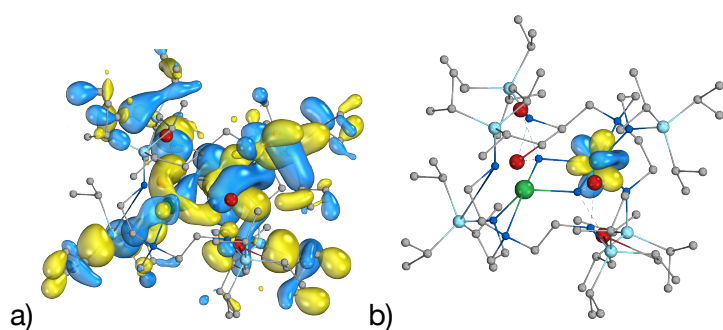
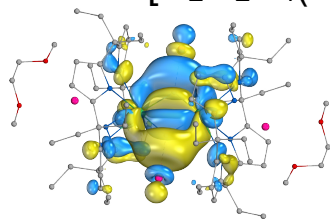
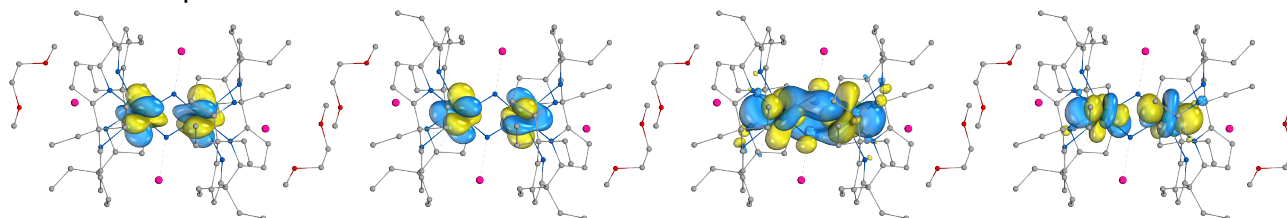


Figure S4: α U_2N_2 SOMO of $\text{U(V)/U(V)} \mathbf{A}^{3+}$ and its KS energy eigenvalue in Hartree (a). The 5f electron on the U(V) centre is delocalised, likely due to energy degeneracy with the amide ligand orbitals, so the $5f_{\text{U}}$ IBOs are additionally shown (b).

1.2 Bⁿ [U₂N₂K₄(Calix-[4]pyrrole)₂]ⁿ



α : 0.0008 β : 0.0006



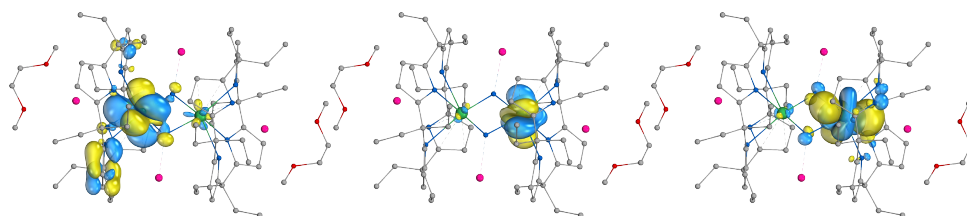
0.0462

0.0474

0.0514

0.0548

Figure S5: α U₂N₂ SOMOs of U(IV)/U(IV) B²⁻ and their KS energy eigenvalues in Hartree

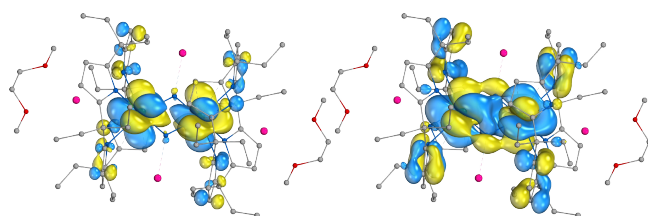


-0.0841

-0.0649

-0.0589

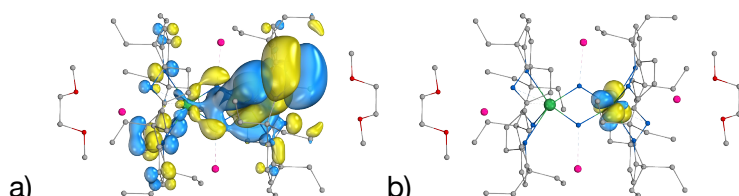
Figure S6: α U₂N₂ SOMOs of U(V)/U(IV) B⁻ and their KS energy eigenvalues in Hartree



-0.1810

-0.1801

Figure S7: α U₂N₂ SOMOs of U(V)/U(V) B and their KS energy eigenvalues in Hartree



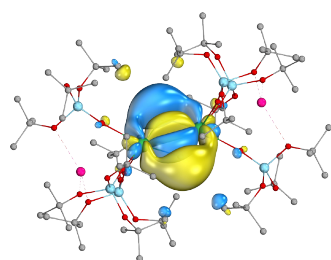
a)

b)

-0.3111

Figure S8: α U₂N₂ SOMO of U(V)/U(V) B⁺ and its KS energy eigenvalue in Hartree (a). The 5f electron on the U(V) centre is delocalised, likely due to energy degeneracy with the pyrrole ligand orbitals, so the 5f_U IBOs are additionally shown (b).

1.3 C^n $[U_2N_2K_2(OSiO^tBu_3)_6]^n$



α : 0.0112 β : 0.0108

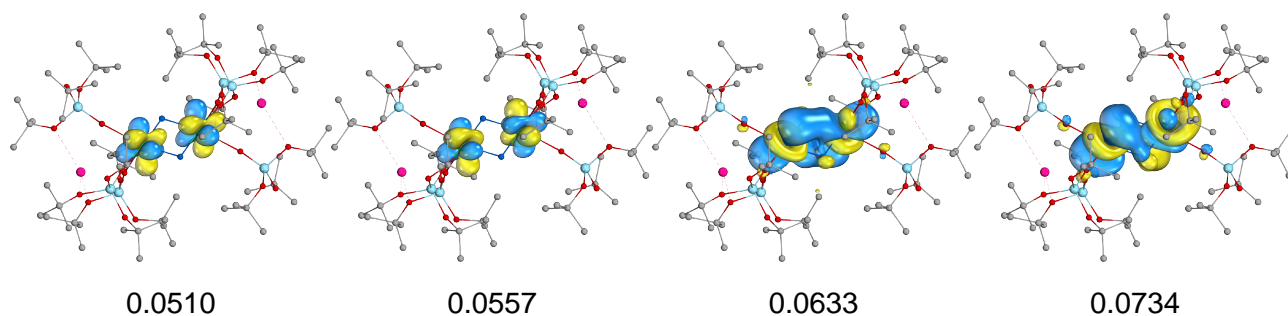


Figure S9: α U_2N_2 SOMOs of $U(IV)/U(IV)$ C^{2-} , and their KS energy eigenvalues in Hartree. Additionally, the α MO with positive energy eigenvalue is shown, and both the α and β orbital energies

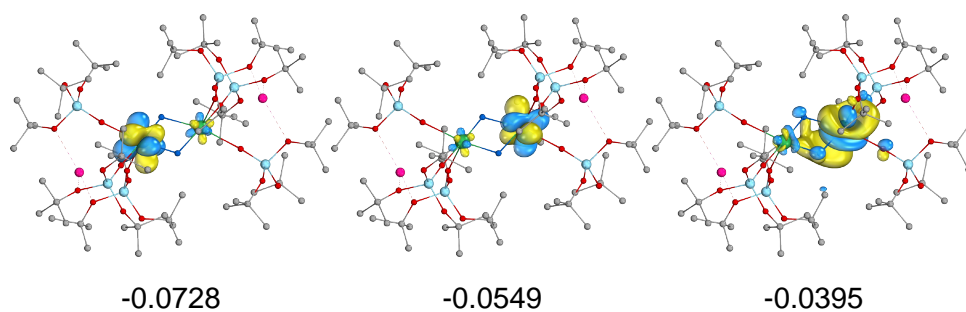


Figure S10: α U_2N_2 SOMOs of $U(IV)/U(V)$ C^- and their KS energy eigenvalues in Hartree

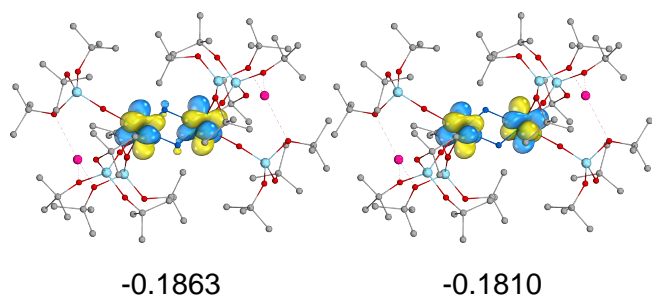
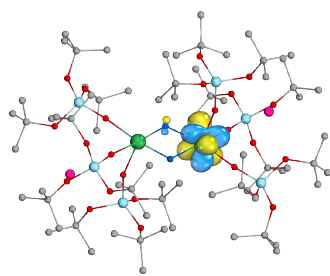
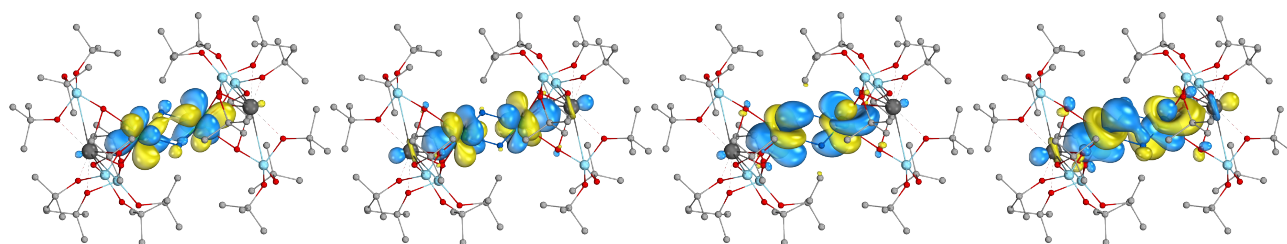


Figure S11: α U_2N_2 SOMOs of $U(V)/U(V)$ C and their KS energy eigenvalues in Hartree



-0.2934

Figure S12: α U_2N_2 SOMO of $\text{U(VI)/U(V)} \text{C}^+$ and its KS energy eigenvalue in Hartree



-0.1240

-0.1229

-0.1145

-0.1074

Figure S13: α U_2N_2 SOMOs of $\text{U(IV)/U(IV)} \text{C-Ca}$ (a neutral U(IV)/U(IV) model where K^+ is replaced by Ca^{2+}) and their KS energy eigenvalues in Hartree

2 Intrinsic Bonding Orbitals

All intrinsic bonding orbital (IBO) isosurfaces encapsulate 90% of the orbital. Even-charged systems have C_i symmetry so only IBOs centred on one nitride are shown, the IBOs on the opposite nitride are equivalent. Odd-charged systems have C_1 symmetry, so both sets of IBOs are shown. For the composition analysis (in the IAO basis), the composition of each sets of IBOs is shown in addition to the average of both sets.

2.1 A^n $[U_2N_2Li_4TrenTIPS_2]^n$

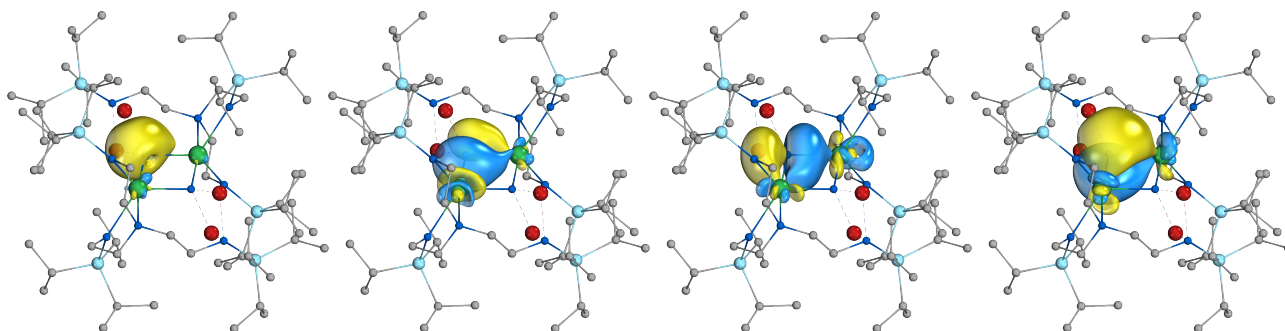


Figure S14: α U_2N_2 IBOs of U(IV)/U(IV) **A**

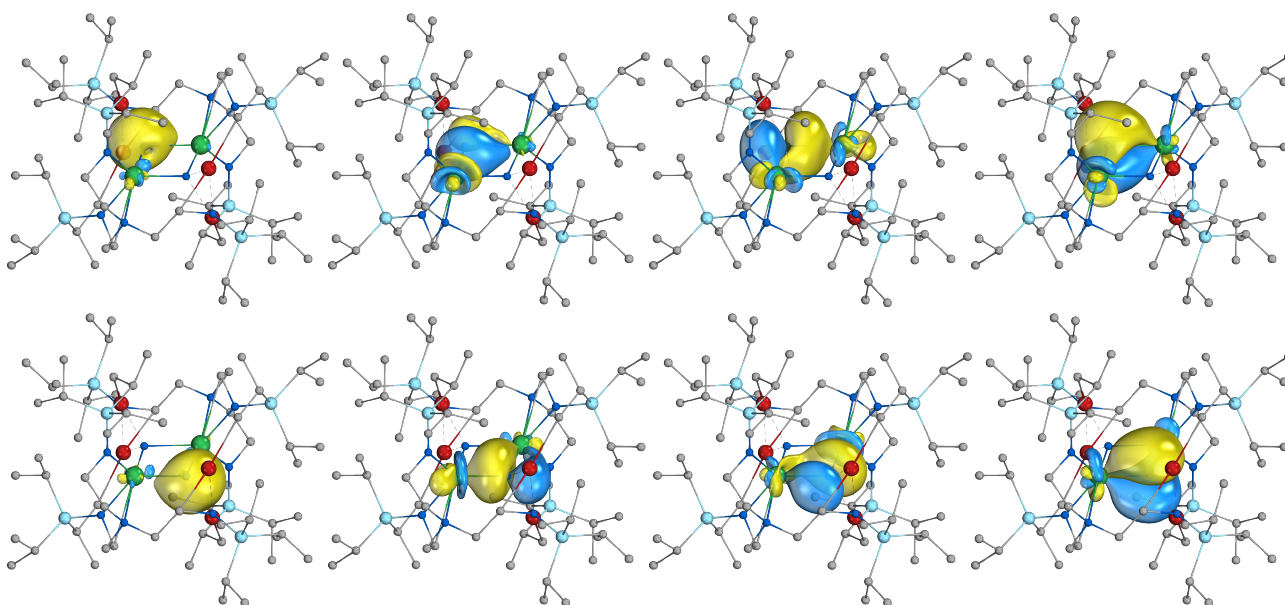


Figure S15: α U_2N_2 IBOs of U(V)/U(IV) **A⁺**

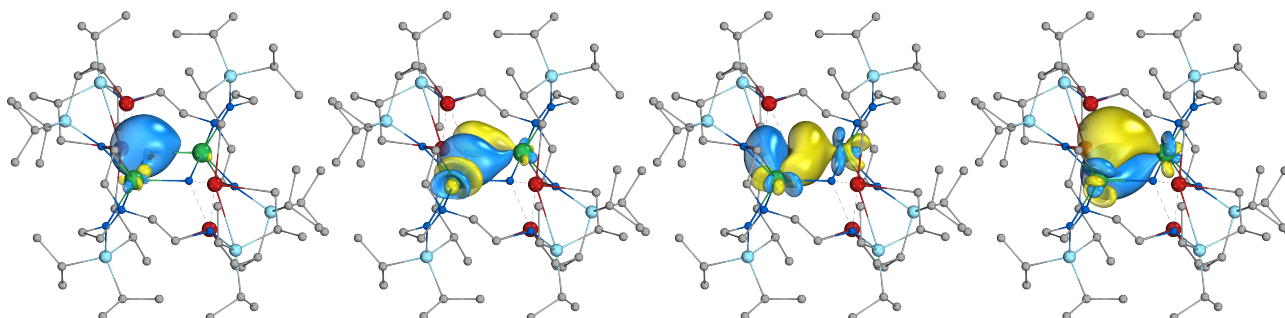


Figure S16: α U_2N_2 IBOs of U(V)/U(V) **A²⁺**

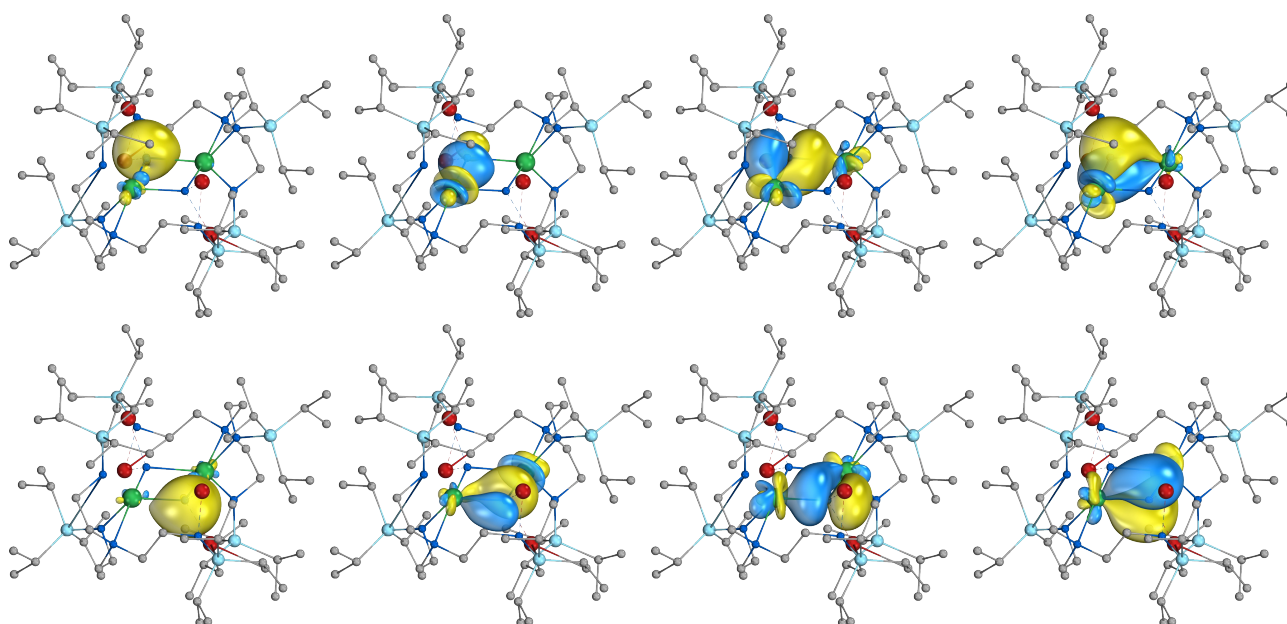


Figure S17: α U_2N_2 IBOs of U(VI)/U(V) **A**³⁺

Figure S17: α U_2N_2 IBOs of U(VI)/U(V) **A**⁴⁺

Table S1: Composition of α IBOs of U(IV)/U(IV) **A**, in the IAO basis

	U 7s	U 6d	U 5f	U other	N 2s	N 2p	N other
N 2s	2.23	5.62	1.69	0.46	55.31	26.50	0.49
U^a-N σ	1.90	18.75	8.85	1.20	12.63	55.95	0.12
U^b-N σ	2.39	19.63	6.98	1.70	9.01	59.41	0.08
U-N-U π	0.00	19.89	6.73	0.87	0.00	68.10	1.20

Table S2: Composition of α IBOs of U(V)/U(IV) **A**⁺, in the IAO basis (IBOs localised on U^a-N^b-U^b)

	U 7s	U 6d	U 5f	U other	N 2s	N 2p	N other
N 2s	2.88	5.79	1.73	0.60	58.50	21.87	1.44
U^a-N σ	0.98	17.55	14.04	2.63	15.04	49.00	0.15
U^b-N σ	2.03	18.53	8.63	2.11	2.78	64.99	0.03
U-N-U π	0.00	18.78	10.52	0.39	0.00	67.83	0.07

Table S3: Composition of α IBOs of U(V)/U(IV) A^+ , in the IAO basis (IBOs localised on U^a-N^a-U^b)

	U 7s	U 6d	U 5f	U other	N 2s	N 2p	N other
N 2s	2.95	6.04	1.73	0.68	58.72	22.16	0.52
U ^a -N σ	1.21	20.11	11.76	1.01	13.36	51.60	0.14
U ^b -N σ	1.53	17.04	10.29	1.75	4.36	64.40	0.04
U-N-U π	0.00	18.86	10.10	0.64	0.00	67.86	0.04

Table S4: Composition of α IBOs of U(V)/U(IV) A^+ , in the IAO basis (average)

	U 7s	U 6d	U 5f	U other	N 2s	N 2p	N other
N 2s	2.92	5.92	1.73	0.64	58.61	22.01	0.98
U ^a -N σ	1.10	18.83	12.90	1.82	14.20	50.30	0.15
U ^b -N σ	1.78	17.78	9.46	1.93	3.57	64.70	0.03
U-N-U π	0.00	18.82	10.31	0.52	0.00	67.84	0.06

Table S5: Composition of α IBOs of U(V)/U(V) A^{2+} , in the IAO basis

	U 7s	U 6d	U 5f	U other	N 2s	N 2p	N other
N 2s	3.90	6.59	2.24	0.57	63.14	18.43	1.03
U ^a -N σ	1.03	16.98	14.75	2.24	1.36	62.42	0.52
U ^b -N σ	0.00	17.21	16.76	1.23	0.00	64.18	0.02
U-N-U π	0.00	14.34	23.19	3.76	12.04	46.01	0.15

Table S6: Composition of α IBOs of U(VI)/U(V) A^{3+} , in the IAO basis (IBOs localised on U^a-N^a-U^b)

	U 7s	U 6d	U 5f	U other	N 2s	N 2p	N other
N 2s	3.45	6.18	1.77	0.49	62.14	19.42	0.64
U ^a -N σ	0.00	14.61	20.05	4.84	12.83	47.02	0.15
U ^a -N π	1.30	17.55	13.83	0.92	1.39	64.20	0.01
U-N-U π	0.00	16.79	14.74	0.87	0.00	65.72	0.38

Table S7: Composition of α IBOs of U(VI)/U(V) A^{3+} , in the IAO basis (IBOs localised on U^a-N^b-U^b)

	U 7s	U 6d	U 5f	U other	N 2s	N 2p	N other
N 2s	3.38	6.93	2.18	0.61	61.65	17.62	1.82
U ^a -N σ	0.00	17.95	13.93	0.41	0.00	65.08	0.72
U ^b -N σ	1.04	18.44	13.61	1.41	4.82	59.72	0.06
U-N-U π	0.66	16.10	17.15	1.69	10.01	53.68	0.11

Table S8: Composition of α IBOs of U(VI)/U(V) A^{3+} , in the IAO basis (average)

	U 7s	U 6d	U 5f	U other	N 2s	N 2p	N other
N 2s	3.42	6.56	1.97	0.55	61.89	18.52	1.23
U ^a -N σ	0.00	16.28	16.99	2.63	6.42	56.05	0.44
U ^a -N π / U ^b -N σ	1.17	17.99	13.72	1.17	3.10	61.96	0.04
U-N-U π	0.33	16.44	15.94	1.28	5.01	59.70	0.25

Table S9: Composition of α IBOs of U(VI)/U(VI) A^{4+} , in the IAO basis

	U 7s	U 6d	U 5f	U other	N 2s	N 2p	N other
N 2s	3.90	6.59	2.24	0.57	63.14	18.43	1.03
U ^a -N σ	1.03	16.98	14.75	2.24	1.36	62.42	0.52
U ^a -N π	0.00	17.21	16.76	1.23	0.00	64.18	0.02
U-N-U π	0.00	14.34	23.19	3.76	12.04	46.01	0.15

2.2 Bⁿ [U₂N₂K₄(Calix-[4]pyrrole)₂]ⁿ

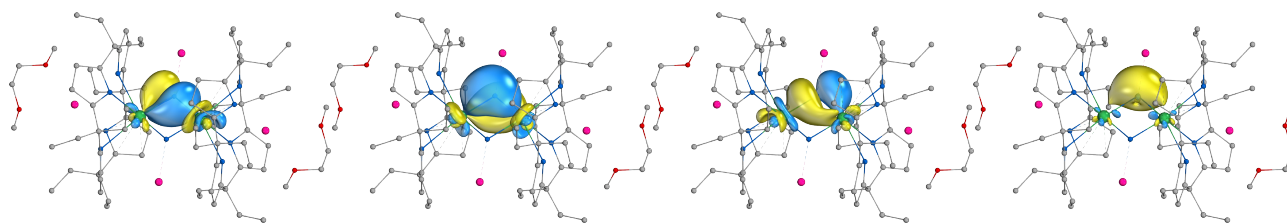


Figure S19: α U₂N₂ IBOs of U(IV)/U(IV) B²⁻

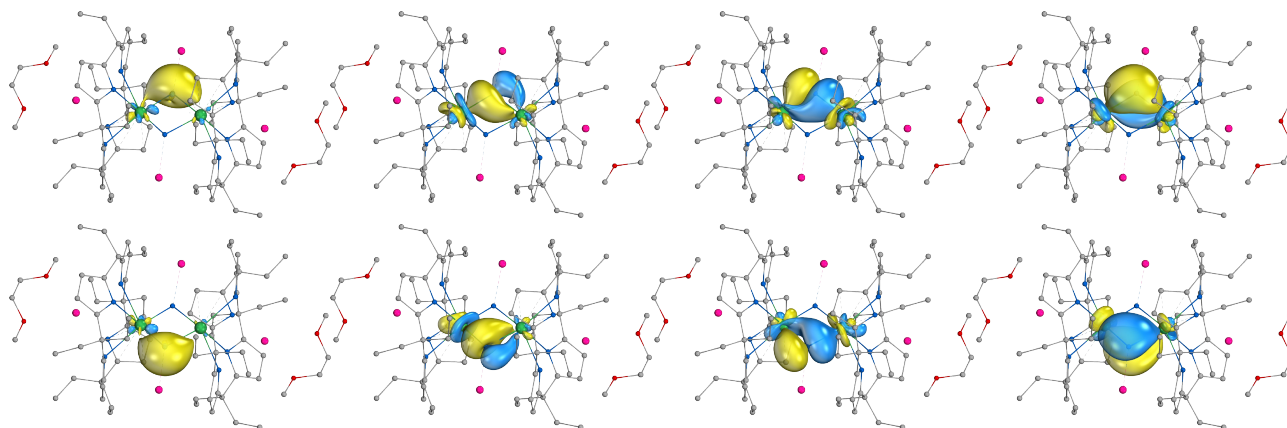


Figure S20: α U₂N₂ IBOs of U(V)/U(IV) B⁻

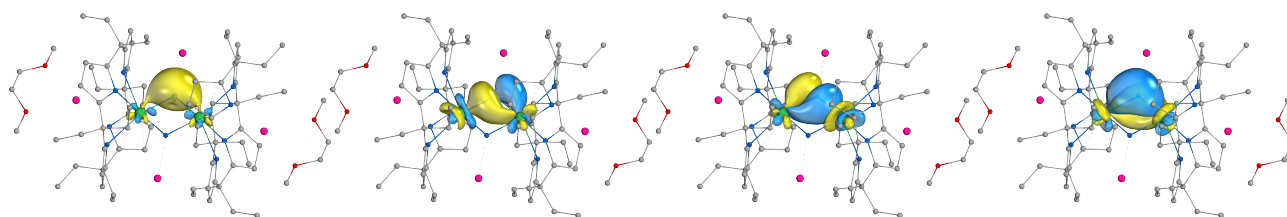


Figure S21: α U₂N₂ IBOs of U(V)/U(V) B

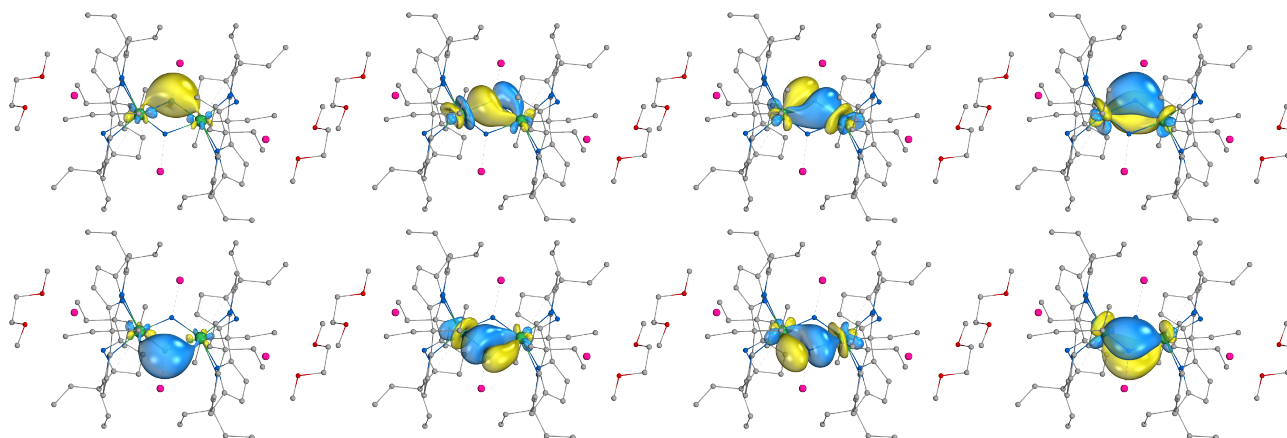


Figure S22: α U₂N₂ IBOs of U(V)/U(IV) B⁺

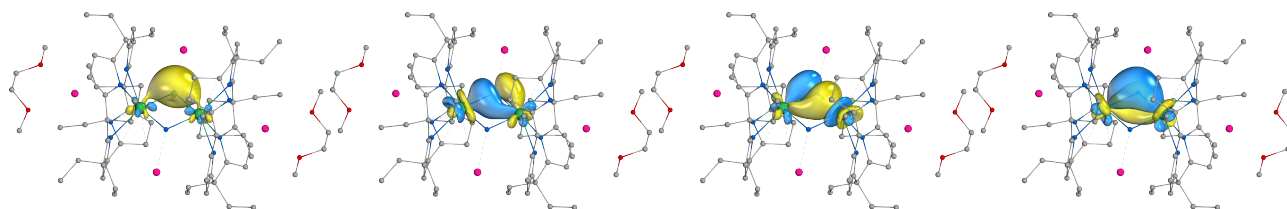


Figure S23: α U_2N_2 IBOs of U(V)/U(IV) B^{2+}

Table S10: Composition of α IBOs of U(IV)/U(IV) B^{2-} , in the IAO basis

	U 7s	U 6d	U 5f	U other	N 2s	N 2p	N other
N 2s	2.63	8.33	1.89	0.85	60.78	21.59	0.53
$\text{U}^{\text{a}}\text{-N } \sigma$	1.72	21.69	11.52	1.66	16.06	45.94	0.41
$\text{U}^{\text{b}}\text{-N } \sigma$	2.02	14.68	11.89	1.81	0.00	68.39	0.01
U-N-U π	0.00	22.33	10.05	1.63	0.00	64.17	0.03

Table S11: Composition of α IBOs of U(V)/U(IV) B^- , in the IAO basis (IBOs localised on $\text{U}^{\text{a}}\text{-N}^{\text{b}}\text{-U}^{\text{b}}$)

	U 7s	U 6d	U 5f	U other	N 2s	N 2p	N other
N 2s	2.78	8.58	2.52	0.61	61.13	20.59	0.78
$\text{U}^{\text{a}}\text{-N } \sigma$	1.38	18.12	15.55	2.75	13.13	48.12	0.15
$\text{U}^{\text{b}}\text{-N } \sigma$	1.60	15.67	13.85	1.78	2.27	63.80	0.03
U-N-U π	0.00	20.63	13.24	0.92	0.00	63.69	0.01

Table S12: Composition of α IBOs of U(V)/U(IV) B^- , in the IAO basis (IBOs localised on $\text{U}^{\text{a}}\text{-N}^{\text{a}}\text{-U}^{\text{b}}$)

	U 7s	U 6d	U 5f	U other	N 2s	N 2p	N other
N 2s	1.31	17.41	16.43	3.06	13.30	47.66	0.15
$\text{U}^{\text{a}}\text{-N } \sigma$	2.83	8.37	2.75	0.44	61.18	20.62	0.90
$\text{U}^{\text{b}}\text{-N } \sigma$	1.59	15.37	14.29	1.85	2.13	63.75	0.02
U-N-U π	0.00	20.61	12.51	1.49	0.00	63.79	0.01

Table S13: Composition of α IBOs of U(V)/U(IV) B^- , in the IAO basis (average)

	U 7s	U 6d	U 5f	U other	N 2s	N 2p	N other
N 2s	2.81	8.48	2.64	0.53	61.16	20.60	0.84
$\text{U}^{\text{a}}\text{-N } \sigma$	1.34	17.77	15.99	2.91	13.21	47.89	0.15
$\text{U}^{\text{b}}\text{-N } \sigma$	1.59	15.52	14.07	1.82	2.20	63.78	0.02
U-N-U π	0.00	20.62	12.87	1.20	0.00	63.74	0.01

Table S14: Composition of α IBOs of U(V)/U(V) **B**, in the IAO basis

	U 7s	U 6d	U 5f	U other	N 2s	N 2p	N other
N 2s	2.88	8.86	3.28	0.58	61.97	19.34	0.58
U^a-N σ	1.37	15.53	18.07	2.43	7.53	53.37	1.00
U^b-N σ	1.39	15.06	18.46	2.20	6.84	54.51	0.75
U-N-U π	0.00	19.13	15.49	1.18	0.00	62.90	0.00

Table S15: Composition of α IBOs of U(VI)/U(V) **B⁺**, in the IAO basis (IBOs localised on U^a-N^b-U^b)

	U 7s	U 6d	U 5f	U other	N 2s	N 2p	N other
N 2s	2.99	8.59	3.27	0.65	62.71	18.60	0.99
U^a-N σ	1.10	14.41	20.82	2.28	10.36	49.86	0.27
U^b-N σ	1.28	14.29	18.61	2.03	3.57	59.24	0.20
U-N-U π	0.00	17.93	17.55	0.91	0.00	62.26	0.34

Table S16: Composition of α IBOs of U(VI)/U(V) **B⁺**, in the IAO basis (IBOs localised on U^a-N^a-U^b)

	U 7s	U 6d	U 5f	U other	N 2s	N 2p	N other
N 2s	2.97	8.52	3.32	0.70	62.70	18.34	1.16
U^a-N σ	1.16	14.27	20.77	2.20	9.86	50.66	0.29
U^b-N σ	1.23	14.50	19.14	1.43	4.06	58.61	0.13
U-N-U π	0.00	17.99	17.75	0.86	0.00	62.16	0.44

Table S17: Composition of α IBOs of U(VI)/U(V) **B⁺**, in the IAO basis (average)

	U 7s	U 6d	U 5f	U other	N 2s	N 2p	N other
N 2s	2.98	8.55	3.29	0.67	62.71	18.47	1.07
U^a-N σ	1.13	14.34	20.79	2.24	10.11	50.26	0.28
U^b-N σ	1.25	14.39	18.88	1.73	3.81	58.93	0.16
U-N-U π	0.00	17.96	17.65	0.89	0.00	62.21	0.39

Table S18: Composition of α IBOs of U(VI)/U(VI) **B²⁺**, in the IAO basis

	U 7s	U 6d	U 5f	U other	N 2s	N 2p	N other
N 2s	2.98	8.58	3.36	0.77	63.08	18.37	0.65
U^a-N σ	1.15	13.24	21.31	1.90	7.31	53.25	1.04
U^a-N π	1.20	13.66	20.33	2.11	6.34	54.53	1.03
U-N-U π	0.00	18.02	17.60	1.28	0.00	62.30	0.00

2.3 C^n $[U_2N_2K_2(OSiO^tBu_3)_6]^n$

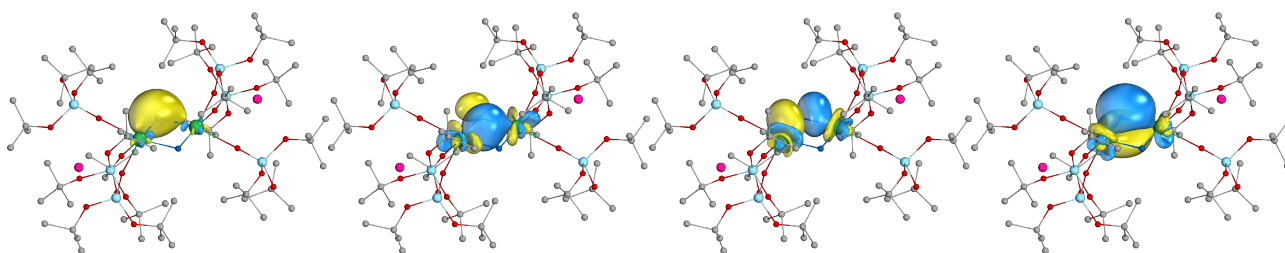


Figure S24: α U_2N_2 IBOs of U(IV)/U(IV) C^{2-}

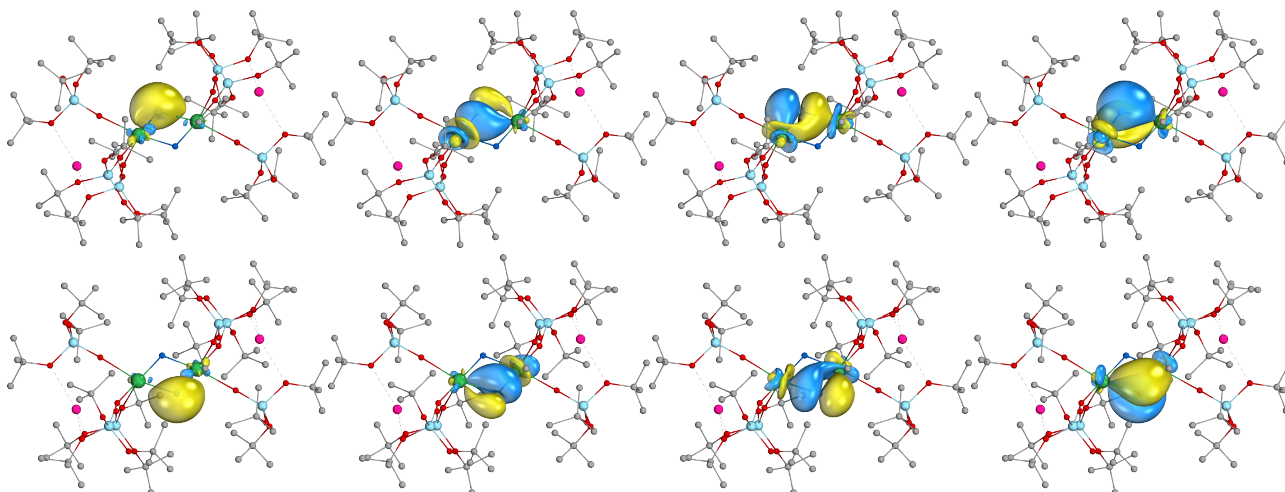


Figure S25: α U_2N_2 IBOs of U(V)/U(IV) C^-

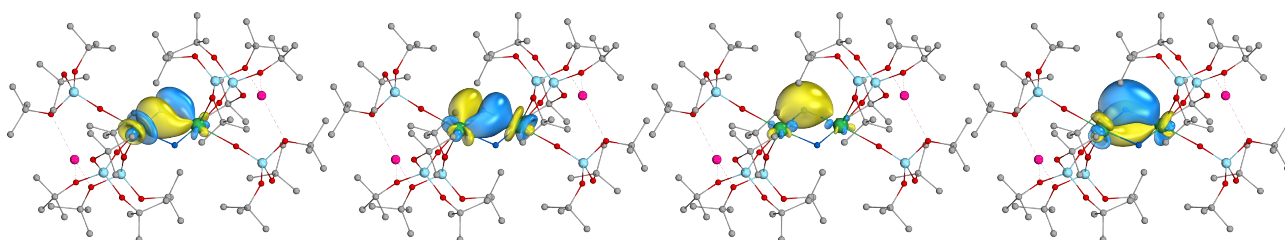


Figure S26: α U_2N_2 IBOs of U(V)/U(V) C

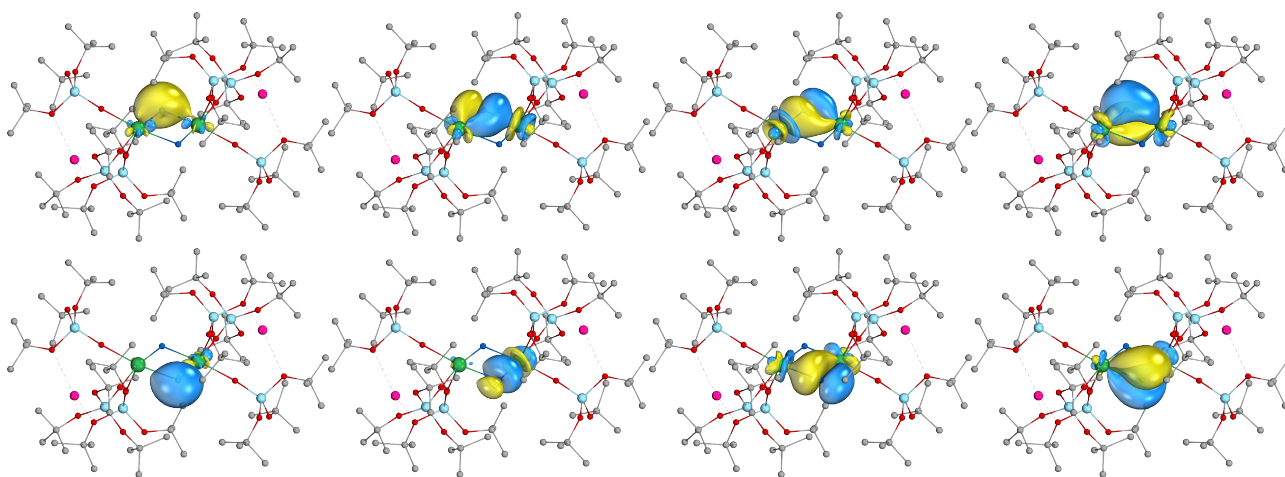


Figure S27: α U_2N_2 IBOs of U(VI)/U(V) C^+

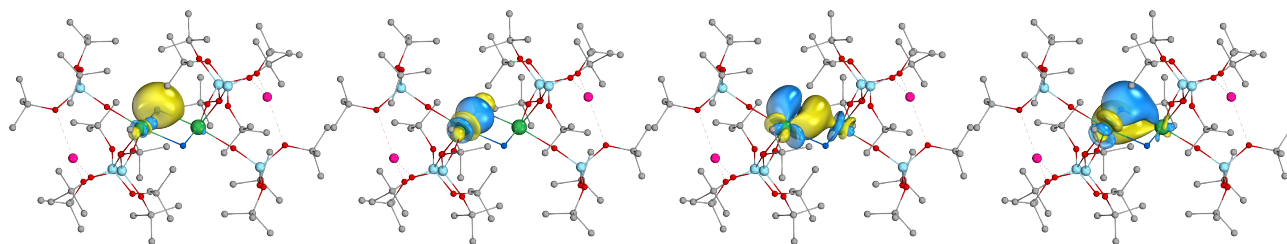


Figure S28: α U_2N_2 IBOs of U(VI)/U(VI) C^{2+}

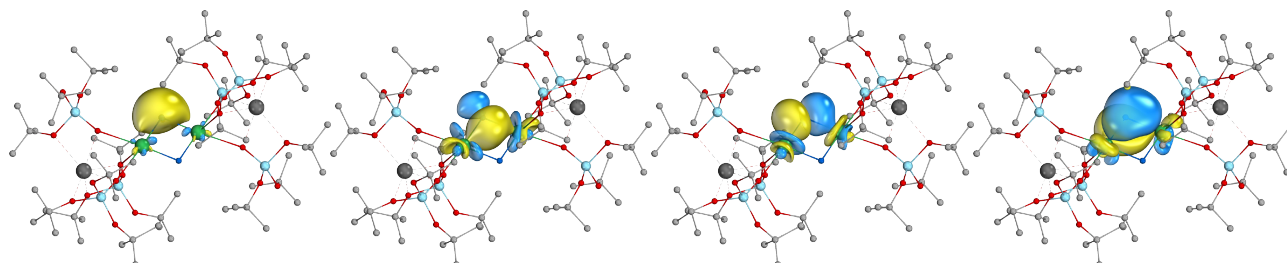


Figure S29: α U_2N_2 IBOs of U(IV)/U(IV) **C-Ca**, a neutral U(IV)/U(IV) model where K^+ is replaced by Ca^{2+}

Table S19: Composition of α IBOs of U(IV)/U(IV) C^{2-} , in the IAO basis

	U 7s	U 6d	U 5f	U other	N 2s	N 2p	N other
N 2s	3.89	8.77	2.06	0.98	64.38	17.64	0.59
U-N-U σ	2.31	15.55	13.08	1.56	0.00	66.90	0.00
U-N-U σ	1.01	22.13	14.14	0.32	12.98	48.08	0.25
U-N-U π	0.00	25.84	8.06	1.30	0.00	62.09	0.91

Table S20: Composition of α IBOs of U(V)/U(IV) C^- , in the IAO basis (IBOs localised on $\text{U}^{\text{a}}\text{-N}^{\text{b}}\text{-U}^{\text{b}}$)

	U 7s	U 6d	U 5f	U other	N 2s	N 2p	N other
N 2s	4.07	8.68	2.32	1.03	63.93	17.87	0.59
$\text{U}^{\text{a}}\text{-N } \sigma$	0.73	17.46	18.92	2.09	10.14	49.44	0.52
$\text{U}^{\text{b}}\text{-N } \sigma$	1.56	17.07	14.73	1.44	2.89	61.25	0.47
U-N-U π	0.00	23.27	11.16	1.47	0.00	62.15	0.65

Table S21: Composition of α IBOs of U(V)/U(IV) C^- , in the IAO basis (IBOs localised on $\text{U}^{\text{a}}\text{-N}^{\text{a}}\text{-U}^{\text{b}}$)

	U 7s	U 6d	U 5f	U other	N 2s	N 2p	N other
N 2s	4.15	8.62	2.37	0.97	63.96	17.74	0.70
$\text{U}^{\text{a}}\text{-N } \sigma$	0.67	17.71	19.05	1.77	10.07	49.28	0.76
$\text{U}^{\text{b}}\text{-N } \sigma$	1.53	16.91	14.95	1.32	2.84	61.73	0.03
U-N-U π	0.00	23.14	11.39	1.27	0.00	62.72	0.18

Table S22: Composition of α IBOs of U(V)/U(IV) \mathbf{C}^- , in the IAO basis (average)

	U 7s	U 6d	U 5f	U other	N 2s	N 2p	N other
N 2s	4.11	8.65	2.34	1.00	63.95	17.81	0.65
U ^a -N σ	0.70	17.58	18.99	1.93	10.10	49.36	0.64
U ^b -N σ	1.54	16.99	14.84	1.38	2.87	61.49	0.25
U-N-U π	0.00	23.21	11.28	1.37	0.00	62.44	0.41

Table S23: Composition of α IBOs of U(V)/U(V) \mathbf{C} , in the IAO basis

	U 7s	U 6d	U 5f	U other	N 2s	N 2p	N other
N 2s	3.88	8.66	2.67	1.19	64.26	16.79	1.16
U ^a -N σ	0.70	15.40	21.53	1.97	7.89	51.91	0.10
U ^b -N σ	0.99	16.13	18.19	3.00	4.74	56.41	0.06
U-N-U π	0.00	21.52	13.93	0.65	0.00	62.79	0.01

Table S24: Composition of α IBOs of U(VI)/U(V) \mathbf{C}^+ , in the IAO basis (IBOs localised on U^a-N^a-U^b)

	U 7s	U 6d	U 5f	U other	N 2s	N 2p	N other
N 2s	3.82	8.05	2.52	0.92	64.46	15.50	3.44
U ^a -N σ	0.00	12.23	25.64	4.63	10.48	46.49	0.13
U ^a -N π	0.92	15.64	17.81	1.52	2.22	61.45	0.03
U-N-U π	0.00	18.63	16.83	0.24	0.00	63.49	0.01

Table S25: Composition of α IBOs of U(VI)/U(V) \mathbf{C}^+ , in the IAO basis (IBOs localised on U^a-N^b-U^b)

	U 7s	U 6d	U 5f	U other	N 2s	N 2p	N other
N 2s	3.64	8.38	3.34	0.84	62.43	18.80	1.27
U ^a -N σ	0.87	15.15	20.77	1.92	7.37	52.73	0.80
U ^b -N σ	0.63	15.00	18.47	2.01	7.10	56.31	0.09
U-N-U π	0.00	19.37	14.84	0.90	0.00	63.94	0.06

Table S26: Composition of α IBOs of U(VI)/U(V) \mathbf{C}^+ , in the IAO basis (average)

	U 7s	U 6d	U 5f	U other	N 2s	N 2p	N other
N 2s	3.73	8.22	2.93	0.88	63.44	17.15	2.35
U ^a -N σ	0.43	13.69	23.21	3.27	8.92	49.61	0.47
U ^a -N π / U ^b -N σ	0.78	15.32	18.14	1.76	4.66	58.88	0.06
U-N-U π	0.00	19.00	15.83	0.57	0.00	63.71	0.04

Table S27: Composition of α IBOs of U(VI)/U(VI) C^{2+} , in the IAO basis

	U 7s	U 6d	U 5f	U other	N 2s	N 2p	N other
N 2s	4.06	7.91	2.31	1.02	65.45	16.94	1.11
U ^a -N σ	0.00	10.88	33.83	0.60	10.34	43.93	0.13
U ^a -N π	0.97	16.13	19.65	1.46	0.00	60.27	1.13
U-N-U π	0.00	17.79	18.30	0.61	0.00	62.60	0.00

Table S28: Composition of α IBOs of U(VI)/U(VI) C^{2+} , in the IAO basis

	U 7s	U 6d	U 5f	U other	N 2s	N 2p	N other
N 2s	4.06	7.91	2.31	1.02	65.45	16.94	1.11
U ^a -N σ	0.00	10.88	33.83	0.60	10.34	43.93	0.13
U ^a -N π	0.97	16.13	19.65	1.46	0.00	60.27	1.13
U-N-U π	0.00	17.79	18.30	0.61	0.00	62.60	0.00

For the odd charged systems, U^a is the higher oxidation centre. U^a-N^a is the shortest U-N_{ring} bond at U^a. For C_i even charged systems, U^a-N^a = U^b-N^b

3 Ring bond lengths

Table S29: Ring bond lengths of **A** in ångstrom for the charges studied

	A	A ⁺	A ²⁺	A ³⁺	A ⁴⁺
	U(IV)/U(IV)	U(V)/U(IV)	U(V)/U(V)	U(VI)/U(V)	U(VI)/U(VI)
U ^a -N ^a	2.145	2.021	2.026	1.911	1.875
U ^b -N ^a	2.204	2.282	2.224	2.371	1.875
U ^b -N ^b	2.145	2.186	2.026	2.054	2.336
U ^a -N ^b	2.204	2.094	2.224	2.156	2.336
average	2.174	2.146	2.125	2.123	2.106

Table S30: Ring bond lengths of **B** in ångstrom for the charges studied

	B ²⁻	B ⁻	B	B ⁺	B ²⁺
	U(IV)/U(IV)	U(V)/U(IV)	U(V)/U(V)	U(VI)/U(V)	U(VI)/U(VI)
U ^a -N ^a	2.075	1.972	2.038	1.959	1.913
U ^b -N ^a	2.085	2.162	2.048	2.129	2.189
U ^b -N ^b	2.075	1.989	2.038	1.972	1.913
U ^a -N ^b	2.085	2.138	2.048	2.113	2.189
average	2.080	2.065	2.043	2.043	2.051

Table S31: Ring bond lengths of **C** in ångstrom for the charges studied, and **C-Ca**, a neutral U(IV)/U(IV) model where K⁺ is replaced by Ca²⁺

	C-Ca	C²⁻	C⁻	C	C⁺	C²⁺
	U(IV)/U(IV)	U(IV)/U(IV)	U(V)/U(IV)	U(V)/U(V)	U(VI)/U(V)	U(VI)/U(VI)
U^a-N^a	2.045	2.085	1.987	2.004	1.890	1.830
U^b-N^a	2.056	2.085	2.146	2.004	2.213	1.830
U^b-N^b	2.045	2.086	1.988	2.084	2.030	2.301
U^a-N^b	2.056	2.086	2.143	2.084	2.027	2.301
average	2.051	2.085	2.066	2.044	2.040	2.066

5 QTAIM bond indices and charges

Table S32: QTAIM charges, $q(X)$, and $\delta(U|N_{\text{ring}})$ and $\delta(U|U)$ delocalisation indices of **A** for the charges studied.

	A	A⁺	A²⁺	A³⁺	A⁴⁺
	U(IV)/U(IV)	U(V)/U(IV)	U(V)/U(V)	U(VI)/U(V)	U(VI)/U(VI)
q(N^a)	2.305	2.517	2.530	2.614	2.602
q(N^b)	2.305	2.327	2.530	2.529	2.602
q(U^a)	-1.817	-1.680	-1.601	-1.429	-1.295
q(U^b)	-1.817	-1.709	-1.601	-1.519	-1.295
$\delta(U^a N^a)$	1.087	1.443	1.419	1.834	1.949
$\delta(U^b N^a)$	0.969	0.785	0.897	0.619	0.653
$\delta(U^b N^b)$	1.087	0.961	1.419	1.329	1.949
$\delta(U^a N^b)$	0.969	1.243	0.897	1.093	0.653
$\delta(U N)$	1.028	1.108	1.158	1.219	1.301
average					
$\delta(U U)$	0.168	0.195	0.207	0.214	0.222

Table S33: QTAIM charges, $q(X)$, and $\delta(U|N_{\text{ring}})$ and $\delta(U|U)$ delocalisation indices of **B** for the charges studied.

	B²⁻	B⁻	B	B⁺	B²⁺
	U(IV)/U(IV)	U(V)/U(IV)	U(V)/U(V)	U(VI)/U(V)	U(VI)/U(VI)
q(N^a)	-1.561	-1.468	-1.365	-1.270	-1.205
q(N^b)	-1.561	-1.460	-1.365	-1.265	-1.205
q(U^a)	2.205	2.430	2.463	2.555	2.569
q(U^b)	2.205	2.285	2.463	2.502	2.569
$\delta(U^a N^a)$	1.181	1.527	1.298	1.612	1.797
$\delta(U^b N^a)$	1.154	0.931	1.270	1.036	0.904
$\delta(U^b N^b)$	1.181	0.984	1.298	1.081	1.797
$\delta(U^a N^b)$	1.154	1.470	1.270	1.566	0.904
$\delta(U N)$ average	1.168	1.228	1.284	1.324	1.350
$\delta(U U)$	0.248	0.264	0.317	0.325	0.315

Table S34: QTAIM charges, $q(X)$, and $\delta(U|N_{\text{ring}})$ and $\delta(U|U)$ delocalisation indices of **C** for the charges studied, and **C-Ca**, a neutral U(IV)/U(IV) model where K⁺ is replaced by Ca²⁺

	C-Ca	C²⁻	C⁻	C	C⁺	C²⁺
	U(IV)/U(IV)	U(IV)/U(IV)	U(V)/U(IV)	U(V)/U(V)	U(VI)/U(V)	U(VI)/U(VI)
q(N^a)	-1.476	-1.555	-1.446	-1.330	-1.175	-1.095
q(N^b)	-1.476	-1.555	-1.448	-1.330	-1.243	-1.095
q(U^a)	2.237	2.324	2.590	2.631	2.771	2.807
q(U^b)	2.237	2.324	2.416	2.631	2.689	2.807
$\delta(U^a N^a)$	1.238	1.212	1.519	1.431	1.928	2.086
$\delta(U^b N^a)$	1.219	1.205	1.009	1.178	0.765	0.653
$\delta(U^b N^b)$	1.238	1.212	1.015	1.431	1.398	2.086
$\delta(U^a N^b)$	1.219	1.205	1.514	1.178	1.289	0.653
$\delta(U N)$ average	1.229	1.209	1.264	1.304	1.345	1.369
$\delta(U U)$	0.288	0.263	0.285	0.321	0.321	0.264

6 NBO bond indices and charges

Table S35: NBO charges ($q(X)$) and U-N ring and U-U Wiberg bond indices (A-B) of **A** for the charges studied.

	A	A⁺	A²⁺	A³⁺	A⁴⁺
	U(IV)/U(IV)	U(V)/U(IV)	U(V)/U(V)	U(VI)/U(V)	U(VI)/U(VI)
q(N^a)	-1.027	-1.133	-1.388	-1.486	-1.667
q(N^b)	-1.027	-1.259	-1.388	-1.525	-1.667
q(U^a)	1.856	1.943	1.867	1.836	1.759
q(U^b)	1.856	1.704	1.867	1.782	1.759
U^a-N^a	1.984	1.929	1.414	1.461	1.057
U^b-N^a	0.692	1.143	0.879	1.222	0.905
U^b-N^b	1.984	1.285	1.414	0.718	1.057
U^a-N^b	0.692	0.610	0.879	0.908	0.905
U-N average	1.338	1.241	1.146	1.077	0.981
U-U	0.236	0.231	0.225	0.209	0.182

Table S36: NBO charges ($q(X)$) and U-N ring and U-U Wiberg bond indices (A-B) of **B** for the charges studied.

	B²⁻	B⁻	B	B⁺	B²⁺
	U(IV)/U(IV)	U(V)/U(IV)	U(V)/U(V)	U(VI)/U(V)	U(VI)/U(VI)
q(N^a)	-0.891	-1.011	-1.174	-1.688	-1.513
q(N^b)	-0.891	-1.018	-1.174	-1.673	-1.513
q(U^a)	1.605	1.714	1.661	2.055	1.517
q(U^b)	1.605	1.586	1.661	1.913	1.517
U^a-N^a	1.858	1.049	1.309	1.269	1.122
U^b-N^a	0.980	1.091	1.283	1.323	1.098
U^b-N^b	1.858	1.685	1.309	0.754	1.122
U^a-N^b	0.980	1.637	1.283	0.717	1.098
U-N average	1.419	1.365	1.296	1.016	1.110
U-U	0.311	0.321	0.314	0.173	0.236

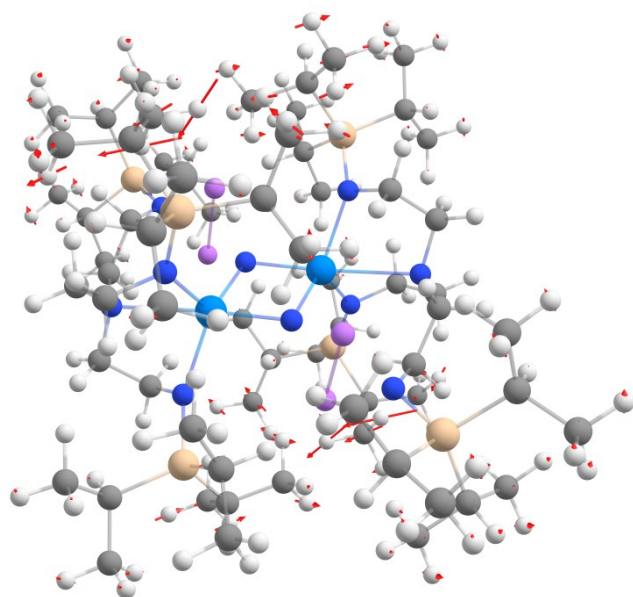
Table S37: NBO charges ($q(X)$) and U-N ring and U-U Wiberg bond indices (A-B) of **C** for the charges studied, and **C-Ca**, a neutral U(IV)/U(IV) model where K^+ is replaced by Ca^{2+}

	C-Ca	C²⁻	C⁻	C	C⁺	C²⁺
	U(IV)/U(IV)	U(IV)/U(IV)	U(V)/U(IV)	U(V)/U(V)	U(VI)/U(V)	U(VI)/U(VI)
q(N^a)	-1.295	-0.694	-0.931	-1.080	-1.917	-2.054
q(N^b)	-1.295	-0.694	-0.822	-1.080	-1.917	-2.054
q(U^a)	1.360	1.728	1.857	1.773	2.403	2.154
q(U^b)	1.360	1.728	1.657	1.773	2.339	2.154
U^a-N^a	1.201	2.230	2.082	1.468	1.121	0.755
U^b-N^a	1.195	0.692	1.371	1.188	1.126	0.755
U^b-N^b	1.201	2.230	1.417	1.468	0.567	0.755
U^a-N^b	1.195	0.692	0.762	1.188	0.568	0.755
U-N average	1.198	1.461	1.408	1.328	0.845	0.755
U-U	0.310	0.287	0.345	0.342	0.160	0.183

7 Imaginary Frequencies

Table S38: The number of imaginary frequencies (#), their frequencies (in cm^{-1}) and symmetry of **A** for the charges studied. Normal modes are given in molder format as a supplementary data file.

	A	A⁺	A²⁺	A³⁺	A⁴⁺
	U(IV)/U(IV)	U(V)/U(IV)	U(V)/U(V)	U(VI)/U(V)	U(VI)/U(VI)
#	0	1	2	0	0
		i12.57 (A)	i16.29 (A _g)		
			i11.38 (A _u)		



i12.57

Figure S30: The imaginary normal mode of **A⁺**

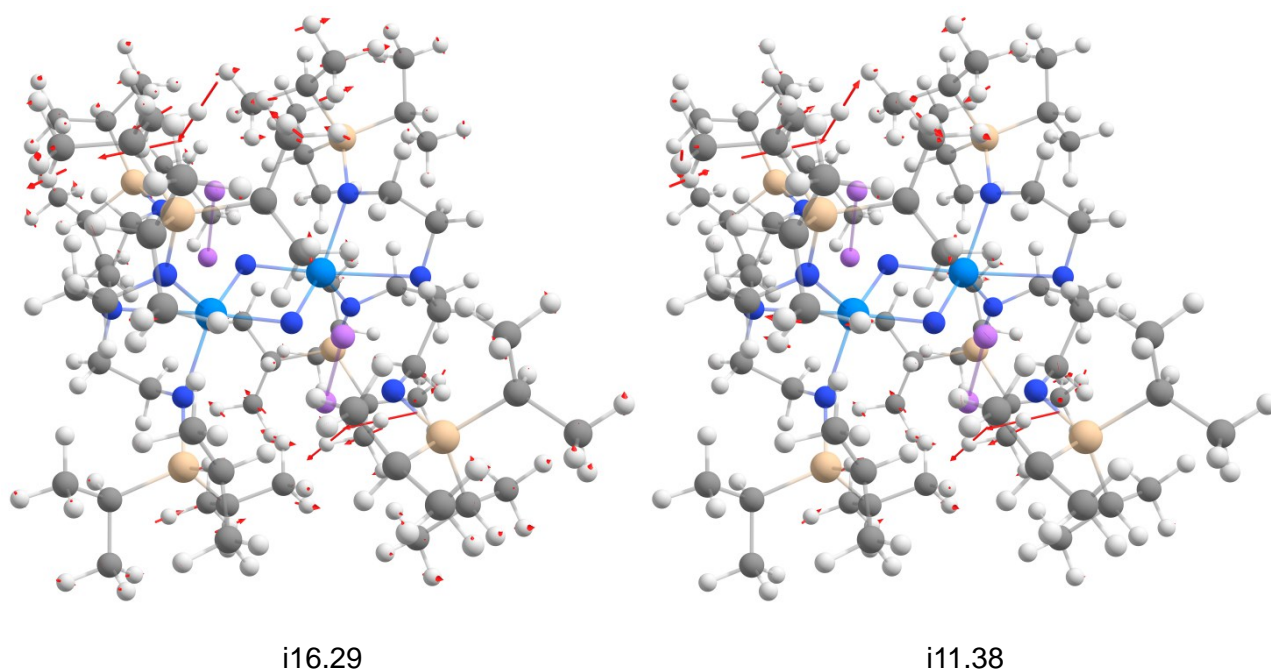


Figure S31: The imaginary normal modes of A^{2+}

Table S39: The number of imaginary frequencies (#), their frequencies (in cm^{-1}) and symmetry of **B** for the charges studied. Normal modes are given in molder format as a supplementary data file.

	B^{2-}	B^{-}	B	B^{+}	B^{2+}
	U(IV)/U(IV)	U(V)/U(IV)	U(V)/U(V)	U(VI)/U(V)	U(VI)/U(VI)
#	1	0	2	0	0
	i9.75 (A_u)		i3.84 (A_g)		
			i3.76 (A_u)		

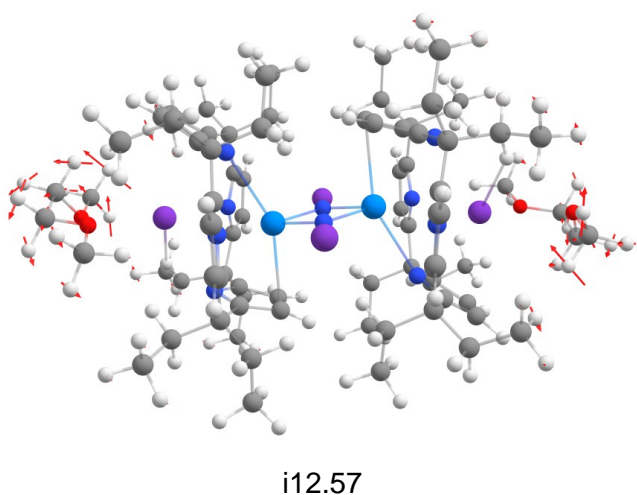


Figure S32: The imaginary normal mode of B^{2-}

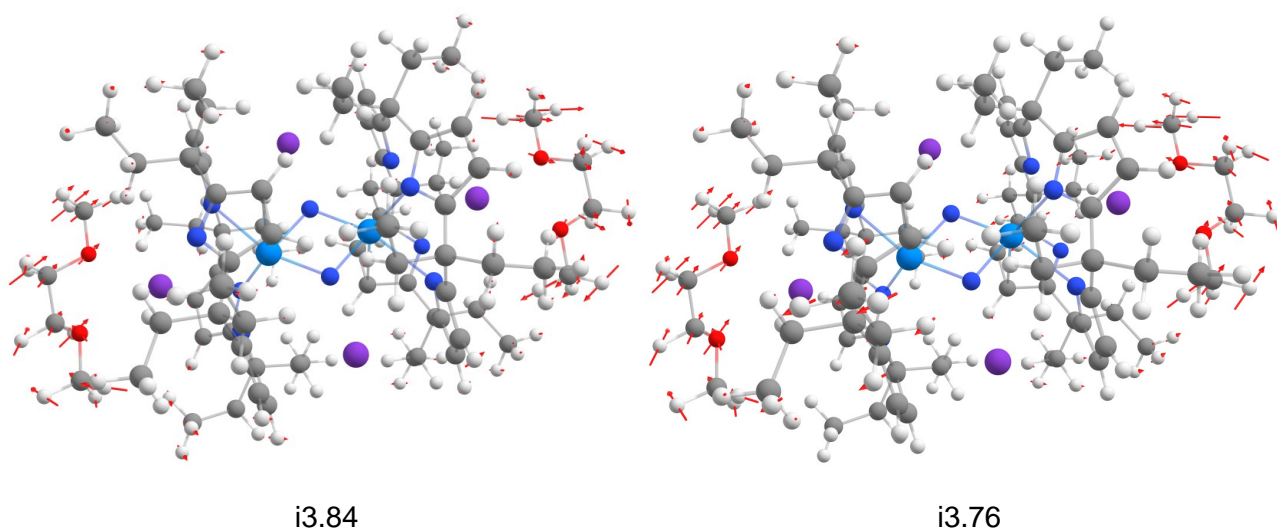


Figure S33: The imaginary normal modes of **B**

Table S40: The number of imaginary frequencies (#), their frequencies (in cm^{-1}) and symmetry of **C** for the charges studied. Normal modes are given in moldern format as a supplementary data file.

	C-Ca	C ²⁻	C ⁻	C	C ⁺	C ²⁺
	U(IV)/U(IV)	U(IV)/U(IV)	U(V)/U(IV)	U(V)/U(V)	U(VI)/U(V)	U(VI)/U(VI)
#	0	1	0	2	1	0
		i6.08 (A_u)		i10.60 (A_u) i10.05 (A_g)	i5.49 (A)	

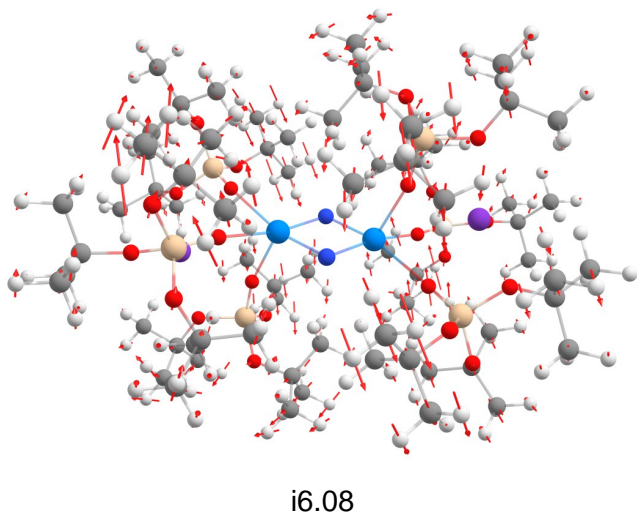
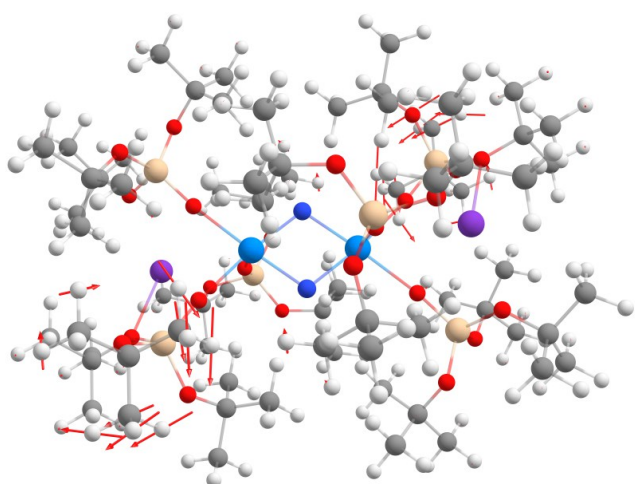
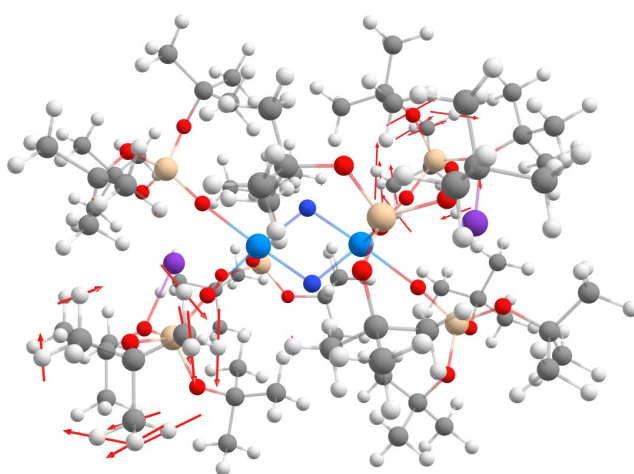


Figure S34: The imaginary normal mode of **C²⁻**

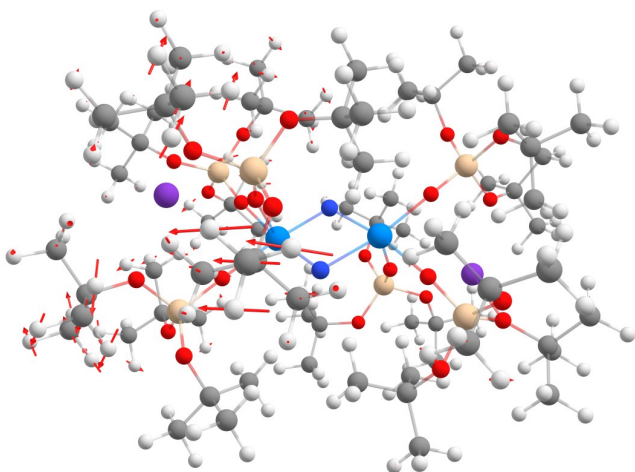


i10.60



i10.05

Figure S35: The imaginary normal modes of **C**



i5.49

Figure S36: The imaginary normal mode of **C⁺**

8 Multiconfigurational Calculations

Table S41: The CASSCF absolute energies in Hartree of **C** with a [2,14] active space, and the energy relative to the 3A_u ground state, in eV. Absolute energies are shifted up by 60758 Hartree

	1A_g			1A_u			3A_g			3A_u		
State	E / Ha	ΔE / eV	E / Ha	ΔE / eV	E / Ha	ΔE / eV	E / Ha	ΔE / eV	E / Ha	ΔE / eV	E / Ha	ΔE / eV
1	-0.5983	0.001	-0.5913	0.189	-0.5915	0.186	-0.5983	0.000	-0.5983	0.000	-0.5983	0.000
2	-0.5943	0.109	-0.5845	0.375	-0.5845	0.376	-0.5944	0.106	-0.5944	0.106	-0.5944	0.106
3	-0.5903	0.217	-0.5809	0.473	-0.5811	0.468	-0.5905	0.213	-0.5905	0.213	-0.5905	0.213
4	-0.5843	0.380	-0.5798	0.502	-0.5799	0.499	-0.5844	0.377	-0.5844	0.377	-0.5844	0.377
5	-0.5805	0.484	-0.5764	0.595	-0.5766	0.589	-0.5806	0.480	-0.5806	0.480	-0.5806	0.480
6	-0.5798	0.504	-0.5735	0.674	-0.5742	0.656	-0.5799	0.501	-0.5799	0.501	-0.5799	0.501
7	-0.5759	0.609	-0.5694	0.786	-0.5697	0.779	-0.5760	0.605	-0.5760	0.605	-0.5760	0.605
8	-0.5739	0.662	-0.5688	0.802	-0.5694	0.785	-0.5741	0.658	-0.5741	0.658	-0.5741	0.658
9	-0.5706	0.752	-0.5625	0.973	-0.5622	0.983	-0.5706	0.752	-0.5706	0.752	-0.5706	0.752
10	-0.5700	0.769	-0.5590	1.068	-0.5594	1.057	-0.5703	0.760	-0.5703	0.760	-0.5703	0.760

Table S42: The CASPT2 absolute energies in Hartree of **C** based on the [2,14] CASSCF reference, and the energy relative to the 3A_u ground state, in eV. States ordered by CASSCF root. Absolute energies are shifted up by 60764 Hartree

	1A_g			1A_u			3A_g			3A_u		
State	E / Ha	ΔE / eV	E / Ha	ΔE / eV	E / Ha	ΔE / eV	E / Ha	ΔE / eV	E / Ha	ΔE / eV	E / Ha	ΔE / eV
1	-0.4040	0.055	-0.4059	0.004	-0.4060	0.001	-0.4036	0.064	-0.4036	0.064	-0.4036	0.064
2	-0.4060	0.000	-0.4000	0.163	-0.3998	0.168	-0.4060	0.000	-0.4060	0.000	-0.4060	0.000
3	-0.3922	0.374	-0.3935	0.339	-0.3942	0.320	-0.3923	0.372	-0.3923	0.372	-0.3923	0.372
4	-0.3993	0.181	-0.3939	0.329	-0.3944	0.315	-0.3989	0.192	-0.3989	0.192	-0.3989	0.192
5	-0.3942	0.322	-0.3895	0.449	-0.3885	0.477	-0.3939	0.328	-0.3939	0.328	-0.3939	0.328
6	-0.3943	0.319	-0.3876	0.501	-0.3873	0.509	-0.3930	0.355	-0.3930	0.355	-0.3930	0.355
7	-0.3873	0.510	-0.3820	0.653	-0.3830	0.625	-0.3871	0.514	-0.3871	0.514	-0.3871	0.514
8	-0.3869	0.521	-0.3798	0.712	-0.3823	0.644	-0.3868	0.521	-0.3868	0.521	-0.3868	0.521
9	-0.3792	0.730	-0.3786	0.746	-0.3772	0.784	-0.3782	0.757	-0.3782	0.757	-0.3782	0.757
10	-0.3811	0.677	-0.3723	0.917	-0.3728	0.905	-0.3817	0.661	-0.3817	0.661	-0.3817	0.661

Table S43: The RASSCF absolute energies in Hartree of **C** with a (6, 8, 6; 14, 2, 2) active space, and the energy relative to the 3A_u ground state, in eV. Absolute energies are shifted up by 60758 Hartree

	1A_g			1A_u			3A_g			3A_u		
State	E / Ha	ΔE / eV		E / Ha	ΔE / eV		E / Ha	ΔE / eV		E / Ha	ΔE / eV	
1	-0.7785	0.008		-0.7739	0.135		-0.7744	0.120		-0.7788	0.000	
2	-0.7741	0.129		-0.7668	0.328		-0.7671	0.319		-0.7745	0.118	
3	-0.7697	0.249		-0.7624	0.447		-0.7629	0.434		-0.7702	0.235	
4	-0.7667	0.330		-0.7618	0.462		-0.7623	0.449		-0.7671	0.319	
5	-0.7626	0.442		-0.7576	0.577		-0.7581	0.563		-0.7630	0.432	
6	-0.7619	0.459		-0.7506	0.767		-0.7511	0.754		-0.7624	0.446	
7	-0.7577	0.574								-0.7582	0.561	
8	-0.7555	0.634								-0.7558	0.626	
9	-0.7506	0.768								-0.7509	0.760	
10	-0.7457	0.902								-0.7461	0.890	

Table S44: The RASPT2 absolute energies in Hartree of **C**, based on the (6, 8, 6; 14, 2, 2) RASSCF reference, and the energy relative to the 1A_g ground state, in eV. States ordered by RASSCF root. Absolute energies are shifted up by 60764 Hartree

	1A_g			1A_u			3A_g			3A_u		
State	E / Ha	ΔE / eV		E / Ha	ΔE / eV		E / Ha	ΔE / eV		E / Ha	ΔE / eV	
1	-0.3690	0.006		-0.3692	0.001		-0.3689	0.011		-0.3685	0.021	
2	-0.3693	0.000		-0.3626	0.182		-0.3619	0.200		-0.3688	0.011	
3	-0.3583	0.298		-0.3567	0.343		-0.3561	0.359		-0.3585	0.294	
4	-0.3625	0.184		-0.3563	0.351		-0.3555	0.375		-0.3622	0.193	
5	-0.3570	0.334		-0.3519	0.472		-0.3518	0.476		-0.3573	0.326	
6	-0.3566	0.346		-0.3466	0.615		-0.3467	0.613		-0.3565	0.348	
7	-0.3519	0.473								-0.3518	0.475	
8	-0.3457	0.640								-0.3457	0.640	
9	-0.3467	0.614								-0.3467	0.612	
10	-0.3351	0.929								-0.3356	0.915	

Table S45: The MS-RASPT2 absolute energies in Hartree of **C**, based on the (6, 8, 6; 14, 2, 2) RASSCF reference, and the energy relative to the 1A_g ground state, in eV. States ordered by MS-RASPT2 energy. Absolute energies are shifted up by 60764 Hartree

	1A_g		1A_u		3A_g		3A_u	
State	E / Ha	ΔE / eV	E / Ha	ΔE / eV	E / Ha	ΔE / eV	E / Ha	ΔE / eV
1	-0.3694	0.000	-0.3693	0.002	-0.3689	0.013	-0.3691	0.009
2	-0.3690	0.011	-0.3628	0.180	-0.3620	0.200	-0.3685	0.025
3	-0.3627	0.182	-0.3570	0.337	-0.3563	0.357	-0.3622	0.195
4	-0.3587	0.291	-0.3561	0.362	-0.3553	0.382	-0.3589	0.286
5	-0.3571	0.335	-0.3517	0.481	-0.3515	0.485	-0.3577	0.318
6	-0.3563	0.355	-0.3465	0.623	-0.3467	0.617	-0.3562	0.358
7	-0.3516	0.484					-0.3516	0.484
8	-0.3480	0.582					-0.3477	0.589
9	-0.3445	0.677					-0.3445	0.677
10	-0.3348	0.941					-0.3352	0.930

Exchange coupling in complexes containing diuranium diamond cores

Benjamin E. Atkinson, Matthew Gregson, David M. King, Stephen T. Liddle and Nikolas Kaltsoyannis

As has been previously discussed, diuranium complexes are of interest to explore novel bonding motifs, for their potential in catalysis and small molecule activation, and for their magnetic properties.^{4,72–87}

The Mazzanti group has made extensive use of the siloxide ligand $[\text{OSi}(\text{O}^t\text{Bu})_3]^-$ ($=\text{L}$), used in the U(V) complex $\text{U}_2\text{N}_2\text{L}_6\text{K}_2$ studied in Chapter 6. As Barluzzi *et al.* recently summarised,⁸² this siloxide ligand has been employed to isolate a great variety of uranium bonding motifs, and diuranium complexes. This is due to tris-*tert*-butoxysiloxide's multiple bonding modes, ability to trap alkali cations in complexes, and its steric bulk.

In addition to the U(V) complex $\text{U}_2\text{N}_2\text{L}_6\text{K}_2$, several other U(IV) complexes containing U_2X_2 ($\text{X} = \text{NH}, \text{O}, \text{S}$) diamond cores have been reported, which all use the tris-*tert*-butoxysiloxide ligand. I performed DFT and broken-symmetry (BS) DFT calculations on these complexes, in addition to model U_2Se_2 and U_2Te_2 complexes since these have been previously reported for different ligand systems.¹⁰⁸ I additionally performed calculations on dication models of these systems to generate U(V) systems. I explored the relationship between the strength of exchange-coupling

(J) in these systems and various QTAIM and NBO parameters.

There is not a clear relationship between QTAIM and NBO parameters and J for the U(IV) systems studied, possibly due to the small range of values for J calculated, between -7.6 and -15.4 cm^{-1} at the DFT geometries. The U(V) systems have a larger range of calculated exchange-coupling parameters, and a reasonably strong correlation between bond order metrics and J . Further work on a greater variety of model systems could further explore this potential correlation.

Contribution statement

I devised the project, and performed calculations DFT calculations, IBO, NBO and QTAIM analyses, analysed the results and wrote the manuscript, with supervision and input from Prof. Nikolas Kaltsoyannis.

Exchange coupling in complexes containing diuranium diamond cores

Benjamin E. Atkinson and Nikolas Kaltsoyannis
Department of Chemistry, University of Manchester

Abstract

There is substantial interest in diuranium complexes for their magnetic properties and novel bonding motifs. We report calculations on several U(IV) and U(V) complexes featuring a U_2X_2 diamond motif encapsulated by the siloxide ligand $(^t\text{BuO}_3)\text{SiO}^-$ ($\text{X} = \text{O}, \text{N}, \text{NH}, \text{S}, \text{Se}, \text{Te}$). We perform broken-symmetry DFT calculations to model the exchange coupling constant J , and correlate this to various atomic and bond NBO and QTAIM properties. Correlation is poor for the U(IV) systems, possibly due to the small range of J calculated (-7.6 to -11.7 cm^{-1}). A greater range of J is obtained for the U(V) systems, -15.4 to -92.4 cm^{-1} , and correlation between J and QTAIM delocalisation indices in the ring is observed.

Introduction

There is substantial interest in complexes containing multiple uranium centres; to explore novel bonding motifs,^[1–8] for their potential role in catalysis and small molecule activation (typically possible due to their novel bonding motifs),^[5,9–16] and for their magnetic properties.^[17–21] Multiple uranium centre complexes with bridging atoms/ligands frequently use highly sterically bulky ligands, often polydentate, to kinetically stabilise the complex and to create a pocket in which the ring can form.

Complexes featuring a U_2O_2 diamond motif have been studied for their magnetic properties and also to study ‘cation-cation interactions’ (CCIs), prototypically a dimer of U(V) uranyl

UO_2^+ units bridged by an oxide ligand from each uranyl.^[11,17,19,22–26] The first such U(V) dimer was isolated by Nocton *et al.*^[17] The U_2O_2 core has U-O ring bond lengths of 1.94 and 2.38 Å and a $\text{U}=\text{O}$ external bond length of 1.85 Å, slight perturbations of the UO_2^+ monomer. Magnetic susceptibility measurements suggest weak antiferromagnetic supported by theoretical calculations by Teyar *et al.* who performed broken-symmetry (BS) DFT calculations on the dimer and a model. At the crystal structure geometry they obtained an exchange-coupling parameter J of -24.1 cm^{-1} (indicating weak antiferromagnetic coupling). Arnold *et al.* obtained a U(V) diuranium-oxo complex featuring a diamond U_2O_2 core, with average ring U-O bond lengths of either 2.094 Å or 2.081 Å depending on the alkyl group on the ancillary silyl group on the 'Pacman' ligand. Magnetic susceptibility data gives a critical temperature of 17 K, and fitting of this data gives an experimental exchange coupling parameter $J = -33 \text{ cm}^{-1}$ ^[25]

Lam *et al.* isolated dianionic U(IV) bis-sulfide, bis-selenide and bis-telluride complexes, in addition to the related mono-chalcogenide U(IV) neutral analogues. The family of complexes were ligated by a tripodal tris-aryloxide ligand. The U(IV) magnetic susceptibility of the mono-chalcogenide show clear signs of antiferromagnetism, however, the bis-chalcogenides are less clear; the magnetic moments of the complexes are less than that expected of a U(IV) centre which the authors suggest is the influence of the rather short U-E bonds.^[24]

The prospect of novel nitrogen reactivity and catalysis has driven much of the interest in diuranium-nitrogen complexes, given the strength of the N_2 triple bond, and also the strength of uranium-nitrogen bonds due to the unique role that 5f orbitals play in bonding in the actinides.^[5,6,9,11,15,16,27,28] Camp *et al.* identified a U_2N_2 diamond ring-containing complex featuring two U(V) centres which shows signs of multiple bonding; an improved synthesis was later reported where its magnetic properties suggested strong antiferromagnetic properties.^[5,11] We previously reported a theoretical study of this complex and compared it to other U_2N_2 diamond ring-containing complexes previously reported, finding delocalised

bonding analogous to that of the bare molecule. Our multiconfigurational calculations suggested an exchange-coupling parameter $J = -68.8 \text{ cm}^{-1}$.^[16]

In this contribution, we report density functional theory (DFT) calculations on several systems featuring 'U₂X₂' diamond cores and the siloxide ligand (tBuO₃)SiO⁻ (=L) to study their electronic and magnetic properties. The previously isolated U(IV) systems we study are U₂O₂L₆K₂, U₂(NH)₂L₆K₂ and U₂S₂L₆Cs₂(THF)₂, (for brevity U₂O₂, U₂(NH)₂, and U₂S₂). We additionally report calculations on U₂Se₂L₆Cs₂(THF)₂ and U₂Te₂L₆Cs₂(THF)₂, since systems featuring U₂X₂ diamond cores for these heavier chalcogens have been previously reported with different coordination environments.^[24] Furthermore, we report calculations on U(V) dicationic analogues of the above ('U₂X₂²⁺'), to compare to our previous work on U₂N₂L₆K₂.^[16] We use DFT, broken symmetry (BS) DFT, and several analytical techniques to explore the relation of electronic structure with exchange coupling in these diuranium complexes.

Computational Methodology

Density functional theory calculations were performed with Turbomole 7.3.^[29] Calculations were performed spin-unrestricted, using the hybrid PBE0 functional.^[30,31] Grimme's D3 dampening function was used to account for dispersion interactions.^[32] The m4 integration grid in Turbomole was used. The cc-pVDZ basis set was used on all atoms, other than uranium, caesium and tellurium on which the cc-pVDZ-PP basis was used, alongside the associated small-core relativistic effective core potential (60, 46 and 28 electron respectively).^[33–37] To calculate the exchange coupling constant J , high spin and BS-DFT single-point calculations were performed with cc-pVTZ-PP on uranium and tellurium, and cc-pVTZ on other bridging ligand atoms, at the double-zeta optimised geometry. J was calculated with the Yamaguchi formula:^[38]

$$J = \frac{E_{BS} - E_{HS}}{\langle S_{HS}^2 \rangle - \langle S_{BS}^2 \rangle}$$

where E is the energy, and $\langle S^2 \rangle$ is the spin squared expectation value of the broken-symmetry (BS) and high-spin (HS) states. Because of the small energy differences involved in these calculations, the SCF convergence criteria was raised in these single point calculations from the default in Turbomole 7.3 of 10^{-6} to 10^{-8} Ha. For the U(IV) complexes, the $5f_{U^2}$ electrons are spin-parallel on each uranium atom. True minima were confirmed with frequency calculations, though in some cases small ($<16i\text{ cm}^{-1}$) imaginary frequencies corresponding to ligand twisting were found, which could not be eliminated and we believe are due to the integration grid and the very flat potential of these twisting motions. Imaginary frequencies are shown in Tables S16-S17 and Figures S12-S18 of the Supplementary Information. Where available, single point calculations were additionally performed at the crystal structure geometry with only the positions of hydrogen atoms optimised (with the DZ basis set) in addition to the DFT optimised geometries.

Results and Discussion

We performed DFT geometry optimisations with the PBE0 functional, in line with our previous work on $U_2N_2L_6K_2$ and due to its accuracy in our previous work on a U(IV) U_2N_2 complex.^[15,16] Our geometry optimisations are a good match for the crystal structures for $U_2(NH)_2$ and U_2S_2 , differing by at most 0.03 Å, as summarised in Table 1. The alternation in bond lengths seen in the crystal structure of U_2O_2 (with a pair of bond lengths of approximately 2.17 Å, and the other two shorter at 2.11 and 2.08 Å) is not seen in our DFT geometry, however the average is very similar at 2.13 Å in both cases. The heavier chalcogens U_2Se_2 and U_2Te_2 are in line with U_2S_2 , with only small alternation of bond lengths. The U-X formal shortness ratio (FSR), the ratio of the U-X bond length vs. the sum of single covalent U-X radii, is between 0.91 and 0.99 suggesting approximately single bonds in the ring for all 5 systems, though slightly stronger for U_2O_2 and $U_2(NH)_2$ with FSRs of 0.91 and 0.92 (at the DFT optimised geometry).

Table 1: Key interatomic distances, in angstrom, of the U(IV) U_2X_2 systems studied at the crystal structure geometry (XRD) and at the DFT optimised geometry. All systems have C_i symmetry so opposite pairs of bonds in the ring are equal, other than U_2O_2 which is C_1 symmetry. The average U-X bond length (av) is also shown, and the average formal shortness ratio (FSR), the ratio of U-X bond length and the sum of U-X single covalent radii

	U_2O_2		$U_2(NH)_2$		U_2S_2		U_2Se_2	U_2Te_2
U+X cov rad	2.33		2.41		2.73		2.86	3.06
	XRD	DFT	XRD	DFT	XRD	DFT	DFT	DFT
J / cm^{-1}	+2.23	-8.31	-15.37	-11.65	-0.54	-7.58	-7.82	-9.16
U^a-X^a	2.075	2.125	2.192	2.198	2.638	2.648	2.785	3.035
U^b-X^b	2.170	2.127	2.273	2.246	2.678	2.655	2.793	3.022
U^b-X^b	2.114	2.131	2.192	2.198	2.638	2.648	2.785	3.035
U^a-X^a	2.168	2.133	2.273	2.246	2.678	2.655	2.793	3.022
U-X (av)	2.132	2.129	2.233	2.222	2.658	2.652	2.789	3.029
U-X FSR (av)	0.92	0.91	0.93	0.92	0.97	0.97	0.98	0.99
U-U	3.407	3.400	3.569	3.561	4.022	4.011	4.153	4.390
X-X	2.562	2.564	2.686	2.696	3.476	3.468	3.724	4.173

In our previous work on $U_2N_2L_6K_2$, we identified delocalised bonding with four σ and two π bonding orbitals in the U_2N_2 ring. Intrinsic bonding orbital (IBO) analysis gives a similar set of orbitals, localised to one U-X-U half of the ring, with four valence IBOs; one nonbonding ns, two σ and a π bonding orbitals (with an equivalent set on the opposite half of the ring).^[16] The valence IBOs of U_2S_2 are shown in Figure 1, with others being qualitatively similar (other than $U_2(NH)_2$ where the 2s orbital is instead a N-H σ orbital) and shown in Figures S1-S5 of the Supplementary Information. Analogous bonding is observed in these systems, though unsurprisingly substantially less covalent with X^{2-} bridging ligands, compared to N^{3-} . The average population on X for the three bonding IBOs is between 73% and 78% for these U(IV) systems, compared with 63.7% for the U(IV) U_2N_2 dianion we previously studied (detailed compositions are given in Tables S1-S5 of the Supplementary Information).

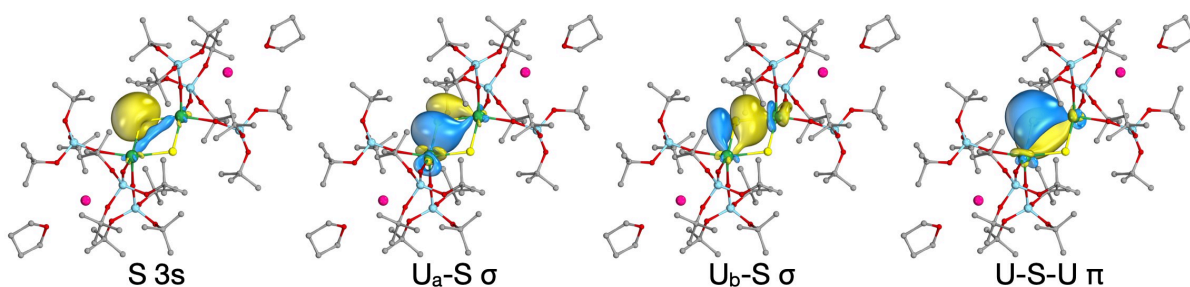


Figure 1: valence α IBOs of U_2S_2 in the ring. The isosurfaces enclose 90% of the orbital. Hydrogen atoms omitted for clarity. Grey: carbon, red: oxygen, light blue: silicon, pink: caesium, green: uranium.

The range of exchange coupling parameters, J , is rather small at the DFT optimised geometry, with the smallest in magnitude (U_2S_2) at -7.58 cm^{-1} and the most negative -11.65 cm^{-1} . There is a significant difference at the crystal structure geometry, with U_2O_2 becoming weakly ferromagnetic ($+2.23 \text{ cm}^{-1}$ vs. -8.31 cm^{-1} at the DFT geometry) and U_2S_2 being only very weakly antiferromagnetically coupled (-0.54 cm^{-1} at the crystal structure geometry vs. -7.58 cm^{-1} at the DFT geometry). As shown in Table 1, the match with the crystal structure geometry is very good, other than U_2O_2 for which the alternation of bonds in the crystal structure is not present at the DFT geometry. This highlights the extreme sensitivity of calculating J with BS-DFT given the very small energy differences.

Table 2: NBO and QTAIM charges and bond indices for the U(IV) systems; the Wiberg bond index BO_W in the NAO basis and the QTAIM delocalisation index $\delta(A|B)$. Bond indices are given as averages in the ring. The charges for U_2O_2 are averages, other molecules are C_i so atoms have the same charges.

		U_2O_2		$\text{U}_2(\text{NH})_2$		U_2S_2		U_2Se_2	U_2Te_2
		XRD	DFT	XRD	DFT	XRD	DFT	DFT	DFT
NBO:	$q(\text{U})$	2.032	2.025	1.984	1.966	1.654	1.606	1.548	1.443
	$q(\text{X})$	-1.049	-1.061	-0.992	-1.004	-0.746	-0.726	-0.660	-0.559
	$\text{BO}_W (\text{U-X})$	0.780	0.768	0.781	0.765	0.947	0.960	0.985	1.030
	$\text{BO}_W (\text{U-U})$	0.101	0.111	0.132	0.136	0.148	0.155	0.172	0.194
QTAIM:	$q(\text{U})$	2.555	2.548	2.530	2.521	2.441	2.433	2.393	2.347
	$q(\text{X})$	-1.214	-1.212	-1.146	-1.135	-1.131	-1.129	-1.080	-1.004
	$\delta(\text{U} \text{X})$	0.883	0.871	0.853	0.850	0.796	0.794	0.775	0.738
	$\delta(\text{U} \text{U})$	0.113	0.109	0.111	0.110	0.079	0.079	0.076	0.069

Atomic charges and bond indices, obtained with QTAIM and NBO, are shown in Table 2.

U-X bond indices approximately indicate single bonding in the ring, however NBO and

QTAIM give some opposing trends. The largest U-X BO_W is U_2Te_2 , at 1.03, however U_2Te_2

has the lowest $\delta(U|X)$ of the set at 0.74. The NBO BO_W is similarly larger than the QTAIM $\delta(U|X)$ for U_2Se_2 and U_2S_2 . Inversely, $\delta(U|X)$ is largest for U_2O_2 , and $\delta(U|X)$ is larger than BO_W for U_2O_2 and $U_2(NH)_2$. The value of these metrics is very similar at the crystal structure and DFT optimised geometries. As Figure 2 (and Table 2, and Tables S6-S7 of the Supplementary Information) shows, the correlation between J and these atom and bond parameters and other QTAIM critical point properties is poor. We did not perform similar analysis at the crystal structure geometries due to the more limited number of data points. The best correlation is the U-X BCP ellipticity ϵ , a measure of the electron density around the bond path where for a cylindrical distribution (a single or triple bond) $\epsilon = 0$. Charges and bond indices show little correlation, with all metrics having R^2 values of below 0.3 – given the expected superexchange antiferromagnetic correlation mechanism we might expect some correlation between bond indices and J , however this is not observed for these U(IV) systems. This poor correlation is likely due to the limited range of rather weak exchange coupling parameters calculated.

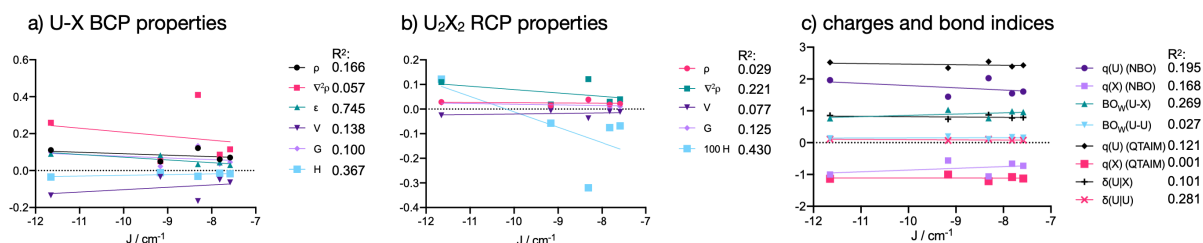


Figure 2: QTAIM and NBO properties (in a.u.) as a function of the exchange-correlation parameter J : a) average bond critical point (BCP) properties of the U-X bond; b) ring critical point properties at the centre of the U_2X_2 ring; and c) QTAIM and NBO charges and bond indices, BO_W from NBO and $\delta(A|B)$ from QTAIM. For a) and b), ρ is the electron density, $\nabla^2\rho$ is the Laplacian of the gradient, ϵ is the ellipticity, V is the potential energy density, G is the kinetic energy density, and H is the total energy density $G + V$, all at the critical point. A linear regression fit and the R^2 value is shown for each property. At the RCP, H is scaled up by 100.

For this reason, we additionally performed geometry optimisations on dictations of the above, to give U(V) model systems. Strong antiferromagnetic coupling was previously observed for the U(V) $U_2N_2L_6K_2$, and we previously calculated $J = -68.8 \text{ cm}^{-1}$ at the MS-RASPT2 level. Greater covalency can be expected to be obtained at the higher

oxidation state, and a greater range of values of J . Key interatomic distances are summarised in Table 3; ring bond lengths are shortened by about 0.04 Å for each system, as would be expected for the higher uranium oxidation state systems. The FSR varies from 0.90 for $\text{U}_2(\text{NH})_2$, to 0.97 for $\text{U}_2\text{Te}_2^{2+}$, slightly lower than the U(IV) systems reflecting the increase in covalency, and 0.86 for U_2N_2 , reflecting the additional covalency from the nitride bridging ligand. The IBOs have similar qualitative character to that shown in Figure 1, but slightly more covalent, as reflected in the average population on X, which for the X^{2-} systems (i.e. all U(V) systems excluding U_2N_2) is 72.8% vs. 76.2 % for the corresponding U(IV) systems (IBOs are shown in Figures S6-11 and compositions are given in Tables S8-S13 of the Supplementary Information).

Table 3: Key interatomic distances, in angstrom, of the U(V) U_2X_2 systems studied at the DFT optimised geometry. All systems have C_i symmetry so opposite pairs of bonds in the ring are equal, whereas U_2O_2 is C_1 symmetry. The DFT optimised geometry of the U(V) U_2N_2 complex we previously studied^[16] is also shown. The average U-X bond length (av) is also shown, and the average formal shortness ratio (FSR), the ratio of U-X bond length and the sum of U-X single covalent radii

	$\text{U}_2\text{O}_2^{2+}$	$\text{U}_2(\text{NH})_2^{2+}$	$\text{U}_2\text{S}_2^{2+}$	$\text{U}_2\text{Se}_2^{2+}$	$\text{U}_2\text{Te}_2^{2+}$	U_2N_2
U-X r_{cov}	2.33	2.41	2.73	2.86	3.06	2.41
J / cm^{-1}	-23.19	-39.83	-25.17	-15.35	-22.04	-92.41
U^a-X^a	2.094	2.159	2.610	2.731	2.966	2.022
U^b-X^b	2.103	2.190	2.614	2.767	2.985	2.101
U^b-X^b	2.098	2.159	2.610	2.731	2.966	2.022
U^a-X^a	2.107	2.190	2.614	2.767	2.985	2.101
U-X (av)	2.111	2.175	2.612	2.749	2.976	2.062
U-X FSR (av)	0.91	0.90	0.96	0.96	0.97	0.86
U-U	3.402	3.531	4.036	4.178	4.441	3.296
X-X	2.465	2.540	3.318	3.573	3.962	2.480

The exchange coupling constants J for the U(V) systems are shown in Table 3, ranging from -15.3 cm^{-1} for $\text{U}_2\text{Te}_2^{2+}$ to -92.4 cm^{-1} for U_2N_2 . This value for U_2N_2 is larger than we previously calculated at the MS-RASPT2 level ($J = -68.8 \text{ cm}^{-1}$), in part due to the BS-DFT value of this work being calculated at the DFT optimised geometry. The BS-DFT calculation at the crystal structure geometry, $J = -81.1 \text{ cm}^{-1}$ is closer to that calculated at the MS-RASPT2 level, however for consistency with the other U(V) systems we study the DFT

optimised value is used. The value of J calculated for $\text{U}_2\text{O}_2^{2+}$, is roughly consistent with that obtained by other complexes U(V) complexes which feature a U_2O_2 motif, Arnold *et al.* obtained $J = -33 \text{ cm}^{-1}$ based on a fit of experimental magnetic susceptibility data,^[19] Teyar *et al.* obtained a theoretical value of -24.1 cm^{-1} at the crystal structure geometry (with the B3LYP functional, but using the B3LYP functional at the BP86 optimised geometry gave a value of -347.6 cm^{-1}).

This increase in covalency is further reflected in the U-X bond indices, shown in Table 4; the average U-X BO_w is 1.07 for the U(V) X^{2-} systems compared with 0.90 for the comparable U(IV) systems, and the average $\delta(\text{U}|\text{X})$ is 0.92 vs. 0.81 for U(V) and U(IV) respectively. A discrepancy between BO_w and $\delta(\text{U}|\text{X})$ is observed, similar to the U(IV) systems discussed above – NBO suggests a higher bond order than the average for the heavier chalcogens (1.18 for $\text{U}_2\text{Se}_2^{2+}$ and 1.21 for $\text{U}_2\text{Te}_2^{2+}$) while the QTAIM $\delta(\text{U}|\text{X})$ is slightly below the average (0.91 in both cases). Both methods are however consistent in assigning the largest bond order to U_2N_2 .

Table 4: NBO and QTAIM charges and bond indices for the U(V) systems; the Wiberg bond index BO_w in the NAO basis and the QTAIM delocalisation index $\delta(\text{A}|\text{B})$. Bond indices are given as averages in the ring. The charges for U_2O_2 are averages, other molecules are C_i so atoms have the same charges.

		$\text{U}_2\text{Se}_2^{2+}$	$\text{U}_2\text{Te}_2^{2+}$	$\text{U}_2\text{O}_2^{2+}$	$\text{U}_2\text{S}_2^{2+}$	$\text{U}_2(\text{NH})_2^{2+}$	U_2N_2
NBO:	$q(\text{U})$	1.601	1.541	2.014	1.712	1.925	1.773
	$q(\text{X})$	-0.307	-0.185	-0.862	-0.436	-0.719	-1.080
	$\text{BO}_w(\text{U-X})$	1.179	1.205	0.901	1.124	0.945	1.328
	$\text{BO}_w(\text{U-U})$	0.256	0.290	0.122	0.217	0.183	0.342
QTAIM:	$q(\text{U})$	2.610	2.525	2.838	2.669	2.787	2.640
	$q(\text{X})$	-0.850	-0.725	-1.087	-0.940	-1.413	-1.330
	$\delta(\text{U} \text{X})$	0.914	0.913	0.922	0.919	0.937	1.325
	$\delta(\text{U} \text{U})$	0.111	0.112	0.122	0.109	0.151	0.328

Figure 3 shows the correlation of J to QTAIM and NBO metrics for the U(V) systems, analogous to as shown previously for the U(IV) systems in Figure 2. Reasonably strong correlation is shown for several QTAIM properties, notably the total energy density H , $\delta(\text{U}|\text{X})$

and $\delta(U|U)$, with R^2 values of 0.89, 0.94 and 0.98 respectively. If the sole X^{3-} system, U_2N_2 , is removed, these R^2 values reduce to 0.40, 0.82 and 0.77 respectively. The strongest correlation observed for the U(IV) systems, ϵ , does not show any strong correlation for these U(V) systems. Stronger U-X bonding resulting in stronger antiferromagnetic coupling is consistent with the expected superexchange coupling mechanism.[ref] In our previous work on U_2N_2 ring containing complexes, we could not identify evidence for U-U bonding and suggested the U-U bond metrics were reflective of overlap induced by much stronger U-N bonds, and any bonding interaction present was weak by comparison.^[15,16] It is likely that the correlation between J and $\delta(U|U)$ is reflective of this observation as direct U-U bonding would favour ferromagnetic coupling *via* exchange interaction.

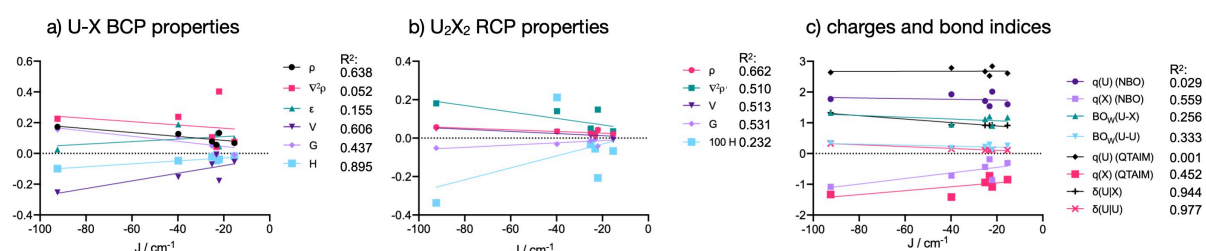


Figure 3: QTAIM and NBO properties (in a.u.) as a function of the exchange-correlation parameter J for the U(V) systems: a) average bond critical point (BCP) properties of the U-X bond; b) ring critical point properties at the centre of the U_2X_2 ring; and c) QTAIM and NBO charges and bond indices, BO_W from NBO and $\delta(A|B)$ from QTAIM. For a) and b), ρ is the electron density, $\nabla^2\rho$ is the Laplacian of the gradient, ϵ is the ellipticity, V is the potential energy density, G is the kinetic energy density, and H is the total energy density $G + V$, all at the critical point. A linear regression fit and the R^2 value is shown for each property. At the RCP, H is scaled up by 100.

There is little correlation between J and the BO_W , perhaps driven by the discrepancy between BO_W and $\delta(U|X)$ discussed above. Overestimation of the U-X bond orders for the heavier chalcogens by NBO would be consistent with the QTAIM, FSR (*i.e.* bond length) and exchange coupling energies (if there is a correlation between bond strength/covalency and the strength of antiferromagnetic coupling) however the number of systems studied in this work do not allow us to answer this conclusively.

Conclusions

Calculations at the BS-DFT level have been used to explore the magnetic coupling of several systems containing a U_2X_2 diamond ring and the same ligand environment, and NBO and QTAIM has been used to explore the relation between bonding in this ring and the strength of coupling between the two uranium atoms. For U(IV) systems studied there is no clear correlation between J , the exchange coupling parameter and various atomic and bond properties, though this is likely due to the rather similar nature of the complexes studied both in terms of their magnetic and electronic properties. The U(V) systems studied show a greater range of coupling and consequently reasonably strong correlation between the QTAIM bond orders $\delta(U|X)$ and $\delta(U|U)$ is observed. NBO bond orders however do not show any strong correlation. Further work on a greater variety of systems could further explore this potential correlation; both exploring a greater variety of bridging ligands and coordination environments to further explore their effects.

Supplementary Information

Supplementary Information is available; SOMOs, IBOs, IBO compositions, ring bond lengths, NBO and QTAIM metrics, motion of small imaginary frequencies, multiconfigurational calculations data tables. Coordinates, in xyz format, are available online at <http://dx.doi.org/10.17632/5nwh67d8cx.1>

References

- [1] P. Roussel, P. Scott, *J. Am. Chem. Soc.* **1998**, *120*, 1070–1071.
- [2] N. Kaltsoyannis, P. Scott, *Chem. Commun.* **1998**, *3*, 1665–1666.
- [3] P. Roussel, W. Errington, N. Kaltsoyannis, P. Scott, *J. Organomet. Chem.* **2001**, *635*, 69–74.
- [4] I. Korobkov, S. Gambarotta, G. P. A. Yap, *Angew. Chemie Int. Ed.* **2002**, *41*, 3433–3436.
- [5] C. Camp, J. Pécaut, M. Mazzanti, *J. Am. Chem. Soc.* **2013**, *135*, 12101–12111.
- [6] B. Vlasisavljević, L. Andrews, X. Wang, Y. Gong, G. P. Kushto, B. E. Bursten, *J. Am. Chem. Soc.* **2016**, *138*, 893–905.
- [7] G. Feng, M. Zhang, P. Wang, S. Wang, L. Maron, C. Zhu, *Proc. Natl. Acad. Sci.* **2019**, *116*, 17654–17658.
- [8] G. Feng, M. Zhang, D. Shao, X. Wang, S. Wang, L. Maron, C. Zhu, *Nat. Chem.* **2019**, 18–23.
- [9] A. R. Fox, S. C. Bart, K. Meyer, C. C. Cummins, *Nature* **2008**, *455*, 341–349.
- [10] B. M. Gardner, J. C. Stewart, A. L. Davis, J. McMaster, W. Lewis, A. J. Blake, S. T. Liddle, *Proc. Natl. Acad. Sci.* **2012**, *109*, 9265–9270.
- [11] M. Falcone, L. Barluzzi, J. Andrez, F. Fadaei Tirani, I. Zivkovic, A. Fabrizio, C. Corminboeuf, K. Severin, M. Mazzanti, *Nat. Chem.* **2019**, *11*, 154–160.
- [12] L. Barluzzi, M. Falcone, M. Mazzanti, *Chem. Commun.* **2019**, *55*, 13031–13047.
- [13] C. T. Palumbo, R. Scopelliti, I. Zivkovic, M. Mazzanti, *J. Am. Chem. Soc.* **2020**, *142*,

3149–3157.

- [14] P. L. Arnold, T. Ochiai, F. Y. T. Lam, R. P. Kelly, M. L. Seymour, L. Maron, *Nat. Chem.* **2020**, 12, 654–659.
- [15] B. E. Atkinson, M. Gregson, D. M. King, N. Kaltsoyannis, S. T. Liddle, *unpublished* **2020**.
- [16] B. E. Atkinson, N. Kaltsoyannis, *unpublished* **2020**.
- [17] G. Nocton, P. Horeglad, J. Pécaut, M. Mazzanti, *J. Am. Chem. Soc.* **2008**, 130, 16633–16645.
- [18] D. P. Mills, F. Moro, J. McMaster, J. van Slageren, W. Lewis, A. J. Blake, S. T. Liddle, *Nat. Chem.* **2011**, 3, 454–460.
- [19] B. Teyar, S. Boucenina, L. Belkhiri, B. Le Guennic, A. Boucekkine, M. Mazzanti, *Inorg. Chem.* **2019**, 58, 10097–10110.
- [20] L. Barluzzi, L. Chatelain, F. Fadaei-Tirani, I. Zivkovic, M. Mazzanti, *Chem. Sci.* **2019**, 10, 3543–3555.
- [21] L. Belkhiri, B. Le Guennic, A. Boucekkine, *Magnetochemistry* **2019**, 5, 15.
- [22] V. Mougél, P. Horeglad, G. Nocton, J. Pécaut, M. Mazzanti, *Angew. Chemie* **2009**, 121, 8629–8632.
- [23] P. L. Arnold, J. B. Love, D. Patel, *Coord. Chem. Rev.* **2009**, 253, 1973–1978.
- [24] O. P. Lam, F. W. Heinemann, K. Meyer, *Chem. Sci.* **2011**, 2, 1538.
- [25] P. L. Arnold, G. M. Jones, S. O. Odoh, G. Schreckenbach, N. Magnani, J. B. Love, *Nat. Chem.* **2012**, 4, 221–227.

- [26] S. X. Hu, J. Jian, J. Li, J. K. Gibson, *Inorg. Chem.* **2019**, 58, 10148–10159.
- [27] D. M. King, S. T. Liddle, *Coord. Chem. Rev.* **2014**, 266–267, 2–15.
- [28] M. Falcone, L. Chatelain, R. Scopelliti, I. Živković, M. Mazzanti, *Nature* **2017**, 547, 332–335.
- [29] University of Karlsruhe and Forschungszentrum Karlsruhe GmbH, **2019**.
- [30] J. P. Perdew, K. Burke, M. Ernzerhof, *Phys. Rev. Lett.* **1996**, 77, 3865–3868.
- [31] J. P. Perdew, M. Ernzerhof, K. Burke, C.-O. Almbladh, A. C. Pedroza, U. von Barth, A. V. Arbuznikov, H. Bahmann, A. Rodenberg, A. V. Arbuznikov, et al., *J. Chem. Phys.* **1996**, 109, 9982–9985.
- [32] S. Grimme, J. Antony, S. Ehrlich, H. Krieg, *J. Chem. Phys.* **2010**, 132, 154104.
- [33] K. A. Peterson, *J. Chem. Phys.* **2015**, 142, 074105.
- [34] J. G. Hill, K. A. Peterson, *J. Chem. Phys.* **2017**, 147, 244106.
- [35] I. S. Lim, H. Stoll, P. Schwerdtfeger, *J. Chem. Phys.* **2006**, 124, 034107.
- [36] M. Dolg, X. Cao, *J. Phys. Chem. A* **2009**, 113, 12573–12581.
- [37] K. A. Peterson, D. Figgen, E. Goll, H. Stoll, M. Dolg, *J. Chem. Phys.* **2003**, 119, 11113–11123.
- [38] K. Yamaguchi, F. Jensen, A. Dorigo, K. N. Houk, *Chem. Phys. Lett.* **1988**, 149, 537–542.

Supplementary Information

Exchange coupling in complexes containing diuranium diamond cores

Benjamin E. Atkinson and Nikolas Kaltsoyannis
Department of Chemistry, University of Manchester

1 U(IV) Intrinsic bonding orbitals	2
2 U(IV) NBO and QTAIM data	4
3 U(V) Intrinsic bonding orbitals	4
4 U(V) QTAIM data	7
5 Imaginary frequencies	8

1 U(IV) Intrinsic bonding orbitals

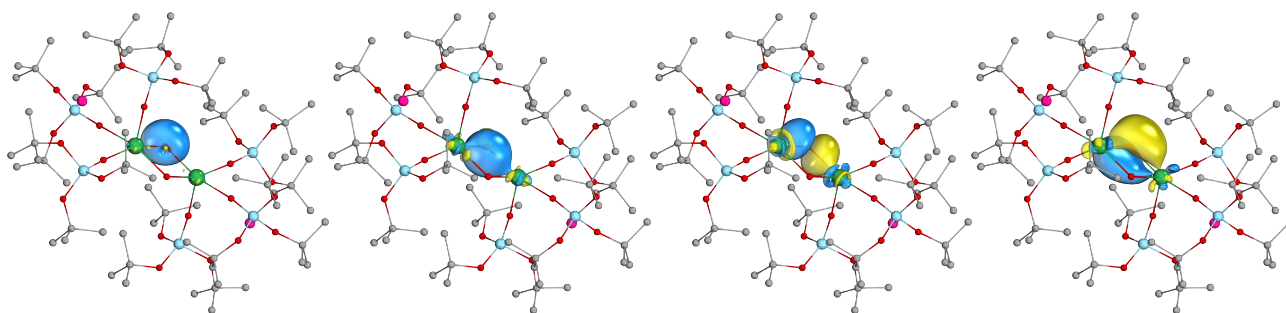


Figure S1: a ring IBOs of U(IV)/U(IV) U_2O_2

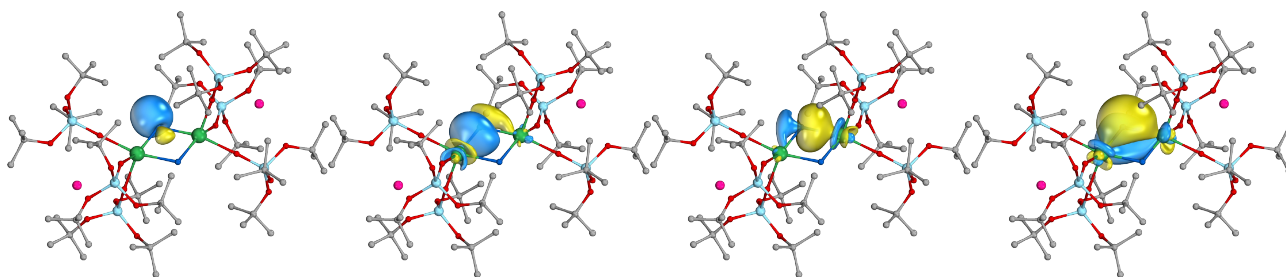


Figure S2: a ring IBOs of U(IV)/U(IV) $\text{U}_2(\text{NH})_2$

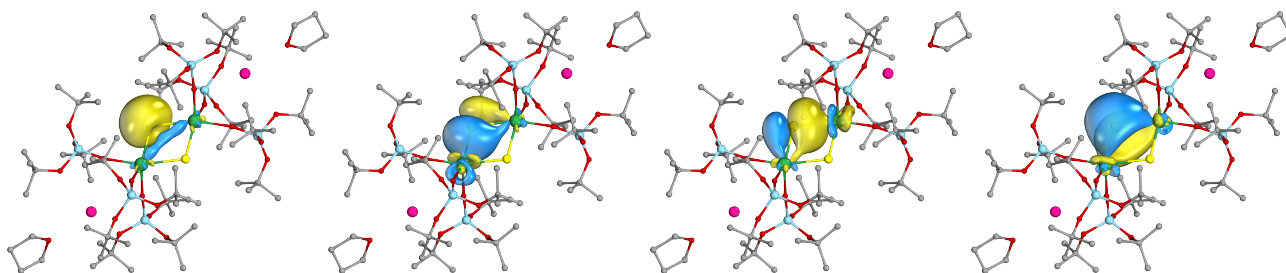


Figure S3: a ring IBOs of U(IV)/U(IV) U_2S_2

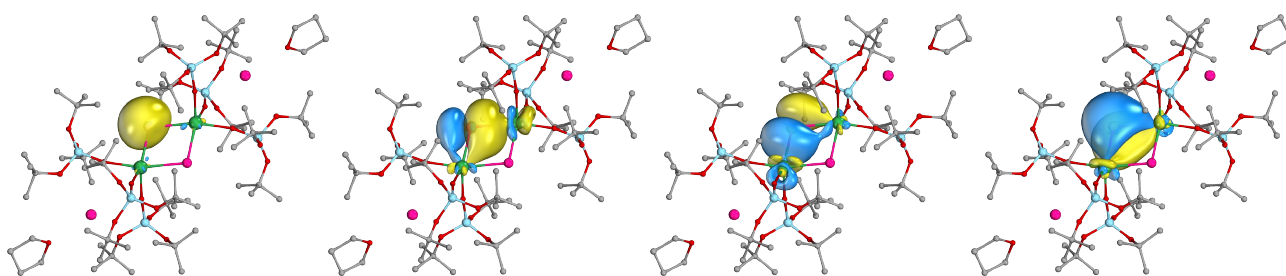


Figure S4: a ring IBOs of U(IV)/U(IV) U_2Se_2

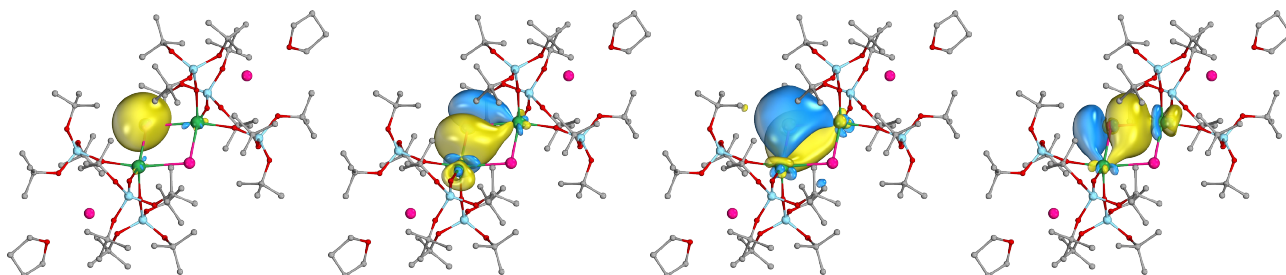


Figure S5: a ring IBOs of U(IV)/U(IV) U_2Te_2

Table S1: Composition of α IBOs of U(IV)/U(IV) U_2O_2 , in the IAO basis

	U 7s	U 6d	U 5f	U other	O 2s	O 2p	O other
O 2s	1.74	4.69	1.29	0.68	60.33	30.09	0.48
U^a-O σ	1.55	15.08	6.14	1.03	24.82	50.73	0.25
U^b-O σ	1.42	10.28	8.94	0.57	0.00	78.38	0.02
U-O-U π	0.00	14.36	4.71	1.13	0.00	79.30	0.00

Table S2: Composition of α IBOs of U(IV)/U(IV) $\text{U}_2(\text{NH})_2$, in the IAO basis

	U 7s	U 6d	U 5f	U other	N 2s	N 2p	N other	H 1s
N-H σ	0.00	0.00	0.00	0.00	14.26	44.71	0.13	38.00
U^a-N σ	2.92	13.93	7.17	0.99	31.40	42.84	0.25	0.00
U^b-N σ	2.81	14.44	6.74	1.82	24.69	48.81	0.20	0.00
U-N-U π	0.00	17.86	7.58	0.56	0.00	71.36	1.35	0.00

Table S3: Composition of α IBOs of U(IV)/U(IV) U_2S_2 , in the IAO basis

	U 7s	U 6d	U 5f	U other	S 3s	S 3p	S other
S 3s	1.31	3.00	1.09	0.30	63.92	26.72	2.66
U^a-S σ	4.09	16.20	5.45	1.16	21.22	50.66	0.72
U^b-S σ	3.10	11.97	6.70	0.83	0.00	76.48	0.12
U-S-U π	0.00	12.88	4.37	0.55	0.00	80.45	0.25

Table S4: Composition of α IBOs of U(IV)/U(IV) U_2Se_2 , in the IAO basis

	U 7s	U 6d	U 5f	U other	Se 4s	Se 4p	Se other
Se 4s	1.08	2.47	0.93	0.23	67.33	23.84	3.02
U^a-Se σ	4.28	14.08	6.22	1.22	12.95	60.04	0.51
U^b-Se σ	3.77	13.40	5.40	1.53	5.63	69.02	0.44
U-Se-U π	0.00	12.39	4.20	0.61	0.00	80.78	0.22

Table S5: Composition of α IBOs of U(IV)/U(IV) U_2Te_2 , in the IAO basis

	U 7s	U 6d	U 5f	U other	Te 5s	Te 5p	Te other
Te 5s	1.74	4.69	1.29	0.68	60.33	30.09	0.48
U^a-Te σ	1.55	15.08	6.14	1.03	24.82	50.73	0.25
U^b-Te σ	1.42	10.28	8.94	0.57	0.00	78.38	0.02
U-Te-U π	0.00	14.36	4.71	1.13	0.00	79.30	0.00

2 U(IV) NBO and QTAIM data

Table S6: QTAIM average bond critical point (BCP) properties of the U-X bond as a function of the exchange-correlation parameter J for the U(IV) systems. ρ is the electron density, $\nabla^2\rho$ is the Laplacian of the gradient, ε is the ellipticity, V is the potential energy density, G is the kinetic energy density, and H is the total energy density $G + V$, all at the critical point.

	J / cm^{-1}	ρ	$\nabla^2\rho$	ε	V	G	H
U_2Se_2	-7.82	0.061	0.086	0.044	-0.050	0.036	-0.014
U_2Te_2	-9.16	0.049	0.051	0.083	-0.034	0.023	-0.011
U_2O_2	-8.31	0.122	0.410	0.034	-0.165	0.134	-0.031
U_2S_2	-7.58	0.070	0.115	0.030	-0.064	0.046	-0.017
$\text{U}_2(\text{NH})_2$	-11.65	0.111	0.259	0.090	-0.134	0.099	-0.035

Table S7: QTAIM average ring critical point (RCP) properties of the U_2X_2 ring as a function of the exchange-correlation parameter J for the U(IV) systems. ρ is the electron density, $\nabla^2\rho$ is the Laplacian of the gradient, ε is the ellipticity, V is the potential energy density, G is the kinetic energy density, and H is the total energy density $G + V$, all at the critical point.

	J / cm^{-1}	ρ	$\nabla^2\rho$	V	G	H
U_2Se_2	-7.82	0.019	0.030	-0.009	0.008	-0.0008
U_2Te_2	-9.16	0.015	0.019	-0.006	0.005	-0.0006
U_2O_2	-8.31	0.039	0.122	-0.037	0.034	-0.0032
U_2S_2	-7.58	0.022	0.040	-0.011	0.011	-0.0007
$\text{U}_2(\text{NH})_2$	-11.65	0.029	0.110	-0.025	0.026	0.0012

3 U(V) Intrinsic bonding orbitals

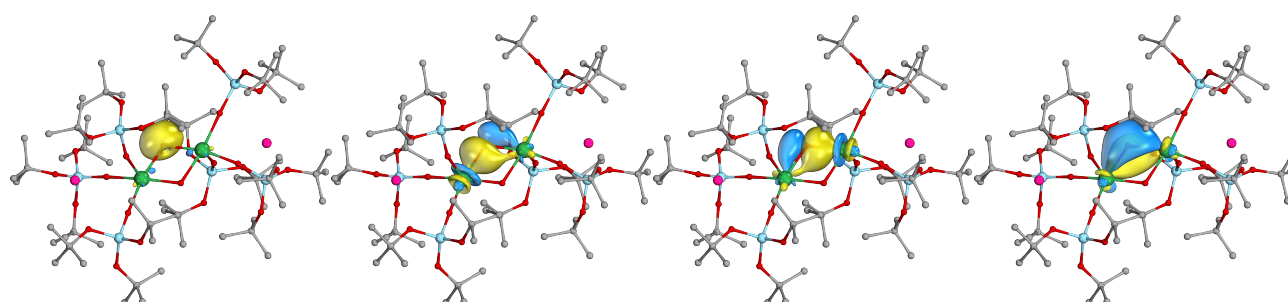


Figure S6: a ring IBOs of U(V)/U(V) $\text{U}_2\text{O}_2^{2+}$

Figure S7: a ring IBOs of U(V)/U(V) $\text{U}_2(\text{NH})_2^{2+}$

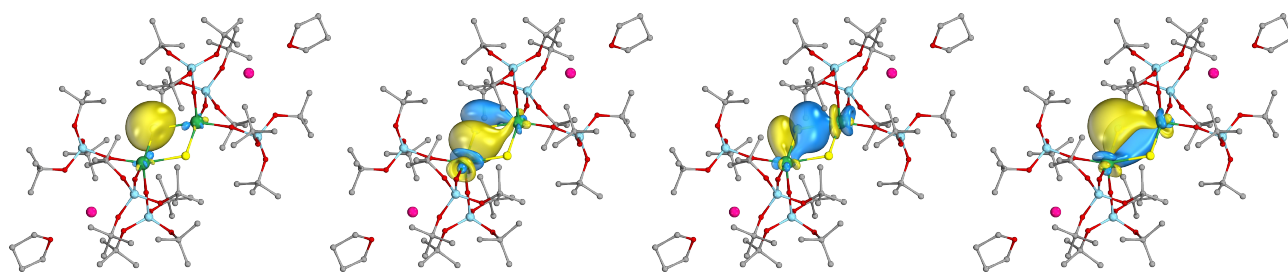


Figure S8: a ring IBOs of U(V)/U(V) $\text{U}_2\text{S}_2^{2+}$

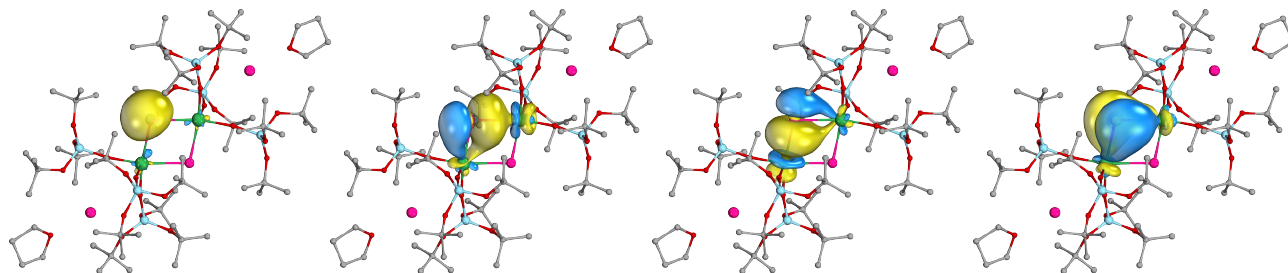


Figure S9: a ring IBOs of U(V)/U(V) $\text{U}_2\text{Se}_2^{2+}$

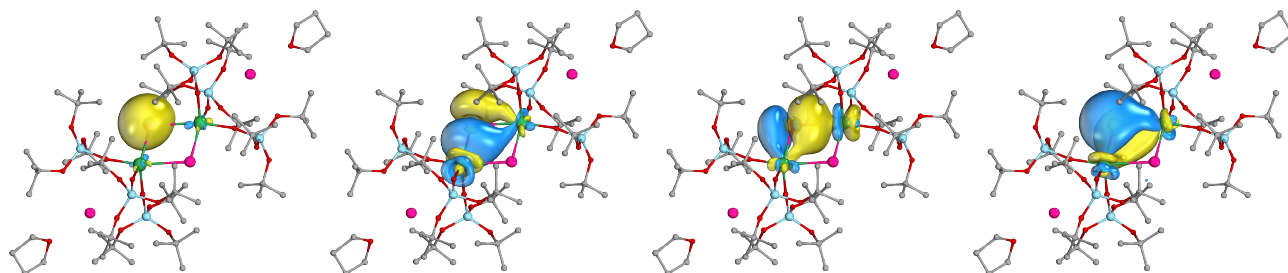


Figure S10: a ring IBOs of U(V)/U(V) $\text{U}_2\text{Te}_2^{2+}$

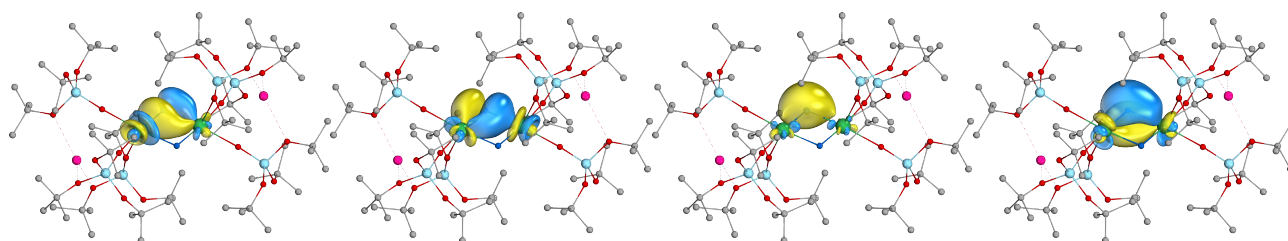


Figure S11: a ring IBOs of U(V)/U(V) U_2N_2

Table S8: Composition of a IBOs of U(V)/U(V) $\text{U}_2\text{O}_2^{2+}$, in the IAO basis

	U 7s	U 6d	U 5f	U other	O 2s	O 2p	O other
O 2s	2.00	4.53	1.78	0.48	62.73	27.07	0.60
U ^a -O σ	0.98	11.19	11.18	1.66	10.98	63.39	0.33
U ^b -O σ	0.97	11.32	11.79	0.92	11.18	62.82	0.70
U-O-U π	0.00	11.80	7.37	0.84	0.00	78.43	0.87

Table S9: Composition of α IBOs of U(V)/U(V) $U_2(NH)_2^{2+}$ in the IAO basis

	U 7s	U 6d	U 5f	U other	O 2s	O 2p	O other	H 1s
N-H σ	0.00	0.00	0.00	0.00	15.38	45.27	0.15	35.50
U^a-O σ	0.74	14.18	9.47	1.21	15.61	57.37	0.12	0.00
U^b-O σ	1.96	13.86	11.45	1.44	24.28	45.30	1.22	0.00
U-O-U π	1.81	13.07	14.04	1.18	15.02	54.08	0.20	0.00

Table S10: Composition of α IBOs of U(V)/U(V) $U_2S_2^{2+}$, in the IAO basis

	U 7s	U 6d	U 5f	U other	S 3s	S 3p	S other
S 3s	1.81	2.93	1.52	0.45	66.91	22.50	3.10
U^a-S σ	2.78	13.44	11.50	1.08	8.99	61.45	0.26
U^b-S σ	2.75	13.47	11.57	0.81	8.73	61.88	0.28
U-S-U π	0.00	12.74	7.59	0.77	0.00	77.52	0.48

Table S11: Composition of α IBOs of U(V)/U(V) $U_2Se_2^{2+}$, in the IAO basis

	U 7s	U 6d	U 5f	U other	Se 4s	Se 4p	Se other
Se 4s	1.64	2.56	1.27	0.33	71.25	19.61	2.54
U^a-Se σ	3.14	13.10	13.94	0.72	7.47	60.72	0.31
U^b-Se σ	2.94	13.68	11.83	0.75	6.58	63.23	0.29
U-Se-U π	0.00	12.16	8.03	0.51	0.00	77.72	0.08

Table S12: Composition of α IBOs of U(V)/U(V) $U_2Te_2^{2+}$, in the IAO basis

	U 7s	U 6d	U 5f	U other	Te 5s	Te 5p	Te other
Te 5s	1.40	2.03	1.08	0.39	74.18	15.22	4.79
U^a-Te σ	4.09	12.73	16.17	0.81	5.31	59.49	0.69
U^b-Te σ	3.75	13.54	13.60	1.01	5.31	60.96	0.93
U-Te-U π	0.00	11.91	7.91	0.98	0.00	76.16	1.14

Table S13: Composition of a IBOs of U(V)/U(V) U_2N_2 , in the IAO basis

	U 7s	U 6d	U 5f	U other	N 2s	N 2p	N other
N 2s	3.88	8.66	2.67	1.19	64.26	16.79	1.16
U ^a -N σ	0.70	15.40	21.53	1.97	7.89	51.91	0.10
U ^b -N σ	0.99	16.13	18.19	3.00	4.74	56.41	0.06
U-N-U π	0.00	21.52	13.93	0.65	0.00	62.79	0.01

4 U(V) QTAIM data

Table S13: QTAIM average bond critical point (BCP) properties of the U-X bond as a function of the exchange-correlation parameter J for the U(V) systems. ρ is the electron density, $\nabla^2\rho$ is the Laplacian of the gradient, ϵ is the ellipticity, V is the potential energy density, G is the kinetic energy density, and H is the total energy density $G + V$, all at the critical point.

	J / cm ⁻¹	ρ	$\nabla^2\rho$	ϵ	V	G	H
U ₂ Se ₂	-15.35	0.068	0.075	0.097	-0.055	-0.008	-0.018
U ₂ Te ₂	-23.19	0.056	0.042	0.131	-0.007	-0.007	-0.046
U ₂ O ₂	-22.04	0.133	0.403	0.046	-0.178	0.139	-0.039
U ₂ S ₂	-25.17	0.078	0.105	0.088	-0.071	0.049	-0.022
U ₂ (NH) ₂	-39.83	0.127	0.238	0.189	-0.154	0.107	-0.047
U ₂ N ₂	-92.41	0.173	0.23	0.025	-0.254	0.155	-0.099

Table S14: QTAIM average ring critical point (RCP) properties of the U₂X₂ ring as a function of the exchange-correlation parameter J for the U(V) systems. ρ is the electron density, $\nabla^2\rho$ is the Laplacian of the gradient, ϵ is the ellipticity, V is the potential energy density, G is the kinetic energy density, and H is the total energy density $G + V$, all at the critical point.

	J / cm ⁻¹	ρ	$\nabla^2\rho$	V	G	H
U ₂ Se ₂ ²⁺	-15.349	0.021	0.036	-0.010	0.010	-0.001
U ₂ Te ₂ ²⁺	-23.187	0.017	0.024	0.007	-0.007	-0.001
U ₂ O ₂ ²⁺	-22.042	0.043	0.148	0.039	-0.041	-0.002
U ₂ S ₂ ²⁺	-25.165	0.025	0.050	0.013	-0.013	-0.000
U ₂ (NH) ₂ ²⁺	-39.833	0.035	0.140	0.033	-0.031	0.002
U ₂ N ₂ ²⁺	-92.414	0.057	0.181	0.049	-0.052	-0.003

5 Imaginary frequencies

U(V)/U(V)						
	$\text{U}_2\text{Se}_2^{2+}$	$\text{U}_2\text{Te}_2^{2+}$	$\text{U}_2\text{O}_2^{2+}$	$\text{U}_2\text{S}_2^{2+}$	$\text{U}_2(\text{NH})_2^{2+}$	U_2N_2
#	2	0	2	3	2	2
	i15.40		i15.60	i13.87	i7.41	i10.60
	i15.15		i4.83	i7.91	i2.65	i10.05
				i7.75		

U(IV)/U(IV)					
	U_2O_2	$\text{U}_2(\text{NH})_2$	U_2S_2	U_2Se_2	U_2Te_2
#	1	1	0	0	!
	i7.22	i8.61			

The ditungsten decacarbonyl dianion

Joseph P. A. Ostrowski,* **Benjamin E. Atkinson**,* Laurence R. Doyle, Ashley J. Wooles, Nikolas Kaltsoyannis, and Stephen T. Liddle (**contributed equally*), *Dalton Trans.*, 2020, **49**, 9330-9335, <https://doi.org/10.1039/D0DT01921F>

This work was in collaboration with the Liddle group, University of Manchester, who synthesised the ditungsten decacarbonyl dianion. The crystal structure they obtained is, surprisingly, in the eclipsed geometry, rather than staggered which is more commonly observed for bimetallic carbonyls.

I performed calculations at several levels of theory, DFT, MP2 and CCSD(T), to determine whether this geometry is a result of the electronic structure of the molecule or due to other effects. At every level of theory the staggered geometry is preferred, driven by the relief of sterics and a slight shortening of the rather diffuse W-W bond. At the DFT and MP2 levels, the eclipsed geometry is a transition state (in the gas phase).

We suggest that the eclipsed geometry is observed due to crystal packing forces, with the eclipsed geometry best able to pack amongst the $[K(2,2,2\text{-cryptand})]^+$ units, and the gas phase transition state becomes a minimum when subjected to crystal packing forces in the solid state.

Contribution statement

I performed the computational work, with supervision and input from N.K.. I calculations at the DFT, MP2 and CCSD(T) levels, QTAIM analysis, and analysed the results. J.P.A.O prepared the compounds and with L.R.D. collected and analysed the characterization data. A.J.W. collected and refined the single crystal data. S.T.L. generated the research idea, supervised the work, and wrote the manuscript with contributions from all authors.

The Ditungsten Decacarbonyl Dianion

Joseph P. A. Ostrowski,[†] Benjamin E. Atkinson,[†] Laurence R. Doyle, Ashley J. Wooles, Nikolas Kaltsoyannis,* and Stephen T. Liddle*

Received 00th January 20xx,
Accepted 00th January 20xx

DOI: 10.1039/x0xx00000x

www.rsc.org/

We report the synthesis and structural authentication of the ditungsten decarbonyl dianion in $[(OC)_5W-W(CO)_5][K(18-crown-6)(THF)_2]_2$ (**1**), completing the group 6 dianion triad over half a century since the area began. The W-W bond is long [3.2419(8) Å] and, surprisingly, in the solid-state the dianion adopts a D_{4h} eclipsed rather than D_{4d} staggered geometry, the latter of which dominates the structural chemistry of binary homobimetallic carbonyls. Computational studies at levels of theory from DFT to CCSD(T) confirm that the D_{4d} geometry is energetically preferred in the gas-phase, being ~ 18 kJ mol⁻¹ more stable than the D_{4h} form, since slight destabilisation of the degenerate W-CO π 5d_{xy} and 5d_{yz} orbitals is outweighed by greater stabilisation of the W-W σ -bond orbital. The gas-phase D_{4h} structure displays a single imaginary vibrational mode, intrinsic reaction coordinate analysis of which links the D_{4h} isomer directly to the D_{4d} forms, which are produced by rotation around the W-W bond by $\pm 45^\circ$. It is therefore concluded that the gas-phase transition state becomes a minimum on the potential energy surface when subjected to crystal packing in the solid-state.

Introduction

Transition metal-carbonyls constitute a class of molecule that has played a pivotal and fundamental role in the advancement of the theory and application of coordination and organometallic chemistries.¹ Within this family, binary homobimetallic carbonyls with unsupported metal-metal bonds, *i.e.* being free of stabilising bridging ligands, occupy a key place at the intersection of seminal developments in metal-metal bond and organometallic areas.² The solid-state structures of $[(OC)_5M-M(CO)_5]$ ($M = Mn, Tc, Re$), $[(OC)_5M-M(CO)_5]^{2-}$ ($M = Cr, Mo$), $[(OC)_4M-M(CO)_4]^{2-}$ ($M = Fe, Ru, Os$), and $[(OC)_4Co-Co(CO)_4]$ have been determined from the 1950s onwards.³ For $[(OC)_5M-M(CO)_5]^n$ ($n = 0, 2-$) complexes the D_{4d} geometry overwhelmingly dominates their solid-state structures, with only one example of D_{4h} symmetry found for Cr,⁴ but the reason for this and any resulting implications were never investigated further and so have remained unknown.⁵ However, studies on the Mn and Re derivatives have shown that kbar pressures are required to force those complexes to convert from D_{4d} into D_{4h} geometries,⁶ suggesting that the former is lower in energy than the latter. However, considering their fundamental importance, there are remarkably few solid-state structures of homobimetallic carbonyls with unsupported metal-metal bonds. This may reflect difficulties in crystallising them, or that the metal-metal bonds are weak and prone to

cleavage or require stabilising bridging ligands or coordinated counter ions.

Prominent by its absence from the exemplars above is structural authentication of the free $[(OC)_5W-W(CO)_5]^{2-}$ dianion, even though $[Na_2W_2(CO)_{10}]$ was first reported in 1963,⁷ and the Cr and Mo congeners were structurally characterised in 1970.^{3d} Much more commonly, $[W_2(CO)_{10}(\mu-X)]$ ($X =$ formally anionic ligand) moieties are known, and structural authentication of $(OC)_5W-W(CO)_5$ as an unbridged unit is limited to $\{[(THF)_2Sm(N_4Et_8)Sm(THF)]_2\{(\mu-CO)_2W_2(CO)_8\}\}$ (**1**, $N_4Et_8 =$ *meso*-octaethylcalix[4]pyrrolide) where the $W_2(CO)_{10}$ unit has D_{4d} symmetry and is stabilised,⁸ and thus influenced, by carbonyl-bound cations as is most likely the case in $[Na_2W_2(CO)_{10}]$ itself.⁷ Thus, after almost six decades a structure of free $[(OC)_5W-W(CO)_5]^{2-}$ unperturbed by bridging ligands or stabilising counter cations has remained elusive, with the closest relative being homotrimetallic $[Na(DME)_3][(OC)_5W-W(CO)_4-W(CO)_5]$ (**II**).⁹

Here, as part of our ongoing studies into metal-metal bonding,¹⁰ we report the synthesis, structural authentication, and characterisation of $[(OC)_5W-W(CO)_5][K(18-crown-6)(THF)_2]_2$ (**1**), completing the triad of structurally authenticated free group 6 homobimetallic binary metal-carbonyls. Surprisingly, the free $[(OC)_5W-W(CO)_5]^{2-}$ dianion is found to adopt a perfectly D_{4h} eclipsed geometry, instead of the D_{4d} staggered form. Computational analysis reveals that in the gas-phase the D_{4h} isomer is linked directly to the D_{4d} form along the intrinsic reaction coordinate and that the former is a transition state, which leads to the conclusion that crystal packing effects render the D_{4h} form a minimum on the potential energy surface in the solid-state.

^a Department of Chemistry, The University of Manchester, Oxford Road, Manchester, M13 9PL, UK.

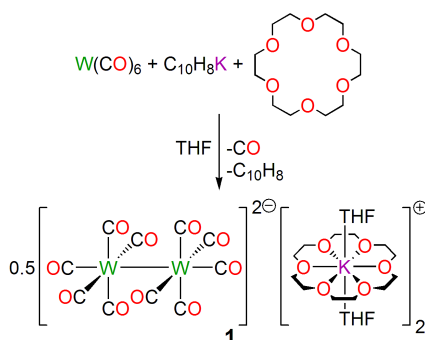
^b E-mail: steve.liddle@manchester.ac.uk; nikolas.kaltsoyannis@manchester.ac.uk.

[†] These authors contributed equally.

Electronic Supplementary Information (ESI) available: synthetic, spectroscopic, electrochemical, and computational detail. See DOI: 10.1039/x0xx00000x

Results and discussion

Synthetic Considerations



Scheme 1. Synthesis of compound **1** from tungsten hexacarbonyl, potassium naphthalenide, and 18-crown-6 ether precursors.

Dropwise treatment of an equimolar THF solution of tungsten hexacarbonyl and 18-crown-6 ether with a freshly prepared solution of potassium naphthalenide in THF results in immediate formation of a bright red solution. After a three day stir, work-up of the resulting brown solution and recrystallization from THF straightforwardly gave yellow $[(OC)_5W-W(CO)_5][K(18\text{-crown-6})(THF)_2]_2$ (**1**) in 58% crystalline yield (Scheme 1).¹¹

Crystallographic Analysis

The solid-state structure of **1** (Figure 1a) confirms (i) the unsupported metal-metal bond formulation with one axial and four equatorial carbonyls per tungsten, (ii) the separated ion pair nature, and (iii) that the $[(OC)_5W-W(CO)_5]^{2-}$ dianion unit surprisingly adopts an exact D_{4h} rather than D_{4d} geometry, since the centre of the W-W bond resides on a crystallographic inversion centre. Point (iii) contrasts to the situation found in **I**,⁸ and for binary homobimetallic carbonyls generally. The W-W distance in **1** is 3.2421(8) Å, which is significantly longer than the values of 2.74 and 2.79(2) Å for the sum of the single bond covalent radii of two tungsten atoms¹² and **II**,⁹ respectively, but it is closer to the W-W bond lengths of 3.1107(6) Å in **I**⁸ and 3.2881(1) Å in $[(\eta^5\text{-C}_5\text{Me}_5)W(CO)_3]_2$.¹³ The W-C3 distance of 1.906(11) Å is shorter than the W-C2-5 distances (av. 2.033, range 2.025(11)-2.043(11) Å), and the C3-O3 distance of 1.201(13) Å is longer than the other four C-O distances (av. 1.143, range 1.133(13)-1.153(12) Å) suggesting, as anticipated, that there is more W-C back-bonding to the two axial carbonyls than the eight equatorial ones. The two $[K(18\text{-crown-6})(THF)_2]^+$ cations are unremarkable.

Spectroscopic and Electrochemical Analyses

The 1H NMR spectrum of **1** exhibits the anticipated crown and THF resonances, with no resonances in the range –8 to –12 ppm suggesting the absence of bridging hydrides that would present with ^{183}W satellites. The $^{13}C\{^1H\}$ NMR spectrum is also consistent with the formulation of **1**, and it exhibits one very

weak resonance at 222.86 ppm, which is attributed to the equatorial CO groups, with the two axial CO groups not being observable due to the poor solubility of **1** in THF.

The ATR-IR spectrum of **1** (Figure 1b) is characteristic of such a system. Specifically, it features three bands in the carbonyl region centred at 1937 (A_{2u}), 1863 (E_u), and 1772 (A_{2u}) cm^{-1} . The first band is sharp and weaker compared to the other two that are much broader and intense, which is consistent with $[M(CO)_5]$ metal-carbonyls with local metal C_{4v} symmetry and other examples of $[(OC)_5M-M(CO)_5]^n$ complexes.^{7,8,14} The Raman spectrum of **1** (Figure 1b) features the anticipated four bands in the carbonyl region at 2019 (A_{1g}), 1960 (B_{1g}), 1904 (E_g), and 1794 (A_{1g}) cm^{-1} , whilst a strong absorption at 97 cm^{-1} (A_{1g}) can be assigned to the W-W bond stretch, which is lower than the value of 130 cm^{-1} for **I**.⁷ The latter observation is consistent with the respective W-W bond lengths of **1** and **I**, and lower than W-W quadruple bonds that typically are observed at 300 cm^{-1} .¹⁵

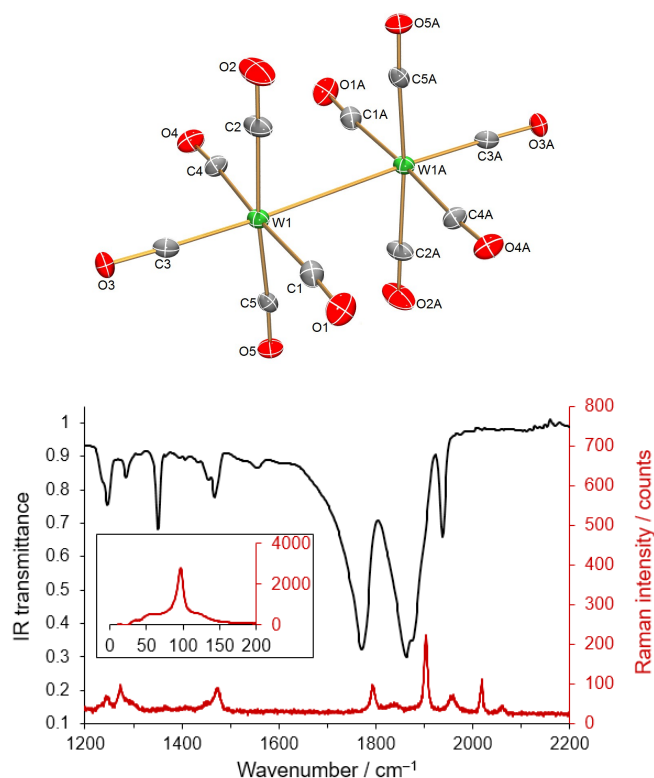


Figure 1. Selected characterisation data for **1**. Top: Molecular structure of the dianion component of crystalline $[(OC)_5W-W(CO)_5][K(18\text{-crown-6})(THF)_2]_2$ (**1**) at 150 K with probability ellipsoids. Selected distances are W1-W1A, 3.2421(8) Å; W1-C1, 2.037(10) Å; W1-C2, 2.026(11) Å; W1-C3, 1.906(11) Å; W1-C4, 2.043(12) Å; W1-C5, 2.025(11) Å; C1-O1, 1.139(12) Å; C2-O2, 1.148(13) Å; C3-O3, 1.201(13) Å; C4-O4, 1.133(14) Å; C5-O5, 1.153(12) Å. Bottom: Solid-state infrared and Raman spectra of **1** emphasising the carbonyl and metal-metal stretching regions.

The UV/Vis spectrum of **1** exhibits absorptions at 232, 350, and 400 nm, which is similar to isoelectronic $[(OC)_5Mn-Mn(CO)_5]$.¹⁶ The first is intense and assigned as $d \rightarrow \pi^*$ MLCT, whereas the other two are weak and assigned as $d \rightarrow d$.

The cyclic voltammogram of **1** in diethyl ether (Figure S2) reveals two well separated and almost irreversible one-

electron oxidation events ($E_{\text{p,ox}} = -0.99$ and -0.5 V) assigned as successive $W^{0/I}$ redox couples. The peak separation of 0.49 V equates to a hypothetical (noting their mostly irreversible nature) comproportionation constant of $K_{\text{com}} = 10^{8.281}$, which would classify $[(OC)_5W-W(CO)_5]^{2-}$ as a Robin-Day Class III mixed valence species. Consistent with the irreversible nature of these oxidations, we could not isolate any oxidised species by chemical oxidations, presumably due to their instability. On the basis of computational studies (see below) the electrons removed during these two oxidation events should derive from the W-W bond, which is the computed highest occupied molecular orbital (HOMO) of **1**. This nicely accounts for the observed oxidatively-induced decomposition and irreversible electrochemical behaviour, and the negative oxidation potentials are consistent with the dianionic nature of the tungsten component of **1** and that the W-W bond is computed to be diffuse and weak.

Computational Analyses

To further explore the bonding in the $[(OC)_5W-W(CO)_5]^{2-}$ dianion component of **1**, we turned to computational methods, and performed relaxed energy scans at several levels of theory (Figure 2 and Tables S1 and S2).¹¹ In-line with the structural and high pressure literature, at all levels the D_{4d} geometry is preferred; by 16.7–17.2 kJ mol⁻¹ with the B3LYP density functional and 18.4 kJ mol⁻¹ using spin-component scaled second-order Møller–Plesset perturbation theory (SCS-MP2, where singlet excitations are scaled up by 1.2, and triplet excitations down by 1/3). Coupled-cluster with single, double and perturbative triple excitations (CCSD(T)) single point energy calculations at the SCS-MP2 geometries reinforces the DFT and SCS-MP2 energies, with the D_{4h} geometry being 17.4 kJ mol⁻¹ higher than the D_{4d} isomer. The CCSD(T) T_1 diagnostic is 0.021 in both cases, suggesting that single-reference techniques should suffice. Because, for the dianion, DFT calculations compute positive eigenvalues for some Kohn-Sham orbitals, we performed further calculations with two

explicit Na^+ cations set 4 Å away from each of the axial carbonyls, however these explicit cation calculations give very similar results to those of the dianion. SCS-MP2 provides the best overall match to the crystal structure geometry (optimized variables are given in Tables S3–S5). At each level of theory, the W-W bond length shortens by about 0.1 Å going from D_{4h} to D_{4d} geometry. The introduction of the explicit Na^+ cations further reduces the W-W bond length by ~0.05 Å for B3LYP calculations, which is consistent with the situation in **1** where the Sm ions perform the same stabilising role as Na^+ .⁸

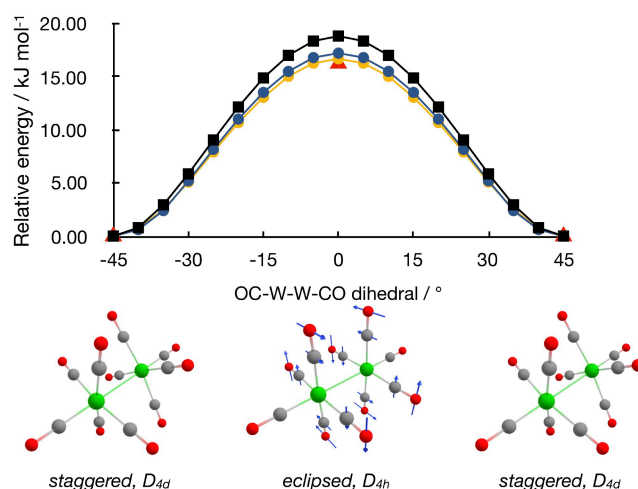


Figure 2. Relaxed energy scans of **1**, where the geometry is optimised at each point while preserving (at least) D_4 symmetry and fixing the dihedral angle. Black square: SCS-MP2, blue circle: B3LYP with Na cations, yellow circle: B3LYP, red triangle: CCSD(T) at SCS-MP2 optimised geometry. Blue arrows indicate the motion of the twisting imaginary mode at the eclipsed geometry.

The frontier Kohn-Sham orbitals of the B3LYP calculation, with explicit Na^+ cations, for the D_{4h} geometry are shown in Figure 3. The a_{1g} HOMO is the W-W σ -bond, consistent with the cyclic voltammogram, and the remaining frontier orbitals are W-CO π -bonding orbitals.

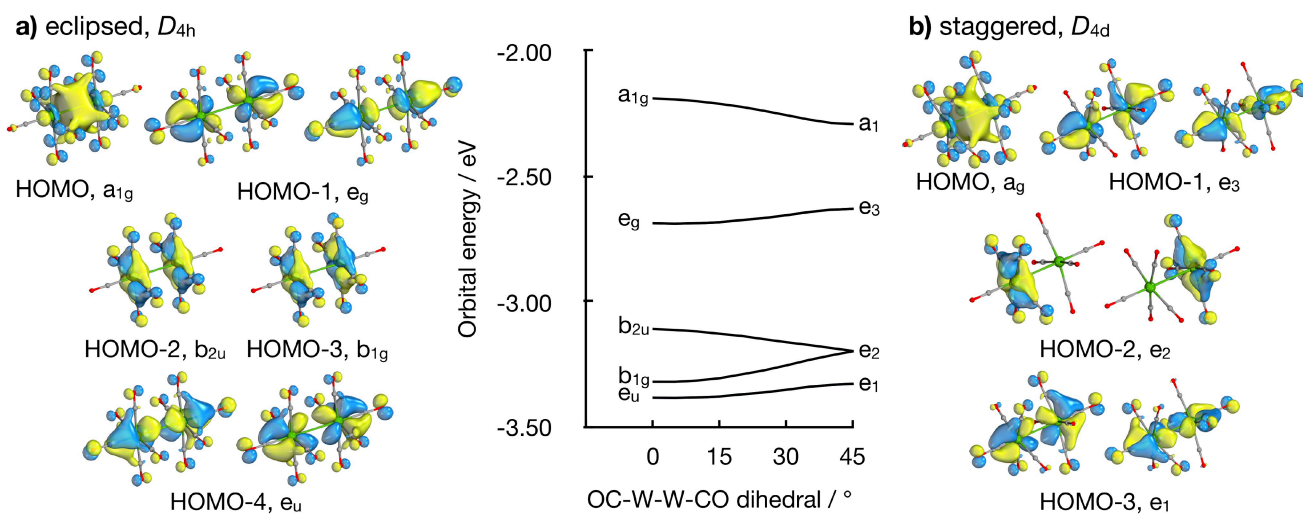


Figure 3. The frontier molecular orbitals of eclipsed (a) and staggered (b) $[(OC)_5W-W(CO)_5]^{2-}$; the W-W σ HOMO and the W-CO π bonding orbitals are shown, at the B3LYP level of theory with explicit Na cations. Only one of the doubly degenerate orbitals is shown. The isosurfaces enclose 60% of the orbital. Green: W, grey: C, red: O. Na omitted for clarity. The energy of these frontier MOs as a function of OC-W-W-CO dihedral angle is plotted (centre).

Topological analysis of the SCS-MP2 density using the quantum theory of atoms in molecules further supports the orbital-based bonding picture. The ellipticity parameter ε of the W-W bond critical point (BCP) is zero, as expected given the cylindrical symmetry of the a_{1g} HOMO. Whilst the delocalization index δ is essentially unchanged from D_{4h} (0.271) to D_{4d} (0.270) geometries, the increase in the BCP electron density ρ (0.029 vs 0.033 au), and the more negative energy density H (−0.007 vs −0.009 au), reflects the increase in covalency due to the shorter bond length, which is consistent with experimental structural and spectroscopic data. The low delocalisation index reflects the weakness of the bond.

To explore the gas-phase preference for the D_{4d} geometry, we analysed the energies of the frontier Kohn-Sham molecular orbitals. Key frontier orbitals, and their energies as a function of the OC-W-W-CO dihedral angle, are shown in Figure 3. Defining the W-W bond as the z-axis, as the OC-W-W-CO dihedral angle moves from D_{4h} (0°) to D_{4d} (45°) geometry, the W-CO π $5d_{xy}$ orbitals are largely unaffected; degenerate at D_{4d} (e_2), with the in- and out-of-phase combinations energetically split for D_{4h} (b_{2u} and b_{1g}) (Figure 3). The four $5d_{xz}$ and $5d_{yz}$ orbitals are slightly destabilized from D_{4h} (0°) to D_{4d} (45°), in contrast to the stabilization of the W-W σ -bond, favouring the D_{4d} geometry. With stabilization of the W-W σ -bond comes a shorter and stronger W-W bond, however the W-W σ -bond remains weak and diffuse, as reflected in the QTAIM analysis, and that the W-W σ -bond HOMO is only 32.9% and 33.6% tungsten-based for D_{4h} (0°) and D_{4d} (45°) respectively.

Frequency analysis of the gas-phase D_{4d} and D_{4h} geometries, using both B3LYP and SCS-MP2, confirms that the D_{4d} geometry is a true minimum structure, with the D_{4h} geometry corresponding to a transition state between two D_{4d} conformations; the imaginary mode of the D_{4h} structure (26.6i

cm^{-1} at SCS-MP2, Figure 2) is characterised by an intrinsic reaction coordinate (IRC) to the two D_{4d} conformations that are $\pm 45^\circ$ of it. Notably, the intensities of the carbonyl absorptions match the experimental pattern (Tables S6 and S7), and the computed W-W stretch is 117.5 cm^{-1} at the D_{4d} geometry vs 100.2 cm^{-1} when D_{4h} (and 97 cm^{-1} experimentally), again reflecting the weakened W-W bond at the D_{4h} geometry.

The majority of binary homobimetallic carbonyls adopt D_{4d} geometries in crystalline phases. For example, of the five reports of $[(\text{OC})_5\text{Cr-Cr}(\text{CO})_5]^{2-}$ four are D_{4d} whilst the fifth is D_{4h} ; with two $[\text{K}(2,2,2\text{-cryptand})]^+$ cations a D_{4h} geometry is adopted,⁴ however replacing K with Na in $[(\text{OC})_5\text{Cr-Cr}(\text{CO})_5][\text{Na}(2,2,2\text{-cryptand})]_2$ results in a D_{4d} geometry,¹⁷ but until now the reason for this was unknown. Our gas-phase calculations on $[(\text{OC})_5\text{W-W}(\text{CO})_5]^{2-}$ from DFT to CCSD(T) levels of theory consistently and decisively give a preference for the D_{4d} geometry over the D_{4h} . However, experimentally we isolate $[(\text{OC})_5\text{W-W}(\text{CO})_5]^{2-}$ in its D_{4h} form. On the basis of our structural and computational data, we conclude that crystal packing is responsible for the adoption of a D_{4h} geometry in **1**, since the predicted preference for the D_{4d} geometry is at most 20 kJ mol^{-1} , and this is certainly in the range of crystal packing forces. This implies that the gas-phase transition state becomes a minimum on the potential energy surface when subject to crystal packing forces. Inspection of the crystal packing diagram of **1** supports this view, Figure 4, since this demonstrates how the D_{4h} geometry of the dianion of **1** packs efficiently with two $[\text{K}(\text{18C6})(\text{THF})_2]^+$ cations, where each channel of $[(\text{OC})_5\text{W-W}(\text{CO})_5]^{2-}$ dianions is surrounded by four symmetrically disposed channels of $[\text{K}(\text{18C6})(\text{THF})_2]^+$ cations when viewed down the plane defined by the crystallographic a axis in between the b and c axes.

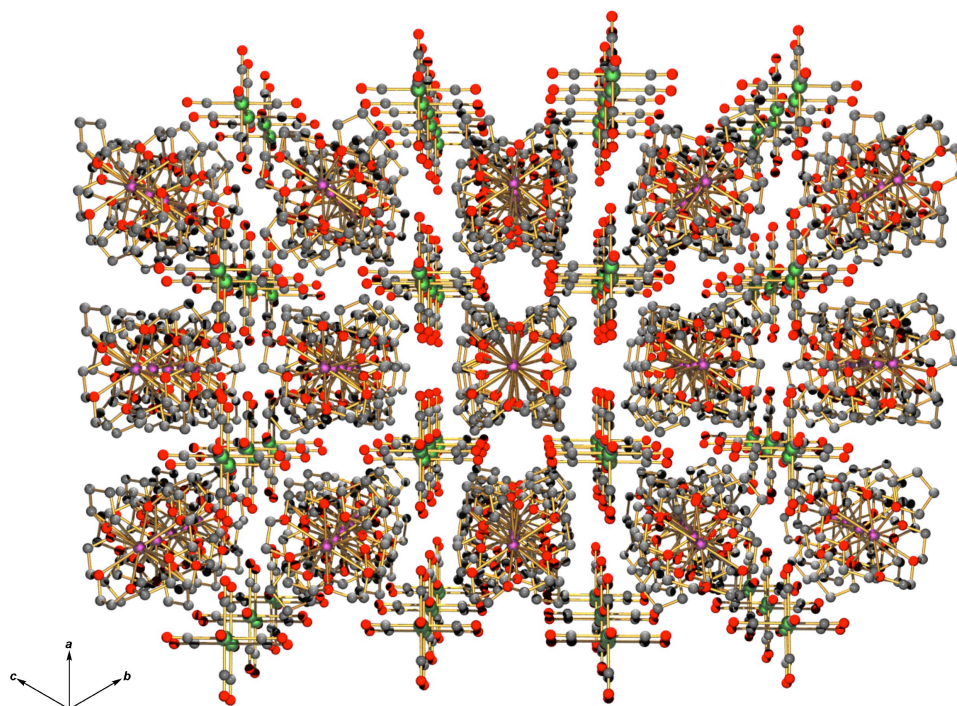


Figure 4. Crystal packing diagram for **1**.

Conclusions

To conclude, we have developed a straightforward synthesis of **1**, which contains the free ditungsten decacarbonyl dianion, completing the triad of structurally authenticated group 6 binary homobimetallic metal-carbonyls first established over half a century ago. Surprisingly, in **1** the $[(OC)_5W-W(CO)_5]^{2-}$ dianion adopts a D_{4h} (eclipsed) geometry in the solid-state and not the anticipated D_{4d} (staggered) isomer; quantum chemical calculations at several levels of theory all point to the latter geometry being intrinsically favoured in the gas-phase, with the D_{4h} structure being a rotational transition state linking D_{4d} minima. It is therefore concluded that the gas-phase transition state becomes a minimum on the potential energy surface when subjected to crystal packing in the solid-state.

Experimental

Preparation of $[(OC)_5W-W(CO)_5][K(18\text{-crown-6})(THF)_2]_2$ (**1**)

THF (20 ml) was added to a mixture of $[W(CO)_6]$ (0.704 g, 2.0 mmol) and 18-crown-6 (0.53 g, 2.0 mmol). THF (20 ml) was then added to a separate mixture of potassium metal (0.08 g, 2.0 mmol) and naphthalene (0.26 g, 2.0 mmol), and the mixture agitated until all the potassium was consumed. The completed potassium naphthalenide solution was added dropwise to the $W(CO)_6$ solution, instantaneously forming a red solution which was allowed to stir over 3 days, resulting in a brown solution. Volatiles were removed *in vacuo* and the resulting brown solid was washed with pentane (2×10 ml), then extracted into THF (5 ml) and filtered away from the remaining solid. Volatiles were removed *in vacuo* to afford **1** as a yellow powder. Crystals of **1** suitable for X-ray diffraction were grown from a concentrated THF solution at ambient temperature. Yield: 0.728 g, 58%. Extended drying under vacuum removes the THF as evidenced by the elemental analyses. Anal. Calc'd for $C_{34}H_{48}K_2O_{22}W_2$: C 32.55; H 3.86%. Found: C 32.80; H 3.90%. 1H NMR (500 MHz, d_8 -THF) δ : 3.64 (48H, s, CH_2), 3.62 (16H, m, $THF(O-CH_2)$), 1.78 (16H, m, $THF(CH_2-CH_2)$). $^{13}C\{^1H\}$ NMR (d_8 -THF) δ : 222.86 (s, W-CO) 70.21 (s, O- CH_2), 66.63 ($THF(O-CH_2)$), 23.33 ($THF(CH_2-CH_2)$). FTIR ν/cm^{-1} (ATR): 2905 (w), 1938 (m), 1863 (s), 1772 (s), 1467 (w), 1351 (w), 1095 (s), 959 (s), 833 (m), 576 (s). Raman ν/cm^{-1} (Neat, ≤ 15 mW): 2019 (w), 1960 (br), 1904 (m), 1794 (w), 595 (w), 447 (s), 405 (m), 97 (vs).

Acknowledgements

We are grateful to the UK Engineering and Physical Sciences Research Council (grants EP/M027015/1, and EP/P001386/1), European Research Council (grant CoG612724), Royal Society (grants UF110005 and RG110238), The University of Manchester, and The University of Manchester Computational Shared Facility for computational resources and associated support services.

Notes and references

‡ CCDC 1953958 (**1**) contains the supplementary crystallographic data for this paper. These data can be obtained free of charge from The Cambridge Crystallographic Data Centre. All other data are available from the corresponding authors on request.

- a) W. Heijser, E. Jan Baerends and P. Ros, *Faraday Symp., Chem. Soc.* 1980, **14**, 211; b) E. W. Abel and F. G. A. Stone, *Q. Rev. Chem. Soc.*, 1969, **23**, 325.
- a) *Molecular Metal-Metal Bonds: Compounds, Synthesis, Properties*, Ed S. T. Liddle, Wiley VCH, Weinheim, Germany, 2015; b) *Multiple Bonds Between Metal Atoms*, 3rd Edition, Eds F. A. Cotton, C. A. Murillo, R. A. Walton, Springer-Verlag, New York, 2005.
- a) T. Y. Garcia, J. C. Fetting, M. M. Olmstead and A. L. Balch, *Chem. Commun.*, 2009, 7143; b) L. -Y. Hsu, N. Bhattacharyya and S. G. Shore, *Organometallics*, 1985, **4**, 1483; c) H. B. Chin, M. B. Smith, R. D. Wilson and R. Bau, *J. Am. Chem. Soc.*, 1974, **96**, 5285; d) L. B. Handy, J. K. Ruff and L. F. Dahl, *J. Am. Chem. Soc.*, 1970, **92**, 7312; e) M. F. Bailey and L. F. Dahl, *Inorg. Chem.*, 1965, **4**, 1140; f) L. F. Dahl, E. Ishishi and R. E. Rundle, *J. Chem. Phys.*, 1957, **26**, 1750.
- H. Borrmann, A. M. Pirani and G. J. Schrobilgen, *Acta Cryst.*, 1997, **C53**, 1007.
- P. Vilarrubias, *Mol. Phys.* 2016, **114**, 1794.
- D. M. Adams, P. D. Hatton, A. C. Shaw and T. -K. Tan, *J. Chem. Soc. Chem. Comm.*, 1981, 226.
- H. Behrens and J. Vogl, *Chem. Ber.*, 1963, **96**, 2220.
- G. B. Deacon, Z. Guo, P. C. Junk and J. Wang, *Angew. Chem. Int. Ed.*, 2017, **56**, 8486.
- I. P. Beletskaya, A. Z. Voskoboynikov, E. B. Chuklanova, A. I. Gusev and A. V. Kisin, *J. Organomet. Chem.*, 1993, **454**, 1.
- a) E. Lu, A. J. Wooles, M. Gregson, P. J. Cobb and S. T. Liddle, *Angew. Chem. Int. Ed.*, 2018, **57**, 6587; b) A. J. Ayres, M. Zegke, J. P. A. Ostrowski, F. Tuna, E. J. L. McInnes, A. J. Wooles and S. T. Liddle, *Chem. Commun.*, 2018, **54**, 13515; c) T. M. Rookes, E. P. Wildman, G. Balázs, B. M. Gardner, A. J. Wooles, M. Gregson, F. Tuna, M. Scheer and S. T. Liddle, *Angew. Chem. Int. Ed.*, 2018, **57**, 1332; d) D. Patel, F. Moro, J. McMaster, W. Lewis, A. J. Blake and S. T. Liddle, *Angew. Chem. Int. Ed.*, 2011, **50**, 10388; e) B. M. Gardner, D. Patel, A. D. Cornish, J. McMaster, W. Lewis, A. J. Blake and S. T. Liddle, *Chem. Eur. J.*, 2011, **17**, 11266; f) B. Vlaisavljevich, P. Miró, C. J. Cramer, L. Gagliardi, I. Infante and S. T. Liddle, *Chem. Eur. J.*, 2011, **17**, 8424; g) B. M. Gardner, J. McMaster, F. Moro, W. Lewis, A. J. Blake and S. T. Liddle, *Chem. Eur. J.*, 2011, **17**, 6909; h) D. Patel, D. M. King, B. M. Gardner, J. McMaster, W. Lewis, A. J. Blake and S. T. Liddle, *Chem. Commun.*, 2011, **47**, 295; i) B. M. Gardner, J. McMaster, W. Lewis and S. T. Liddle, *Chem. Commun.*, 2009, 2851; j) S. T. Liddle, J. McMaster, D. P. Mills, A. J. Blake, C. Jones and W. D. Woodul, *Angew. Chem. Int. Ed.*, 2009, **48**, 1077.
- See the Electronic Supplementary Information for full details.
- P. Pykkö, *J. Phys. Chem. A* 2015, **119**, 2326.
- A. L. Rheingold and J. R. Harper, *Acta Cryst.*, 1991, **C47**, 184.
- G. O. Evans, W. T. Wozniak and R. K. Sheline, *Inorg. Chem.*, 1970, **9**, 979.
- A. P. Sattelberger, K. W. McLaughlin and J. C. Huffman, *J. Am. Chem. Soc.*, 1981, **103**, 2880.
- M. Ciftci, M. A. Tasdelen and Y. Yagci, *Polym. Chem.*, 2014, **5**, 600.
- H. Borrmann, A. M. Pirani and G. J. Schrobilgen, *Acta Cryst.*, 1997, **C53**, 19.

The Ditungsten Decacarbonyl Dianion

Joseph P. A. Ostrowski,[†] Benjamin E. Atkinson,[†] Laurence R. Doyle, Ashley J. Wooles, Nikolas Kaltsoyannis,* and Stephen T. Liddle*

Department of Chemistry, The University of Manchester, Oxford Road, Manchester, M13 9PL, UK.

*E-mail: steve.liddle@manchester.ac.uk; nikolas.kaltsoyannis@manchester.ac.uk

[†] These authors contributed equally.

Experimental Details

General Considerations

All manipulations were carried out using Schlenk techniques, or an MBraun UniLab glovebox, under an atmosphere of dry nitrogen. Solvents were dried by passage through activated alumina towers and degassed before use. All solvents were stored over potassium mirrors except for ethers which were stored over activated 4 Å sieves. Deuterated solvent was distilled from potassium, degassed by three freeze-pump-thaw cycles and stored under nitrogen. Tungsten hexacarbonyl, potassium, naphthalene, and 18-crown-6 ether were purchased from Sigma Aldrich and dried for 4 hours under vacuum before use.

NMR spectra were acquired on a Bruker AV400 spectrometer operating at 400.2 (¹H) and 100.6 (¹³C{¹H}) MHz; chemical shifts are quoted in ppm and are relative to SiMe₄. Attenuated total reflectance (ATR) infrared (IR) spectra were obtained using a Bruker Alpha Platinum-ATR FTIR spectrometer or a Thermo Scientific™ Nicolet™ iS™5 FTIR spectrometer with iD5 ATR

accessory. A Horiba XploRA Plus Raman microscope with a 638 nm laser (power: ≤ 150 mW) was used to obtain all Raman spectra. The power of the laser was adjusted for each sample using a filter to prevent sample decomposition. UV/Vis spectra were obtained using a PerkinElmer Lambda 750 spectrometer. All samples were prepared under a nitrogen atmosphere and collected using a 1 mm path length quartz cuvette. Samples were run *vs.* THF solvent. Electrochemical experiments were carried out using an μ AutoLab Type III potentiostat controlled by Nova. Measurements were performed inside a sealed N₂ vessel at room temperature, and subsequently calibrated through the addition of ferrocene. A three-electrode configuration was employed: a Pt working electrode; a Pt wire counter electrode; and an Ag wire pseudo-reference electrode. All electrodes were polished using alumina/H₂O. CHN microanalyses were carried out by Mr M Jennings at the University of Manchester. Crystals were examined using a Rigaku FR-X diffractometer, equipped with a HyPix 6000HE photon counting pixel array detector with mirror-monochromated Mo K α ($\lambda = 0.71073$ Å) or Cu K α ($\lambda = 1.5418$ Å) radiation. Intensities were integrated from a sphere of data recorded on narrow (1.0°) frames by ω rotation. Cell parameters were refined from the observed positions of all strong reflections in each data set. Gaussian grid face-indexed absorption corrections with a beam profile correction were applied. The structures were solved either by dual methods using SHELXT¹ and all non-hydrogen atoms were refined by full-matrix least-squares on all unique F^2 values with anisotropic displacement parameters with exceptions noted in the respective cif files. Hydrogen atoms were refined with constrained geometries and riding thermal parameters; $U_{\text{iso}}(\text{H})$ was set at 1.2 (1.5 for methyl groups) times U_{eq} of the parent atom. The largest features in final difference syntheses were close to heavy atoms and were of no chemical significance. CrysAlisPro was used for control and integration,² and SHELXL and Olex2 were employed for structure refinement.^{3,4} ORTEP-3 and POV-Ray were employed for molecular graphics.^{5,6}

Preparation of $[(OC)_5W-W(CO)_5]/[K(18\text{-crown-6})(THF)_2]_2$ (1**)**

THF (20 ml) was added to a mixture of $[W(CO)_6]$ (0.704 g, 2.0 mmol) and 18-crown-6 (0.53 g, 2.0 mmol). THF (20 ml) was then added to a separate mixture of potassium metal (0.08 g, 2.0 mmol) and naphthalene (0.26 g, 2.0 mmol), and the mixture agitated until all the potassium was consumed. The completed potassium naphthalenide solution was added dropwise to the $W(CO)_6$ solution, instantaneously forming a red solution which was allowed to stir over 3 days, resulting in a brown solution. Volatiles were removed *in vacuo* and the resulting brown solid was washed with pentane (2×10 ml), then extracted into THF (5 ml) and filtered away from the remaining solid. Volatiles were removed *in vacuo* to afford **1** as a yellow powder. Crystals of **1** suitable for X-ray diffraction were grown from a concentrated THF solution at ambient temperature. Yield: 0.728 g, 58%. Extended drying under vacuum removes the THF as evidenced by the elemental analyses. Anal. Calc'd for $C_{34}H_{48}K_2O_{22}W_2$: C 32.55; H 3.86%. Found: C 32.80; H 3.90%. 1H NMR (500 MHz, d_8 -THF) δ : 3.64 (48H, s, CH_2), 3.62 (16H, m, THF(O- CH_2)), 1.78 (16H, m, THF(CH_2 - CH_2)). $^{13}C\{^1H\}$ NMR (d_8 -THF) δ : 222.86 (s, W-CO) 70.21 (s, O- CH_2), 66.63 (THF(O- CH_2)), 23.33 (THF(CH_2 - CH_2)). FTIR ν/cm^{-1} (ATR): 2905 (w), 1938 (m), 1863 (s), 1772 (s), 1467 (w), 1351 (w), 1095 (s), 959 (s), 833 (m), 576 (s). Raman ν/cm^{-1} (Neat, ≤ 15 mW): 2019 (w), 1960 (br), 1904 (m), 1794 (w), 595 (w), 447 (s), 405 (m), 97 (vs).

Experimental Data

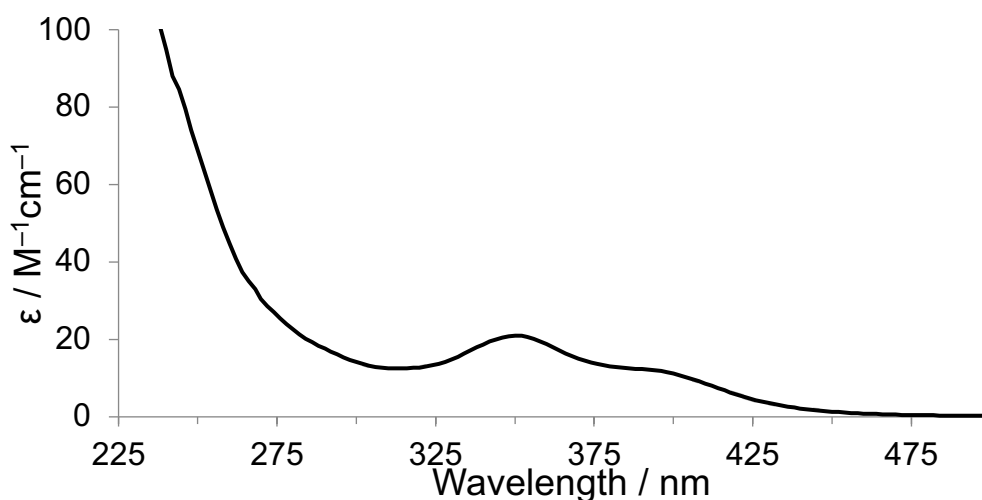


Figure S1. UV/Vis spectrum of complex 1 in THF.

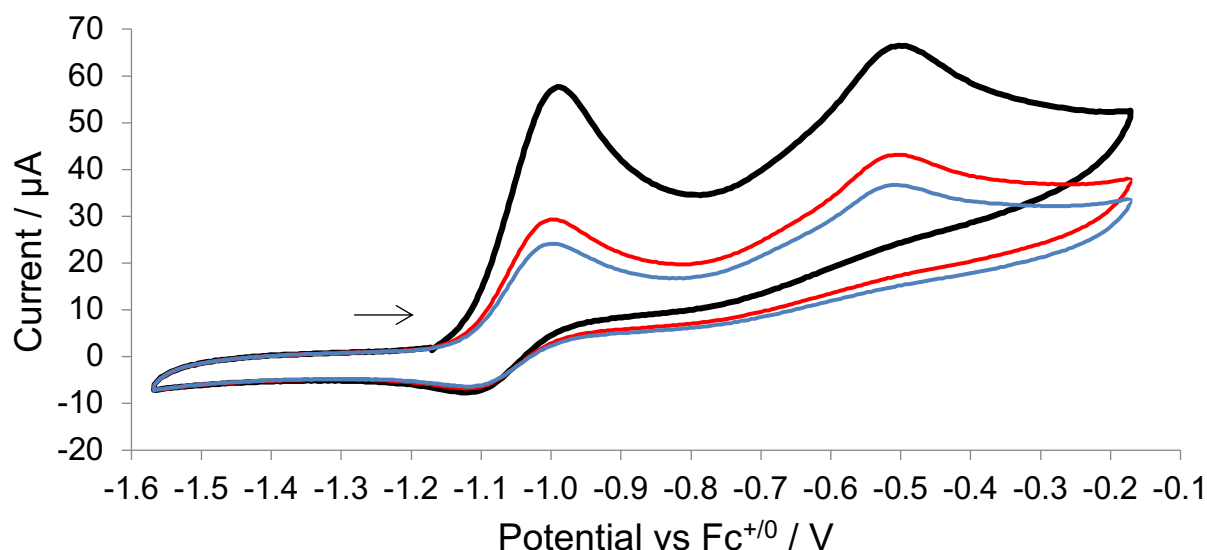


Figure S2. Cyclic voltammogram of **1** (0.42 mM) vs. $\text{Fc}^{+/0}$ (2 mM), with $[\text{nBu}_4\text{N}][\text{BF}_4]$ (0.5 M) as electrolyte, showing first (black), second (red) and third (blue) scans. Arrow shows scan directions.

Computational Details

General Considerations

All calculations were performed in Molpro 2018.2.⁷ Calculations were performed at the density functional theory (DFT) level of theory, using the hybrid B3LYP⁸⁻¹¹ functional. DFT calculations included dispersion with Grimme's D3 dispersion correction, and Becke-Johnson damping.¹² Additional calculations were performed with spin-coupled scaled second-order Møller-Plesset perturbation theory (SCS-MP2, where singlet excitations are scaled up by 1.2, and triplet excitations down by 1/3, which has previously been shown to perform well for transition metals^{13,14}), and coupled cluster with singles, doubles and perturbative triple excitations (CCSD-(T)). Density fitting was employed for DFT and SCS-MP2 calculations.¹⁵ The def2-ATZVPP basis set, from the Molpro basis set library, was used on all elements, alongside the analogous auxiliary basis set for density fitting calculations. This is the def2-TZVPP basis set augmented with one set of diffuse functions,^{16,17} and uses the 60 electron quasi-relativistic effective core potential of the

Stuttgart/Cologne Group.^{18,19} Calculations were constrained to preserve the four-fold symmetry, *i.e.* D_{4h} when eclipsed, D_{4d} when staggered and D₄ between. Orbital isosurfaces were generated by IBOView.²⁰ QTAIM calculations were performed with AIMALL version 17.11.14²¹ with .wfx files generated by Molden2AIM.²²

Table S1. Z-matrix used for all calculations

W,
W, 1, BWW,
C, 1, BCWeq, 2, ACWWeq,
C, 1, BCWeq, 2, ACWWeq, 3, Deq, 0
C, 1, BCWeq, 2, ACWWeq, 4, Deq, 0
C, 1, BCWeq, 2, ACWWeq, 5, Deq, 0
C, 1, BCWax, 3, 180.0-ACWWeq, 2, Dax, 0
O, 1, BOCe_q + BCWeq, 2, AOWWeq, 6, Deq, 0
O, 1, BOCe_q + BCWeq, 2, AOWWeq, 8, Deq, 0
O, 1, BOCe_q + BCWeq, 2, AOWWeq, 9, Deq, 0
O, 1, BOCe_q + BCWeq, 2, AOWWeq, 10, Deq, 0
O, 1, BOCax + BCWax, 3, 180.0-ACWWeq, 2, Dax, 0
C, 2, BCWeq, 1, ACWWeq, 4, Dspin, 0
C, 2, BCWeq, 1, ACWWeq, 13, Deq, 0
C, 2, BCWeq, 1, ACWWeq, 14, Deq, 0
C, 2, BCWeq, 1, ACWWeq, 15, Deq, 0
C, 2, BCWax, 13, 180.0-ACWWeq, 15, Dax, 0
O, 2, BOCe_q + BCWeq, 1, AOWWeq, 4, Dspin, 0
O, 2, BOCe_q + BCWeq, 1, AOWWeq, 13, Deq, 0
O, 2, BOCe_q + BCWeq, 1, AOWWeq, 14, Deq, 0
O, 2, BOCe_q + BCWeq, 1, AOWWeq, 15, Deq, 0
O, 2, BOCax + BCWax, 13, 180.0-ACWWeq, 15, Dax, 0
[Na, 2, BOCax + BCWax + 4.0, 13, 180.0 - ACWWeq, 15, Dax, 0
Na, 1, BOCax + BCWax + 4.0, 3, 180.0 - ACWWeq, 2, Dax, 0]*
*B3LYP with explicit Na counter cations only

The following variables were fixed to preserve four-fold symmetry:

Deq= -90.0°
Dax= 180.0°

Table S2. Energies at the optimized geometries, in Hartree, and energies relative to the staggered (D_{4h} , $DSPIN=45^\circ$) geometry, in kJ mol^{-1}

DSPIN:	B3LYP			B3LYP (Na)			SCS-MP2			CCSD(T)		
	E_{el}/Ha	$\Delta E/\text{kJ mol}^{-1}$	E_{el}/Ha	$\Delta E/\text{kJ mol}^{-1}$	E_{el}/Ha	$\Delta E/\text{kJ mol}^{-1}$	E_{el}/Ha	$\Delta E/\text{kJ mol}^{-1}$	E_{el}/Ha	$\Delta E/\text{kJ mol}^{-1}$	E_{el}/Ha	$\Delta E/\text{kJ mol}^{-1}$
0	-1267.805545	16.705	-1592.160471	17.247	-1265.085309	18.846	-1265.359032	16.271				
5	-1267.805699	16.301	-1592.160632	16.823	-1265.085484	18.387						
10	-1267.806174	15.053	-1592.161129	15.519	-1265.085999	17.035						
15	-1267.806927	13.077	-1592.161882	13.543	-1265.086810	14.906						
20	-1267.807831	10.704	-1592.162838	11.031	-1265.087851	12.174						
25	-1267.808886	7.934	-1592.163925	8.179	-1265.089033	9.069						
30	-1267.809970	5.087	-1592.165053	5.216	-1265.090251	5.872						
35	-1267.810945	2.528	-1592.166123	2.407	-1265.091363	2.952						
40	-1267.811649	0.679	-1592.166805	0.616	-1265.092179	0.809						
45	-1267.811908	0.000	-1592.167040	0.000	-1265.092488	0.000	-1265.365230	0.000				

Table S3. SCS-MP2 Optimized variables of the dihedral angle scan, at the SCS-MP2 level of theory^a

DSPIN	0 ^b	5	10	15	20	25	30	35	40	45*
BWW	3.207714	3.205534	3.198146	3.186576	3.171761	3.155722	3.139449	3.125010	3.114489	3.110459
BCWeq	2.044314	2.044254	2.044253	2.044267	2.044300	2.044198	2.044118	2.044063	2.043978	2.043899
ACWWeq	88.116673	88.064066	87.915310	87.680933	87.358749	86.961957	86.502715	86.025675	85.645275	85.489581
BCWax	1.959445	1.959674	1.960249	1.961236	1.962430	1.963911	1.965453	1.966856	1.967906	1.968386
BOCeq	1.166804	1.166835	1.166917	1.167047	1.167207	1.167384	1.167545	1.167659	1.167725	1.167738
AOWWeq	89.109728	89.041356	88.843500	88.530667	88.097918	87.567329	86.950694	86.307080	85.791849	85.580466
BOCax	1.185489	1.185473	1.185446	1.185401	1.185349	1.185276	1.185209	1.185156	1.185114	1.185096

^a All bond lengths in Å, angles in °. ^b used in CCSD(T) single point calculation.

Table S4. B3LYP 2Na Optimized variables of the dihedral angle scan, at the B3LYP level of theory, with explicit Na counter-cations^a

DSPIN	0	5	10	15	20	25	30	35	40	45
BWW	3.314492	3.313175	3.305539	3.294024	3.279057	3.262748	3.246023	3.230976	3.219814	3.216735
BCWeq	2.055137	2.055193	2.055189	2.055158	2.055103	2.055038	2.054971	2.054829	2.054785	2.054755
ACWWeq	87.301779	87.250715	87.121868	86.923234	86.629732	86.299500	85.905615	85.490037	85.196145	85.066023
BCWax	1.929241	1.929309	1.929794	1.930502	1.931502	1.932607	1.933829	1.934963	1.935846	1.936115
BOCeq	1.153515	1.153539	1.153625	1.153754	1.153924	1.154082	1.154227	1.154339	1.154376	1.154386
AOWWeq	88.288964	88.219519	88.037124	87.759386	87.345793	86.885413	86.333001	85.747354	85.332721	85.150919
BOCax	1.186098	1.186107	1.186108	1.186111	1.186120	1.186130	1.186147	1.186174	1.186184	1.186198

^a All bond lengths in Å, angles in °.

Table S5. B3LYP Optimized variables of the dihedral angle scan, at the B3LYP level of theory

DSPIN	0	5	10	15	20	25	30	35	40	45
BWW	3.367564	3.365385	3.357152	3.344652	3.328927	3.311011	3.292854	3.276094	3.264940	3.260837
BCWeq	2.050460	2.050467	2.050414	2.050375	2.050355	2.050251	2.050192	2.050032	2.049957	2.049918
ACWWeq	87.074757	87.028042	86.908714	86.713119	86.440194	86.123182	85.741191	85.346919	85.049774	84.954740
BCWax	1.957723	1.957805	1.958353	1.959167	1.960220	1.961453	1.962736	1.964055	1.964969	1.965041
BOCeq	1.157383	1.157407	1.157481	1.157598	1.157731	1.157865	1.157978	1.158056	1.158072	1.158084
AOWWeq	87.920528	87.856168	87.688549	87.413078	87.026822	86.582565	86.045523	85.488928	85.069641	84.937037
BOCax	1.174288	1.174290	1.174274	1.174259	1.174244	1.174223	1.174221	1.174213	1.174208	1.174231

Table S6. Calculated CO, W-W and imaginary frequencies and IR intensities at the eclipsed D_{4h} geometry

				SCS-MP2		B3LYP		B3LYP 2Na	
				IR		IR		IR	
				intensity /		intensity /		intensity /	
D_{4h}	Exp. ν /			ν / cm^{-1}	km mol^{-1}	ν / cm^{-1}	km mol^{-1}	ν / cm^{-1}	km mol^{-1}
irrep	cm^{-1}								
CO	A_{1g}	2019	Raman	2012.38	0.00	2069.70	0.00	2075.77	0.00
CO	A_{2u}	1937	IR	1955.69	1085.36	1990.13	1085.36	2009.68	783.08
CO	B_{1g}	1960	Raman	1903.10	0.35	1966.19	0.35	1988.72	0.00
CO	E_u	1863	IR	1895.74	4368.02	1954.59	4368.02	1979.03	3894.70
CO	B_{1u}	-	-	1858.37	0.01	1928.79	0.01	1952.91	0.00
CO	E_g	1904	Raman	1827.38	0.00	1897.31	0.00	1924.56	0.00
CO	A_{1g}	1794	Raman	1812.19	0.00	1865.75	0.00	1808.16	0.00
CO	A_{2u}	1772	IR	1794.88	3258.81	1850.15	3258.81	1792.85	3055.36
W-W	A_{1g}	97	Raman	100.20	0.01	88.19	0.01	91.99	0.00
W-W									
twist	A_{2g}	-	-	26.60i	-	26.39i	-	25.63i	-
	$A_{1g},$							65.03i,	
Na	A_{2u}	-	-	-	-	-	-	69.41i	-

Table S7. Calculated CO, W-W and imaginary frequencies and IR intensities at the staggered D_{4d} geometry

			SCS-MP2		B3LYP		B3LYP 2Na	
	D_{4d}	Exp ν / irrep cm^{-1}	ν / cm^{-1}	IR intensity / km mol^{-1}	ν / cm^{-1}	IR intensity / km mol^{-1}	ν / cm^{-1}	IR intensity / km mol^{-1}
CO	A_1	2019 Raman	2011.99	0.07	2068.69	0.00	2077.97	0.00
CO	B_2	1937 IR	1951.85	727.93	1988.22	1110.72	2007.39	544.34
CO	E_1	1863 IR	1893.77	4313.89	1951.33	4068.49	1976.63	3871.40
CO	E_2	1960 Raman	1882.76	0.03	1947.39	0.00	1971.00	200.00
CO	E_3	1904 Raman	1827.56	0.01	1898.92	0.00	1926.34	0.01
CO	A_1	1794 Raman	1809.78	5.21	1864.71	0.01	1806.67	0.01
CO	B_2	1772 IR	1793.60	3692.31	1848.48	3083.97	1790.16	3706.87
W-W	A_1	97 Raman	117.49	0.01	105.37	0.00	106.47	0.00
Na	A_1, B_2						64.04i, 69.31i	

References

1. G. M. Sheldrick, *Acta Cryst. Sect. A*, 2015, **71**, 3.
2. CrysAlisPRO version 39.46, Oxford Diffraction /Agilent Technologies UK Ltd, Yarnton, England.
3. G. M. Sheldrick, *Acta Cryst. Sect. C*, 2015, **71**, 3.
4. O. V. Dolomanov, L. J. Bourhis, R. J. Gildea, J. A. K. Howard, H. Puschmann, *J. Appl. Cryst.*, 2009, **42**, 339.
5. L. J. Farugia, *J. Appl. Cryst.*, 2012, **45**, 849.
6. Persistence of Vision (TM) Raytracer, Persistence of Vision Pty. Ltd., Williamstown, Victoria, Australia.
7. MOLPRO, version 2018.2, a package of ab initio programs, H.-J. Werner, P. J. Knowles, G. Knizia, F. R. Manby, M. Schütz, and others , see <https://www.molpro.net>.
8. A. D. Becke, *J. Chem. Phys.*, 1993, **98**, 5648.
9. C. Lee, W. Yang, R. G. Parr, *Phys. Rev. B*, 1988, **37**, 785.
10. S. H. Vosko, L. Wilk, M. Nusair, *Can. J. Phys.*, 1980, **58**, 1200.
11. J. P. Perdew, K. Burke, M. Ernzerhof, *Phys. Rev. Lett.*, 1996, **77**, 3865.
12. S. Grimme, J. Antony, S. Ehrlich, H. Krieg, *J. Chem. Phys.*, 2010, **132**, 154104.
13. I. Hyla-Kryspin and S. Grimme *Organometallics*, 2004, **23**, 5581-5592.
14. T. Schwabe, Stefan Grimme, and Jean-Pierre Djukic *J. Am. Chem. Soc.*, 2009, **131**, 14156-14157.
15. S. Grimme, J. Antony, S. Ehrlich, H. Krieg, *J. Chem. Phys.*, 2010, **132**, 154104.
16. F. R. Manby, P. J. Knowles, A. W. Lloyd, *J. Chem. Phys.*, 2001, **115**, 9144.
17. H. -J. Werner, F. R. Manby, P. J. Knowles, *J. Chem. Phys.*, 2003, **118**, 8149.
18. F. Weigend, R. Ahlrichs, *Phys. Chem. Chem. Phys.*, 2005, **7**, 3297.
19. F. Weigend, *Phys. Chem. Chem. Phys.*, 2006, **8**, 1057.
20. D. Andrae, U. Haeussermann, M. Dolg, H. Stoll, H. Preuss, *Theor. Chim. Acta*, 1990, **77**, 123.

- *Electronic Supplementary Information* -

21. G. Knizia, J. E. M. N. Klein, *Angew. Chem. Int. Ed.*, 2015, **54**, 5518.
22. AIMAll (Version 17.11.14), T. A. Keith, T. K. Gristmill Software, Overland Park KS, USA, 2019 (aim.tkgristmill.com).

Part III

Conclusion

This thesis's major focus has been novel bonding in uranium-containing molecules, and in particular uranium-nitrogen chemistry. The importance of using appropriate levels of theory is highlighted across this work, such as the reduced bond order on enlarging the active space in CASPT2 calculations of PUF_3 and AsUF_3 in Chapter 3, the varying $\text{U}-\text{N}_2$ bond lengths in the $\text{U(V)}-\text{N}_2$ complex of Chapter 4, and the use of DFT to perform calculations on a large number of model systems in Chapters 6 and 7. Various analytical techniques, such as NBO, IBO and QTAIM analyses have been used to study a spectrum of bonding motifs, from a $\text{U}\equiv\text{N}$ triple bond in NUF_3 , delocalised bonding in Chapters 5 and 6, to a weak $\text{U(V)}-\text{N}_2$ π backbond in Chapter 4.

The molecules EUF_3 ($\text{E} = \text{N-Bi}$) were studied in Chapter 3; NUF_3 , PUF_3 and AsUF_3 at the CASPT2 level, and SbUF_3 and BiUF_3 at the CASSCF level of theory. A [6,16] active space was used, to include σ and π bonding and antibonding orbitals, and nonbonding uranium and pnictogen orbitals. NUF_3 was identified as having a triple bond, consistent with previous calculations using a smaller [6,6] active space (including only σ and π bonding and antibonding orbitals).⁶⁰ However, for PUF_3 and AsUF_3 , the bonding description differs compared to previous work with the [6,6] active space which suggested an $\text{E}\equiv\text{U}$ triple bond. Instead, we identified a single bond with the π bond almost entirely broken in both cases. This is due to the occupation of nonbonding uranium f-orbitals and pnictogen d-orbitals, with occupancies of approximately 0.50 and 0.07 respectively in both cases. The smaller active space does not include these orbitals, favouring the triple bond description.

In Chapter 4, calculations were performed at various levels of theory on a novel uranium(v)-dinitrogen complex. The long $\text{U}-\text{N}_2$ bond length in the crystal structure (2.61 Å) is significantly underpredicted by DFT calculations (2.39 Å, PBE). Potential energy scans along the $\text{U}-\text{N}_2$ bond, on the full molecule and a model, demonstrate the potential is very shallow. Higher-level calculations (MP2 and RASSCF) give a longer $\text{U}-\text{N}_2$ bond length, with minima at 2.51 and 2.56

Å with MP2 and RASSCF respectively. For the RASSCF calculation, the crystal structure bond length 2.61 Å is only 0.80 kJ mol⁻¹ higher in energy than the minimum point of the scan, 2.56 Å.

The synthesis, characterisation and electronic structure of two U(IV) diuranium complexes were reported in Chapter 5. The diuranium bisnitride complex is the first such U(IV) complex isolated. The electronic structure in the U₂N₂ ring is similar to that of the bare molecule U₂N₂⁷⁷ with a delocalised 12-electron binding system composed of two σ and four π bonding orbitals. Negligible U-U bonding is observed, with remaining electrons occupying nonbonding 5*f_U* orbitals.

This work on U₂N₂ ring-containing complexes was furthered in Chapter 6, where the U(IV) complex studied in Chapter 5 is compared to a mixed U(IV)/U(V) and a U(V) diuranium bisnitride complex which have previously been reported.^{75,76,82} Similar bonding was found in all three complexes; a delocalised 12-electron bonding system. Calculations on charged models of these complexes show that higher uranium oxidation states result in greater degrees of covalency, driven by the increased 5*f_U* character of the bonding orbitals. U(IV) and U(V) model systems showed similar delocalised bonding to the experimentally isolated complexes, but U(VI) systems feature distinct bonding in the ring, with a pair of triple bonds and a pair of single bonds.

The complexes studied in Chapter 6 have implications for dinitrogen and other small molecule activation. The anionic complex featuring the calix-[4]-pyrrole ligand, **B** is a rare example of complete reduction of dinitrogen to nitride,⁷⁵ this is in contrast to the complex studied in Chapter 4 where dinitrogen is only very slightly activated. The complex encapsulated by siloxide ligands, **C**, shows reactivity to small molecules such as H₂ and additionally magnetic data suggests strong antiferromagnetic coupling. The novel properties and reactivity of these complexes underlines the importance of studying these bonding motifs. Future work will further

explore the capability of uranium to reduce N_2 , and induce small molecule activation, with the ultimate goal of uranium catalysis.

The magnetic properties of several U(IV) and U(V) complexes featuring a 'U₂X₂' diamond motif was studied in Chapter 7. Broken-symmetry DFT calculations were used to calculate the exchange coupling parameter J , and correlated with various NBO and QTAIM atomic and bond properties. Because the range of calculated values of J for the U(IV) systems was quite small, between -7.6 and -11.7 cm^{-1} , correlation to atomic and bond properties was poor. A greater range of calculated values of J for the U(V) systems was found, -15.4 to -92.4 cm^{-1} . Correlation between J and the QTAIM delocalisation indices $\delta(U|X)$ and $\delta(U|U)$ was identified. This work could be furthered by using a greater variety of bridging and bonding motifs, with a focus on those which exhibit significant covalency; model complexes could be used to reduce computational cost.

Finally, in Chapter 8 a brief foray was made into transition metal chemistry where the isolation of the ditungsten decacarbonyl dianion was reported. Surprisingly, the geometry of the crystal structure obtained was in the eclipsed geometry. Calculations at several levels of theory, from DFT to CCSD(T), were performed on $W_2CO_{10}^{2-}$ in the gas phase. These calculations demonstrated a consistent preference for the staggered geometry, suggesting the observed eclipsed conformer is due to crystal packing forces.

Bibliography

- (1) D. M. King, F. Tuna, E. J. McInnes, J. McMaster, W. Lewis, A. J. Blake and S. T. Liddle, *Nature Chemistry*, 2013, **5**, 482–488.
- (2) M. J. Bezdek, I. Pappas and P. J. Chirik, in *Nitrogen Fixation*, ed. Y. Nishibayashi, Springer International Publishing, Cham, 2017, pp. 1–21.
- (3) H. Liu, T. Ghatak and M. S. Eisen, *Chem. Commun.*, 2017, **53**, 11278–11297.
- (4) M. Falcone, L. Barluzzi, J. Andrez, F. Fadaei Tirani, I. Zivkovic, A. Fabrizio, C. Corminboeuf, K. Severin and M. Mazzanti, *Nature Chemistry*, 2019, **11**, 154–160.
- (5) B. E. Atkinson, H.-S. Hu and N. Kaltsoyannis, *Chem. Commun.*, 2018, **54**, 11100–11103.
- (6) E. Lu, B. E. Atkinson, A. J. Wooles, J. T. Boronski, L. R. Doyle, F. Tuna, J. D. Cryer, P. J. Cobb, I. J. Vitorica-Yrezabal, G. F. S. Whitehead, N. Kaltsoyannis and S. T. Liddle, *Nature Chemistry*, 2019, **11**, 806–811.
- (7) J. P. A. Ostrowski, B. E. Atkinson, L. R. Doyle, A. J. Wooles, N. Kaltsoyannis and S. T. Liddle, *Dalton Trans.*, 2020, **49**, 9330–9335.
- (8) P. W. Atkins and R. S. Friedman, *Molecular Quantum Mechanics*, Oxford University Press, 2011.
- (9) J. G. Hill, *International Journal of Quantum Chemistry*, 2013, **113**, 21–34.
- (10) F. Jensen, *Introduction to computational chemistry*, John Wiley & Sons, 2009.
- (11) C. J. Cramer, *Essentials of Computational Chemistry: Theories and Models*, John Wiley and Sons, 2014.
- (12) In, *Ideas of Quantum Chemistry*, ed. L. Piela, Elsevier, Amsterdam, 2007, pp. 498–566.

- (13) In, *Multiconfigurational Quantum Chemistry*, John Wiley & Sons, Ltd, 2016, ch. 9, pp. 103–130.
- (14) J. Paldus, *The Journal of Chemical Physics*, 1974, **61**, 5321–5330.
- (15) L. Gagliardi, B. O. Roos, P. Å. Malmqvist and J. M. Dyke, *Journal of Physical Chemistry A*, 2001, **105**, 10602–10606.
- (16) V. Sauri, L. Serrano-Andrés, A. R. M. Shahi, L. Gagliardi, S. Vancoillie and K. Pierloot, *Journal of Chemical Theory and Computation*, 2011, **7**, 153–168.
- (17) In, *Multiconfigurational Quantum Chemistry*, John Wiley & Sons, Ltd, 2016, ch. 12, pp. 143–156.
- (18) P. Pulay, *International Journal of Quantum Chemistry*, 2011, **111**, 3273–3279.
- (19) P.-O. Löwdin, *Phys. Rev.*, 1955, **97**, 1474–1489.
- (20) P. Hohenberg and W. Kohn, *Physical Review*, 1964, **136**, B864–B871.
- (21) J. P. Perdew and K. Schmidt, *AIP Conference Proceedings*, 2001, **577**, 1–20.
- (22) P. A. M. Dirac, *Mathematical Proceedings of the Cambridge Philosophical Society*, 1930, **26**, 376–385.
- (23) S. H. Vosko, L. Wilk and M. Nusair, *Canadian Journal of Physics*, 1980, **58**, 1200–1211.
- (24) J. P. Perdew, K. Burke and M. Ernzerhof, *Physical Review Letters*, 1996, **77**, 3865–3868.
- (25) C. Lee, W. Yang and R. G. Parr, *Phys. Rev. B*, 1988, **37**, 785–789.
- (26) J. Tao, J. P. Perdew, V. N. Staroverov and G. E. Scuseria, *Phys. Rev. Lett.*, 2003, **91**, 146401.
- (27) Y. Zhao and D. G. Truhlar, *The Journal of Chemical Physics*, 2006, **125**, 194101.
- (28) A. D. Becke, *The Journal of Chemical Physics*, 1993, **98**, 5648–5652.

- (29) J. P. Perdew, M. Ernzerhof and K. Burke, *Journal of Chemical Physics*, 1996, **105**, 9982–9985.
- (30) S. Grimme, *The Journal of Chemical Physics*, 2006, **124**, 034108.
- (31) L. Goerigk and S. Grimme, *Physical Chemistry Chemical Physics*, 2011, **13**, 6670.
- (32) N. Mardirossian and M. Head-Gordon, *Molecular Physics*, 2017, **115**, 2315–2372.
- (33) M. G. Medvedev, I. S. Bushmarinov, J. Sun, J. P. Perdew and K. A. Lyssenko, *Science*, 2017, **355**, 49–52.
- (34) K. P. Kepp, *Science*, 2017, **356**, 496.2–496.
- (35) D. Reta, F. Ortu, S. Randall, D. P. Mills, N. F. Chilton, R. E. Winpenny, L. Natrajan, B. Edwards and N. Kaltsoyannis, *Journal of Organometallic Chemistry*, 2018, **857**, 58–74.
- (36) S. Grimme, J. Antony, S. Ehrlich and H. Krieg, *The Journal of Chemical Physics*, 2010, **132**, 154104.
- (37) L. Gagliardi and B. O. Roos, *Chemical Society Reviews*, 2007, **36**, 893.
- (38) R. D. Reynolds and T. Shiozaki, *Journal of Chemical Theory and Computation*, 2019, **15**, 1560–1571.
- (39) S. Knecht, H. J. A. Jensen and T. Saue, *Nature Chemistry*, 2019, **11**, 40–44.
- (40) X. Cao, M. Dolg and H. Stoll, *Journal of Chemical Physics*, 2003, **118**, 487–496.
- (41) M. Dolg and X. Cao, *The Journal of Physical Chemistry A*, 2009, **113**, 12573–12581.
- (42) K. A. Peterson and J. G. Hill, in *Annual Reports in Computational Chemistry*, Elsevier B.V., 1st edn., 2018, vol. 14, pp. 47–74.
- (43) F. Aquilante, J. Autschbach, A. Baiardi, S. Battaglia, V. A. Borin, L. F. Chibotaru, I. Conti, L. De Vico, M. Delcey, I. Fdez. Galván, N. Ferré, L. Freitag, M. Garavelli, X. Gong, S. Knecht, E. D. Larsson, R. Lindh, M. Lundberg, P. Å. Malmqvist, A. Nenov, J. Norell,

- M. Odelius, M. Olivucci, T. B. Pedersen, L. Pedraza-González, Q. M. Phung, K. Pierloot, M. Reiher, I. Schapiro, J. Segarra-Martí, F. Segatta, L. Seijo, S. Sen, D.-C. Sergentu, C. J. Stein, L. Ungur, M. Vacher, A. Valentini and V. Veryazov, *The Journal of Chemical Physics*, 2020, **152**, 214117.
- (44) G. Knizia, *Journal of Chemical Theory and Computation*, 2013, **9**, 4834–4843.
- (45) G. Knizia and J. E. M. N. Klein, *Angewandte Chemie International Edition*, 2015, **54**, 5518–5522.
- (46) F. Weinhold, *Journal of Computational Chemistry*, 2012, **33**, 2363–2379.
- (47) R. F. Bader, *Atoms in molecules: a quantum theory*, Clarendon Pr., 1990.
- (48) J. Pipek and P. G. Mezey, *The Journal of Chemical Physics*, 1989, **90**, 4916–4926.
- (49) J. M. Foster and S. F. Boys, *Rev. Mod. Phys.*, 1960, **32**, 300–302.
- (50) I. Mayer, *Journal of Computational Chemistry*, 2007, **28**, 204–221.
- (51) S. S. Rudel, H. L. Deubner, M. Müller, A. J. Karttunen and F. Kraus, *Nature Chemistry*, 2020, DOI: 10.1038/s41557-020-0505-5.
- (52) R. J. Boyd, *An Introduction to the Quantum Theory of Atoms in Molecules*, 2007, pp. 1–8.
- (53) A. R. Mountain and N. Kaltsoyannis, *Dalton Transactions*, 2013, **42**, 13477–13486.
- (54) Q. R. Huang, J. R. Kingham and N. Kaltsoyannis, *Dalton Transactions*, 2015, **44**, 2554–2566.
- (55) R. Beekmeyer and A. Kerridge, *Inorganics*, 2015, **3**, 482–499.
- (56) M. L. Neidig, D. L. Clark and R. L. Martin, *Coordination Chemistry Reviews*, 2013, **257**, 394–406.
- (57) R. G. Denning, *Journal of Physical Chemistry A*, 2007, **111**, 4125–4143.

- (58) D. W. Green and G. T. Reedy, *The Journal of Chemical Physics*, 1976, **65**, 2921–2922.
- (59) D. M. King and S. T. Liddle, *Coordination Chemistry Reviews*, 2014, **266-267**, 2–15.
- (60) L. Andrews, X. Wang, R. Lindh, B. O. Roos and C. J. Marsden, *Angewandte Chemie International Edition*, 2008, **47**, 5366–5370.
- (61) L. Andrews, X. Wang and B. O. Roos, *Inorganic Chemistry*, 2009, **48**, 6594–6598.
- (62) X. Wang and L. Andrews, *Dalton Transactions*, 2009, 9260.
- (63) X. Wang, L. Andrews and C. J. Marsden, *Chemistry - A European Journal*, 2007, **13**, 5601–5606.
- (64) X. Wang, L. Andrews and C. J. Marsden, *Chemistry - A European Journal*, 2008, **14**, 9192–9201.
- (65) L. Andrews, H.-G. Cho, K. S. Thanthiriwatte and D. A. Dixon, *Inorganic Chemistry*, 2017, **56**, 2949–2957.
- (66) D. M. King, F. Tuna, E. J. L. McInnes, J. McMaster, W. Lewis, A. J. Blake and S. T. Liddle, *Science*, 2012, **337**, 717–720.
- (67) B. M. Gardner, G. Balázs, M. Scheer, F. Tuna, E. J. McInnes, J. McMaster, W. Lewis, A. J. Blake and S. T. Liddle, *Nature Chemistry*, 2015, **7**, 582–590.
- (68) M. R. Duttera, V. W. Day and T. J. Marks, *Journal of the American Chemical Society*, 1984, **106**, 2907–2912.
- (69) Q. Y. Wu, J. H. Lan, C. Z. Wang, Y. L. Zhao, Z. F. Chai and W. Q. Shi, *Journal of Physical Chemistry A*, 2015, **119**, 922–930.
- (70) B. M. Gardner, G. Balázs, M. Scheer, F. Tuna, E. J. McInnes, J. McMaster, W. Lewis, A. J. Blake and S. T. Liddle, *Angewandte Chemie - International Edition*, 2014, **53**, 4484–4488.

- (71) T. M. Rookes, E. P. Wildman, G. Balázs, B. M. Gardner, A. J. Wooles, M. Gregson, F. Tuna, M. Scheer and S. T. Liddle, *Angewandte Chemie - International Edition*, 2018, **57**, 1332–1336.
- (72) P. Roussel and P. Scott, *Journal of the American Chemical Society*, 1998, **120**, 1070–1071.
- (73) N. Kaltsoyannis and P. Scott, *Chemical Communications*, 1998, **3**, 1665–1666.
- (74) P. Roussel, W. Errington, N. Kaltsoyannis and P. Scott, *Journal of Organometallic Chemistry*, 2001, **635**, 69–74.
- (75) I. Korobkov, S. Gambarotta and G. P. A. Yap, *Angewandte Chemie International Edition*, 2002, **41**, 3433–3436.
- (76) C. Camp, J. Pécaut and M. Mazzanti, *Journal of the American Chemical Society*, 2013, **135**, 12101–12111.
- (77) B. Vlaisavljevich, L. Andrews, X. Wang, Y. Gong, G. P. Kushto and B. E. Bursten, *Journal of the American Chemical Society*, 2016, **138**, 893–905.
- (78) G. Feng, M. Zhang, D. Shao, X. Wang, S. Wang, L. Maron and C. Zhu, *Nature Chemistry*, 2019, 18–23.
- (79) G. Feng, M. Zhang, P. Wang, S. Wang, L. Maron and C. Zhu, *Proceedings of the National Academy of Sciences*, 2019, **116**, 17654–17658.
- (80) A. R. Fox, S. C. Bart, K. Meyer and C. C. Cummins, *Nature*, 2008, **455**, 341–349.
- (81) B. M. Gardner, J. C. Stewart, A. L. Davis, J. McMaster, W. Lewis, A. J. Blake and S. T. Liddle, *Proceedings of the National Academy of Sciences*, 2012, **109**, 9265–9270.
- (82) L. Barluzzi, M. Falcone and M. Mazzanti, *Chemical Communications*, 2019, **55**, 13031–13047.

- (83) C. T. Palumbo, R. Scopelliti, I. Zivkovic and M. Mazzanti, *Journal of the American Chemical Society*, 2020, **142**, 3149–3157.
- (84) P. L. Arnold, T. Ochiai, F. Y. Lam, R. P. Kelly, M. L. Seymour and L. Maron, *Nature chemistry*, 2020, **12**, 654–659.
- (85) G. Nocton, P. Horeglad, J. Pécaut and M. Mazzanti, *Journal of the American Chemical Society*, 2008, **130**, 16633–16645.
- (86) D. P. Mills, F. Moro, J. McMaster, J. van Slageren, W. Lewis, A. J. Blake and S. T. Liddle, *Nature Chemistry*, 2011, **3**, 454–460.
- (87) B. Teyar, S. Boucenina, L. Belkhiri, B. Le Guennic, A. Boucekkine and M. Mazzanti, *Inorganic Chemistry*, 2019, **58**, 10097–10110.
- (88) F. A. Cotton and C. B. Harris, *Inorganic Chemistry*, 1965, **4**, 330–333.
- (89) B. O. Roos, A. C. Borin and L. Gagliardi, *Angewandte Chemie - International Edition*, 2007, **46**, 1469–1472.
- (90) L. N. Gorokhov, A. Emelyanov and Y. S. Khodeev, *High temperature*, 1974, **12**.
- (91) L. Gagliardi and B. O. Roos, *Nature*, 2005, **433**, 848–851.
- (92) B. O. Roos, P. Å. Malmqvist and L. Gagliardi, *Journal of the American Chemical Society*, 2006, **128**, 17000–17006.
- (93) P. F. Souter, G. P. Kushto, L. Andrews and M. Neurock, *Journal of the American Chemical Society*, 1997, **119**, 1682–1687.
- (94) J. Raab, R. H. Lindh, X. Wang, L. Andrews and L. Gagliardi, *The Journal of Physical Chemistry A*, 2007, **111**, 6383–6387.
- (95) X. Zhang, W. Li, L. Feng, X. Chen, A. Hansen, S. Grimme, S. Fortier, D. C. Sergentu, T. J. Duignan, J. Autschbach, S. Wang, Y. Wang, G. Velkos, A. A. Popov, N. Aghdassi, S.

- Duhm, X. Li, J. Li, L. Echegoyen, W. H. Schwarz and N. Chen, *Nature Communications*, 2018, **9**, 1–8.
- (96) M. Falcone, L. Chatelain, R. Scopelliti, I. Živković and M. Mazzanti, *Nature*, 2017, **547**, 332–335.
- (97) S. M. Mansell, J. H. Farnaby, A. I. Germeroth and P. L. Arnold, *Organometallics*, 2013, **32**, 4214–4222.
- (98) F. G. N. Cloke and P. B. Hitchcock, *Journal of the American Chemical Society*, 2002, **124**, 9352–9353.
- (99) S. M. Mansell, N. Kaltsoyannis and P. L. Arnold, *Journal of the American Chemical Society*, 2011, **133**, 9036–9051.
- (100) P. B. Duval, C. J. Burns, W. E. Buschmann, D. L. Clark, D. E. Morris and B. L. Scott, *Inorganic Chemistry*, 2001, **40**, 5491–5496.
- (101) M. Falcone, C. E. Kefalidis, R. Scopelliti, L. Maron and M. Mazzanti, *Angewandte Chemie - International Edition*, 2016, **55**, 12290–12294.
- (102) M. Falcone, L. N. Poon, F. Fadaei Tirani and M. Mazzanti, *Angewandte Chemie*, 2018, **130**, 3759–3762.
- (103) J. Du, D. M. King, L. Chatelain, E. Lu, F. Tuna, E. J. McInnes, A. J. Wooles, L. Maron and S. T. Liddle, *Chemical Science*, 2019, **10**, 3738–3745.
- (104) M. Falcone, L. Chatelain and M. Mazzanti, *Angewandte Chemie - International Edition*, 2016, **55**, 4074–4078.
- (105) R. Schlögl, *Angewandte Chemie - International Edition*, 2003, **42**, 2004–2008.
- (106) V. Mougel, P. Horeglad, G. Nocton, J. Pécaut and M. Mazzanti, *Angewandte Chemie*, 2009, **121**, 8629–8632.

- (107) P. L. Arnold, J. B. Love and D. Patel, *Coordination Chemistry Reviews*, 2009, **253**, 1973–1978.
- (108) O. P. Lam, F. W. Heinemann and K. Meyer, *Chemical Science*, 2011, **2**, 1538.
- (109) P. L. Arnold, G. M. Jones, S. O. Odoh, G. Schreckenbach, N. Magnani and J. B. Love, *Nature Chemistry*, 2012, **4**, 221–227.
- (110) S. X. Hu, J. Jian, J. Li and J. K. Gibson, *Inorganic Chemistry*, 2019, **58**, 10148–10159.
- (111) L. Chatelain, R. Scopelliti and M. Mazzanti, *Journal of the American Chemical Society*, 2016, **138**, 1784–1787.
- (112) F. Burdet, J. Pécaut and M. Mazzanti, *Journal of the American Chemical Society*, 2006, **128**, 16512–16513.
- (113) K. Yamaguchi, F. Jensen, A. Dorigo and K. Houk, *Chemical Physics Letters*, 1988, **149**, 537–542.
- (114) J. L. Brown, G. Wu and T. W. Hayton, *Organometallics*, 2013, **32**, 1193–1198.
- (115) C. Camp, M. A. Antunes, G. García, I. Ciofini, I. C. Santos, J. Pécaut, M. Almeida, J. Marçalo and M. Mazzanti, *Chem. Sci.*, 2014, **5**, 841–846.
- (116) B. M. Gardner, D. M. King, F. Tuna, A. J. Wooles, N. F. Chilton and S. T. Liddle, *Chemical Science*, 2017, **8**, 6207–6217.
- (117) P. L. Arnold, L. Puig-Urrea, J. A. Wells, D. Yuan, F. L. Cruickshank and R. D. Young, *Dalton Transactions*, 2019, **48**, 4894–4905.
- (118) G. Blyholder, *The Journal of Physical Chemistry*, 1964, **68**, 2772–2777.